学位論文

X-ray Spectral Studies with *Suzaku* of Hot Flows Accreting onto Weakly-Magnetized Neutron Stars
(「すざく」のX線分光を用いた弱磁場中性子星への高温降着流の研究)

平成29年12月博士(理学)申請

東京大学大学院理学系研究科
物理学専攻
小野 光

Abstract

A Low-Mass X-ray Binary (LMXB) is a close binary consisting of a low-mass star and a weakly magnetized ($\lesssim 10^9$ G) neutron star (NS). It becomes a luminous X-ray source, as the matter which accretes from the star onto the NS release most of the gravitational energies into X-rays. Because the mass and radius of NSs are relatively well understood, LMXBs provide an ideal environment to construct a general picture of mass accretion under extremely strong gravity but without affected by strong magnetic fields. In the present thesis, we aim at this goal through X-ray spectroscopy.

LMXBs exhibit two typical state in view of X-ray spectrum. One is called the Soft State realized when the luminosity is $L_{\rm t} \gtrsim 10^{37}$ erg s^{-1}, wherein the spectrum has a convex shape typical of a thermal emission. It is understood as a sum of emission from an optically thick and geometrically thin multi-color disk (Mitsuda et al. 1984), plus a hotter blackbody emission from the NS surface which is weakly Comptonized by a hotter electron cloud called "corona". The other is called the Hard State, typically showing a much harder power-low shape spectrum extending to $>$ 20 keV with a cut-off at high energy around $\gtrsim$ 50 keV. Since smaller number of photons (due to lower luminosity) are is spread over a wider energy range, observational studies of the Hard State had to wait for the advent of X-ray astrophysics satellites, including Japanese *Suzaku*, with high sensitivities in the hard X-ray range of 10–100 keV.

Analyzing wide-band (1–100 keV) *Suzaku* spectra of LMXBs, Sakurai (2015) revealed that LMXB spectra in the Hard State can be explained with the same model as described above, but with much stronger Comptonization by even hotter accreting coronal flows. However, such unified view was primarily based only on one object called Aquila X-1. In addition, the Comptonizing agent was understood rather phenomenologically just as a hot electron cloud, rather than an accretion flow. Specifically, the geometry of the Comptonizing corona represented by its scale height, its motion, and its density, have all remained rather unknown.

To solve the problem described above, we analyzed 19 *Suzaku* archival data sets of 5 sources. They were selected via two criterion; either those objects which happened to be observed at an epoch close to a transition between the two states, or the sources which were observed both in the Soft and Hard States. The former criterion left us with 3 data sets of 3 sources in total, including Aql X-1, and the latter 16 data sets of 3 sources (overlapping 1 source). The luminosity of these LMXBs ranged from $L_{\rm t} \sim 10^{36}$ erg s^{-1} to $\sim 10^{38}$ erg s^{-1}; 5 observations out of the 19 were in the Hard State, 13 were in the Soft State, and the remaining one very fortunately caught a very narrow timing of Hard-to-Soft transition of Aquila X-1.

Through standard model-fitting analysis, essentially all the spectra have been explained by the unified spectral model of Sakurai et al. (2012; 2014) described above, with physically reasonable parameter values. Therefore, we can now regard this model as a true unification of the two States of LMXBs. The bimodal behavior of these objects was found to manifest itself

most clearly as very sensitive changes of the luminosities of the Comptonized photons and of the multi-color disk emission, in response to small change of $L_{\rm t}$ across the state transition. The blackbody luminosity of all the sources was systematically lower than expected; this suggests that $\lesssim 15\%$ of the accretion energy is used to spin up the NS, rather than to emit blackbody photons.

The previously known hysteresis effects in the transition were confirmed clearly, as a large (factor ~ 5) scatter of the transition threshold luminosity among the objects, and between the rising and declining phases of the same object. To remove the contributions from distance uncertainties on this scatter, we have introduced a distance-free new quantity $Q \equiv T_{\rm e}/T_{\rm BB}$, which represents the balance of Coulomb heating and Compton cooling of the Comptonizing electrons. Then, the behavior of various spectral parameters has been described in a unified way as a function of Q, and the pure effects of hysteresis have been identified; the clearest one is a common elongated loop on the $R_{\rm BB}$ vs $T_{\rm BB}$ plane, along which all the sources evolve through their long-term luminosity changes.

The hysteresis effect make the coronal scale height larger when $L_{\rm t}$ is increasing than it is decreasing; in response, the blackbody-emitting area on the NS surface varies, to produce the hysteresis loop rather than a single-valued $R_{\rm BB}$ vs $T_{\rm BB}$ relation. The Hard State is characterized by a disk truncation at $20-30$ km from the NS center, where the flow changes into the hot and inflated corona with a large scale height. In the Soft State, the disk gets closer to the NS, and the corona shrinks both horizontally and vertically. Thus, these clear differences between the two states can be understood as the theoretically predicted bimodality between optically-thin and geometrically-thick flows, versus optically-thick and geometrically-thin disk. Through all the observations, the Comptonizing corona was found to fall radially with a relatively low velocity, which is only $\lesssim 10\%$ of the free fall velocity.

In the present thesis, we have thus obtained a unified understanding of accretion flows in LMXBs, including the state-transition phenomena and the hysteresis effects.

Contents

List of Figures

List of Tables

Chapter 1

INTRODUCTION

Since the discovery of a pulsar by Hewish (1968), neutron stars (NSs) have attracted us as an ideal laboratory to study high-density nuclear matter, mass accretion dynamics under strong gravity, and physics of ultra-strong magnetic fields. In the present thesis, we focus on accretion physics onto NSs, which gives clearer view and has large impact on other accreting systems. Since the radiation luminosity of an accreting NS is directly proportional to its mass accretion rate, it provides a simpler system than an accreting blackhole (BH), where some (often unknown) fraction of the gravitational energy release disappears beyond the event horizon. We especially choose NS Low-Mass X-ray Binaries (hereafter LMXBs), which are close binaries consisting of weakly magnetized ($\lesssim 10^8$ G) NSs working as mass accretors, and low-mass stars (with masses of $< 1\ M_\odot$) as mass donors. In these systems, pure effects of strong gravity on the accreting matter (usually Hydrogen-rich plasma) can be evaluated under well constrained mass and radius of the compact star. Understanding of such basic systems can provide a basis for studying other systems with additional complexity, such as strong magnetic fields. Since the gravitational potential energy at an NS surface reaches $\sim 20\%$ of the rest-mass energy, the accreting gas is strongly heated up to $\sim 10^7$ K or higher, to emit most of its energy as X-rays. Thus, the X-ray wavelengths provide the most suited tool to study the physics of accretion in LMXBs.

As represented by the first discovered cosmic X-ray object, Scorpius X-1 (Giacconi et al. 1962), LMXBs constitute a major fraction of bright Galactic X-ray sources, and have been studied for more than 4 decades. They are associated with the Galactic bulge rather than the disk. So far, as many as ∼200 LMXBs have been identified (§2.2.1), with their X-ray luminosities spaning a range of 10^{32} erg s^{-1} to 10^{38} erg s^{-1}. Many of them show X-ray intensity fluctuations on various time scales, from seconds, minutes to several months (Parsignault & Grindlay 1978). Most of them lack pulsations, which implies that the magnetic fields of NSs in LMXBs are weak, typically $\lesssim 10^9$ G (§2.2.1). Although the optical counterparts have been detected from a fair fraction of the catalogued LMXBs, their optical light is dominated by those arising from accretion disks surrounding the NSs, rather than the intrinsic emission from their low-mass companion stars.

In the 1980s, the X-ray spectra of LMXBs were extensively studied, with several X-

ray satellites including *Tenma* (Tanaka et al. 1984). These spectra show convex shapes as presented in figure 1.1 in black, and were explained successfully as blackbody from the NS surface (with weak Comptonization), plus softer thermal radiation from so called standard accretion disk (Mitsuda et al. 1984). The standard accretion disk is optically thick and geometrically thin, and the matter motion at any radius is nearly Keplerian (§2.3.2). This typical state of the spectrum is called the Soft State, and is realized when the X-ray luminosity is $L \gtrsim 10^{36}$ erg s^{-1}.

As the X-ray observations at higher energy range became more and more sensitive, many LMXBs with lower luminosity at $L \lesssim 10^{36}$ erg s^{-1} were found. As shown in figure 1.1 in red, their spectra extend up to $\sim 50 - 100$ keV with a power-law like shape, and appear totally different from those in the Soft State. This spectral state is called the Hard State. Thanks to the Japanese *Suzaku* X-ray observatory with high sensitivity over a broad energy band, LMXBs have been observed down to $L \sim 10^{32}$ erg s^{-1}. These rich *Suzaku* data enabled us to study their Hard State in detail (Sakurai et al. 2012; 2014; Zhang et al. 2014; Ono et al. 2016; 2017). These works revealed that the hard-state spectra are explained with the same two-component model as that for the Soft State, but with considerably different parameters. The largest difference is that the blackbody component in the Hard State is very strongly Comptonized by hot thermal electrons (often called coronae) to form the hard continuum up to ~ 100 keV. Another difference is that the inner disk edge recedes farther from the NS surface in the Hard State.

The two spectral states of LMXBs are generally explicable in terms of intrinsic binmodality of accretion flows. Under high accretion rates, the in-flowing matter has high densities, so that enhanced radiation emissivity makes it much cooler (e.g., ~ 1 keV) than the free-fall temperature (~ 200 MeV). The matter, with its angular momentum, hence forms a "geometrically-thin and optically thick" cool accretion disk, which rotates around the NS with nearly Keplerian velocities. This is the Soft State. When the accretion rate decreases and the flow density gets lower, the matter becomes very hot due to reduced radiation emissivity. Then, the flow is vertically inflated, leading to further emissivity decrease. As a result, the accreting matter takes a form of "geometrically-thick and optically-thin" hot flow which is observed as a corona, having a significant radial velocity component. This is the Hard State, wherein blackbody photons from the heated NS surface are strongly Comptonized by the following coronal in-flow. Although the gross picture is thus simple, the reality is more complex: e.g., the corona is present even in the Soft State, and produce some Comptonization effects in the spectra. Thus, we need to improve our understanding of the hot coronae, including its physical state, geometry, dynamics, and response to the accretion-rate changes. Here, the difficulty resides partially in the fact that ions and electrons in such low-density hot flows tend to take distinct temperatures, and only the electron temperature can be measured.

Since the most dramatic changes of the coronal flows take place during transitions between the two states, the best way to understand their behavior is to utilize observations which were made just around or across the transition thresholds. Fortunately, we have already made a good first step with a particular *Suzaku* observation of Aquila X-1 (hereafter

Aql X-1), which happened to catch a Hard-to-Soft state transition (Ono et al. 2017). There, the geometry and dynamics of the Comptonizing corona were both found to change significantly but continuously across the transition. Then, by studying similar observations of this or other sources, we can generalize the results from Aql X-1 to other LMXBs, and better understand the behavior of the corona. Nevertheless, the state transitions are rare and not frequently observed. Thus, we analyze the available archive X-ray data using the following two strategies. One is to utilize those data sets of any LMXBs that were by chance acquired near their sate-transition thresholds. The other is to study those LMXBs which were observed both in the Soft and Hard states, usually on different occasions. The latter includes transient LMXBs exhibiting large outbursts (such as Aql X-1). In either case, the data do not necessarily need to cover the exact moments of transition. We utilize data from the Japanese X-ray observatory *Suzaku*, which carries onboard two detectors; the XIS (X-ray Imaging Spectrometer) sensitive in the 0.2–12 keV range, and the HXD (Hard X-ray Detector) which observes in the 10– 600 keV band. The XIS data will allow us to quantify the optically-thick thermal radiation from LMXBs, and the HXD data will tell us information about the Comptonization in the Hard State. In the present thesis, the cgs system of units is used.

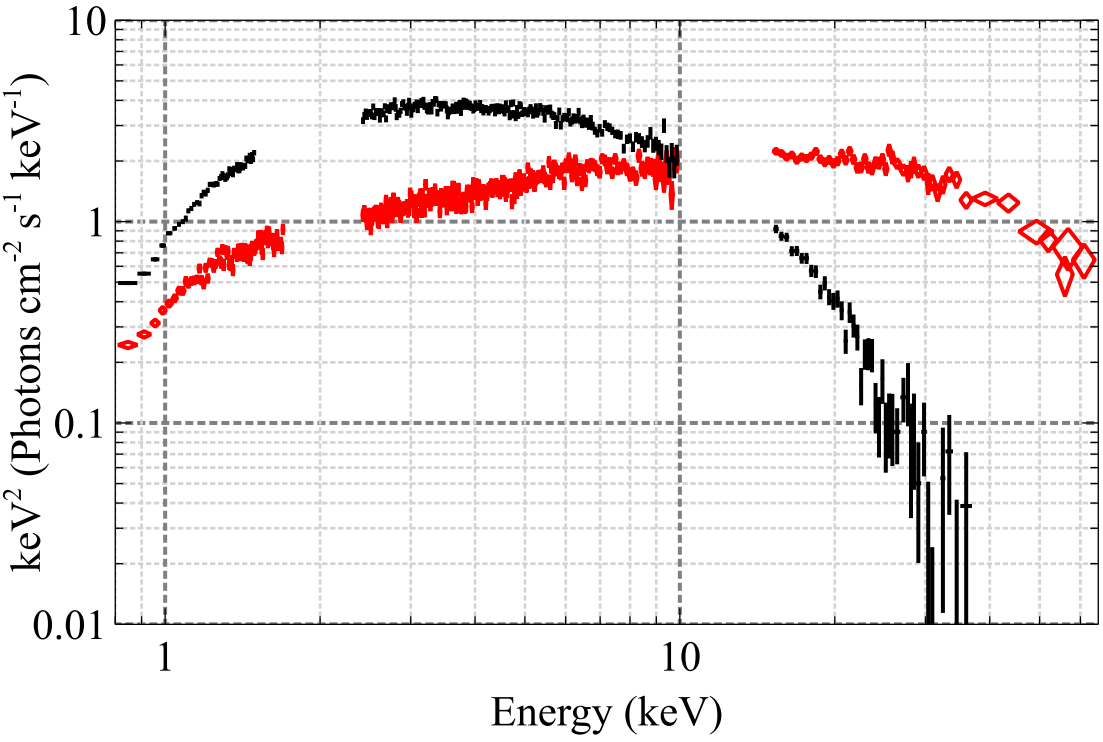

Figure 1.1: $\nu F\nu$ spectra of Aquila X-1 in the Soft State (black) and the Hard State (red), obtained with the *Suzaku* XIS (< 10 keV) and HXD (> 10 keV).

Chapter 2

Review

2.1 Cosmic X-ray Sources

When observed in X-rays, the universe reveals, on various spatial and temporal scales, its dynamical and energetic aspects which are totally different from those seen in optical light. The cosmic X-ray sources were first recognized by serendipity in 1962 with a sounding rocket flying only a few minutes above the opaque atmosphere. The strongest source discovered on that occasion was named Scorpius X-1 and identified optically, by the 188 cm Okayama telescope of the Tokyo Astronomical Observation, with a 13 magnitude unusually blue object (Sandage et al. 1966); it was later understood as an LMXB. Subsequent X-ray satellites, including a series of Japanese missions, revealed wealth of X-ray sources including white dwarfs, NSs, black holes, supernova remnants, and galaxy clusters, spanning a scale of $\sim$ km to $\sim 10^{20}$ km.

Among the variety of X-ray sources, compact objects (white dwarfs, NSs, and black holes) are interesting not only as the end points of nuclear burning stars, but also as laboratories of matters under extreme conditions, including ultra-high densities, relativistic motions, strong gravity, and intense magnetic fields. When these objects with strong gravity form close binary systems with ordinary stars, some portion of the stellar gas is gravitationally captured by the compact objects, and accretes onto them, while converting its gravitational energy into radiation.

Observationally, NSs are classified in various ways. As figure 2.1 shows, they are for example classified in terms of their magnetic fields and (i.e., rotational) pulse periods. Radio pulsars, the most dominant popuation, are rotation-powered NSs with relatively strong magnetic fields and short pulse periods, and magnetars with the strongest magnetic fields ($B_{\rm d} \gtrsim 10^{13}$ G) are magnetically-powered ones. Accretion-powered NSs are largely classified into two categories, LMXBs and Binary X-ray Pulsars, with different values of B as indicated in figure 2.1. Most of Binary X-ray Pulsars have massive ($\gtrsim 10 M_\odot$) primary stars and are classified into High-Mass X-ray Binaries (HMXBs). While NSs in HMXBs capture dense stellar winds from the high-mass stars and emit strongly pulsed X-rays, NSs in LMXBs accrete mass via Roche-lobe overflow (§2.2.2). Further details of LMXBs are given in §2.2.

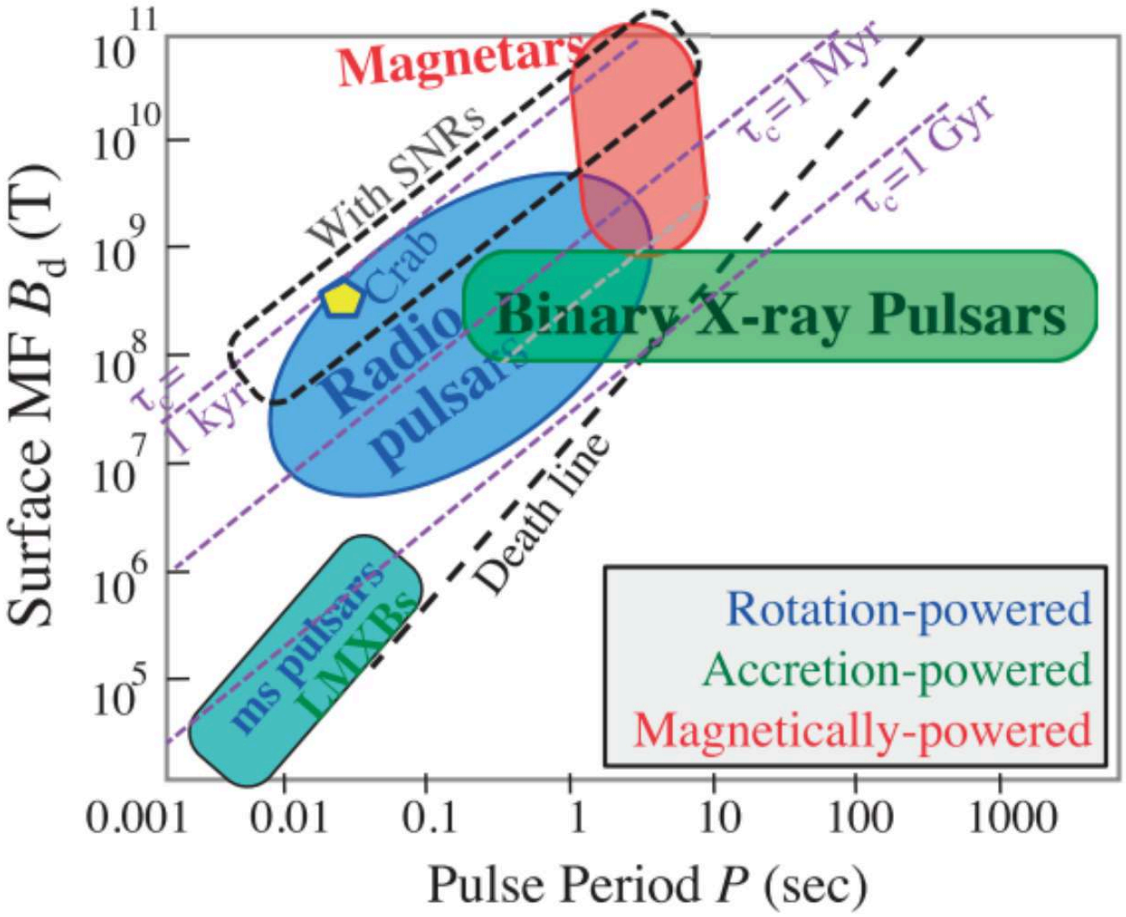

Figure 2.1: A schematic classification of NSs referring to the pulse period P and the surface magnetic field (dipole component) $B_{\rm d}$, taken from Makishima (2016). 10^8 T is equal to 10^{12} G. Blue, green, and red indicate rotation powered, accretion powered, and magnetically powered NSs, respectively.

2.2 Low-Mass X-ray Binaries

2.2.1 Basic properties

As already described in Chapter 1, LMXBs are binaries consisting of weakly-magnetized ($< 10^9$ G) NSs and Low-Mass ($\lesssim 1 M_\odot$) stars. Figure 2.2 shows their Galactic distribution, in comparison with that of HMXBs. While HMXBs are strongly concentrated in the galactic plane, LMXBs have much larger scale heights. This is because LMXBs are old systems with a typical life time of $\sim 10^{7-9}$ yr, while HMXBs are young with short life times of $\sim 10^{5-7}$ yr. LMXBs are ubiquitous X-ray sources not only in the Milky way but also in nearby galaxies. In our Galaxy, the integrated luminosity of LMXBs is dominant among all X-ray sources, and is an order of magnitude higher than that of HMXBs (Grimm et al. 2002). In nearby galaxies, the integrated X-ray luminosity of LMXBs exhibits strong positive correlation with the galaxy stellar mass (Boroson et al. 2011; Zhang et al. 2012).

So far, at least 187 Galactic LMXBs have been identified (Liu et al. 2007). Their companion stars are main-sequence or slightly evolved K–M type ones with masses of $\lesssim 1\ M_\odot$. Orbital periods of the known LMXBs are diverse, ranging from 0.19 to 398 hours, while those of transients, which account for about half the LMXBs, are typically $\lesssim 15$ hours. Transients occasionally undergo outbursts, during which the luminosity increases in a few days, followed by a gradual decay lasting less than a few months.

Many of LMXBs do not, or hardly, exhibit coherent pulsations, and hence, the magnetic fields of the NSs in LMXBs are considered to be weak as $\lesssim 10^9$ G. Yet the pulsation is sometimes observed when the luminosity is low and magnetic pressure becomes comparable to the thermal pressure, or when Type-I bursts are ignited and blackbody radiation on the NS surface is slightly non-uniform. The confirmed spin periods of NSs in LMXBs are typically $\sim 2 - 5$ ms, or longer in some cases. This is considered to result from long-term spin up of the NSs via mass accretion. For this reason, NSs in LMXBs are considered to be progenitors of radio milli-second pulsars which are also found sometimes in binaries, and often in globular clusters like LMXBs. Indeed, transitions between the radio milli-second pulsar phase and the accretion powered LMXB phase were recently found from three sources (Takata et al. 2014; Patruno et al. 2014; Stappers et al. 2014; Papitto et al. 2013).

2.2.2 Mass accretion in LMXBs

The X-ray luminosity of an LMXB is calculated as

$$L = G\frac{M_{\rm NS}\dot{M}}{R_{\rm NS}} \sim 0.19\dot{M}c^2 \tag{2.1}$$

where G is the gravitational constant, $M_{\rm NS} \sim 1.4\ M_\odot$ is a typical NS mass, $M_\odot$ is the solar mass, $R_{\rm NS} = 11$ km is a typical NS radius, $\dot{M}$ is the mass accretion rate from the companion star which is assumed to be constant independent of the radius. This L generally ranges from $\sim 10^{32}$ erg s^{-1} to $\sim 10^{38}$ erg s^{-1}. Usually, LMXBs cannot be more luminous than the

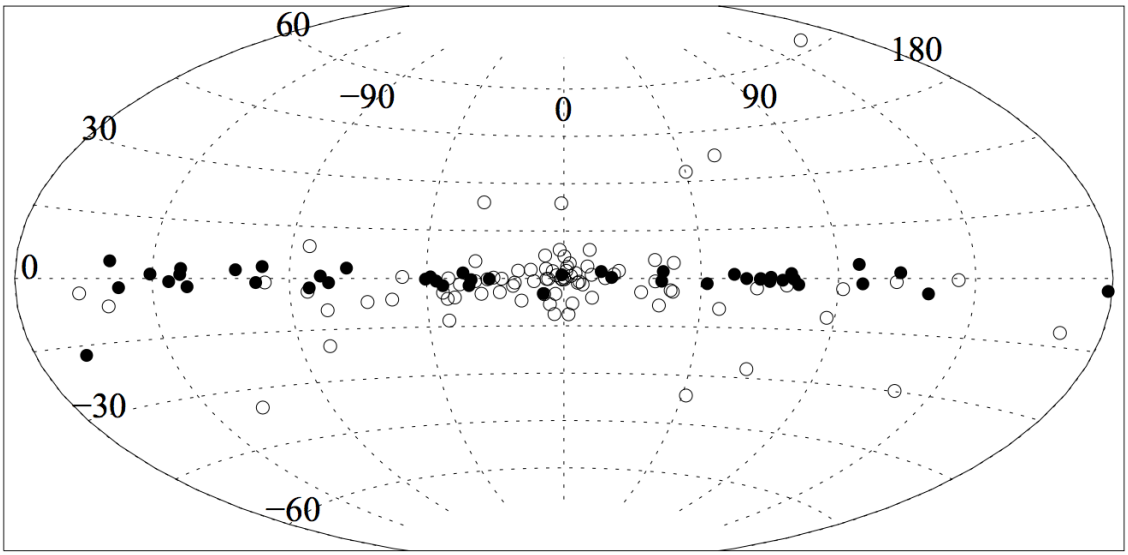

Figure 2.2: Distributions of LMXBs (open circles) and HMXBs (filled circles) in the Milky Way, presented in Galactic coordinates (Grimm et al. 2002).

Eddington luminosity expressed as

$$L_{\rm Edd} = \frac{4\pi\mu c G M_{\rm NS} m_{\rm p}}{\sigma_{\rm T}} \sim 2\left(\frac{\mu}{1.2}\right) \times 10^{38}\ {\rm erg\ s^{-1}}, \tag{2.2}$$

where $\mu = 1.2$ is the nucleon-to-electron number ratio in the accreting gas, $m_{\rm p}$ is the proton mass, and $\sigma_{\rm T}$ is the Thomson cross section. At this luminosity, the inward gravitational force working on nucleons becomes balanced by outward radiation pressure acting on electrons, and hence $\dot{M}$ cannot increase any more. As a result, L generally saturates at $L_{\rm Edd}$.

Figure 2.3 shows a gravitational potential of a close binary in a co-rotating frame on a plane of revolution, where the less massive component is assumed to carry one third of the total system mass. When that component fills its Roche lobe (i.e., the region inside the potential separatrix), and the heavier component is an NS, the system becomes an LMXB, and the gas flows through the saddle point (a Lagrangian point) with nearly Keplerian motion in the inertial system. This form of matter transfer is called Roche-lobe overflow, and the gas, with its angular momentum, forms an accretion disk around the NS. The Roche-lobe radius is expressed as

$$r_{\rm R} = \frac{0.49 q^{2/3}}{0.6 q^{2/3} + \ln(1+q^{1/3})} \times \left(\frac{G(M_{\rm NS}+M_*)}{4\pi^2}\right)^{1/3} P^{2/3} \tag{2.3}$$

where $q = M_{\rm NS}/M_*$, M_* is the companion mass, and P is the orbital period. When $M_* = 0.2 M_\odot$ and $P = 15$ hours for example, $r_{\rm R} = 2 R_\odot$ is obtained. In this particular case, the companion has to be somewhat evolved to fill the Roche lobe. In contrast, it can be a main-sequence star if $P = 1$ hr, because this case leads to $r_{\rm R} \simeq 0.3\ R_\odot$.

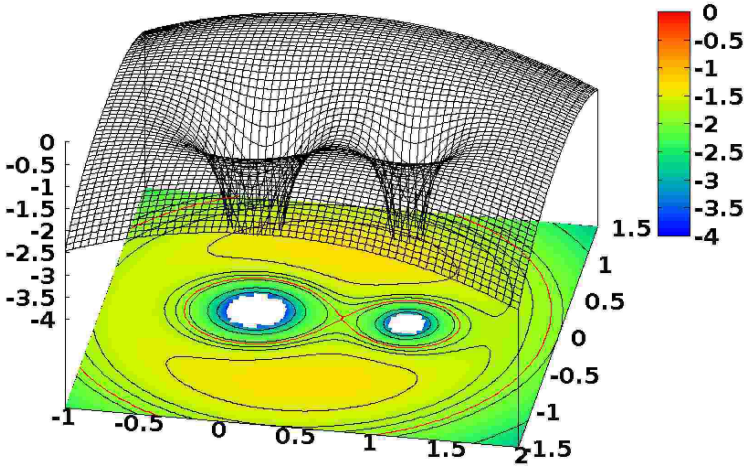

Figure 2.3: Contours of the gravitational potential of a close binary system in its co-rotational frame cut along the orbital plane. The axes are normalized by the separation between the two components. The heavier component (on the left) and the lighter companion are assumed to have masses of 1.4 $M_\odot$ and 0.7 $M_\odot$, respectively.

2.2.3 Outbursts of transient LMXBs

As already mentioned in §2.2.1, about half the LMXBs are classified as transients, which usually stay in a quiescent state with low luminosities and sometimes undergo outbursts involving luminosity increases by $\gtrsim 2$ orders of magnitude. The intervals between outbursts are $\lesssim 1$ month to tens of years, and can be irregular or quasi-periodic depending on sources. The duration of each outburst is typically less than several months. Figure 2.4 shows a light curve of the recurrent transient 4U 1608-52 obtained with the GSC (Gas Slit Camera) comprising the Japanese X-ray all-sky monitor *MAXI* (Monitor of All Sky X-ray Image; Matsuoka et al. 2009) onboard the International Space Station. In this particular object, the outbursts take place in a time scale of within a few years.

The outbursts are considered to arise from thermal and viscosity instabilities of the disk at temperatures around 10^4 K (Osaki 1974; Meyer & Meyer-Hofmeister 1981). When $\dot{M}$ is low, the disk temperature at large radii is low, and the material is mostly neutral. As a result, the opacity is much lower than that of the free-free processes dominant in ionized gas (or plasma). However, a small increase of the temperature induces an increase of the opacity at 10^{4-5} K due to Hydrogen ionization. Photons are then trapped in the disk and the temperature further increases by a positive feed back, until Hydrogen atoms are completely ionized. Associated with the rise of the temperature and hence the pressure, the α-viscosity (§2.3.2) increases. As a result, at large radii, the local accretion rate increases and becomes higher than the gas supply from the companion star. Consequently, the gas pressure, and thus heating as well decreases, and the temperature decreases until Hydrogen recombines.

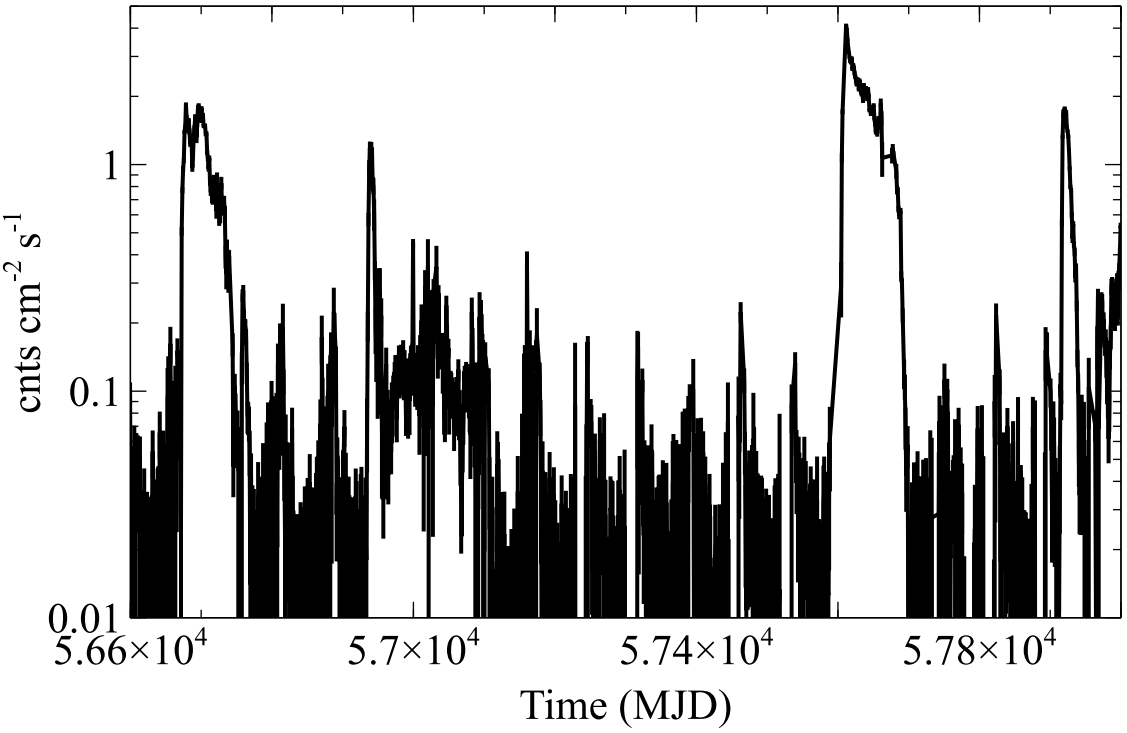

Figure 2.4: The 1.3–12 keV MAXI GSC light curve of 4U 1608-52 with 1 day bin.

The instabilities propagate inward as the matter in a highly ionized annulus falls toward the NS (Lasota 2001). Because the disk becomes then illuminated by strong radiation from the NS vicinity, the disk is kept ionized even at large radii, until the irradiation becomes too weak to keep the gas in the outer disk ionized. In this way, $\dot{M}$ suddenly rises, and relaxes in a few months.

2.2.4 Thermonuclear flashes

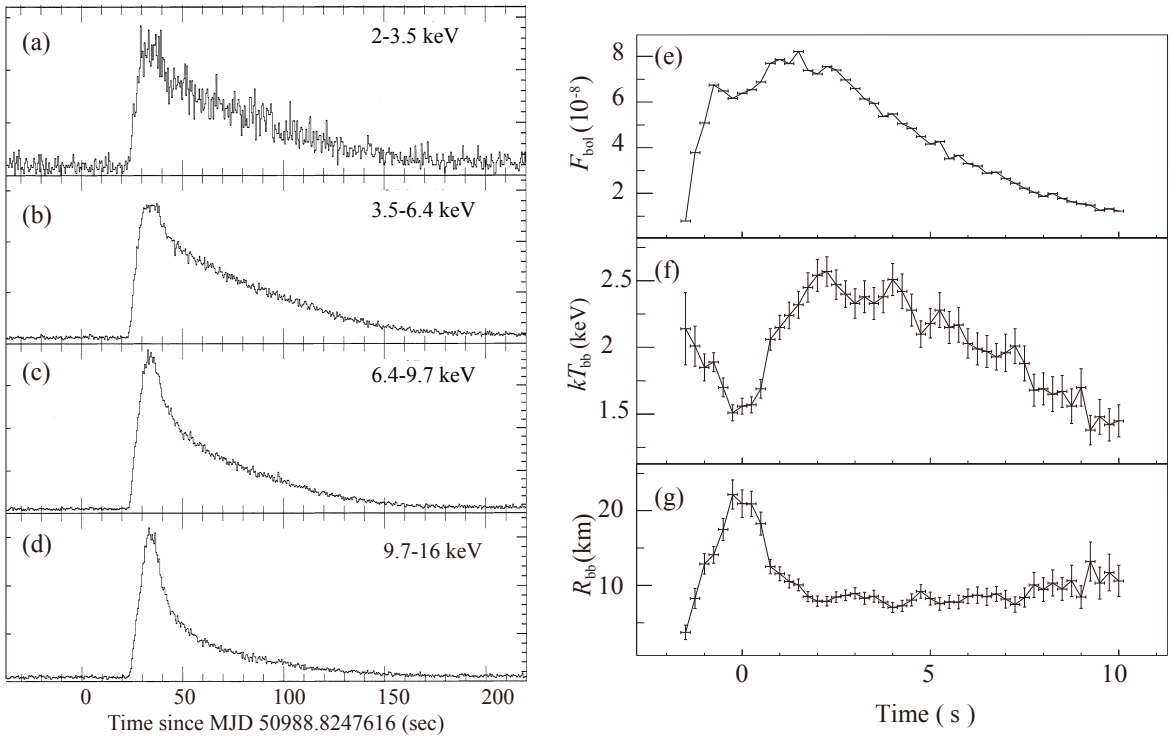

Figure 2.5: (a–d) Profiles of a Type-I burst from GS 1826-238, measured in different energy bands with the *RXTE*/PCA (Kong et al. 2000). Right panels show time evolutions of (e) the bolometric flux, (f) blackbody temperature, and (g) the blackbody radius, obtained by fitting spectra of a Type-I burst from IGR J17474-2721 with a blackbody model (Chen et al. 2010).

About 70 sources out of the $\sim$ 200 LMXBs are known to occasionally produce short and intense X-ray flashes with similar profiles, called Type-I bursts. As figure 2.5 (a–d) shows, their rise time is very short, typically $\lesssim$ 2 s to $\sim$ 10 s, and their decay time is longer as 10 s to several minutes. The ratio of the total energy $\epsilon_{\rm p}$ radiated as persistent X-ray emission in between consecutive bursts and the energy $\epsilon_{\rm b}$ released in a burst is typically $\alpha \equiv \epsilon_{\rm p}/\epsilon_{\rm b} \sim 100$, ranging from 10 to $\sim 10^3$. This is roughly the same as the ratio between

the gravitational energy of the NS surface ($\sim 0.17 \times mc^2$) and the nuclear burning energy from Helium or Hydrogen into Iron ($\sim 0.002 - 0.009 \times mc^2$). As a result, Type-I bursts are interpreted as unstable thermonuclear flashes taking place in hydrogen-rich materials that have accumulated on the NS surface. Although the nuclear fusion is considered to proceed in multiple chain reactions, the most dominant energy-production stages are the Hydrogen to Helium fusion involving beta decay, and the triple-alpha reaction from Helium to Carbon which requires a high density and temperature. The burst ceases when the persistent luminosity is above a critical level of $\sim 10^{37}$ erg s^{-1}, because nuclear burning becomes stable on the NS surface due to high temperature and pressure.

Spectra of Type-I bursts are successfully explained as a blackbody emission. This is because the NS surface is heated by the nuclear burning to emit blackbody photons, which dominate the spectrum. After the flux reaches the maximum, the temperature gradually decreases by cooling, which causes the flux to decrease as well. This is evidenced in figure 2.5 (a–d) by the faster decay in the higher energy bands. As shown in figure 2.5 (g), the apparent blackbody radius stays nearly constant at ~ 10 km during a burst (except at early phase), and is also the same among different Type-I bursts from the same source. This implies that the whole NS surface is emitting the blackbody photons with approximately the same temperature.

When a burst is energetic enough and the energy production rate by nuclear fusion exceeds $L_{\rm Edd}$, the excess energy is spent in the work to lift up the photosphere. Such bursts are called photospheric radius expansion (PRE) bursts. Figure 2.5 (e) is a typical PRE burst profile observed with *RXTE*. Soon after the blackbody radius exceeds the NS radius (figure 2.5 g), the blackbody temperature steeply decreases down to ~ 1.5 keV, and the radius reaches ~ 20 km. Then, the expanded photosphere falls back to the NS surface ("touchdown") with the blackbody radius of $R_{\rm NS} \sim 10$ km, and the blackbody temperature reaches the maximum at ~ 2.5 keV. The X-ray luminosity saturates at $L_{\rm Edd}$ and kept constant until the touchdown. As a result, PRE bursts can be used as a standard candle to estimate the distance to LMXBs (van Paradijs 1978). Using LMXBs in globular clusters with known distances, it is confirmed that PRE bursts can be used as standard candles within $\sim 15\%$ accuracy of the luminosity (Kuulkers et al. 2003).

2.3 Physics of Mass Accretion

2.3.1 An overview

Since the matter supplied by the companion has significant angular momentum, it forms, on the binary orbital plane, a flat disk which differentially rotates at local Keplerian velocities around the NS. This is called an accretion disk. In order for the matter in the disk to accrete onto the NS, it must throw away both angular momentum and dynamical energy, in a well synchronized manner. At larger radii, the transport of angular momentum becomes the rate-determining step, whereas that of energy determines the accretion rate at smaller radii. This subject has hence been studied theoretically since the 1970's, as various accreting

objects were discovered through X-ray observatories.

In an accretion disk, the gravitational energy release from the matter at a given radius is carried away via three major channels; the radiation which acts as cooling process, the conversion into kinetic (rotational plus radial) energies, and the advective energy transport inwards. This conversion scheme involves an inherent bimodality. If the radiation becomes stronger than an equilibrium value, the gas will be excessively cooled and will become denser, and the radiation will be further enhanced because the Bremsstrahlung emissivity is proportional to the density squared. This positive feedback will shape the flow into an optically-thick and geometrically-thin cool disk, with nearly Keplerian rotation. If, on the other had, the radiation becomes weaker, the gas will be heated to become hotter and less dense. Hence the radiation becomes inefficient, and the disk will be inflated vertically into an optically-thin and geometrically-thick hot flow. As a result, the accretion flow becomes bimodal, between a cool flat disk and an inflated hot flow (Shibazaki & Hōshi 1975; Ichimaru 1976). Any intermediate condition between these two states is considered unstable.

As an optically-thick and geometrically-thin solution to the flow equations, the idea of standard accretion disk, explained in §2.3.2, was proposed (Shakura & Sunyaev 1973). Mitsuda et al. (1984) examined spectra of several luminous LMXBs with *Tenma*, and showed that the softer part of their spectra can be understood as integrated emission from a standard accretion disk. Makishima et al. (1986) further found that the standard accretion disk explains the whole X-ray spectrum from the black hole binary (BHB), GX339-4, when the source is bright. Thus, the concept of standard accretion disks has been firmly established and widely accepted.

As an optically-thin and geometrically-thick solution, Lightman & Eardley (1974) proposed the radiatively inefficient accretion model, and Narayan & Yi (1994) formulated the advection-dominated accretion disk (ADAF model). In these cases, the gravitational energy is not radiated efficiently but is advected toward compact objects. Since the gas becomes hot and radiatively inefficient, Comptonization process (§2.3.4) becomes dominant over free-free emission. As the detector sensitivity at hard X-ray (e.g., 10–100 keV) band improved, the Comptonization effects have repeatedly been confirmed observationally (§2.4.3), in LMXBs, BHBs (Narayan et al. 1998; Makishima et al. 2008), and Active Galactic Nuclei (Narayan et al. 1998).

These accretion-flow solutions described so far are summarized in figure 2.6 on a diagram of the mass accretion rate and the disk surface density. The solid lines on the left and right represent the optically thin and thick solutions. When the mass accretion rate is low, an accretion disk obeys the solution on the left side with systematically small surface density, but as $\dot{M}$ increases, the flow jumps to the solution on the right side with higher surface density.

2.3.2 The Standard accretion disk

As mentioned in §2.3, Shakura & Sunyaev (1973) derived an analytical solution to the accretion-flow equations, and established the concept of standard accretion disks. This work

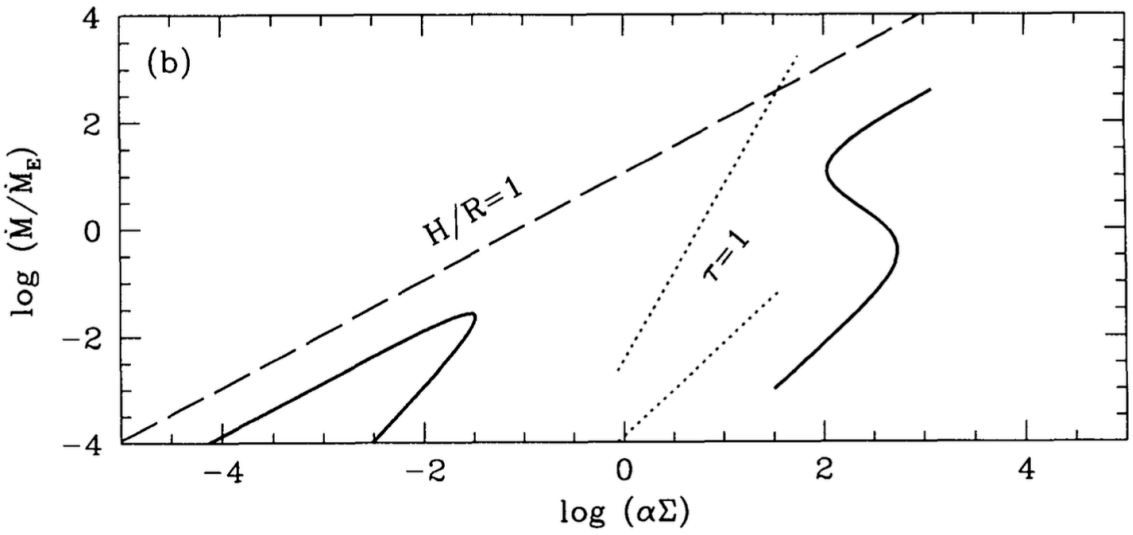

Figure 2.6: Various accretion-flow solutions, drawn on a diagram of the mass accretion rate vs. surface density (Abramowicz et al. 1995). The solid line at $\log(\alpha\Sigma) < 0$ is an optically thin solution, while the S shaped curve represents an optically thick solution including the standard disk regime.

has given a great impact on the study of accretion physics. Partly due to this achievement, R. Sunyaev was awarded Kyoto Prize in 2011. Below, let us review the formalism of Shakura & Sunyaev.

In a standard accretion disk, the angular momentum is transported outwards by viscosity and the gas gradually falls to the central object losing its gravitational energy. To formulate the standard accretion disk, we assume that the disk is geometrically thin and axisymmetric. In other words, its density scale height H is small as

$$\frac{H}{R} \sim \frac{c_{\rm s}}{v_{\rm K}(R)} \ll 1 \tag{2.4}$$

at a radius R, where $c_{\rm s}$ is the local sound speed, $v_{\rm K}(r) = \sqrt{GM/R}$ is the Keplerian velocity at R, and M is the mass of the central star. In this case, $c_{\rm s} \ll v_{\rm K}(R)$, and the gas azimuthal velocity is close to $v_{\rm K}(R)$. The emission from standard accretion disks has been widely observed from LMXBs (Mitsuda et al. 1984; Makishima et al. 1989), as well as BHBs (Makishima et al. 1986), and accounts for their soft X-ray photons.

At any radius, both the mass flow and the angular momentum flux should be conserved. The mass conservation in the radial direction takes the form as

$$R\frac{\partial \Sigma}{\partial t} + \frac{\partial}{\partial R}(R\Sigma u_{\rm R}) = 0 \tag{2.5}$$

where $\Sigma(R,t)$ is the surface density of the disk and $u_{\rm R}(R,t)$ is the disk radial velocity. The

angular momentum δL of an annulus at a radius R, with an infinitesimal width of ΔR, is

$$\delta L = 2\pi R^3 \Delta R \Sigma \Omega \tag{2.6}$$

where $\Omega(R) = (GM/R^3)^{1/2} = v_{\rm K}/R$ is the Keplerian angular velocity. Differentiating eq. (2.6) with respect to time, the equation of motion is given as

$$\frac{d\delta L}{dt} = \frac{\partial \delta L}{\partial t} + u_{\rm R} \cdot \nabla \delta L = T(R + \Delta R, t) - T(R, t) \tag{2.7}$$

where $T(R,t) = 2\pi\nu\Sigma R^3(\partial\Omega/\partial R)$ is the torque exerted on the inner annulus from the outer adjacent annulus, $\nu \equiv \alpha c_{\rm s} H$ is the viscosity of the gas and α is a free parameter. Dividing both sides with ΔR, the equation of angular momentum conservation is obtained as

$$R\frac{\partial}{\partial t}\left(\Sigma R^2 \Omega\right) + \frac{\partial}{\partial R}\left(\Sigma R^3 \Omega u_{\rm R}\right) = \frac{\partial}{\partial R}\left(\nu \Sigma R^3 \frac{\partial \Omega}{\partial R}\right). \tag{2.8}$$

Combining equations (2.5) and (2.8), we obtain

$$\frac{\partial \Sigma}{\partial t} = \frac{3}{R}\frac{\partial}{\partial R}\left[R^{1/2}\frac{\partial}{\partial R}\left(\nu\Sigma R^{1/2}\right)\right], \tag{2.9}$$

which describes the evolution of the disk. When $\nu > 0$ is constant, eq. (2.9) yields a diffusion equation about $\sqrt{R}\Omega$ with a positive diffusion coefficient. As a result, the mass at a radius R diffuses radially, and accretes onto the central star. Since $\partial/\partial t = 0$ is of our interest, eq. (2.8) can be integrated to yield

$$\nu\Sigma = \frac{\dot{M}}{3\pi}\left[1 - \left(\frac{R_{\rm in}}{R}\right)^{1/2}\right] \tag{2.10}$$

where $R_{\rm in}$ is the inner disk radius.

When the gas is rotating with a Keplerian velocity, it must obey virial theorem, and thus, the dissipated energy, or equivalently half the released gravitational energy, must be radiated. Supposing that the radiation is blackbody, its surface emission is equated as

$$\sigma_{\rm SB} T^4 = \frac{1}{2}\nu\Sigma\left(R\frac{\partial\Omega}{\partial R}\right)^2 \tag{2.11}$$

where $\sigma_{\rm SB}$ is the Stefan-Boltzmann constant. The right hand side is half the energy production rate per unit time per unit area due to viscosity, derived by considering dissipation. Substituting eq. (2.10), the disk temperature at a radius R is derived as

$$T_{\rm std}(R) = \left\{\frac{3GM\dot{M}}{8\pi R^3 \sigma_{\rm SB}}\left[1 - \beta\left(\frac{R_{\rm in}}{R}\right)^{1/2}\right]\right\}^{1/4} \tag{2.12}$$

where $0 \leqq \beta \leqq 1$ is a dimensionless parameter determined by the boundary condition of the disk at $R_{\rm in}$. The formalism presented above has been adopted from Camenzind (2006).

2.3.3 Multi-color disk (MCD) formalism

An approximate and simpler formalism of the standard disk solution, called multi-color disk (MCD) formalism, can be obtained by considering the energy flux at a radius R, instead of considering the angular momentum transport (§2.3.2). Since the azimuthal velocity of the disk at R is faster than that at $R + \Delta R$, not only is the angular momentum transferred outwards, but also the adjacent gas generates heat due to viscosity. The disk is more and more heated towards smaller radii because $v_{\rm K}(R) \propto R^{-2}$ becomes faster. Supposing that this heating rate, $\Delta(\dot{M} v_{\rm K}^2)/2 \propto R^{-2}\Delta R$ from the gravitational energy, can be equated with the cooling rate ($4\pi r \Delta r \sigma T^4$) due to the blackbody radiation from the disk surface, the MCD temperature is calculated as

$$T_{\rm MCD}\,(R) = \left\{ \frac{3GM\dot{M}}{8\pi R^3 \sigma_{\rm SB}} \right\}^{1/4}. \tag{2.13}$$

This expression is identical to eq. (2.12) except at $R \sim R_{\rm in}$, and predicts that the temperature increases towards $R_{\rm in}$.

Using eq. (2.13), namely under the MCD approximation, the radially integrated emission spectrum from a standard disk, tilted by an inclination θ with respect to the line of sight and located at a distance D (Mitsuda et al. 1984), is calculated as

$$f_{\rm MCD}(E) = \frac{\cos\theta}{D^2} \int_{R_{\rm in}}^{R_{\rm out}} 2\pi R B(E,T) dR = \frac{8\pi R_{\rm in}^2 \cos\theta}{3D^2} \int_{T_{\rm out}}^{T_{\rm in}} \left(\frac{T}{T_{\rm in}} \right)^{-11/3} B(E,T) \frac{dT}{T_{\rm in}} \tag{2.14}$$

where E is the photon energy, $R_{\rm out}$ is the outer disk radius, $T_{\rm in} = T\,(R_{\rm in})$, $T_{\rm out} = T\,(R_{\rm out})$, and $B(E,T)$ is is the Planckian distribution. This spectral form is presented in figure 2.7. By integrating eq. (2.14) over the photon energy, the disk luminosity is obtained as

$$L_{\rm MCD} = \int_{R_{\rm in}}^{R_{\rm out}} 4\pi R \sigma_{\rm SB} T^4\,(R)\, dR \cong 4\pi R_{\rm in}^2 \sigma_{\rm SB} T_{\rm in}^4 \tag{2.15}$$

using the Stefan-Boltzmann law, where $R_{\rm in} \ll R_{\rm out}$ is assumed. Thus, independent parameters are two out of $L_{\rm MCD}$, $T_{\rm in}$ and $R_{\rm in}$. Equation (2.15) implies that the integrated luminosity of a standard accretin disk is just equal to the luminosity of a sphere of radius $R_{\rm in}$ and temperature $T_{\rm in}$.

Let us evaluate asymptotic forms of eq. (2.14). Substituting $B(E,T)$, eq. (2.14) can be written as

$$f_{\rm MCD} \propto E^{1/3} \int_{E/T_{\rm in}}^{\infty} \frac{x^{5/3}}{{\rm e}^x - 1} dx \tag{2.16}$$

where $x \equiv E/kT$, and $R_{\rm out}$ is approximated as infinity. When $E/T_{\rm in} \ll 1$, the integration of eq. (2.16) becomes nearly constant since $\int_{E/T_{\rm in}}^{1} x^{5/3}/({\rm e}^x - 1) dx \sim \int x^{2/3} dx$. Thus, as shown in figure 2.7, the spectrum at $E \ll T_{\rm in}$ is approximated as a power-law with an energy index of 1/3 or a photon index of -2/3. When $E/T_{\rm in} > 1$, on the other hand, the integral in eq.

(2.14) becomes dominated by $B(E,T)$ with $T \sim T_{\rm in}$, so that $f_{\rm MCD}$ takes a spectral form similar to a single-temperature blackbody with $T \sim 0.7T_{\rm in}$. This is also shown in figure 2.7. In this way, an MCD spectrum is softer than the single-temperature blackbody spectrum, simply because of the contributions from outer cooler regions, as represented by the name of "multi-color".

Since the matter motion in an MCD is nearly periodic, Virial theorem must hold at any radius. Therefore, the kinetic (including internal) energy $< T(R) >$ and the average potential energy $< V(R) >$, both averaged over the Keplerian period, need to satisfy the relation as

$$< T(R) >= -\frac{1}{2} < V(R) > . \tag{2.17}$$

This implies that half the gravitational energy is converted to the kinetic energy. The remaining half must be radiated locally, since the condition $c_{\rm s} \ll v_{\rm K}$ of eq. (4.1) means that the internal energy is negligible. As a result, eq. (2.17) and eq. (2.1) lead to

$$L_{\rm MCD} = G\frac{M\dot{M}}{2R_{\rm in}} = \frac{R_{\rm NS}}{R_{\rm in}} \times \frac{L}{2}. \tag{2.18}$$

Thus, the parameters derived from observations must satisfy both eq. (2.15) and eq. (2.18).

In Chapter 5, we analyze actual X-ray spectra of LMXBs employing an XSPEC model named `diskbb`, which reproduces the spectrum from an MCD (Mitsuda et al. 1984; Makishima et al. 1986). Comparing eq. (2.12) and eq. (2.14), a standard accretion disk can be approximated as an MCD with its radius multiplied by $\xi = 0.412$ (Kubota et al. 1998), where $\beta = 1$ (eq. 2.12) is assumed for an NS without spin. Furthermore, the local color temperature of an optically-thick disk is generally higher than the effective temperature, by so-called color hardening factor $\kappa \sim 1.7 - 2.0$ (Shimura & Takahara 1995). Then, the true accretion disk radius can be estimated as

$$R_{\rm in} = \xi\kappa^2 R_{\rm in}^{\rm MCD} \tag{2.19}$$

from the apparent radius $R_{\rm in}^{\rm MCD}$ derived with the `diskbb` model. Hereafter, we employ eq. (2.19) with $\kappa = 1.7$; namely, $R_{\rm in} = 1.19R_{\rm in}^{\rm MCD}$.

2.3.4 Hot accretion flows and Comptonization

In the Hard State realized at luminosities bellow $\sim 10^{36-37}$ erg s^{-1}, the spectra of LMXBs become hard, and approximated by a power-law with a photon indices Γ of $\lesssim 2$ and a cut-off at ~ 100 keV, where $\Gamma > 0$ means a photon flux decreases toward higher energies. They are successfully interpreted as photons which are Compton up-scattered by a hot thermal electron cloud with a temperature of $\gtrsim 30$ keV and an optical depth of a few or less. As described in §2.3.1 and figure 2.6, this Comptonizing cloud can be identified with a geometrically-thick and optically-thin accretion flow (hereafter corona) around the NS. In a corona, ions are heated by gravity up to nearly the virial temperature of ~ 200 MeV through

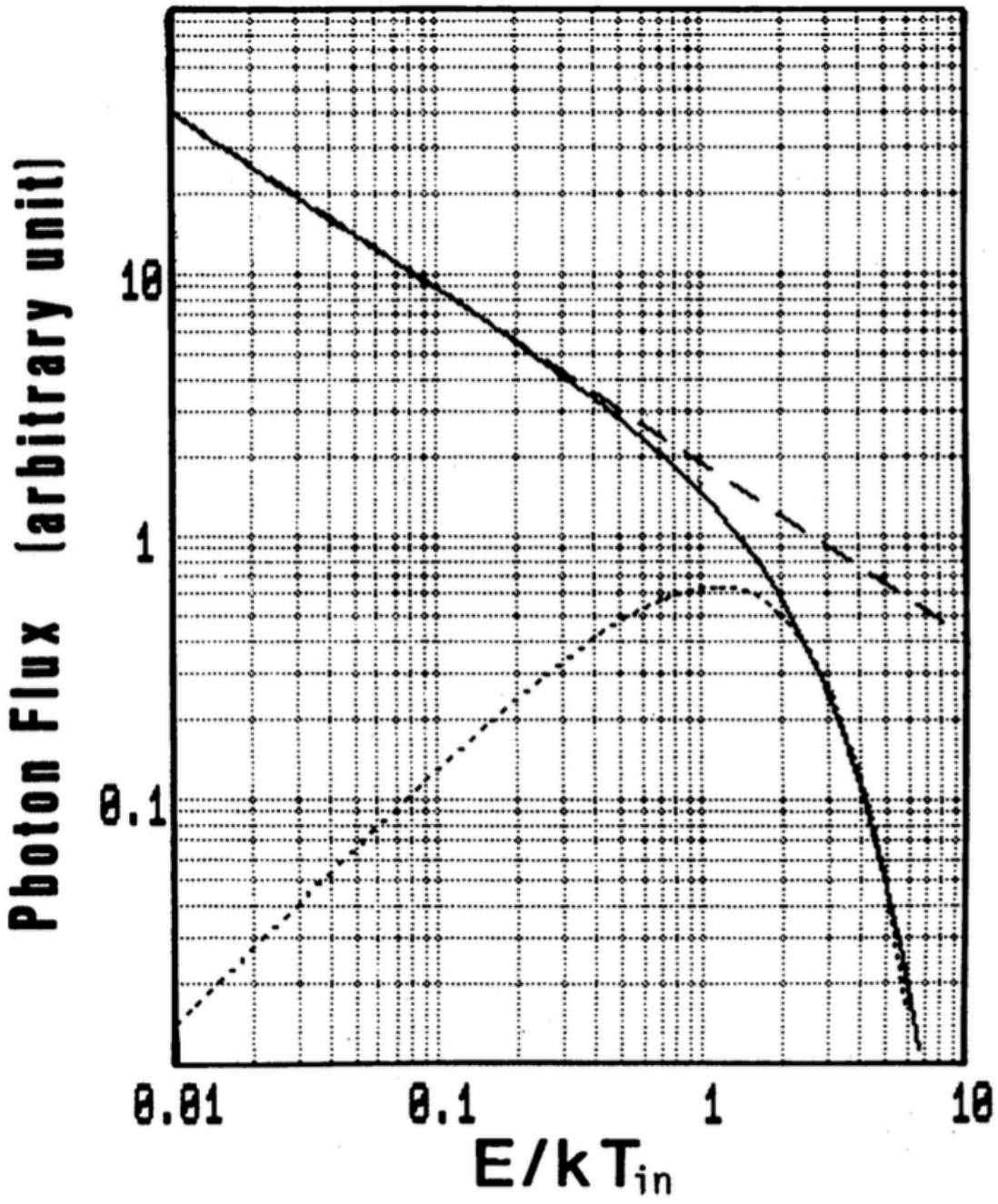

Figure 2.7: The MCD spectrum (a photon number spectrum rather than flux density spectrum) as a function of $E/T_{\rm in}$ (Makishima et al. 1986). Dashed and dotted lines represent a power law with photon index of -2/3 and a blackbody spectrum with a temperature of $0.71T_{\rm in}$, respectively.

viscosity and also presumably by a shock, giving part of their energy to electrons by Coulomb collision. The heated electrons then Compton scatter soft seed photons arising from the NS surface or its vicinity, and are cooled. Physical conditions of these flows are generally more complicated than those of the standard accretion disk, because the ions, electrons, and seed photons have different temperatures. However, the heating vs. cooling balance on electrons is considered thermally stable: if electrons become too hot by fluctuations, the Coulomb coupling with ions decreases, and the energy transfer to soft photons becomes more efficient, so that the electrons temperature is brought back to the equilibrium value.

When the energy of individual seed photons injected to the corona is much lower than those of the coronal electrons, the energy is transferred from the electrons to the photons. To understand such a process, let us recall the ordinary Compton scattering of a photon by an electron at rest. In this case, the momentum and energy conservations require

$$\epsilon_{\rm f} = \frac{\epsilon_i}{1 + \frac{\epsilon_{\rm i}}{m_{\rm e}c^2}\,(1 - \cos\theta)}, \tag{2.20}$$

where $\epsilon_{\rm i}$ and $\epsilon_{\rm f}$ are the initial and final energies of the photon, and θ is the scattering angle. When the electron is moving relativistically with a Lorentz factor γ, the photon energy in the electron rest frame becomes $\sim \gamma\epsilon_{\rm i}$ by Lorentz transformation. Supposing that $\gamma\epsilon_{\rm i} \ll m_{\rm e}c^2$, and transforming back to the observer's frame after calculating eq. (2.20) with head-on collision, the electron gains energy as $\epsilon_{\rm f} \sim \gamma^2\epsilon_{\rm i}$.

Now let us consider scattering of seed photons with an isotropic distribution in a thermal electron cloud having a Maxwellian distribution. When the electron velocity $v_{\rm e}$ is much slower than the speed of light and thus $\gamma \sim 1$, the mean fractional change of the seed photon energy is expressed as

$$\left\langle \frac{\Delta\epsilon_\gamma}{\epsilon_\gamma} \right\rangle = \frac{4T_{\rm e} - \epsilon_\gamma}{m_{\rm e}c^2} \tag{2.21}$$

where ϵ_γ is the photon energy, $\Delta\epsilon_\gamma$ is its change by a single scattering, and $<>$ represents the average. Thus, the energy is statistically transferred from the electrons to seed photons when $4T_{\rm e} > \langle\epsilon_\gamma\rangle$, whereas the opposite takes place when $4T_{\rm e} < \langle\epsilon_\gamma\rangle$.

When the corona has a typical size of l, the average number of scattering for a photon depends on the ratio between l and the mean free path defined as $\lambda_\gamma = (n_{\rm e}\sigma_{\rm T})^{-1}$, where $\sigma_{\rm T}$ is the Thomson cross section. The ratio defined as $\tau = l/\lambda_\gamma = n\sigma_{\rm T}l$ is called the optical depth. When $\lambda \ll l$, the average scattering number for a photon is derived as τ^2 from random-walk arguments. When $\lambda \gg l$, on the other hand, the average number of scattering for a photon to experience is $1 - \exp(-\tau) \sim \tau$. Hence, by multiplying eq. (2.21) and the scattering number, the strength of Comptonization can be expressed by a quantity

$$y \equiv \frac{4T_{\rm e}}{m_{\rm e}c^2}\max\left(\tau, \tau^2\right) \sim \frac{4(T_{\rm e} - T_{\rm BB})}{m_{\rm e}c^2}\tau\left(1 + \frac{\tau}{3}\right). \tag{2.22}$$

This is so-called Compton y-parameter.

When $y \gtrsim 1$, the energy of photons is significantly increased by the scattering as they get through the corona, and the spectral shape changes. The seed photons that experienced

the inverse Compton scattering form a spectral "bridge" between the two thermal peaks, corresponding to $T_{\rm e}$ and the seed photon temperature $T_{\rm seed}$. The bridge has a power-law shape with a well defined photon index Γ, expressing

$$N(E) = N_0 \times E^{-\Gamma}, \tag{2.23}$$

where N represents the photon number. This is analytically expressed (Lightman & Zdziarski 1987) as

$$\Gamma = -\frac{1}{2} + \sqrt{\frac{9}{4} + \frac{4}{y}}. \tag{2.24}$$

To construct a spectral model arising via Comptonization, the photon displacements from one position in the spectrum to another position should be calculated under constraints of the photon number conservation. Supposing that only Compton scattering takes place in a homogeneous corona, the evolution of the number density of photons $n(\omega)$ as a function of frequency ω is written as

$$\frac{\partial n(\omega)}{\partial \omega} = \int d^3p \int d\Omega \left(\frac{d\sigma}{d\Omega}\right) c\Big\{n(\omega')\left[1+n(\omega)\right]N(E') + n(\omega)\left[1+n(\omega')\right]N(E)\Big\} \tag{2.25}$$

where p is the electron momentum, Ω is the scattering angle, $\sigma(\omega)$ is the Compton cross section (which reduces to $\sigma_{\rm T}$ at $\omega \to 0$), $N(E)$ is the number density of the electrons with energy E, and (E, ω), (E', ω') are the energy of the electrons and the frequency of the photons, before and after individual scattering, respectively. The factor $1 + n(\omega)$ is to represent stimulated emission effects. We suppose that the corona is thermal and $N(E)$ obeys a Maxwell-Boltzmann distribution. When electrons are not relativistic, $\Delta\omega/\omega \ll 1$ where $\omega' = \omega + \Delta\omega$. Expanding as $n(\omega') = n(\omega + \Delta\omega)$, and performing the integration, eq. (2.25) reduces to Kompaneets equation (Kompaneets 1956) which is given as

$$\frac{\partial n}{\partial y} = \frac{1}{x^2}\frac{\partial}{\partial x}\left[x^4\left(n' + n + n^2\right)\right] \tag{2.26}$$

where $x \equiv \hbar\omega/m_{\rm e}c^2$, $\hbar$ is the Dirac constant and

$$y \equiv \int^t \tau \frac{T_{\rm e}}{m_{\rm e}c^2} n_{\rm e}\sigma_{\rm T} c dt'. \tag{2.27}$$

This y in eq. (2.27) is essentially the same as eq. (2.22) except a factor 4, but is more microscopic.

Figure 2.8 shows the $\nu F\nu$ spectra of Comptonized blackbody, calculated using an XSPEC model `nthcomp` with the electron temperature of $T_{\rm e} = 10$ keV and various values of y according to the approximation in eq. (2.22). There, the spectrum in black ($y = 0.04$) is nearly the same as the original blackbody spectrum before Comptonization. As y increases, the spectrum gets harder (blue, green and red), and their spectral slope indeed becomes close to the value approximated by eq. (2.24). At $y = 2.3$, the spectrum exhibits a peak emerging at ~ 30 keV, which is the Wien peak characteristic of saturated ($\tau > 1$) Comptonization.

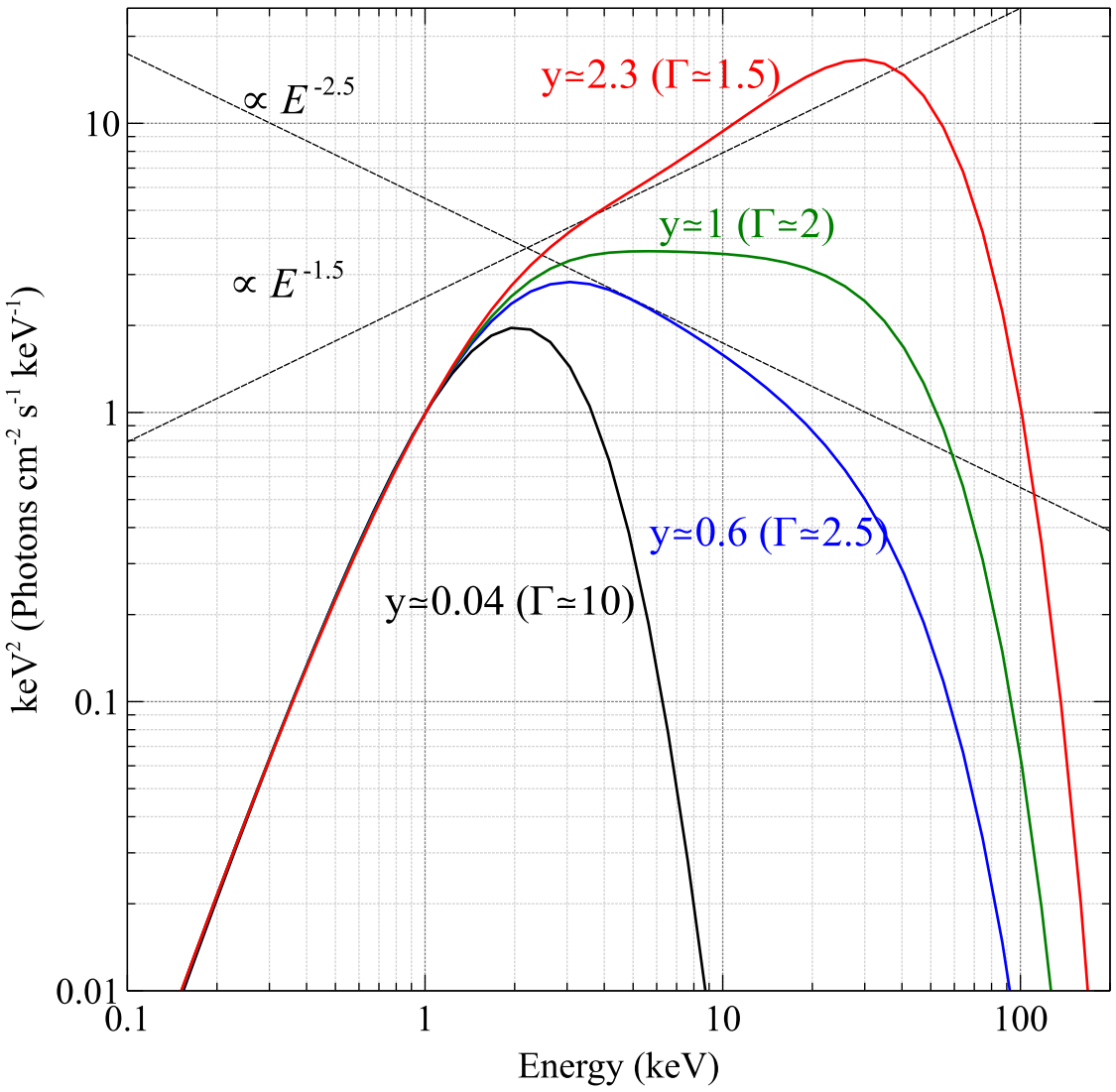

Figure 2.8: Comptonized blackbody spectra in a $\nu F\nu$ form, calculated with `nthcomp` for different values of y. The underlying blackbody has a temperature of 0.5 keV, whereas the electron clound has $T_{\rm e} = 10$ keV. The black, blue, green and red solid lines represent $y \sim$0.04, 0.6, 1, and 2.3, respectively. They are respectively equivalent to $\Gamma \sim 10, 2.4, 2$ and 1.5 from eq. (2.24). Additional straight lines are those with photon indices of 1.5 and 2.5, meant to guide the eyes.

2.4 X-ray Spectra from LMXBs

2.4.1 An overview

As already touched on in Chapter 1, LMXBs are known to make transitions between the two spectral states, the Soft State and the Hard State (White & Mason 1985; Mitsuda et al. 1989). These states are realized respectively when the luminosity is higher and lower than the threshold, which is 1% to several tens percent of the Eddington limit (Asai et al. 2012). In figure 2.9, we show how the spectral shapes of LMXBs differ between the two states. There, the Soft-State spectrum has a convex shape, and is dominated by photons with energies below $\sim$ 30 keV. This is because the accretion flow forms a standard disk (§2.3.2) due to efficient radiative cooling under the high accretion rate, and the emission has a characteristic of optically-thick thermal emission (2.3.3). In contrast, the Hard-State spectrum is much harder, exhibiting a power-law like shape with $\Gamma \sim 2$, up to 50–100 keV where it starts bending exponentially. This is because the luminosity bellow the threshold makes the radiative cooling inefficient, so that the accretion disk turns, at a certain radius, into an optically-thin and geometrically-thick flow (§2.3.4). Then, the Coulomb-heated electrons produce the observed hard X-rays via thermal Comptonization, just as explained in §2.3.4.

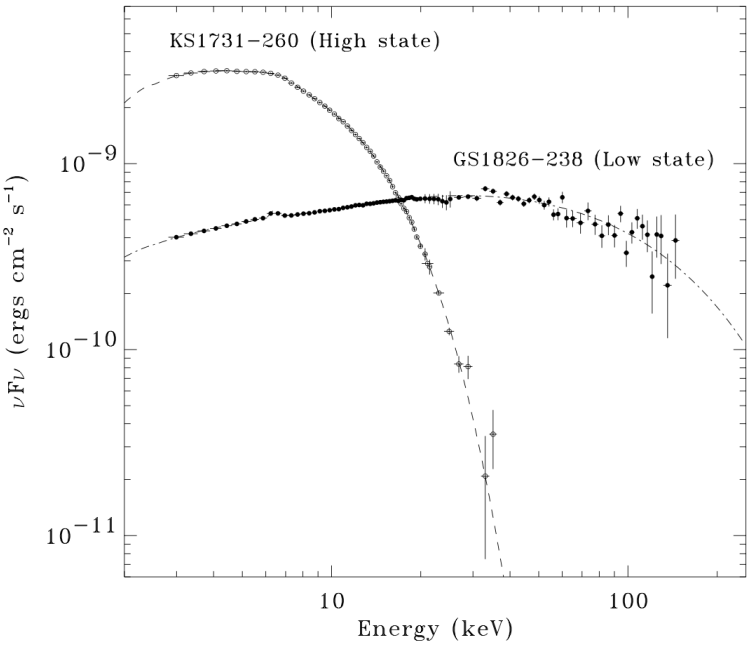

Figure 2.9: The spectrum of KS1731-260 and GS1826-238 obtained with *RXTE* and presented in a $\nu F\nu$ form (Barret et al. 2000), representing the Soft State (or High state in this literature) and the Hard State (or Low state), respectively.

2.4.2 Spectra in the Soft State

Although luminous LMXBs in the Soft State were detected and studied from an early stage of the history of X-ray astronomy, it was not until 1980s that their spectra were correctly understood. Current basic understandings of the Soft State was constructed by Mitsuda et al. (1984) through observations with *Tenma* (Tanaka et al. 1984). They analyzed data of four LMXBs which all showed significant intensity variations, particularly in energies above 10 keV. As shown in figure 2.10, these authors divided the data of each source and made a pair of spectra, one covering those periods when the $10 - 20$ keV intensity is higher, and the other when it is lower than the average. Figure 2.10 (b) indicates that the ratio of the high intensity spectrum to the low intensity one increases from unity at ~ 1 keV towards ~ 10 keV, and keeps a constant level above ~ 10 keV. This implies that the spectrum consists of a stable softer component, and a harder one which varies in intensity with it shape kept constant. In all the four sources, the difference between the intensity-sorted spectrum pair was reproduced with a single blackbody having a temperature of ~ 2 keV, which is considered to originate from the NS surface. The spectrum of the stable soft component of all the sources was successfully reproduced by the MCD model (§2.3.3) with the inner disk temperature of ~ 1.5 keV. Finally, the spectrum of each source as a whole was successfully explained as a sum of the MCD and blackbody. This result has been reinforced by a series of subsequent works, including Makishima et al. (1989) using *Ginga*, Takahashi et al. (2011) using *RXTE*, and Sakurai et al. (2012) using Suzaku. Thus, the presence of a standard accretion disk in a Soft State LMXB is now established.

In figure 2.11 (a), a high quality spectrum of Aql X-1 in the Soft State taken with *Suzaku* is shown as a demonstration. The spectrum is successfully explained with an MCD model and a weakly Comptonized blackbody. After removing the absorption, the MCD model approaches $E^{-2/3}$ at lower energies (§2.3.3). The Soft State spectrum has a convex shape, compared with the spectrum of the Hard State in figure 2.11 (b), which exhibits a power-low like shape.

2.4.3 Spectra in the Hard State

Spectra of LMXBs in the Hard State exhibit cut-off power-law like shape as demonstrated in figure 2.11 (b). When in the Hard State, LMXBs are dimmer than in the Soft State by more than an order of magnitude, with a typical luminosity of $\lesssim 10^{36}$ erg s^{-1}. Furthermore, the emission in the Hard State is spread over a much broader energy range, than that on the Soft State. For these two reasons, the overall shape of the spectrum was not clearly understood until 1990s, when the Hard State spectra in a hard energy band of $35 - 200$ keV were clearly detected with *Sigma* in 1990 (Barret et al. 1991). As instruments working in the hard X-ray range (e.g., 10–100 keV) improved, the cut-off power-law like shape of the Hard State was recognized with the *CGRO*/BATSE (Barret et al. 1996), and was interpreted to be arising from a Comptonization process or bremsstrahlung. Thanks to observatories with wide-band coverage and good sensitivities such as *BeppoSAX* (Boella et al. 1997), *RXTE*

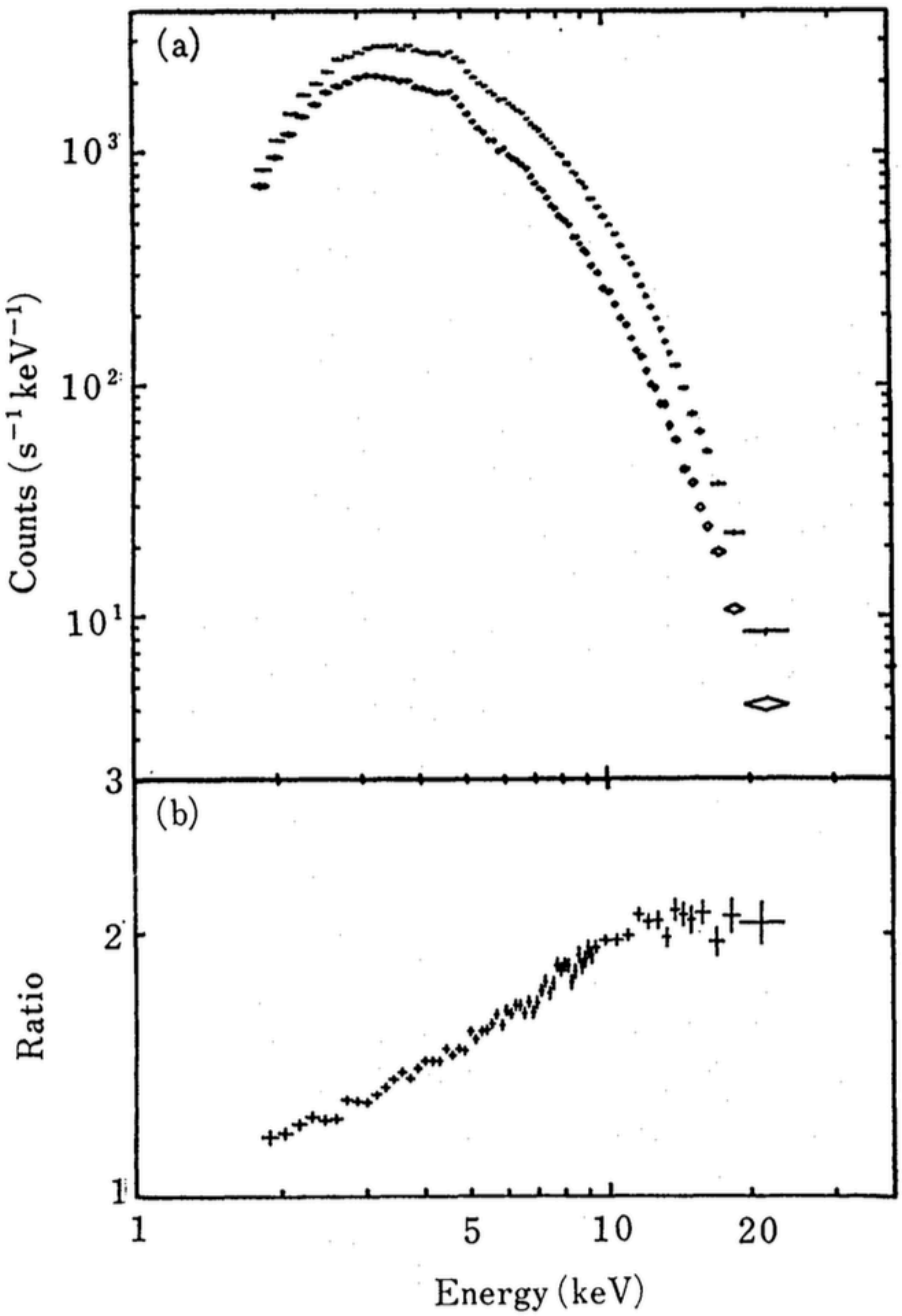

Figure 2.10: Spectral changes observed in Sco X-1 (Mitsuda et al. 1984). (a) A pair of photon-number spectra, sampling those periods when the 10–20 keV intensity is higher and lower. The instrumental responses are inclusive. (b) The ratio of the two spectra.

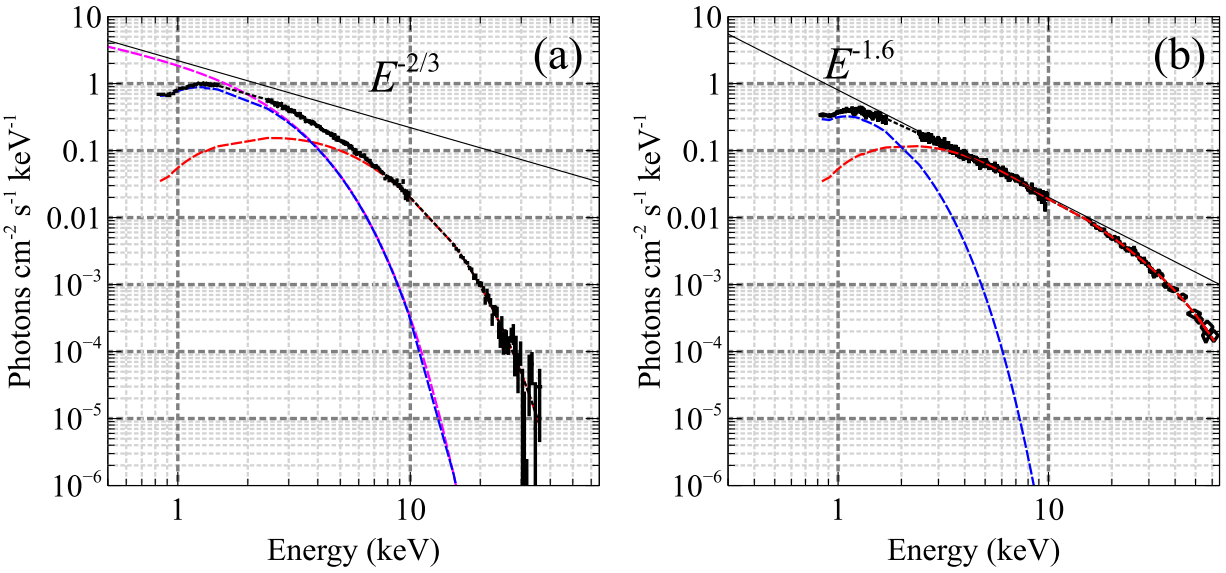

Figure 2.11: (a) A Soft State photon-number spectrum of Aql X-1 obtained with Suzaku. It is explained with an MCD emission (blue) and a weakly Comptonized blackbody (red). Unlike figure 2.10, the instrumental responses of the XIS and HXD (Chapter 3) have been removed. The same MCD model after removing absorption (mostly interstellar), to be compared with figure 2.7, is shown in magenta. (b) A Hard State spectrum of Aql X-1 taken with Suzaku in the same presentation as panel (a).

(Bradt et al. 1993) and *INTEGRAL* (Winkler et al. 2003), the understanding of the Hard State made further progress. It was shown that the Hard State spectrum can be reproduced by a combination of two main components; one is a blackbody or an MCD, appearing as a relatively weak excess in energies below ~ 2 keV, and the other is a Comptonized blackbody or a Comptonized MCD (Guainazzi et al. 1998; Gierliński & Done 2002; Tarana et al. 2008), forming the dominant cutoff-power-law like continuum. In this way, the spectral modeling became physical rather than empirical, but it still remained ambiguous.

To understand the Hard State in which the spectrum spans a much broader energy range than in the Soft State (figure 2.9), wide-band coverage from $\lesssim 1$ keV to ~ 200 keV is important. In addition, unified studies of the Hard State and the Soft State are essential. Following an early attempt by Mitsuda et al. (1989), such a comprehensive studies were enabled with *Suzaku* (§3). Specifically, Sakurai et al. (2012; 2014) analyzed 7 data sets of Aql X-1 taken with *Suzaku*, as the luminosity decreased monotonically from 1.7×10^{37} erg s^{-1} to 1.6×10^{34} erg s^{-1} during an outburst decaying phase. Across the 7 observations, the source evolved from the Soft State to the Hard State as presented in figure 2.12. There, the MCD plus Comptonized blackbody modeling has given acceptable fits to all the 7 spectra, and yielded physically reasonable parameters. The source evolution from the Soft State to the Hard State was characterized mainly by a progressive weakening of the Comptonization on the blackbody emission, and a gradual decrease in $R_{\rm in}$. Thus, an apparently unified description on the Hard State was obtained. However, this is based on the observation of only one LMXB, so that it remains unkown if this picture applies to other LMXBs as well. Actually, in some other sources including 4U 1915-05 (Zhang et al. 2014) and GS 1826-238 (Ono et al. 2016), and even in Aql X-1 itself observed on a different occasion (Sakurai 2015), not only the blackbody photons but also the MCD component was suggested to undergo significant Comptonization. Thus, the unified view of the Hard State is yet to be constructed.

2.4.4 Observations of state transitions

The presence of the Soft State and Hard State suggests that a transition between the two states should take place, and it would be very important to catch such rare occasions with wide-band coverage. Indeed, as presented in figure 2.13, a transition of BHB (not an LMXB) was recorded. There, as the source brightened, the 3–6 keV cont rate increased by a factor of ~ 4, whereas that in 6–10 keV was halved, thus exhibiting a very clear Hard to Soft State transition (Maejima et al. 1984). However, this was thanks to a unique capability of the rotating modulation collimators on board *Hakucho* (Kondo et al. 1981), which allowed to monitor a wide ($\sim 18^\circ$ diameter) sky region with a good ($\sim 0.2^\circ$) position resolution. Similar attempts were carried out with *RXTE* (Bloser et al. 2000a;b; Gierliński & Done 2002; Seifina & Titarchuk 2012), employing a large number of snap-shot pointings, but the obtained results were often inconclusive because of the lack of spectral sensitivity in < 3 keV, which is important to accurately constrain the MCD component as evident in figure 2.11.

The best chance to observe transitions would be the outbursts of transient LMXBs.

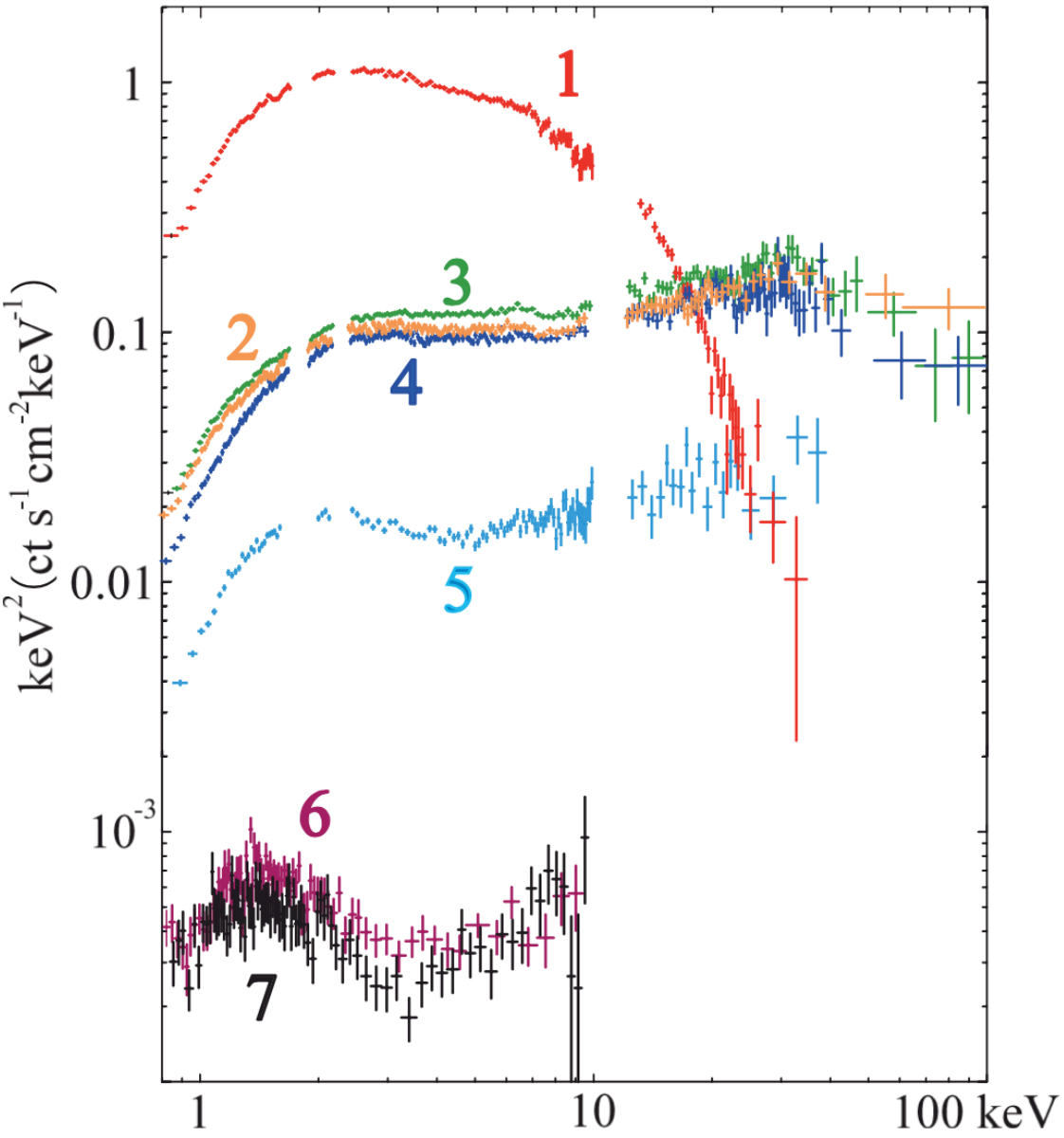

Figure 2.12: Spectra of Aquila X-1 in $\nu F\nu$ form acquired with *Suzaku* during a decaying phase of an outburst (Sakurai et al. 2012). The numbers from 1 to 7 represent the order of the observations.

However, as presented in figure 2.14, the source resides mostly either in the Soft State or the Hard State, and is in between the two states just a few percent of the whole observation. Furthermore, the transition luminosities of a single LMXB fluctuate across different outbursts (Yu & Yan 2009), and are different by a factor of several between the rising phase and the decaying phase of an outburst due to hysteresis. Therefore, even if near-real-time information is available with all-sky-monitor type observatory (e.g., *MAXI*), it is very difficult to point a telescope-type X-ray observatory (e.g., *Suzaku*) just to catch a transition.

Even under such conditions, a very moment of a transition of Aql X-1 was very fortunately observed with *Suzaku*, during a rising phase of an outburst. In the observation, the hardness ratio between 20–40 keV and 5–10 keV count rates decreased by more than an order of magnitude within $\sim$ 20 ks (§4.2.1). The spectral evolution was studied, and the results were already published in Ono et al. (2017). In §5.1.1, we revisit this precious data set, and use it as a prototype in the present thesis.

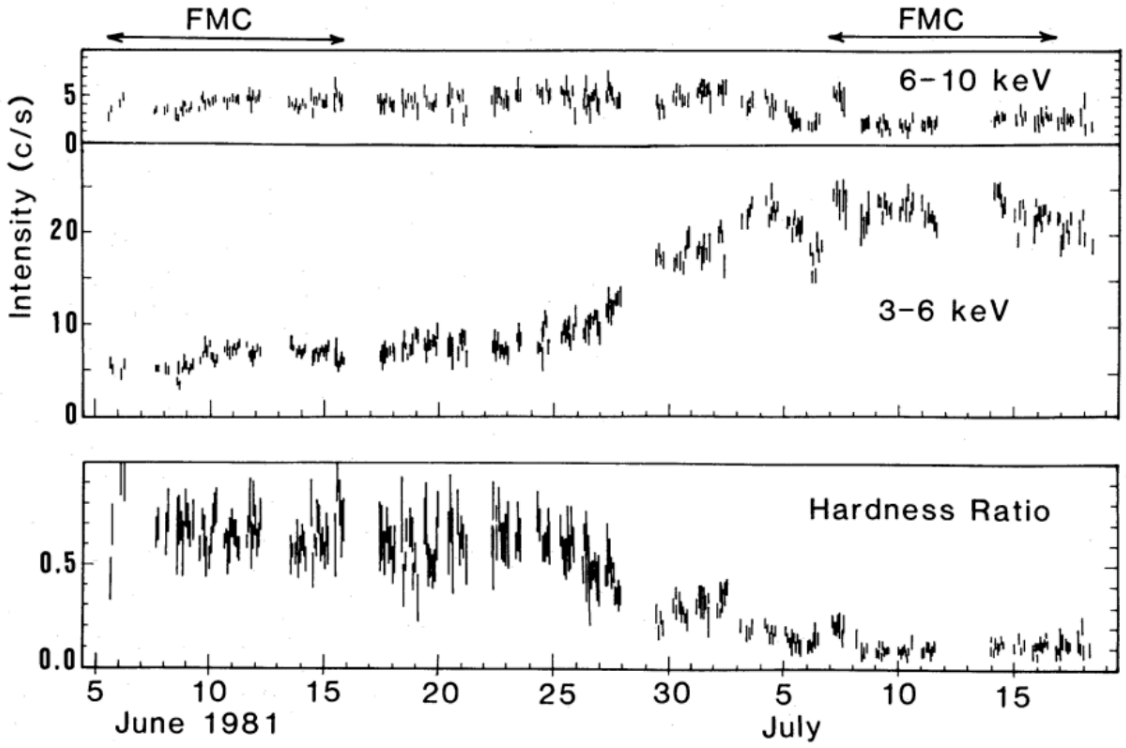

Figure 2.13: The 6–10 keV (top) and 3–6 keV (middle) light curves and the hardness ratio (bottom) of the BHB GX339-4, observed with *Hakucho* across a Hard-to-Soft state transition (Maejima et al. 1984).

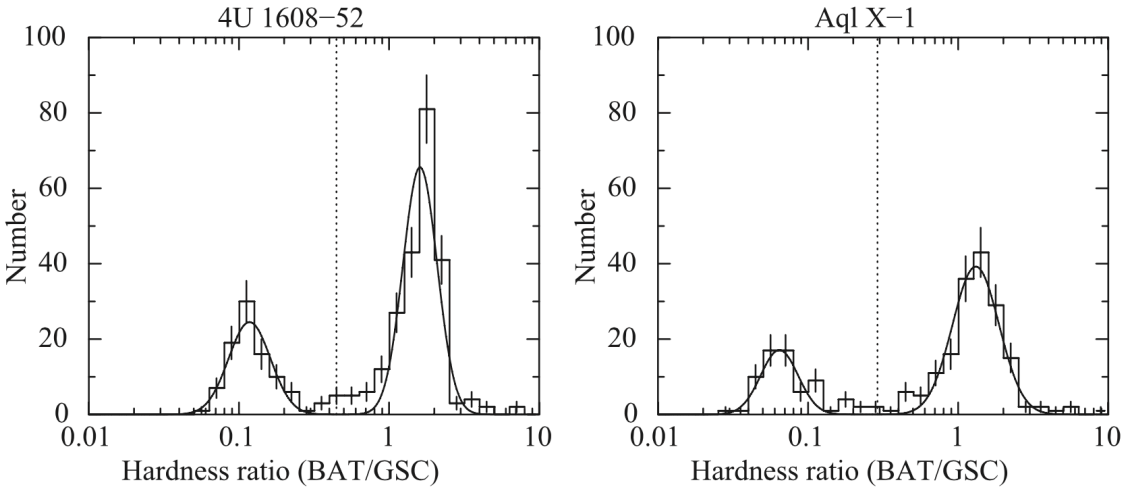

Figure 2.14: One day binned histograms of the hardness ratios between *Swift*/BAT and *MAXI*/GSC for 4U1608-52 (left) and Aql X-1 (right). Error bars are 1–σ statistical uncertainty. Data are fitted with log-normal distributions (solid line). Taken from Asai et al. (2012).

Chapter 3

Instrumentation

3.1 Overview

ASTRO-E2 was launched from Uchinoura Space Center on 2005 July 10, after a loss of ASTRO-E in 2000 due to a failure in a launch. ASTRO-E2 was put into an orbit of $\sim$ 570 km altitude and 32° inclination, and was named Suzaku. It is the fifth Japanese X-ray satellite as the successor of four previous satellites, Hakucho (Kondo et al. 1981), Tenma (Tanaka et al. 1984), Ginga (Makino 1987) and ASCA (Tanaka et al. 1994). It orbits in about 96 minutes, and go through the South Atlantic Anomaly (SAA) every orbit. Since instruments are turned off while *Suzaku* is passing through the SAA, data during that time is lost every 96 minutes.

Overall *Suzaku* is shown in figure 3.1. It carries three instruments, X-ray Spectrometer (XRS), X-ray Imaging Spectrometer (XIS) and Hard X-ray Detector (HXD). Although XRS lost its helium one month after the launch and had become unavailable, XIS and HXD covers 0.5–600 keV simultaneously. Wide-band coverage is essentially important to study LMXBs, since their spectrum often extends to above 15 keV, and those below $\sim$ 10 keV and those above $\sim$ 10 keV are from different components, an accretion disk (§2.3.3) and Comptonized blackbody (§2.4.3, 2.3.4). Its high energy resolution of $\sim$ 160 keV (FWHM) at 6 keV enables us to study iron lines which are occasionally observed from LMXBs. HXD with its high sensitivity at 15–60 keV plays an important role particularly to study the Hard State. *Suzaku* had been operated for about 10 years from 2005 to 2015 June and 3055 observations are available as archive data and is suited for our study.

3.2 X-ray telescope

In order to have better statistics and signal-to-noise ratio, *Suzaku* has five X-ray telescopes (XRTs) as illustrated in figure 3.2, shown together with its picture of an XRT (Serlemitsos et al. 2007). They are combined with XIS 0, 1, 2, 3 (§3.3) and an X-ray spectrometer (XRS) placed on focal planes. They are Wolter-I type telescopes consisting of thin nested foil, and

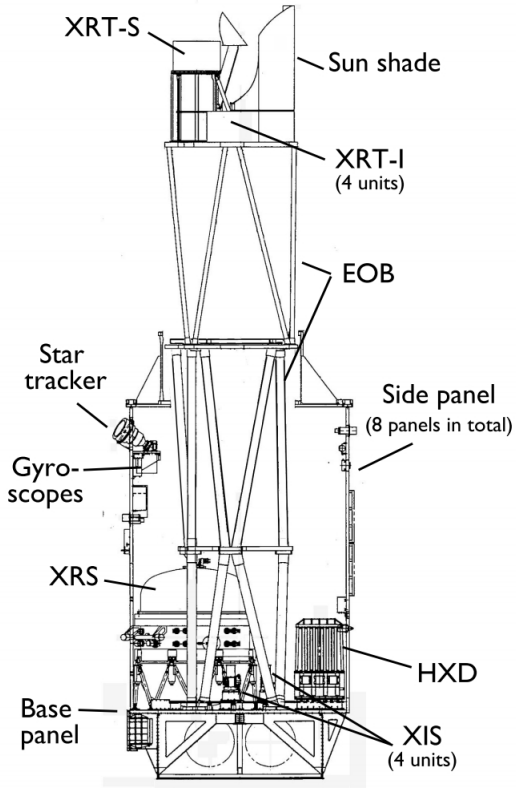

Figure 3.1: An overall structure of *Suzaku*, taken from Mitsuda et al. (2007)

bend X-ray by total reflection and Bragg reflection onto focal planes at a distance of 4.75 m. XRT for XIS 0, 1, 2 and 3 are named as XRT-I1, 2, 3 and 4, and the one for XRS is named as XRT-S. The summed effective area of XRT-I1, 2, 3, and 4 is shown in figure 3.3. The effective area of > 100 cm^2 at ~ 1 to 10 keV is even larger than that of Chandra but smaller than that of XMM-Newton. The edges at around 1.8 keV and 2.3 keV are the instrumental Silicon K-edge and the gold M-edge. In current thesis, data at 1.7–1.9 keV and 2.2–2.4 keV are not used since the systematic uncertainty is comparable with or larger than the statistical errors.

Figure 3.4 shows images of a point source, and point spread functions (PSFs) which are radial profiles of X-ray distributions on XRTs' focal plane, made from the images in the figure. The half power-diameters (HPDs) of XRT-I in which half of the total focused photons are accumulated, are $< 2'$. While the good angular resolution of $2'$ is important for diffuse sources, they cause the pile-up effect when a bright point source is observed. In such a case, events in a central region of the source need to be discarded (§3.5.1).

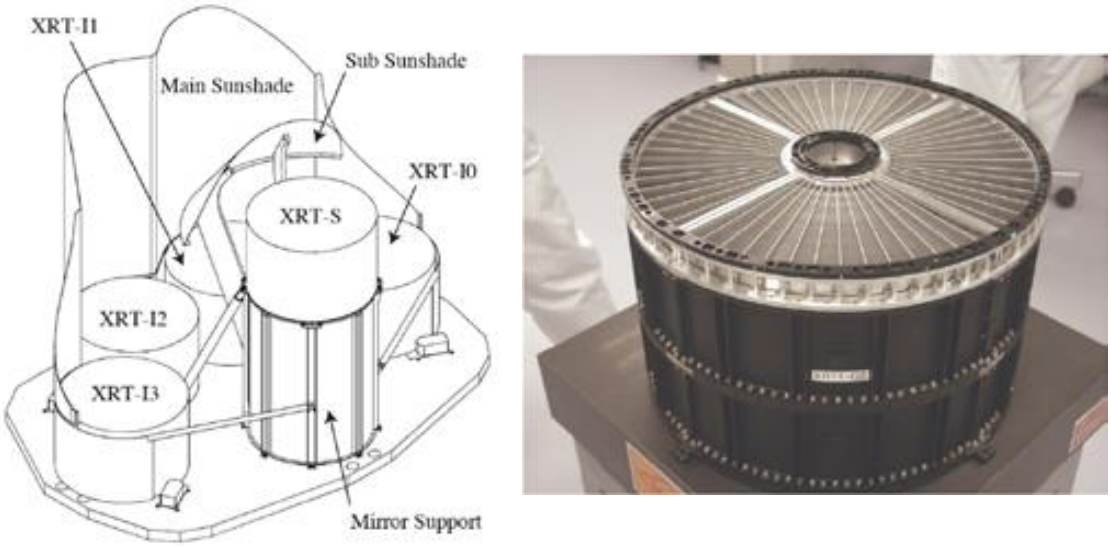

Figure 3.2: Illustration of XRTs onboard *Suzaku* (left), and a photograph of XRTI-1 (right). The figures are taken from Serlemitsos et al. (2007).

3.3 X-ray Imaging Spectrometer

On *Suzaku*, X-ray Imaging Spectrometer (XIS) which comprises of 4 charge-coupled device (CCD) cameras is mounted. Figure 3.5 shows one of the 4 cameras. Each of them is placed at a focus of XRT-I (§3.2), and detects soft X-ray photons at $0.2 - 12$ keV. They provide X-ray image and photon energy at each pixel. It is made of Silicon with thicker depletion layer (maximum ~ 65 μm) compared with CCDs on ASCA to have better sensitivity. Three

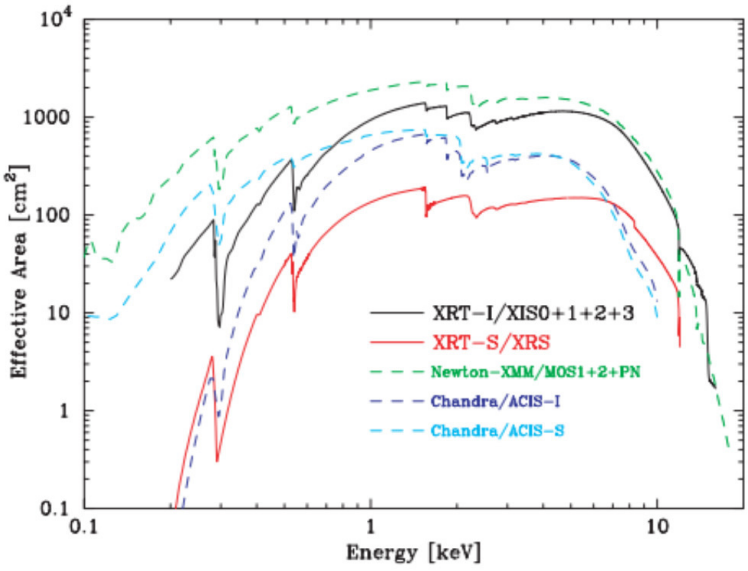

Figure 3.3: Total effective area of the four XRT-I (black) compared with those of *XMM-Newton* (green) and *Chandra* (blue and cyan). Taken from Serlemitsos et al. (2007)

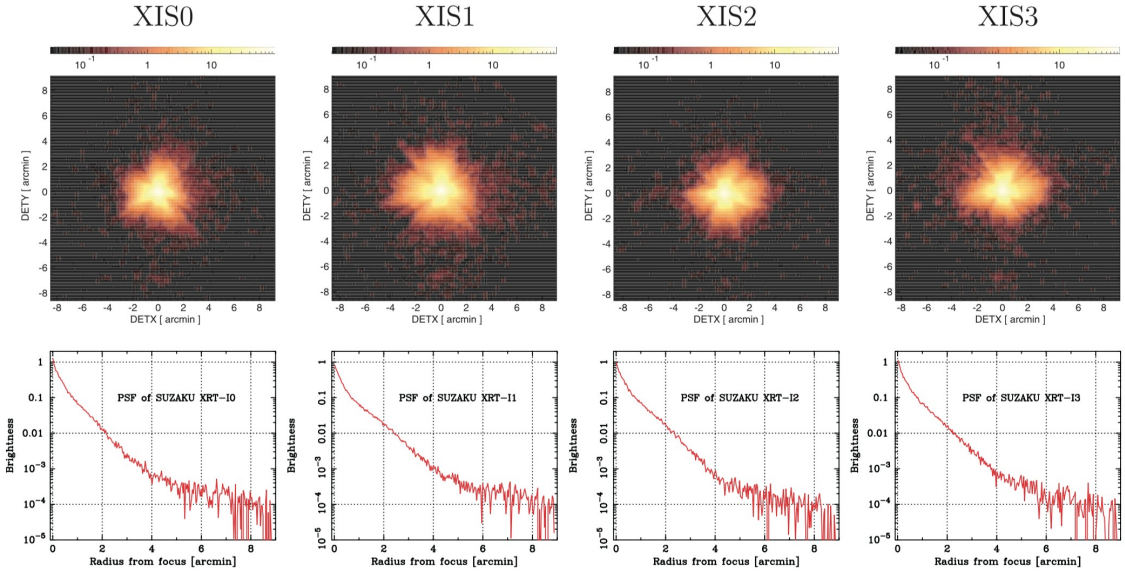

Figure 3.4: Images of a telestial point source taken in orbit (top), and their point spread functions (bottom), taken from Serlemitsos et al. (2007).

CCD cameras, XIS0, XIS2, and XIS3 are front-illuminated (FI) CCDs, with a gate structure on the front side which reduces sensitivity to X-rays bellow ~ 4 keV, while XIS1 is a back-illuminated (BI) CCD with the gate on the backside.

The XIS has several observation modes. In a normal mode, photons are accumulated on the whole CCD surface for an exposure of 8 seconds, and then are read out. Only 1/4, 1/8, or 1/16 of each CCD can also be operated with shorter read-out intervals of 0.5 second, 0.25 second and 0.125 second, respectively. These operation modes are particularly advantageous to the present thesis, because they provide us less piled-up events from bright point sources. To further reduce pile-up effects, burst mode can be further applied during observations. In this mode, the exposure times can be set even smaller between the read-out interval. When data still contains non-negligible amount of piled-up events, some data need to be discarded in an appropriate way (§3.5.1).

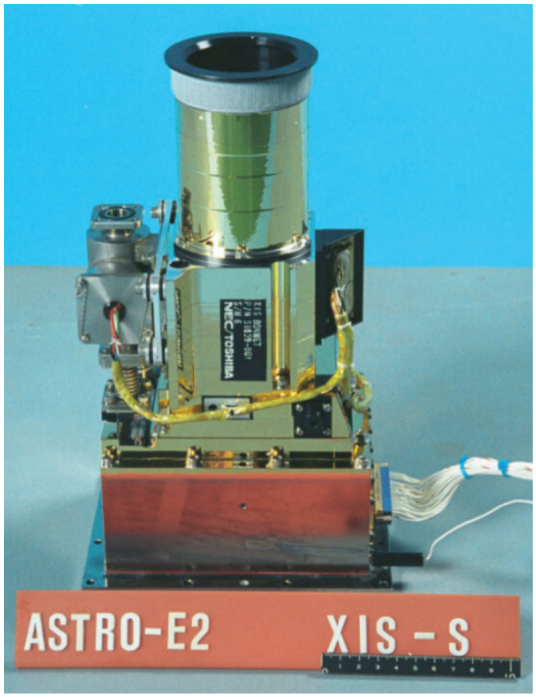

Figure 3.5: A photograph of the XIS sensor. Taken from Koyama et al. (2007).

3.4 Hard X-ray Detector

Hard X-ray Detector (HXD) is a non-imaging detector and covers 10–600 keV. As illustrated in figure 3.6, it consists of 4×4 well-type phoswich units called "well units" surrounded by 20 BGO active shields. Active shields not only stop X-rays from the direction outside the observation field of view (FOV) by photo absorption, but also reduce such X-rays significantly

by anti-coincidence rejecting events when they are scattered in the shields. Fine collimators are further installed in well units to realize the FOV of $35' \times 35'$ bellow $\sim$ 100 keV. Each well unit has four 2 mm thick Si-PIN diodes and Gd_2SiO_5 (hereafter GSO) glued to BGO active shields. Photons at 10–70 keV are absorbed in the PIN diodes above the GSO, and those at 40–600 keV passing through the PIN diodes are detected in the GSO.

Signals from the GSO and BGO glued to each other are read out with a common photomultiplier tube. Since the effective decay time of the GSO is about 122 ns at -20 °C while that of the BGO at the same temperature is 706 ns, a combined signal from these two can be distinguished by Pulse height (PH) with different shaping times. Figure 3.7 shows a fast-slow diagram, scatter plot of the fast shaped (150 ns) and slow shaped (1 μs) PHs. There, GSO events have much higher fast shaped PHs and are successfully distinguished from BGO events by fast-to-slow shaped PHs ratio. GSO and BGO share a trigger with PIN to realize an anti-coincidence screening.

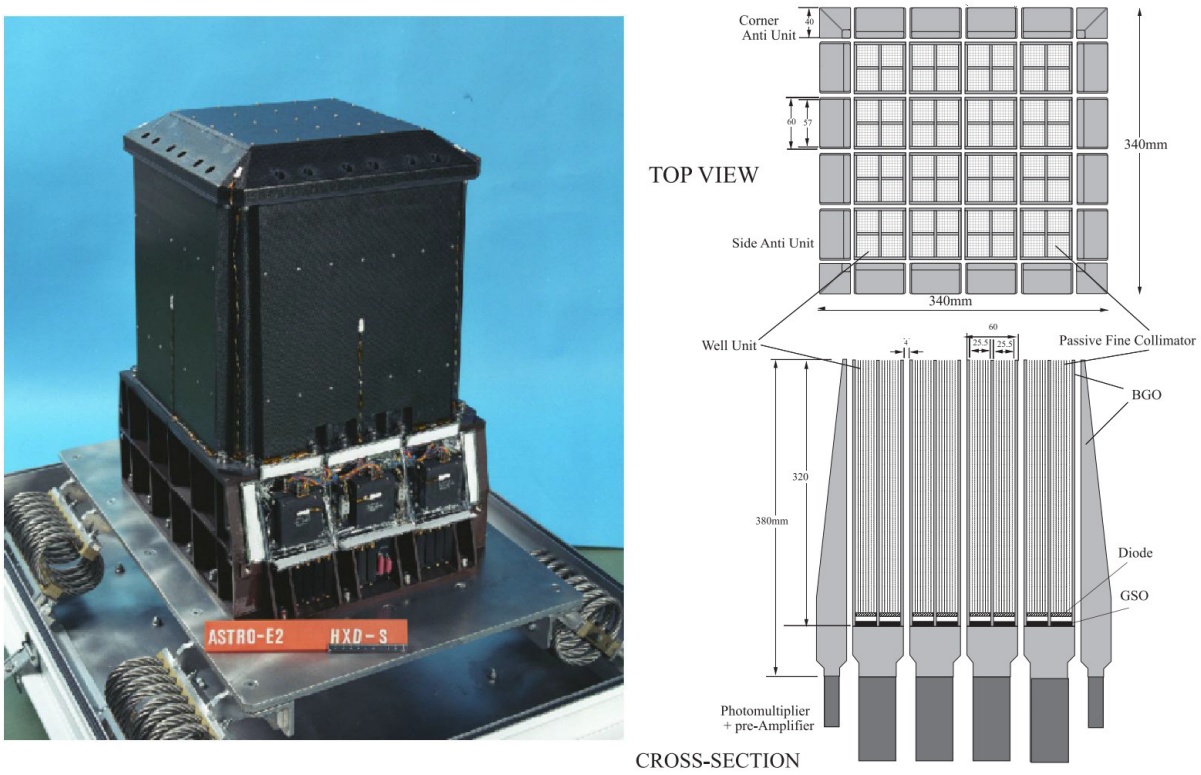

Figure 3.6: A photograph of the HXD and its schematic drawings (Takahashi et al. 2007).

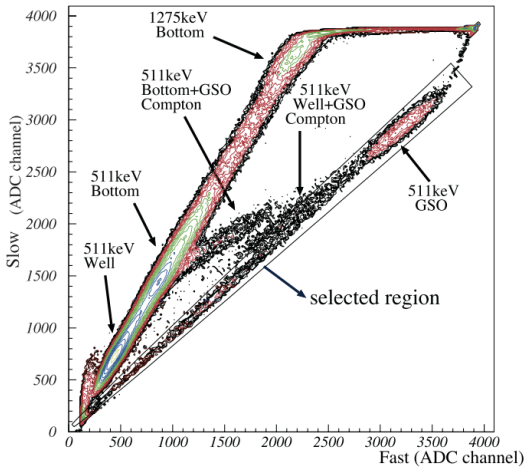

Figure 3.7: A scatter plot of pulse heights with shape times of 1 μs and 150 ns for each events, utilizing ^{22}Na and ^{133}Ba irradiation data. Taken from Takahashi et al. (2007)

3.5 Dada Reduction

All the *Suzaku* data are processed with HEASoft 6.17 to produce spectra and light curves. Processing method is described in the following sections.

3.5.1 XIS

In order to fully make use of XIS, data of the XIS-FI (XIS 0 and XIS 3) are combined. Events of GRADE 0, 2, 3, 4 and 6 are utilized. All the XIS data are reprocessed with ftool "aepipeline" with the default criteria; elapsed time after a SAA passage for the HXD is required to be longer than 436 s, earth elevation angle is $> 5°$ and day-earth elevation angle is $> 20°$, for example. The details of the criteria are described on a webpage[1].

Since the sources are observed when they are close to the Soft State, many of them are too bright that pile-up effects should be corrected (Yamada et al. 2012). The degree of pileup effects $f_{\rm pl}$ is expressed by the ratio of the probability that two or more than two photons are detected to the probability that only one photon is detected, per snap time per detection cell. The fraction can be approximately calculated with detected piled-up counts. Spectra tend to become harder when pile up takes place. Although the degree of spectral hardening due to pile-up effects depends on the original spectral shape, the hardness ratios of 7.0–10.0 keV to 0.5–10.0 keV count rates of 17 sources (Yamada et al. 2012) with $f_{\rm pl} = 0.03$ are typically $\sim$ 10% larger than those with $f_{\rm pl} = 0.001$. Thus, to safely remove piled-up counts, we discarded the data in a circle on the XIS images containing $f_{\rm pl} > 0.01$ pixels, and produced spectra and light curves. The background data is accumulated either in a rectangular or an

[1]https://heasarc.gsfc.nasa.gov/docs/suzaku/processing/criteria_xis.html/

annulus region which are outside the region for sources.

For our analysis, spectra at 0.8–10 keV are extracted as described in the previous paragraph. The data at 1.7–1.9 keV and 2.2–2.4 keV are ignored to avoid calibration uncertainties associated with silicon K-edge and gold M-edge. When Type-I bursts are observed, the data from the peak to > 300 s before and after the peak are removed, because this thesis concentrates on accretion but thermo-nuclear reaction.

3.5.2 HXD

Cleaned event data of HXD-PIN is utilized for on-source data. To construct spectra and light curves, we applied dead-time correction to on-source data. We reproduced Non-X-ray background (NXB) spectrum and light curves from the events distributed by the HXD team (Fukazawa et al. 2009), with the default criterion[2] such as the elapsed time after a SAA passage to be longer than 500s. The reproduced NXB spectra and light curves are then subtracted from the on-source ones. Cosmic-X-ray background (CXB) spectrum is effectively subtracted from the on-source spectrum by taking into account a fixed CXB model to the models for the sources as

$$\mathrm{CXB}(E) = 9.41 \times 10^{-3} \left(\frac{E}{1\ \mathrm{keV}} \right) \exp \left(-\frac{E}{40\ \mathrm{keV}} \right) \tag{3.1}$$

where the units are photons $\mathrm{cm}^{-2}\ \mathrm{s}^{-1}\ \mathrm{keV}^{-1}\mathrm{FOV}^{-1}$, and E is the energy in keV. The cross normalization between XIS and HXD is corrected by multiplying constant factors of 1.16 and 1.18 to the model for HXD, when the observation is in "XIS nominal" or "HXD nominal", respectively (Kokubun et al. 2007).

HXD-GSO data is reprocessed with aepipeline with the default criteria as described in the previous section. The on-source spectrum is constructed after dead-time correction. The NXB spectrum is reproduced from the events distributed by the HXD team, and then is subtracted from the on-source spectrum.

[2] https://heasarc.gsfc.nasa.gov/docs/suzaku/processing/criteria_hxd.html

Chapter 4

Observation

4.1 Data Selection

4.1.1 Objective of the present thesis

As reviewed in §2.4.2 and §2.4.3, spectral shapes of LMXBs change between the Soft State ($L \gtrsim 10^{37}$ erg s^{-1}) and the Hard State ($L \lesssim 10^{37}$ erg s^{-1}). In terms of the common spectral modeling with an MCD emission from a standard accretion disk plus blackbody emission from the NS surface, the most major difference between the two states is that the blackbody Comptonization is much stronger in the Hard State than in the Soft State (§2.4.3). As reviewed in §2.4, this is presumably because a standard accretion disk in the Soft State continues down to a close vicinity of the NS, whereas the disk in the Hard State changes, e.g., at several times the NS radius, into an optically-thin/geometrically-thick accretion flow. Thus, to understand the accretion in LMXBs and the differences between the two states, it is essential to better understand the physics of the hot accretion flow, or corona.

The best way to achieve the above goal is to utilize luminosity-dependent changes in the Compotonization properties. Because these changes are most prominent through transitions between the two States (§2.4.4), of particular importance is the broad-band source behavior near or across the boundaries between the two States. So far, we have already found a data set of Aql X-1 containing a Hard-to-Soft state transition, and its analysis in Ono et al. (2017) gave rich information on the behavior of the Comptonizing corona (§2.4.4). Nevertheless, we are still left with the following basic questions about the Comptonizing corona. The questions are; (A-i) To what extent the model consisting of an MCD and a Comptonized blackbody is valid (A-ii) are model parameters always determined by basic parameters, such as the X-ray luminosity and the inclination of the binaries, (B-i) are the properties of hot accretion flows universal among LMXBs, (B-ii) if so, what is the essential difference of the hot flows between the two States, and finally, (C) what is the essential differences due to the hysteresis in the luminosity rising and decreasing phases (§2.4.4).

4.1.2 Selection criteria

In order to achieve the above stated goals, we select data close to the state transitions, from the *Suzaku* archive which provides high-quality spectra in a wide energy band. To find such data, a spectral hardness ratio and the luminosity are good parameters to characterize each data set, as easily understood from figure 1.1, figure 2.9, figure 2.12, and figure 2.14. Figure 4.1 shows a scatter plot of all the *Suzaku* data of LMXBs, on the plane of the hardness ratio H vs. the absorbed luminosity, taken from Sakurai (2015). There, each data point represents one *Suzaku* observation, which typically lasted several tens ksec. In calculating H, the soft energy band was chosen to be 5–10 keV to avoid absorption, while the hard energy band to be 20–40 keV to obtain good contrasts of H. Thus H is defined as

$$H = (20 - 40\,\mathrm{keV\ HXD\ count\ rate})/(5 - 10\,\mathrm{keV\ XIS\ count\ rate}). \tag{4.1}$$

The absorbed luminosities were calculated from the 0.8–10 keV XIS-FI flux and the 12–60 keV HXD-PIN flux, both multiplied by $4\pi D^2$, where D is the distance to each source.

In figure 4.1, the data points form two clusters, at $H \sim 0.08$ and $H \sim 0.006$, corresponding to the Hard State and the Soft State, respectively. This is more clearly seen in figure 4.2 in the form of occurrence histogram in H. Across the transition of Aql X-1 analyzed by Ono et al. (2017), the hardness ratio decreased by an order of magnitude from $H = 0.12$ to $H = 0.008$, connecting the two States. Thus, it is most likely that transitions similar to that of Aql X-1 occur when the source is at around $H \sim 0.03$ in between the two clusters. Further considering the histogram in figure 4.2, we select the following data.

(1) data located at $H = 0.01 - 0.03$ in figure 4.2,

(2) data sets of those objects which have multiple observations both in the range of $H > 0.03$ and $H < 0.01$

With the criterion (1), it is the most likely that the sources were varying around the transition threshold during that particular observation. Data with the criterion (2) allow us to compare the results obtained in the Soft State ($H < 0.01$) and those in the Hard State ($H > 0.3$). As a result, in addition to the obvious case of Aql X-1, the criterion (1) has left us with 4 observations in total, namely, that of 4U1636-536, 4U1728-34, GX 349+2 and GX17+2. The criterion (2) has yielded further 16 data from 3 sources; 4 additional observations of 4U1636-536, 8 observations of 4U1705-44, and 4 observations of 4U1608-52. These data sets are listed in table 4.1, where different observations of the same source are specified with the data set numbers #1,#2$\cdots$. Among the total 6 sources, those with "GX" (GX sources) or the constellation name (Aquila) are the brightest cosmic X-ray sources which were already known in the 1960's. The remaining are "4U" sources, discovered by *Uhuru*, the first X-ray satellite launched in 1970. We are thus dealing with very typical bright LMXBs, focusing on their state-transition behavior which has remained still unexplored.

Let us examine if the data sets selected with criterion (1) are really close to transitions (or hopefully, even covering a transition episode). Figure 4.3 shows scatter plots of the

relevant data sets between the soft photon count rates and H. There, H of 4U 1636-536 and 4U1728-34 decreases by about an order of magnitude when the soft photon count rate increases by $\sim$ 30%. This agrees with the general behavior of LMXBs when they move between the two spectral states, because the soft count rate should increase from the Hard to Soft State while the hard photon counts should decrease. In contrast, the values of H for GX 349+2 and GX 17+2 depend little on, or increase slowly with, the soft count rate. This sort of behavior would not be expected around the transition.

As shown in figure 4.4, we further made time-averaged spectra of these data sets, and then fitted them with a model consisting of an MCD and a Comptonized blackbody components with a common absorption. The fit results indicate that the 4U source spectra are strongly Comptonized as evidenced by their power-law like shape toward higher energies, whereas those of the GX sources are rather close to blackbody spectra. After removing the photoelectric absorption (of which the effect is still inclusive in figure 4.1), the unabsorbed 0.1–100 keV model luminosities of 4U1636-536 and 4U1728-34 became 1.2×10^{37} erg s^{-1} and 1.4×10^{37} erg s^{-1}, respectively, which fall in the typical range of transition luminosities, from $\sim 10^{36}$ erg s^{-1} to a few 10^{37} erg s^{-1} (Asai et al. 2012). In contrast, those of GX 349+2 and GX17+2 are too high as 5.9×10^{37} erg s^{-1} and 3.0×10^{38} erg s^{-1}. These differences in the spectral shapes and the luminosities indicate that the present 4U sources were observed when they are close to spectral transitions, while the GX sources were in the Soft State as is usually the case for them. We hence select 4U 1636-536 and 4U1728-34, tentatively regarding them as in a luminous Hard State, while exclude GX 349+2 and GX 17+2 from our analysis.

4.2 The selected data

4.2.1 Aquila X-1

Aql X-1 is a typical recurrent transient LMXB, with an optical counterpart of $V = 21.6$ in quiescence (Chevalier et al. 1999), and the binary orbital period of 18.95 hours (Welsh et al. 2000). Outbursts take place quasi-periodically every 125–300 days (Priedhorsky & Terrell 1984; Kitamoto et al. 1993). Through observations of Type-I bursts with PRE (§2.2.4) (Jonker & Nelemans 2004), the distance to the source is constrained at 5.2 ± 0.7 kpc. During another Type-I burst, nearly a coherent milli-second X-ray pulsation was found at 549 Hz (Zhang et al. 1998). It was also detected, though only $\sim$ 150 s, in persistent emission at 550.27 Hz (Casella et al. 2008). These high frequency pulsations are considered to arise from the NS spin. The slight frequency difference between these measurements is considered to arise from the NS's orbital motion.

Figure 4.5 shows a long-term light curve of Aql X-1 with the *MAXI*/GSC. It repeats outbursts, each lasting $\sim 10 - 50$ days, after a long quiescence of $\sim$ 300 days. The source was observed with *Suzaku* on 2011 October 21, as indicated with red lines in figure 4.5, during a rising phase of an outburst.

Figure 4.6 shows *Suzaku* light curves of Aql X-1 obtained on this occasion, covering about

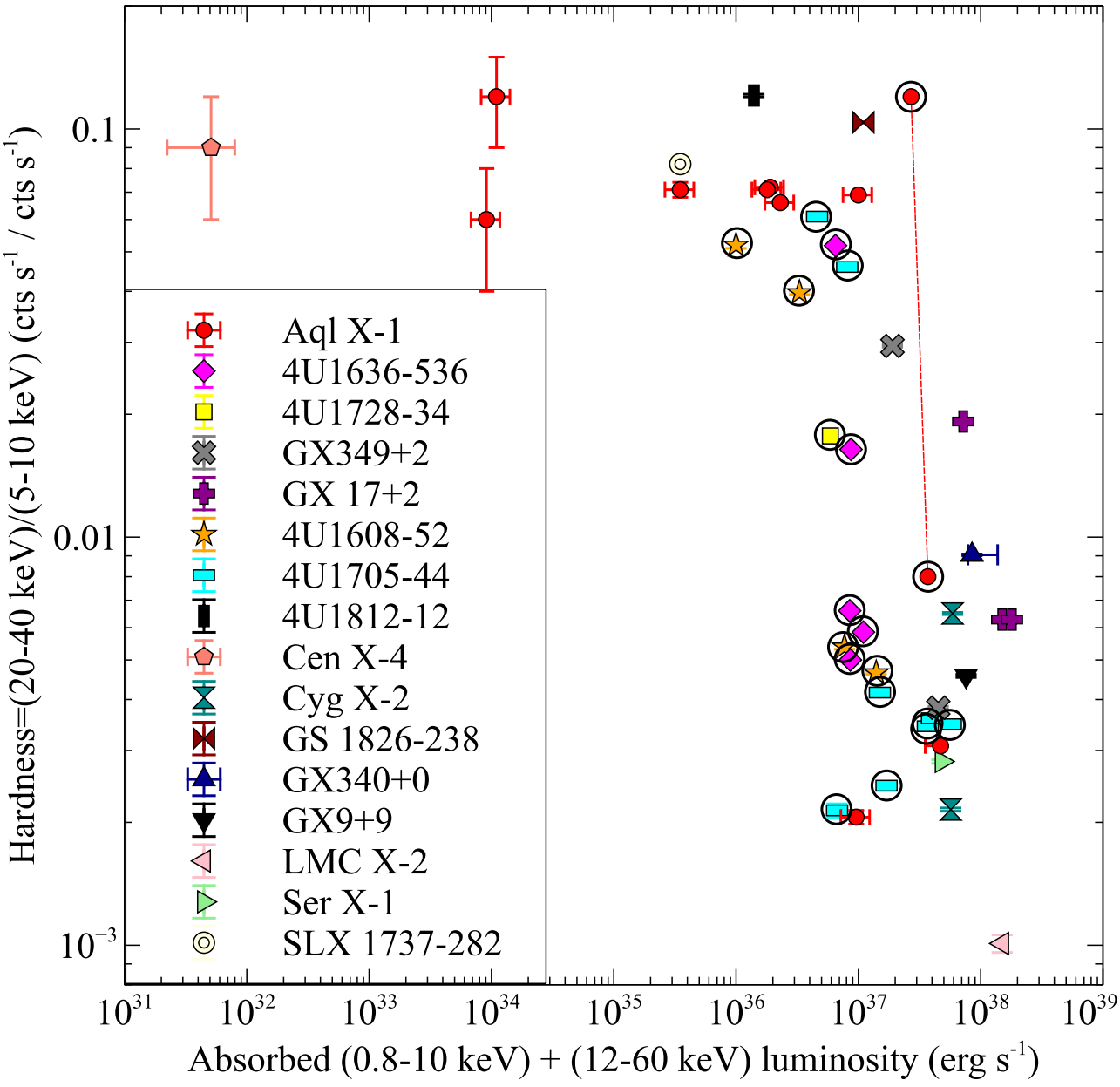

Figure 4.1: A scatter plot of LMXBs listed in table A.1 and A.2, on the plane between the (20–40 keV)/(5–10 keV) hardness ration H of eq. (4.1) and the absorbed 0.8–10 keV plus 12–60 keV luminosity. The maximum and minimum H values of Aql X-1 during the transition are connected with a red dashed line. Except this particular pair, each data point represents one *Suzaku* observation (= one data set). The data sets analyzed in the present thesis are indicated with open circles.

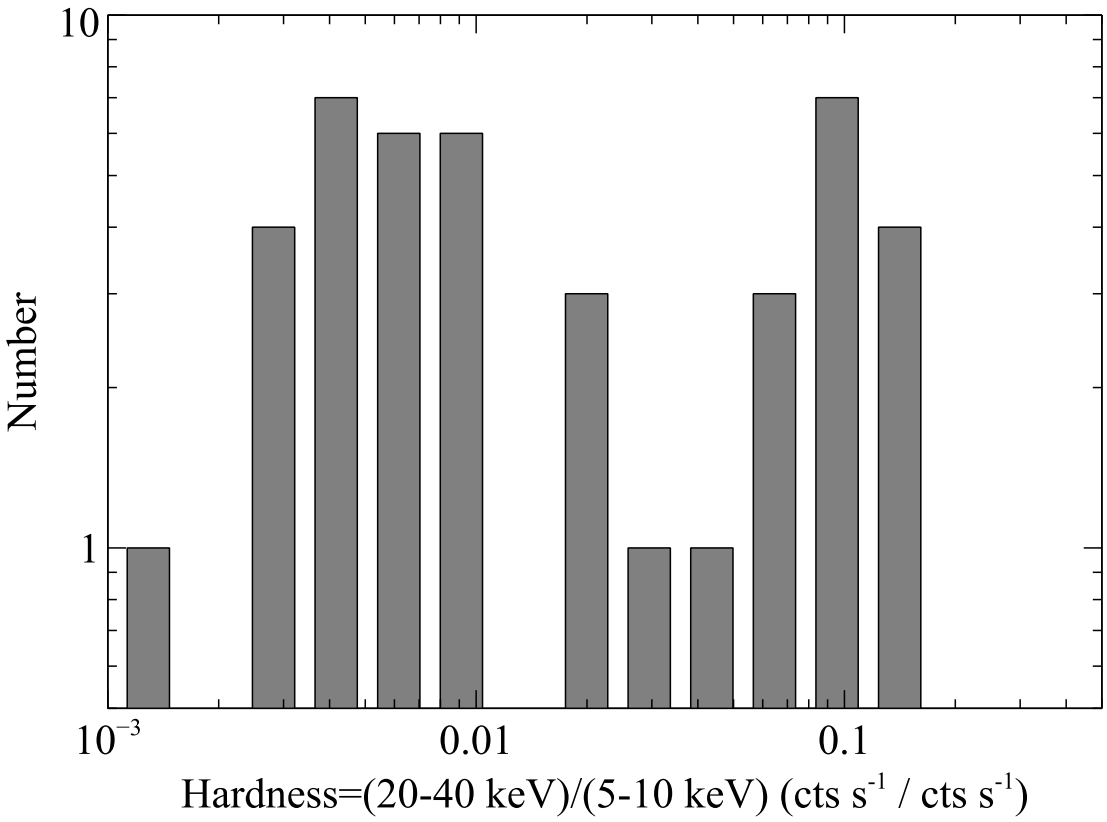

Figure 4.2: The occurrence histogram of the hardness ratio in figure 4.1.

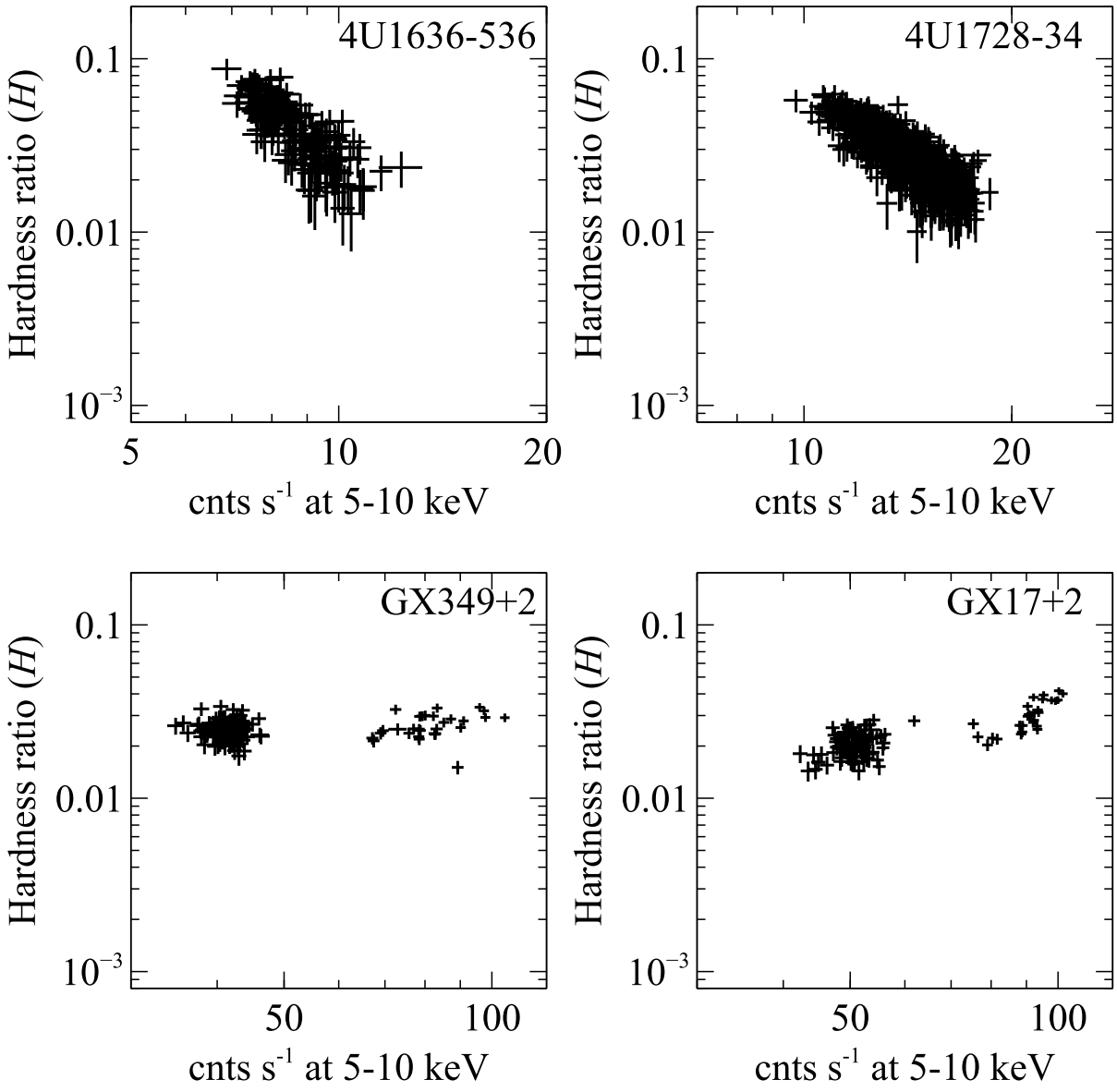

Figure 4.3: Scatter plots of 4U1636-536 (#2), 4U1728-34, GX 349+2 and GX 17+2 between the background-subtracted 5–10 keV count rates with XIS0+XIS3 and the hardness ratio H defined in eq. (4.1).

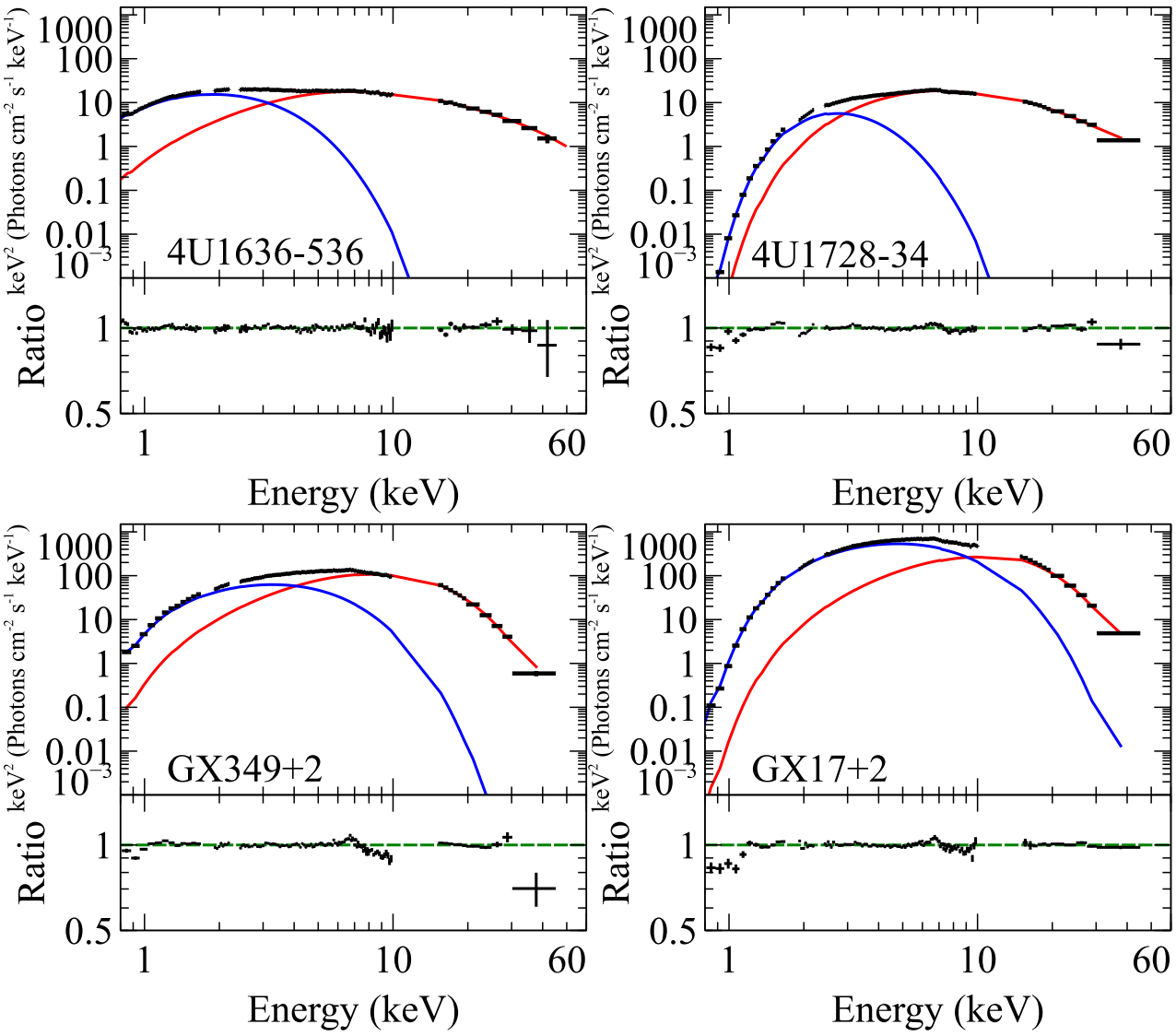

Figure 4.4: Time-averaged $\nu F\nu$ spectra of 4U1636-536(#2), 4U1728-34, GX 349+2, and GX 17+2, normalized to a distance of 1 kpc so as to make their luminosities directly comparable. Their best fit `tbabs*(diskbb+nthcomp)` model and the data-to-model ratios are shown. The instrumental responses are approximately removed, whereas the effects of photoelectric absorption are still inclusive. The MCD and Comptonized blackbody comonents (§2.3.3, §2.3.4) are indicated in blue and red, respectively.

Table 4.1: The *Suzaku* data of LMXBs selected with the criteria (1) and (2) in §4.1.2.

Name	Obs. ID[a]	data sets[b]	Date	E[c]	$L_{\rm abs}$[d] ($\times 10^{37}$)	H ($\times 10^{-3}$)	D (kpc)
Aql X-1	406010020(1)	-	11/10/21	35.2	$2.7-3.7$	$120-8$	5.2 ± 0.7
4U1608-52	404044010(2)	#1	10/03/11	28.0	1.4	4.65 ± 0.04	3.6
	404044020(2)	#2	10/03/15	25.2	0.77	5.38 ± 0.07	
	404044030(2)	#3	10/03/18	14.2	0.33	39.7 ± 0.4	
	404044040(2)	#4	10/03/22	14.5	0.10	51.9 ± 0.9	
4U1636-536	401050020(2)	#1	07/02/22	33.2	1.1	5.85 ± 0.07	5.9
	401050030(1)	#2	07/03/01	45.2	0.87	16.4 ± 0.1	
	401050040(2)	#3	07/03/27	26.1	0.85	6.6 ± 0.1	
	401050050(2)	#4	07/03/29	11.0	0.86	5.0 ± 0.1	
	401050010(2)	#5	07/02/09	20.3	0.65	51.8 ± 0.5	
4U1705-44	401046020(2)	#1	06/09/18	14.7	1.7	2.46 ± 0.06	$7.4^{+0.8}_{-1.1}$
	401046030(2)	#2	06/10/06	16.7	0.67	2.14 ± 0.08	
	402051010(2)	#3	07/09/05	8.8	5.7	3.48 ± 0.06	
	402051020(2)	#4	07/10/08	14.8	3.7	3.44 ± 0.06	
	402051030(2)	#5	08/02/20	19.5	1.5	4.16 ± 0.09	
	402051040(2)	#6	08/03/18	12.4	4.0	3.60 ± 0.06	
	401046010(2)	#7	06/08/29	14.4	0.81	45.9 ± 0.5	
	406076010(2)	#8	12/03/27	84.5	0.46	61.0 ± 0.4	
4U1728-34	405048010(1)	-	10/10/04	88.3	0.59	1.77 ± 0.01	5.2
GX349+2	400003020(1)	-	06/03/19	23.9	7.6	4.57 ± 0.04	5
GX17+2	402050020(1)	-	07/09/27	17.7	7.2	19.2 ± 0.1	9.8

[a] The applied criterion (§4.1) is indicated in the parenthesis.
[b] Specifications of data sets of each source.
[c] Net exposure per XIS (ks).
[d] Absorbed 0.8–60 keV luminosity (erg s^{-1}).

a day. Thus, the soft photon count rate in 5–10 keV increased monotonically by a factor of ~ 2 on ~ 30 ks towards the end of observation. At the same time, the hard photon count rate in 20–40 keV decreased by about an order of magnitude, resulting in a strong negative correlation between H and the 5–10 keV count rate. As already confirmed by Ono et al. (2017), and indicated in figure 4.1 by a line running from $H \sim 0.12$ to $H \sim 0.008$, this behavior represents a Hard-to-Soft state transition, and is considered to provide a prototype of state transitions (§1, §2.4.4). Referring to Ono et al. (2017), we briefly re-analyze the state-transition data in §5.1.1.

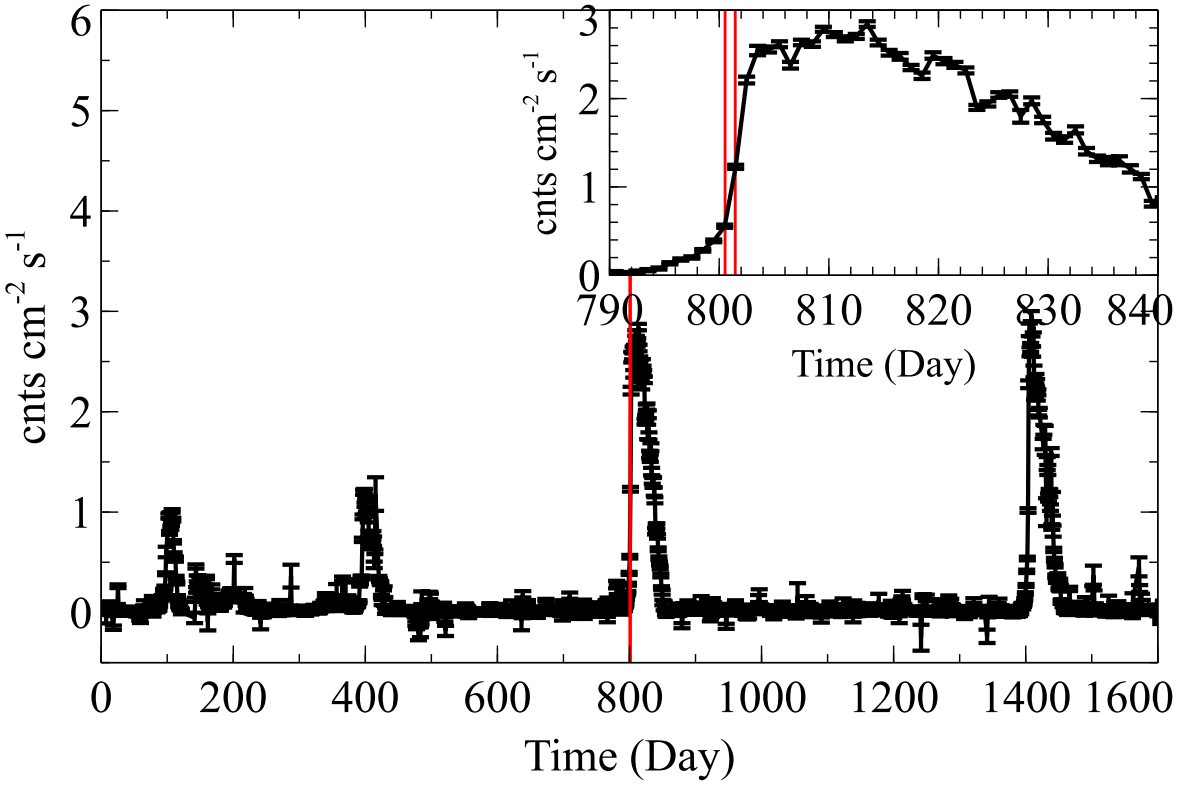

Figure 4.5: A long-term light curve of Aql X-1, obtained with the *MAXI*/GSC in 2–20 keV. The time origin is 2009 August 12. The *Suzaku* observation period in table 4.1 is indicated with red lines. The inset shows an expanded view around this epoch.

4.2.2 4U1636-536

This is a typical persistent LMXB, exhibiting frequent Type-I bursts (Swank et al. 1976) and a spin frequency of 581 Hz (Zhang et al. 1997; Strohmayer & Markwardt 2002). The source has long been studied in multi-wavelengths from optical, UV, to X-rays. Together with a low-mass (0.4 $M_\odot$) companion star (Fujimoto & Taam 1986; van Paradijs et al. 1990), it forms

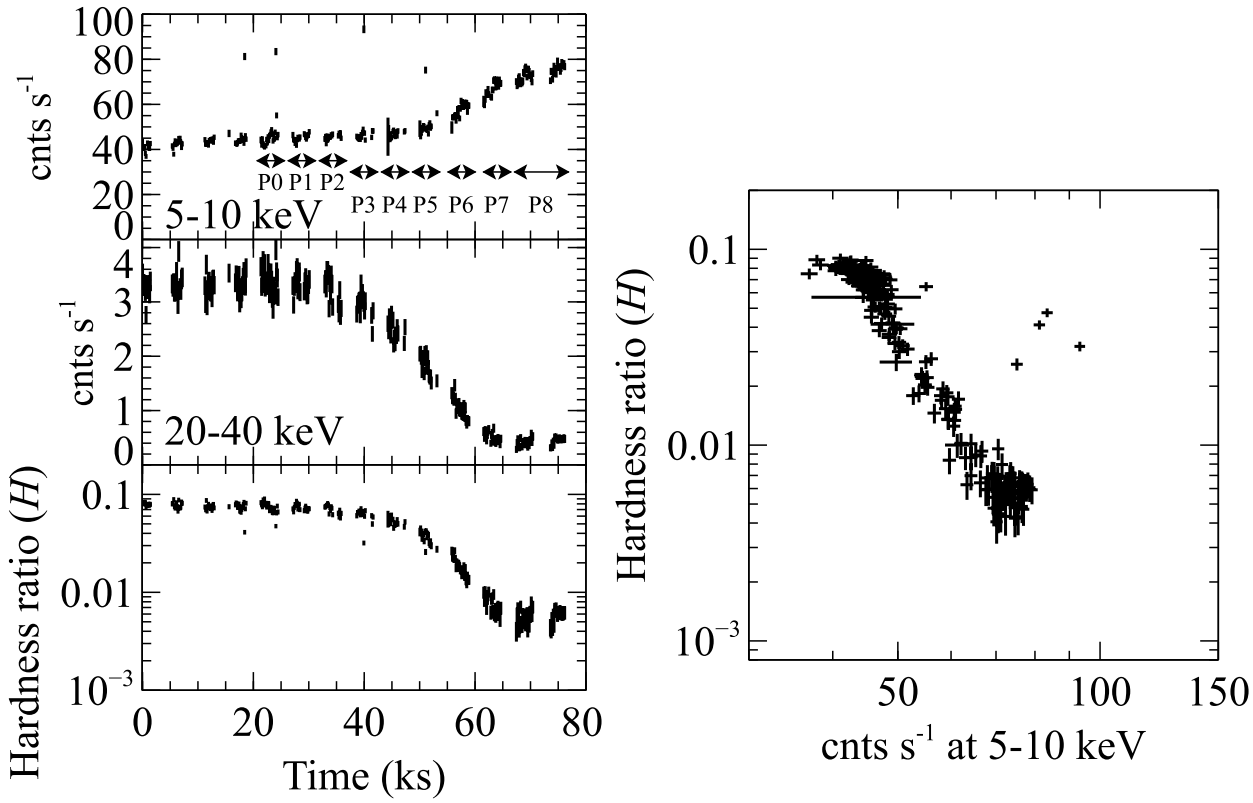

Figure 4.6: (Left) Background subtracted one-day light curves of Aql X-1, taken with XIS 0 plus XIS 3 in 5–10 keV, and with HXD-PIN in 20–40 keV. The bottom panel shows the hardness ratio H defined in eq. (4.1). (Right) A scatter plot between the 5–10 keV XIS0+3 count rate and H. Several irregular data points are caused by Type-I bursts (§2.2.4) which are also seen in the 5–10 keV light curve.

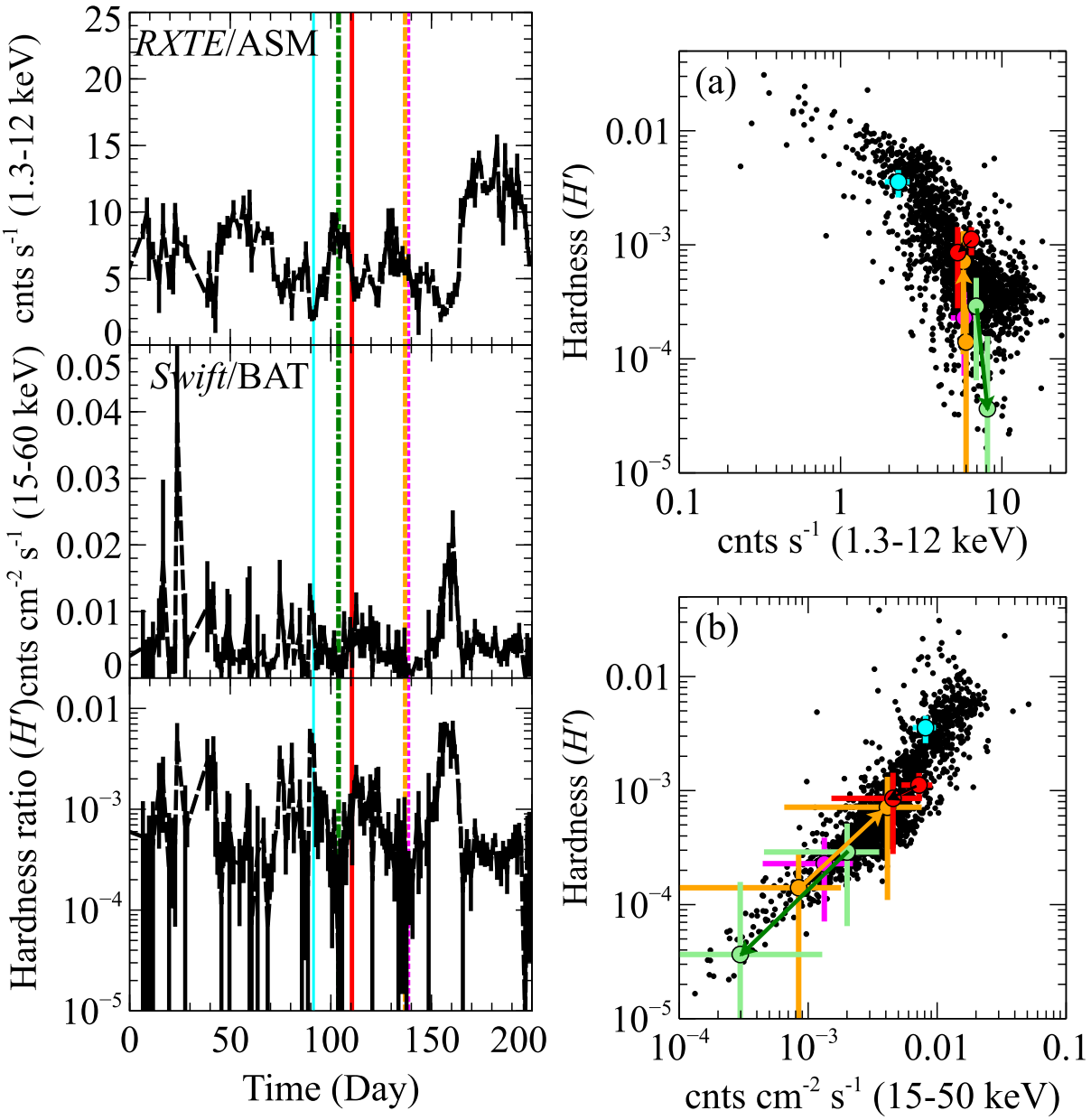

Figure 4.7: (Left) Long-term light curves of 4U1636-53, obtained with the *RXTE*/ASM in 1.3–12 keV (top) and *Swift*/BAT in 15–50 keV (middle). The bottom panel shows their ratios representing H' in eq. (4.2). The periods of *Suzaku* observations (#1, #2, #3, #4, and #5) are indicated with green dash-dot line, red solid line, orange dashed line, magenta dotted line, and cyan solid line, respectively. The time origin is 2006 November 11. (Right) The hardness ratio H' in eq. (4.2) is plotted against the count rates with (a) the *RXTE*/ASM, and (b) the *Swift*/BAT. The whole data shown on the left panels are included, with one-day binning. The data overlapping with the *Suzaku* observations are indicated with the same color as in the left panels.

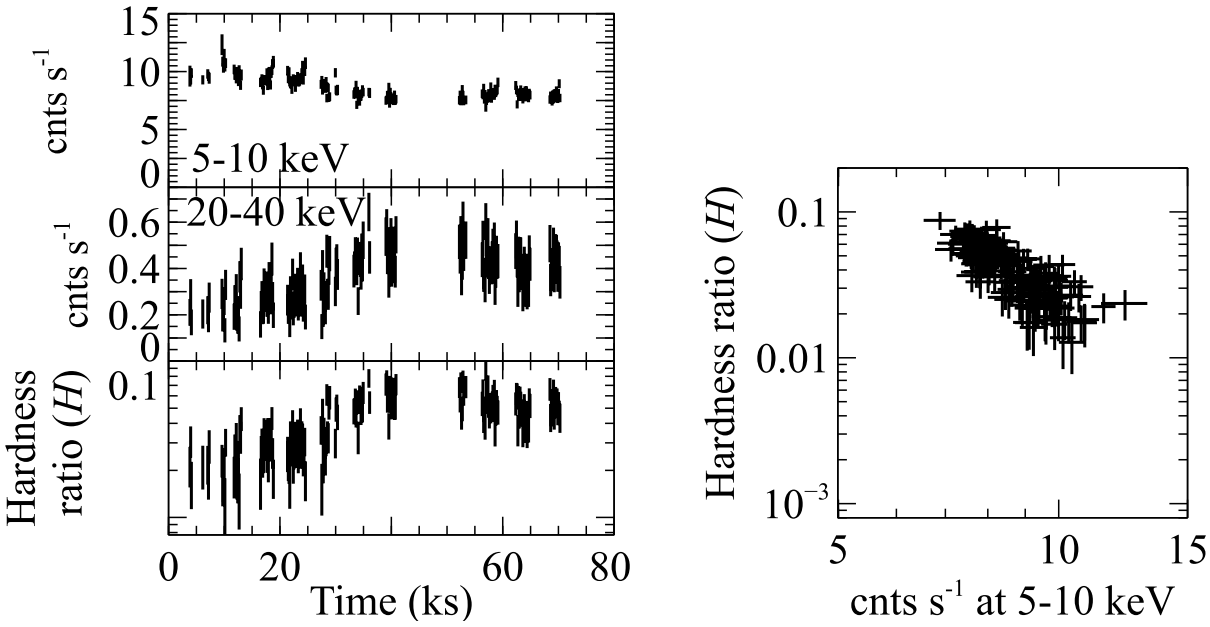

Figure 4.8: The same *Suzaku* data as figure 4.6, but for 4U1636-536 #2. The bin width is 128 s.

a binary with the orbital period of 3.8 hour (van Paradijs et al. 1990). Figure 4.7 (left) shows long-term light curves of this source, taken with the *RXTE*/ASM and *Swift*/BAT, covering 200 days. Here, we utilized the *RXTE* and *Swift* data, because *MAXI* had not been launched yet when the *Suzaku* observations were conducted (in 2007). The source shows quasi-periodic intensity variations on a time scale of ~ 40 days (Shih et al. 2005). Since the *RXTE*/ASM data are available only in two energy bands, and those of the *Swift*/BAT in energies above 15 keV, here we define the hardness ratio H' as

$$H' = (RXTE/\mathrm{ASM}\ 1.3-12\ \mathrm{keV\ count\ rate})/(Swift/\mathrm{BAT}\ 15-50\ \mathrm{keV\ count\ rate}). \quad (4.2)$$

This H' is considered to play a similar role to H of eq. (4.1), except systematic differences in their absolute values because of different instruments employed. As presented in figure 4.7 (a) and (b), this H' varies significantly, in negative correlation with the 1.3–12 keV count rate, and positive correlation with the 15–50 keV count rate. As a result, the source is thought to undergo transitions frequently, and move between the two states.

The observations with *Suzaku* were conducted five times, and all of them have been selected (table 4.1). These periods are indicated in figure 4.7 with different colors. Among the five observations, 4U1636-536 #2 (red in figure 4.7) has been selected by the criterion (1) in §4.1.2. It is characterize by $H = 0.016$ in figure 4.1 and $H' = 0.001$ in figure 4.7. The *Suzaku* light curves of this data set with a net exposure of ~ 70 ksec is presented in figure 4.8. The XIS count rate decreased by $\sim 30\%$ while that of HXD-PIN increased (figure

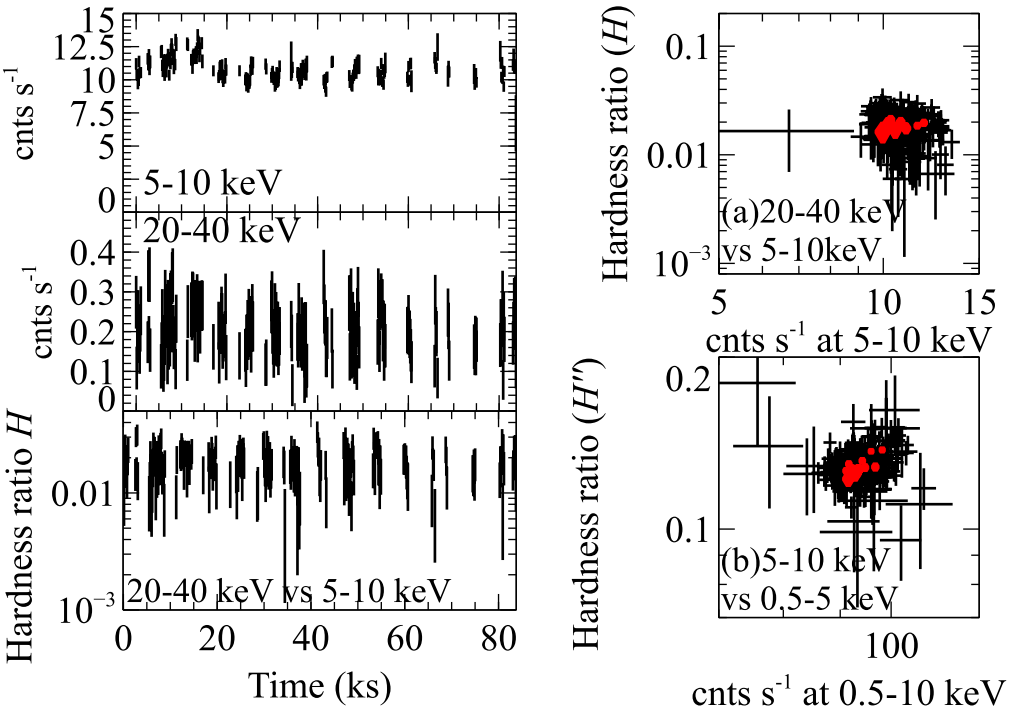

Figure 4.9: (Left) The same as figure 4.6 but for 4U1636-536 #1. (Right) The 5–10 keV XIS count rate, shown against H of eq. (4.1), and the 5–10 keV vs 0.5–5 keV hardness ratio.

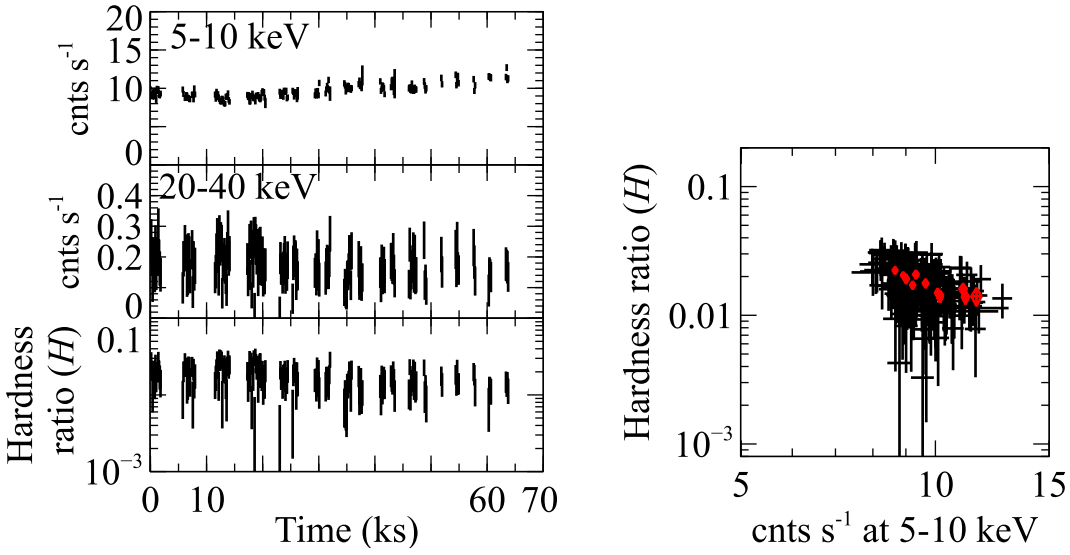

Figure 4.10: The same as figure 4.9 for 4U1636-536 #3.

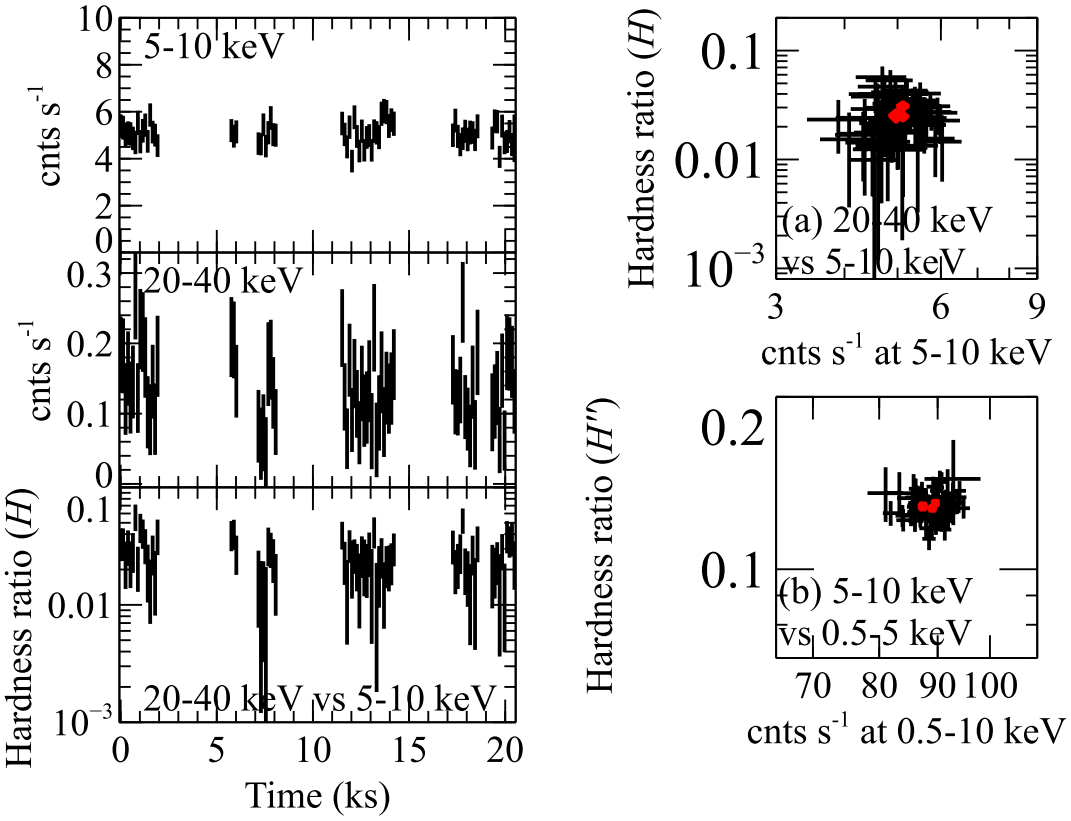

Figure 4.11: The same *Suzaku* data as figure 4.9, but for 4U1636-536 #4.

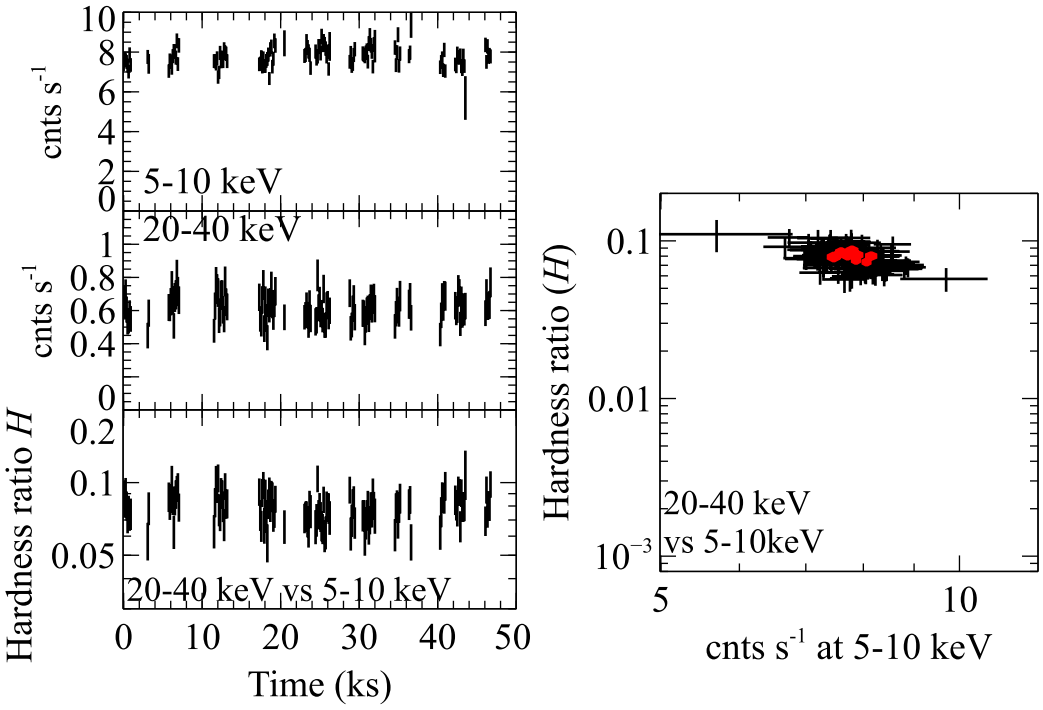

Figure 4.12: The same as figure 4.9 for 4U1636-536 #5.

4.8 left) in an anti-correlation (figure 4.8 right), involving a factor ~ 6 change in H. This is qualitatively the same correlation as that in figure 4.6, although the time dependence is reversed, and the source did not become softer than $H \sim 0.01$. Further considering that the spectrum in figure 4.4 is rather hard, we infer, as in §4.1.2, that the source was in the most luminous end of the Hard State. This tentative assignment needs to be verified (or modified) through our subsequent analysis.

Of the other 4 observations, #1, #3, and #4, with $H \sim 5 \times 10^{-3}$ (table 4.1, figure 4.1), were clearly performed in the Soft State. In the remaining one, i.e., #5, the source was in the Hard State, because we find $H \sim 0.1$. Thus, these 4 data sets satisfy the criterion (2).

The basic source behavior in #1, #3, and #4 is presented in figures 4.9, 4.10, 4.11, and 4.12, respectively. Data binned into 96 minutes are also plotted in red on the right side of these figures, in order to improve statistics and synchronize the sampling with the *Suzaku* orbital period of 96 minutes. The observations #1 and #3 showed significant intensity variation in the 5–10 keV band. The associated variation of H, if any, was yet much weaker compared with those of Aql X-1 (figure 4.6) and 4U 1636-536 #2 (figure 4.8). In #1, when the source was the brightest, the correlation between H and 5–10 keV intensity is slightly positive, like the GX sources in the Soft Sstate (figure 4.3), while it is slightly negative in #3 (figure 4.10) when the source is relatively less luminous. As presented in figure 4.11, the observation #4 was relatively short with an exposure of ~ 20 ksec, and variation was not clearly detected in either of the two-color intensities, or in the hardness ratio H. In figure 4.12, the source during the observation #5 is clearly in the Hard State with $H \sim 0.1$, with little variation in the count rates and H.

4.2.3 4U 1728-34

4U1728-34 is a persistent LMXB near the Galactic center, and was discovered with the SAS-3 satellite (Lewin et al. 1976; Hoffman et al. 1976). It frequently exhibits Type-I bursts (Basinska et al. 1984), often with PRE (§2.2.4) which constrained the distance to the source to be 4.1–5.1 kpc (Di Salvo et al. 2000; Galloway et al. 2003). Bursts also revealed a nearly coherent oscillation at 363 ± 5 Hz (Strohmayer et al. 1996), which is again interpreted as the neutron star's spin frequency. Its optical counterpart has not yet been identified due to strong optical extinction near the Galactic center.

Figure 4.13 presents long-term light curves with the *RXTE*/ASM and *Swift*/BAT. The source is persistently bright and varies on a time scale of ~ 50 days. The hardness ratio H' changes significantly by ~ 2 orders of magnitude. Like in the case of 4U 1636-536 (figure 4.7), the source forms two clusterings at $H' \sim 0.01$ and $H' \lesssim 0.001$, which are connected at $H \sim 0.001$. Thus, the source is considered to switch occasionally between the Hard State at $H' \sim 0.01$ and the Soft State at $H' \lesssim 0.001$.

The *Suzaku* observation of this LMXB was performed only once on 2010 October 4. This data set has been selected with the criterion (1) in §4.1.2. Indeed, in figure 4.13 (a,b), the source was presumably in between the two states during the *Suzaku* observation. In more detail, figure 4.14 shows *Suzaku* light curves with a net exposure of ~ 200 ksec. The

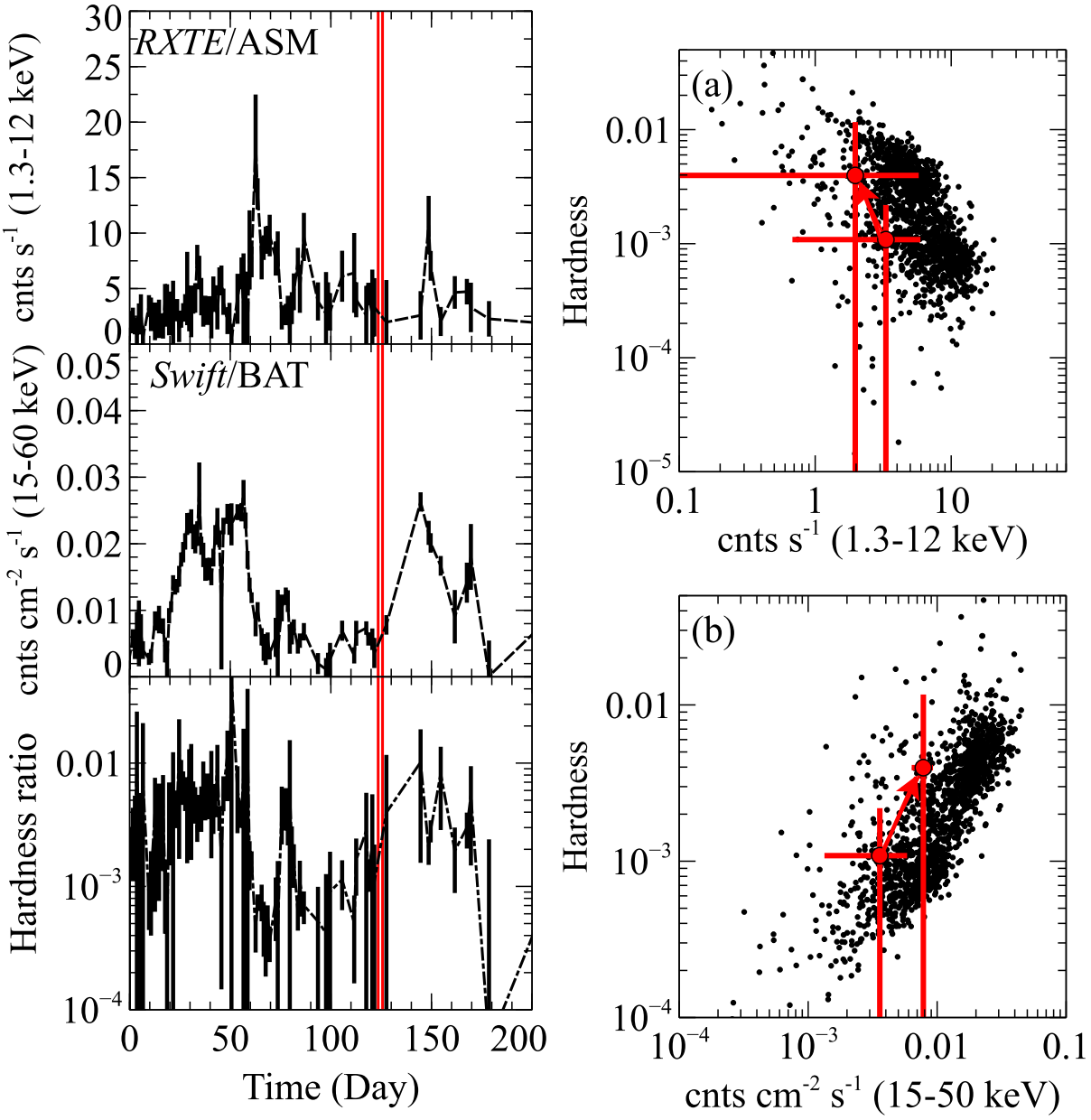

Figure 4.13: The same long-term light curves as figure 4.7, but for 4U1728-34. The period of the *Suzaku* observation is shown with red.

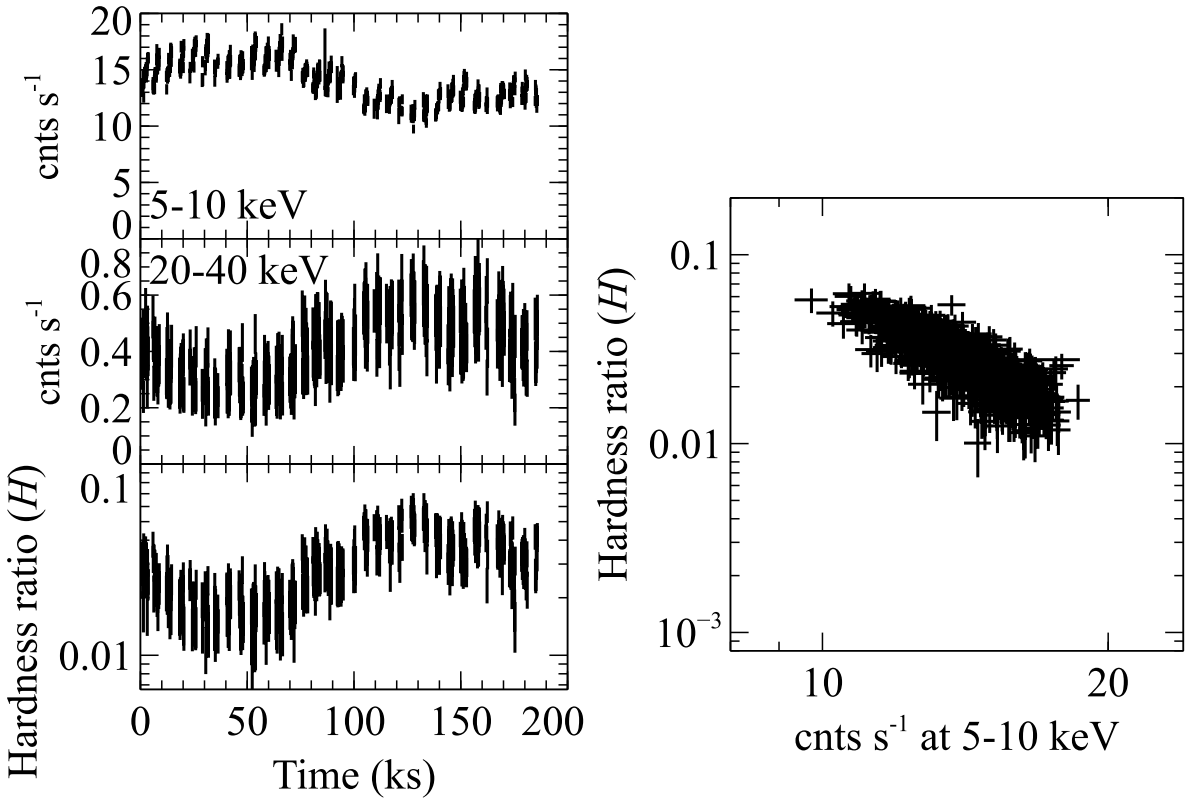

Figure 4.14: The same *Suzaku* data as figure 4.6, but for 4U 1728-34 (405048010).

XIS 5–10 keV count rate decreased monotonically in $\lesssim 50$ ks at around the middle of the observation, involving an increase of the HXD-PIN count rate. The hardness ratio H is strongly anti-correlated with the XIS count rate (figure 4.14), as would be if the source was actually making a transition. However, like in 4U 1636-536 (#2), the source remained at $H > 0.01$ (figure 4.14) rather than falling to $H < 8 \times 10^{-3}$ (cf. figure 4.11), and the spectrum in figure 4.4 exhibits a hard continuum. Therefore, we tentatively conclude, with some reservation, that 4U 1728-34 too was in the most luminous end of the Hard State.

4.2.4 4U 1608-52

4U 1608-52 is a recurrent transient LMXB, producing outbursts with intervals of ~ 85 or ~ 150 days (Lochner & Roussel-Dupre 1994). Like Aql X-1 and 4U 1728-34, the source exhibits Type-I bursts with PRE (§2.2.4), with which the distance is estimated to be 3.6 kpc (Nakamura et al. 1989). Like Aql X-1, 4U 1608-52 makes clear transitions between the two states along its outburst evolution (Mitsuda et al. 1989).

Figure 4.15 shows long term light curves with the the *RXTE*/ASM and *Swift*/BAT. Like Aql X-1, it shows an outburst after a quiescence, again returning to quiescence. In the diagram between the hardness ratio H and *RXTE*/ASM 1.3–12 keV count rate in figure 4.15, the source forms two clusterings like 4U 1728-34, but even more distinctively.

As presented in figure 4.15, the source was observed with *Suzaku* 4 times, when it was decaying after an outburst. The 1.3–12 keV *RXTE*/ASM count rate decreased from ~ 30 cts s^{-1} to ~ 1 cts s^{-1} from #1 to #4, so the source moved from the Soft State with $H' \sim 1 \times 10^{-4}$ to the Hard State with $H' \sim 1 \times 10^{-3}$. Thus, the 4 data are selected from the criterion (2). Figure 4.16, through 4.19 show the *Suzaku* light curves. The observations #1 and #2 are in the soft state with $H \lesssim 0.01$, with little variation in H, like the Soft State data of 4U 1636-536. The observations #3 and #4 are in the hard state with $H \sim 0.1$, which correspond to the hardest end of Aql X-1, again with little variation in H.

4.2.5 4U 1705-44

The final object, 4U1705-44, is also a persistently bright source. Its 2–12 keV intensity varies by more than an order of magnitude (Barret & Olive 2002). When the intensity is low, it produces Type-I bursts (§2.2.4) which constrained the source distance at $\lesssim 7.8$ kpc (Galloway et al. 2008). The source is known to switch between the Soft and Hard States, across a 0.1–200 keV threshold luminosity of 6.9×10^{36} erg s^{-1} to 3.1×10^{37} erg s^{-1} at 7.4 kpc (Haberl & Titarchuk 1995; Lin et al. 2010).

Figure 4.20 presents long-term light curves 4U 1705-44, again obtained with the *RXTE*/ASM and *Swift*/BAT. Although the source behaves in a similar way to 4U 1636-536 (figure 4.7) and 4U 1728-37 (figure 4.13), the bimodality between the Soft State ($H' \sim 10^{-4}$) and the Hard State ($H' \sim 10^{-2}$) is clearer. The same figure for #8 but only with *RXTE* is shown in figure A.1.

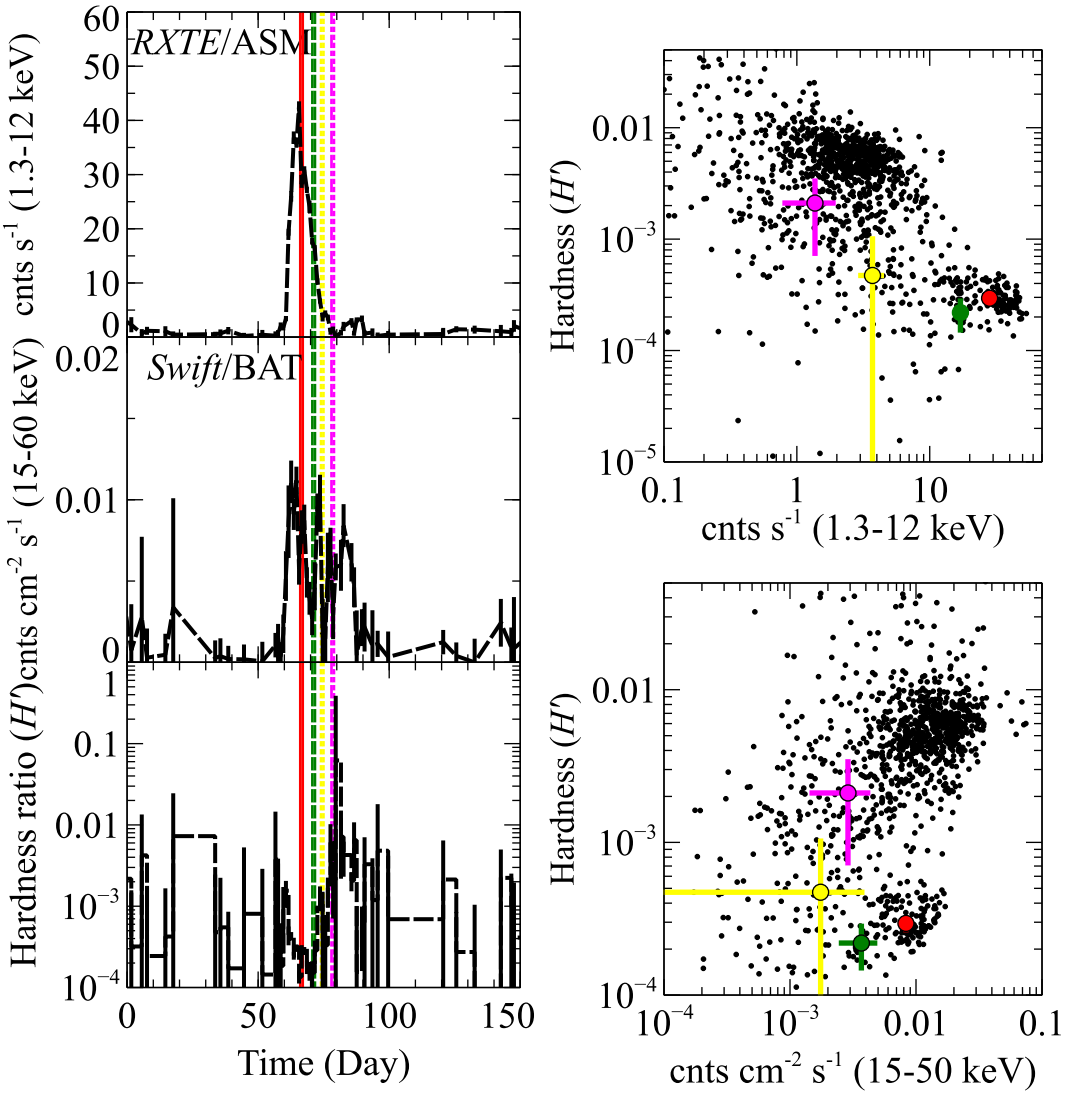

Figure 4.15: The same long-term light curves as figure 4.7, but for 4U1608-52. The observation periods of #1, #2, #3 and #4 are shown with red line, green dashed line, orange dotted line, and magenta dash-dotted line, respectively. The data overlapping with the *Suzaku* observations are indicated with the same color as in the left panels.

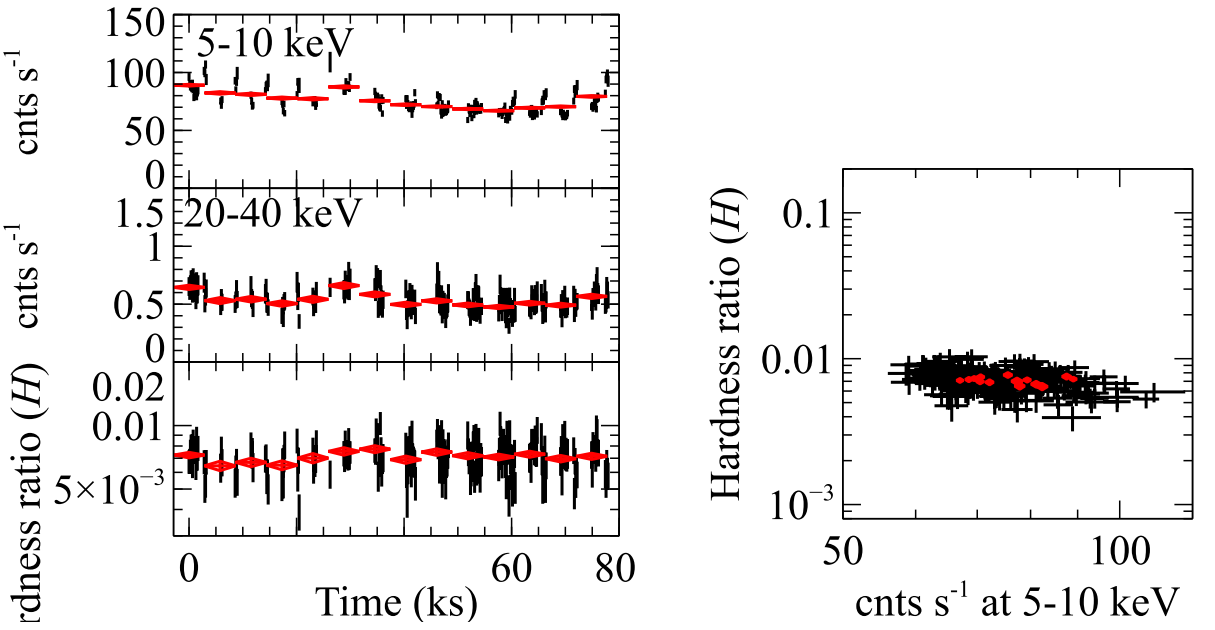

Figure 4.16: The same *Suzaku* data as figure 4.6, but for 4U1608-52 #1.

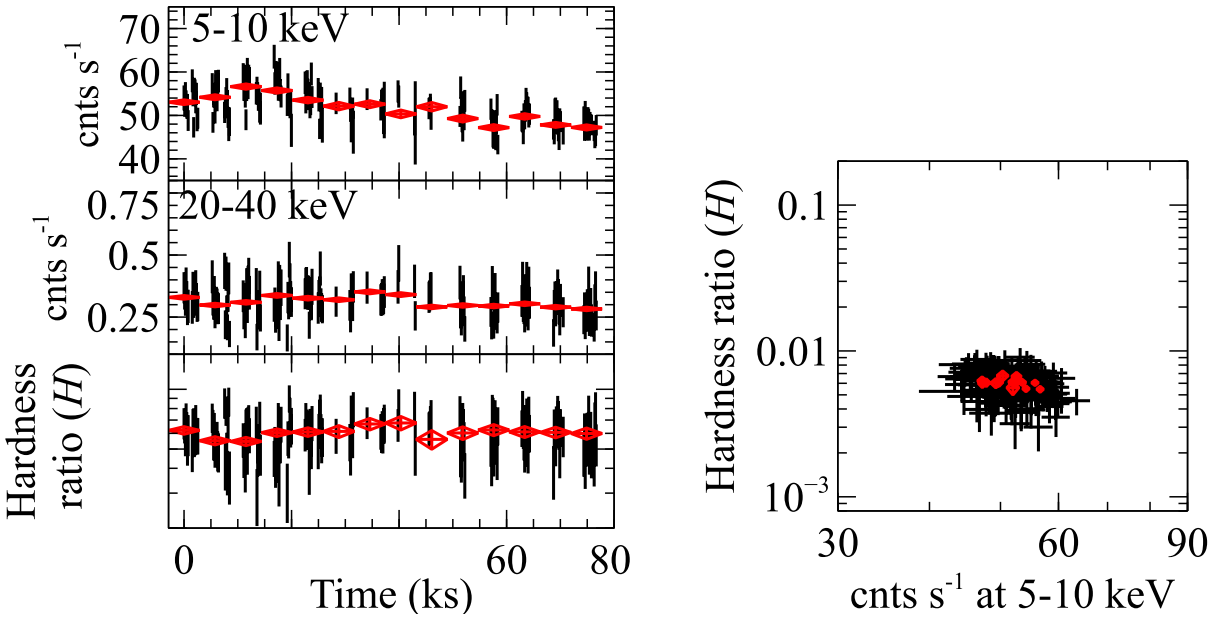

Figure 4.17: The same *Suzaku* data as figure 4.6, but for 4U1608-52 #2.

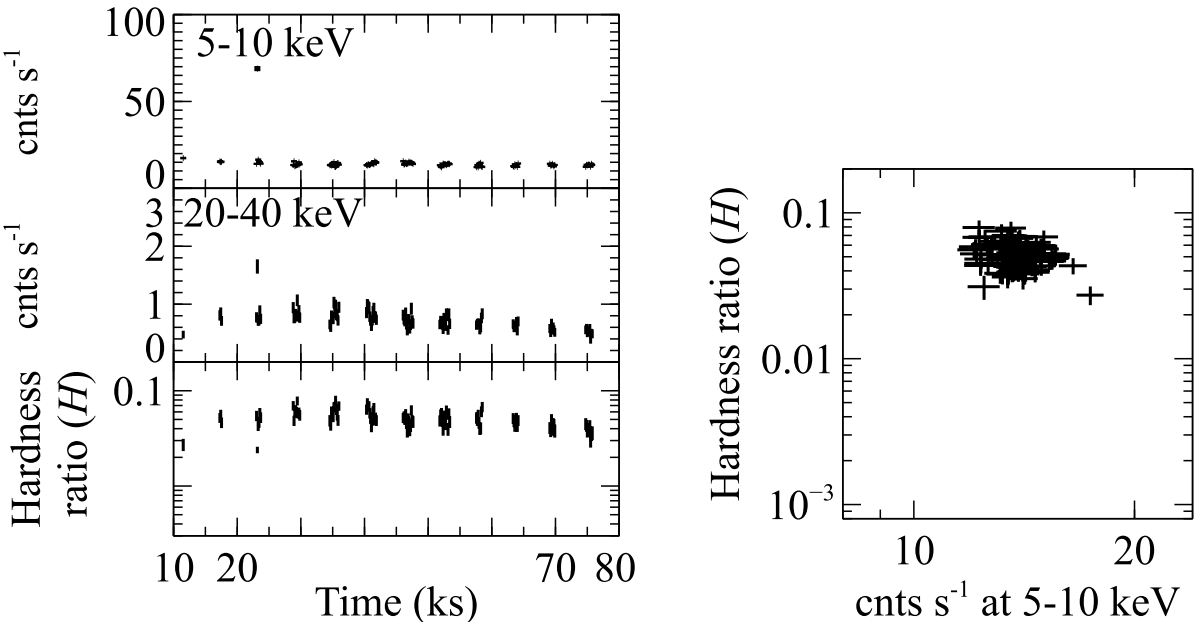

Figure 4.18: The same *Suzaku* data as figure 4.6, but for 4U1608-52 #3.

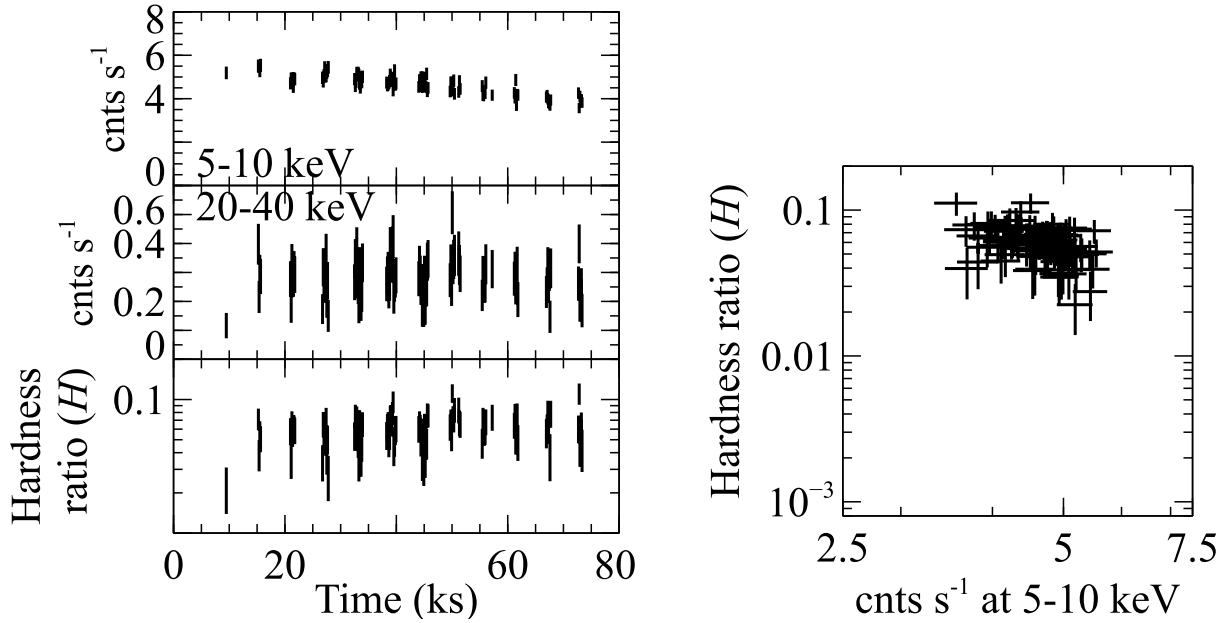

Figure 4.19: The same *Suzaku* data as figure 4.6, but for 4U1608-52 #4.

This LMXB was observed 8 times with *Suzaku*, from 2006 to 2012. As representative cases, figure 4.21, 4.22 and 4.23 show *Suzaku* light curves of 4U1705-44 #1, #7, and #8, respectively. The same figure for #2 to #6 are presented in Appendix A. Thus, the source was in the Soft State in #1 to #6, with 5–10 keV count rate of $\gtrsim 10$ cts s^{-1}, and $H \lesssim 0.01$. In contrast, it was in the Hard State in the other 2 observations, wherein the 5–10 keV count rate was $\lesssim 10$ cts s^{-1}, with $H \gtrsim 0.01$. As a result, the 8 observations have been selected via the criterion (2). In all these observations, the source was relatively constant, with at most factor 1.5 variations. The value of H was also relatively constant in each data set.

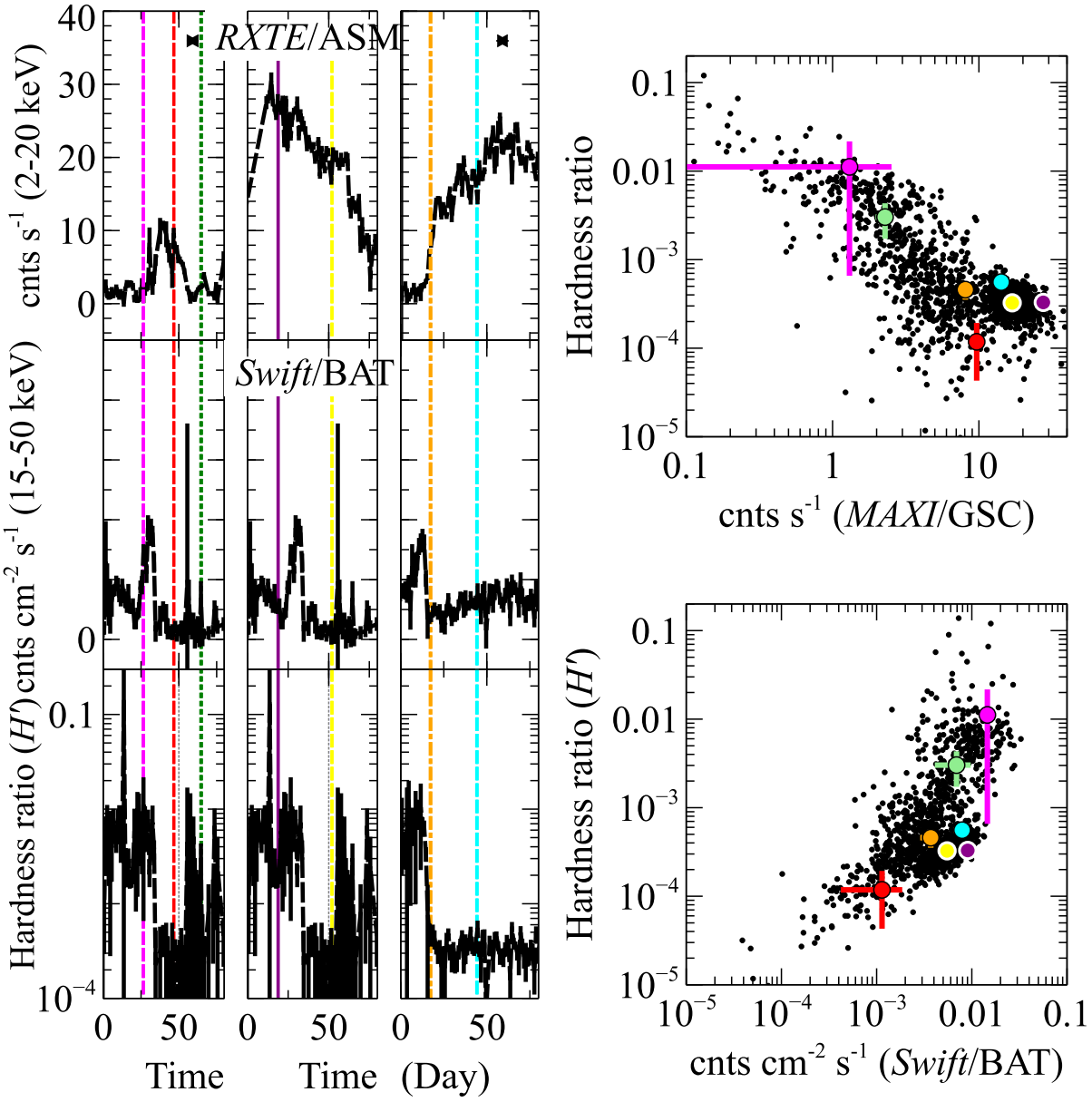

Figure 4.20: The same long-term light curves as figure 4.7, but for 4U1705-44. The observation periods of #1, #2, #3, #4, #5, #6, and #7 are shown with red dashed line, green dotted line, purple solid line, yellow dashed line, orange dash-dotted line, cyan dashed line, and magenta dashed-line, respectively. The data overlapping with the *Suzaku* observations are indicated with the same color as in the left panels. The observation #8 was not covered by both *RXTE* and *Swift*.

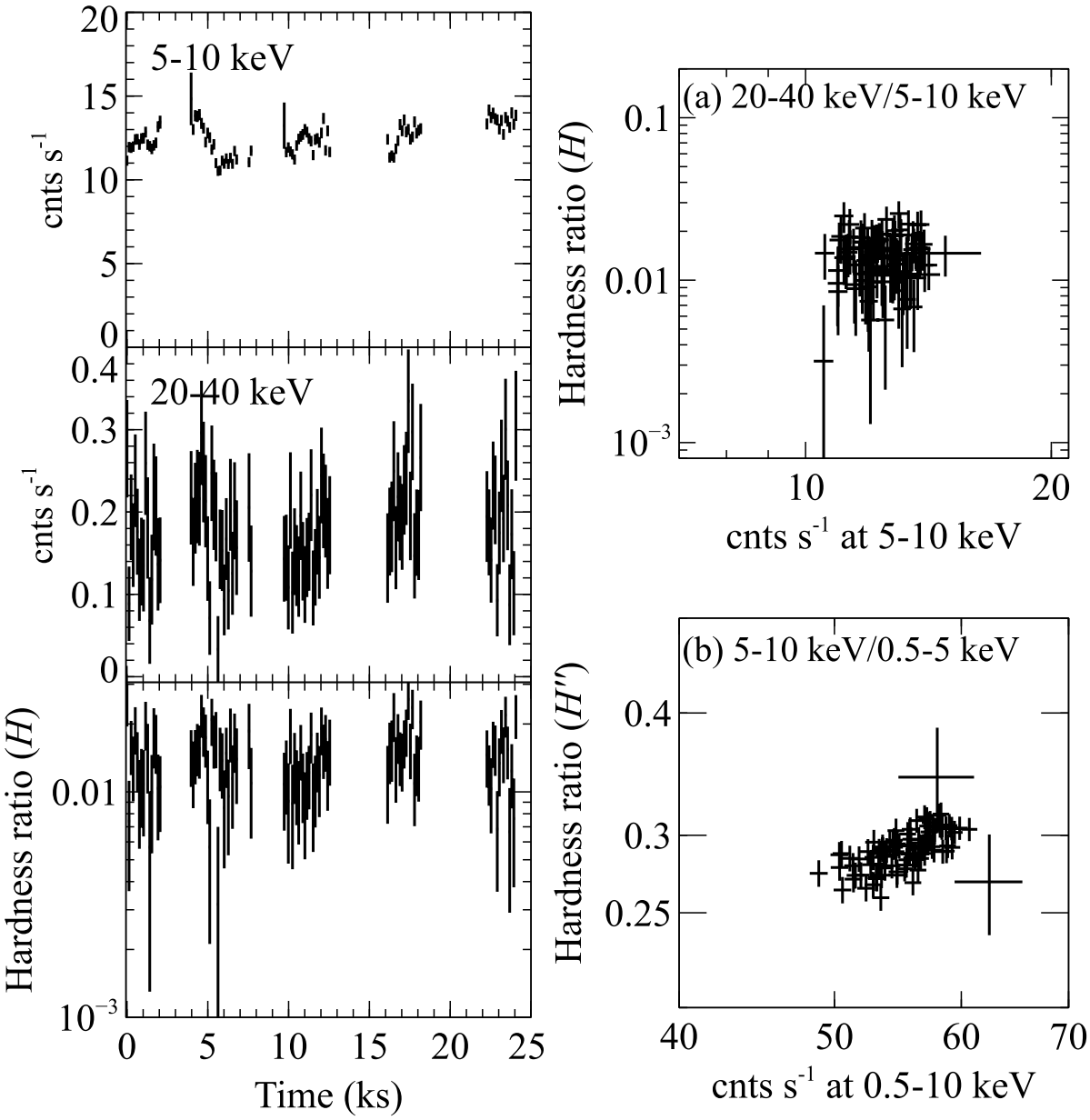

Figure 4.21: The same *Suzaku* data as figure 4.9, but for 4U1705-44 #1.

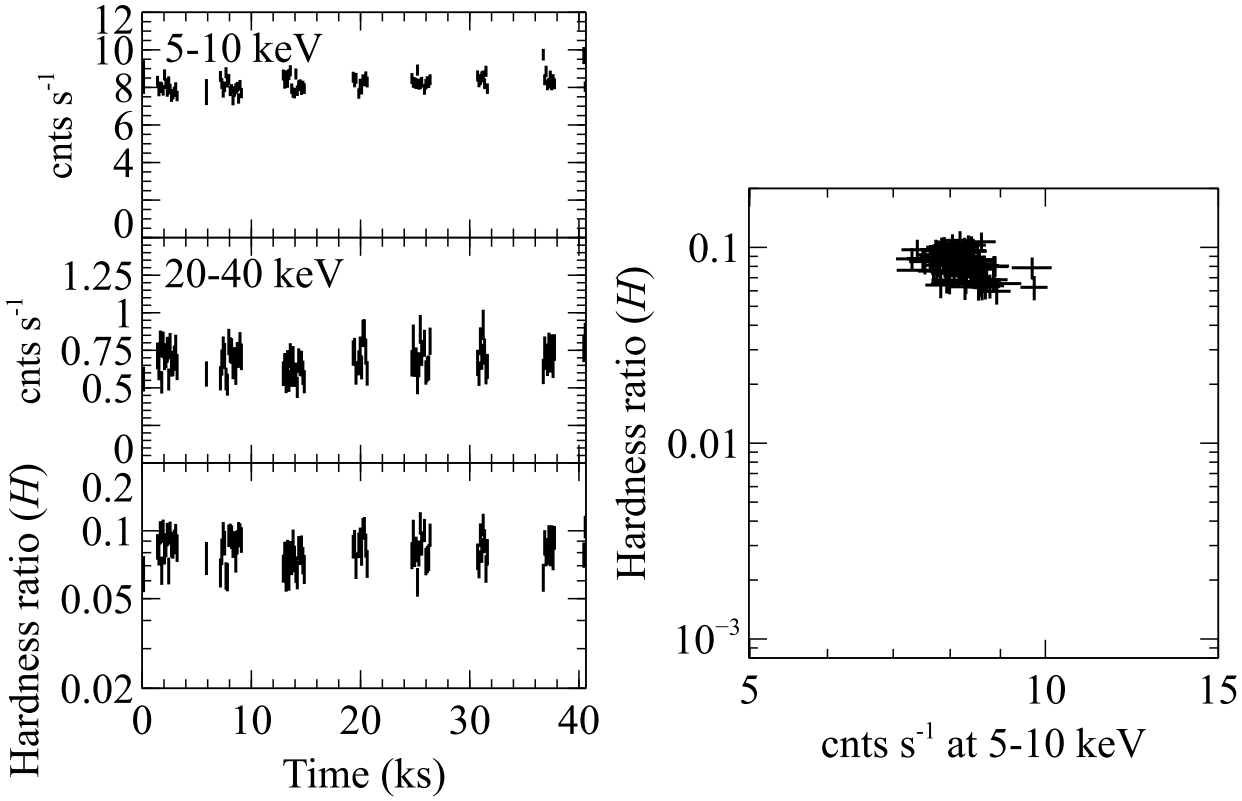

Figure 4.22: The same *Suzaku* data as figure 4.6, but for 4U1705-44 #7.

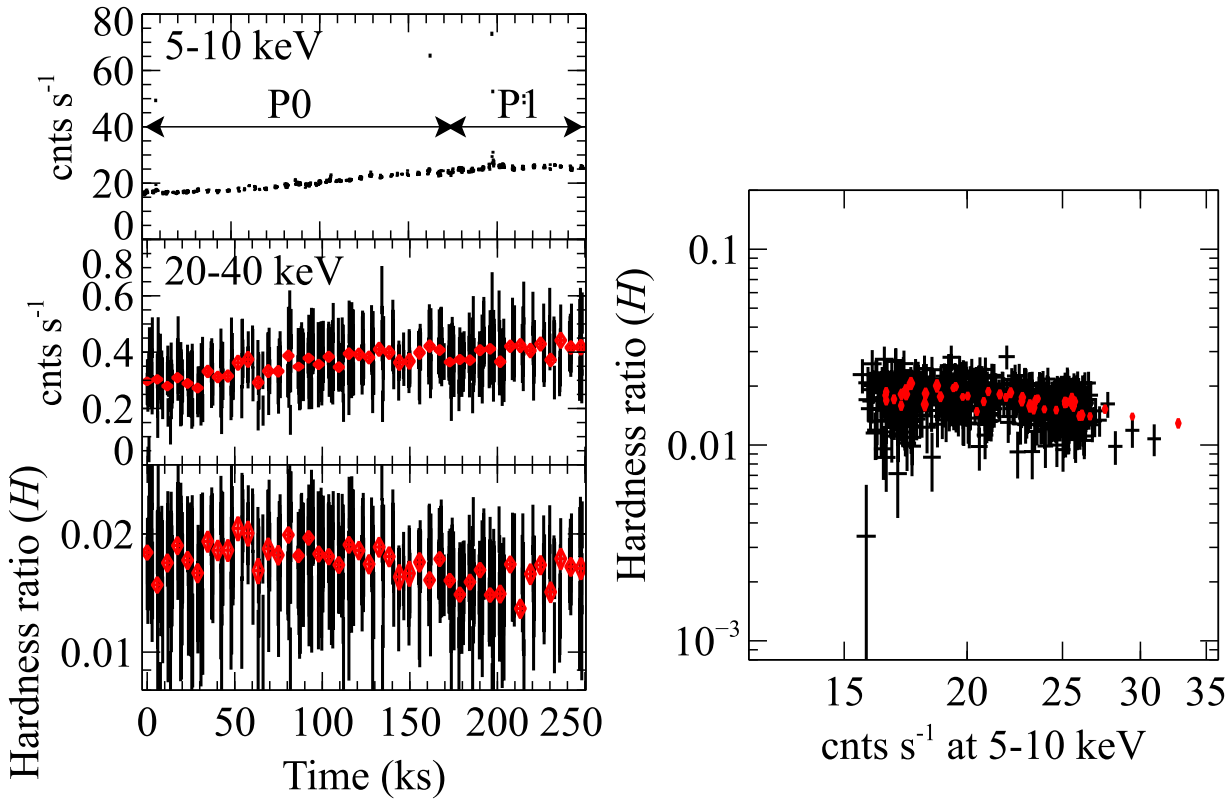

Figure 4.23: The same *Suzaku* data as figure 4.6, but for 4U1705-44 #8. Data binned with 5760 sec are overlaid with red.

Chapter 5

Data Analysis and Results

Following the procedure described in §3.5, we produce the XIS and HXD spectra from the data selected in §4.1.2. In order to examine spectral differences between the Soft and Hard States, or around transitions, the data are time-divided when the source showed significant variations in 0.5–10 keV. Otherwise, a pair of XIS and HXD spectra were derived from an individual data set.

5.1 Data with the criterion (1)

5.1.1 Aquila X-1

As confirmed in §4, the data of Aquila X-1 acquired on 2011 October 21 (table 4.1) still remains the only *Suzaku* observation that actually caught the moment of a spectral transition (from the Hard to Soft States). After Ono et al. (2017), we briefly re-analyze this precious data set, to obtain a fiducial view of the state transition.

Given the monotonic evolutions of the 5–10 keV and 20–40 keV count rates, and the hardness ratio H in figure 4.6, we divided the *Suzaku* transition data into 9 time periods, from P0 to P8. The spectra derived from these periods are shown in figure 5.1 after approximately removing the instrumental responses. The spectrum above ~ 10 keV thus softened dramatically in only ~ 20 ksec from P0 to P8, and at the same time, the spectrum bellow ~ 10 keV became more dominant toward P8. Indeed, these spectral changes produced the impressive count-rate evolution seen in figure 4.6. This kind of large but continuous spectral shape change, with a pivot at ~ 10 keV, has never been observed before. Since the spectral shape gradually changed from a power-law like ones in P0–P5, typical of the Hard State, to a more convex ones typical of the Soft State in P7 and P8, we regard this evolution as a state transition.

After the successful fit in Sakurai et al. (2012; 2014) and Zhang et al. (2014), we fitted the spectra with a model composed of a multi-color disk (MCD) and a Comptonized blackbody (§2.3.4). We utilized an XSPEC model of `diskbb` for MCD and `nthcomp` (Zdziarski et al. 1996; Życki et al. 1999) for Comptonized blackbody. The use of `nthcomp` for Comptoniza-

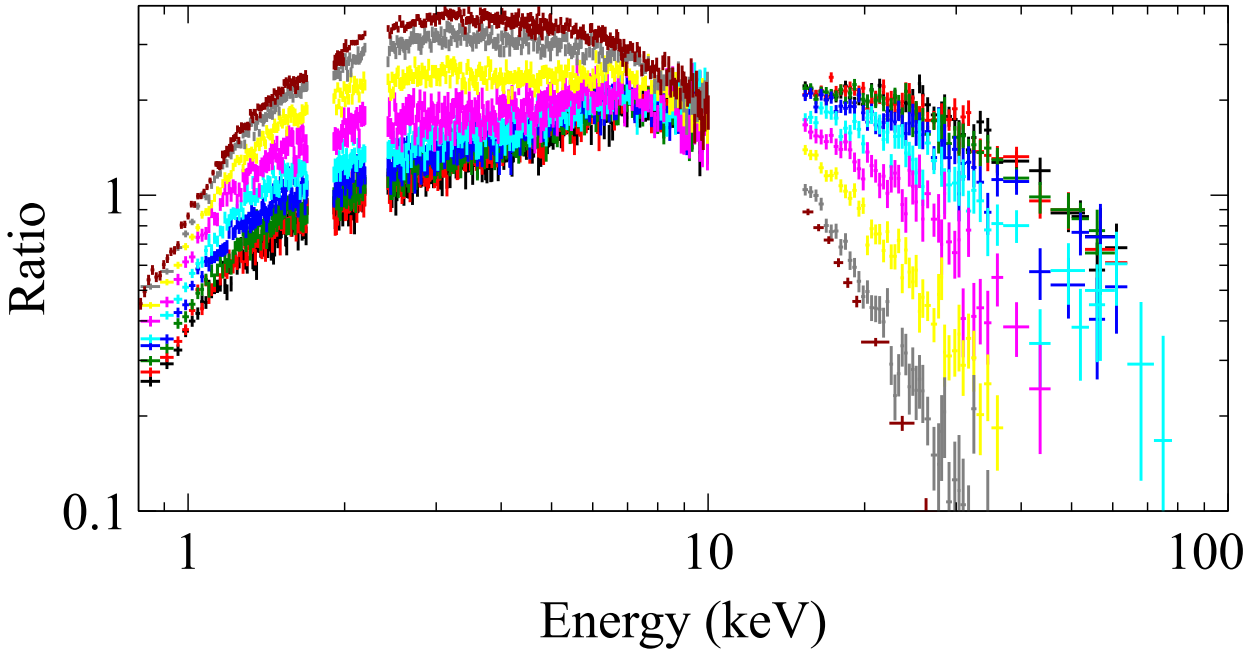

Figure 5.1: Background subtracted spectra of Aql X-1 taken with XIS0 plus XIS3 in 0.8–10 keV, HXD-PIN in 15–60 keV, and HXD-GSO in > 50 keV. Refering to the light curves in figure 4.6, the time periods P0, P1,.. and P8 are represented by black, red, green, blue, cyan, magenta, orange, grey, and dark red, respectively. They are normalized with power-law (convolved through the detector response), of which the photon index is 2.0 and the normalization is 1 photon cm^{-2} s^{-1} keV^{-1} at 1 keV.

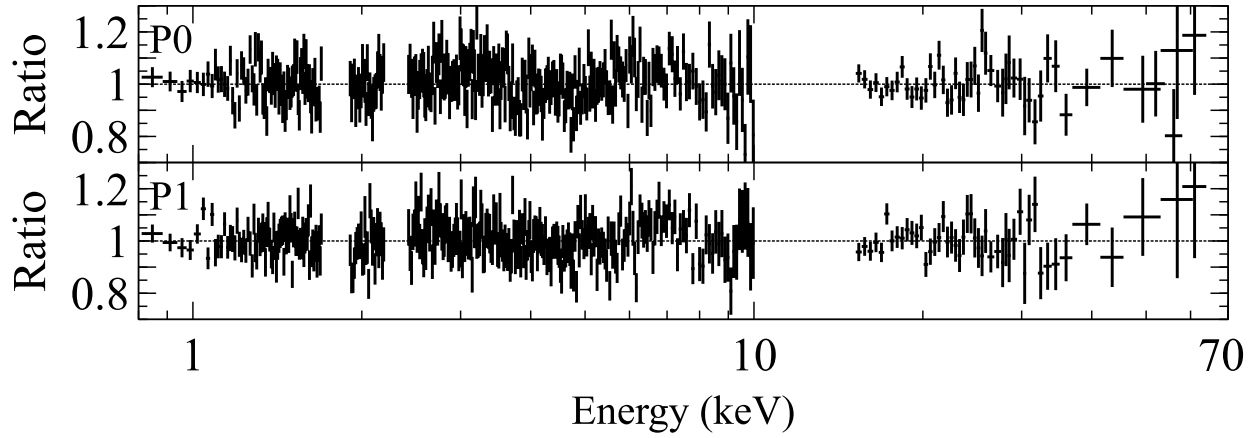

Figure 5.2: The ratios between the spectra for P0 and P1 in figure 5.1 to the best-fit models of `wabs*const*(diskbb+nthcomp)`.

tion is appropriate, because this particular numerical code is optimized for $\tau \gtrsim 2$ (Zdziarski et al. 1996), which is expected around a transition (Ono et al. 2016) and in the Soft State (Sakurai et al. 2012). To make the analysis consistent with those in Sakurai et al. (2012; 2014), the low-energy photoelectric absorption was expressed by a multiplicative model `wabs` in XSPEC, even though it is somewhat old. In order to account for the known inconsistency in the cross-normalization between the XIS and the HXD, an appropriate constant factor was multiplied to the model for the HXD data (§3.5.2). Thus, the model expressed as `wabs*const*(diskbb+nthcomp)` was utilized for both the XIS and the HXD data simultaneously. The free parameters of the constructed model are the absorption $N_{\rm H}$, the inner disk temperature $T_{\rm in}$, the inner disk radius $R_{\rm in}$, the blackbody temperature $T_{\rm BB}$, the blackbody radius $R_{\rm BB}$, the coronal electron temperature $T_{\rm e}$, and the coronal optical depth τ. This expresses a condition that the emission from the optically-thick accretion disk is directly visible to us, all blackbody photons from the NS surface undergo Comptonization in the single-zone hot corona, and the corona does not emit spontaneously (e.g., bremsstrahlung).

As presented in figure 5.2, overall features of the spectra were successfully reproduced, but positive residuals remained at around $6.4 - 7$ keV from P0 to P7. This structure is considered to be ionized iron-K lines, because the disk should continue close to the NS around the transition, and the disk should be efficiently illuminated by the hard X-rays from the vicinity of the NS. Thus, to account for this structure in P0–P7, we added an XSPEC model `diskline` which takes into account relativistic effects due to the disk rotation and the NS gravity (Fabian et al. 1989), equating its inner disk radius with $R_{\rm in}$ and assuming the inclination to be 45°. Its free parameters are the energy centroid $E_{\rm c}$, the emissivity index β, and normalization. We avoided using a gaussian for this data set, because the round shape of a gaussian easily couples with `diskbb`, to take up the disk component at ~ 5 keV and decrease $T_{\rm in}$ to unphysical values.

The spectra have all been fitted successfully after including `diskline`, with the reduce chi-squared of $\chi^2_\nu \lesssim 1.3$ for 354–365 degree of freedom. Figure 5.3 shows the spectra together with the respective best-fit models. The spectra at lower energies band are dominated by `diskbb`, and those at higher energies by `nthcomp`.

Figure 5.4 shows the evolutions of the best-fit parameters against the periods, and the total luminosity $L_{\rm t}$, which is calculated as

$$L_{\rm t} = L_{\rm MCD} + L_{\texttt{nthcomp}} \tag{5.1}$$

$$L_{\rm MCD} = 4\pi D^2 \times F_{0.1-100\ \rm keV}(\texttt{diskbb})/\cos i \tag{5.2}$$

$$L_{\rm nthcomp} = 4\pi D^2 \times F_{0.1-100\ \rm keV}(\texttt{nthcomp}) \tag{5.3}$$

where $F_{0.1-100\ \rm keV}()$ is the 0.1–100 keV energy flux of each model in parenthesis. Thus, the parameters all changed rather continuously through P0–P8. Due to the increasing accretion rate, $T_{\rm in}$ and $T_{\rm BB}$ increased, while $T_{\rm e}$ decreased from ~ 10 keV to 3 keV. At the same time, the disk approached the NS surface from ~ 50 km to ~ 20 km, and $R_{\rm BB}$ decreased. The decreasing flux above the pivot of the spectrum (figure 5.1) is explained by the decreasing coronal temperature $T_{\rm e}$, while the increasing flux bellow the pivot is explained by the in-

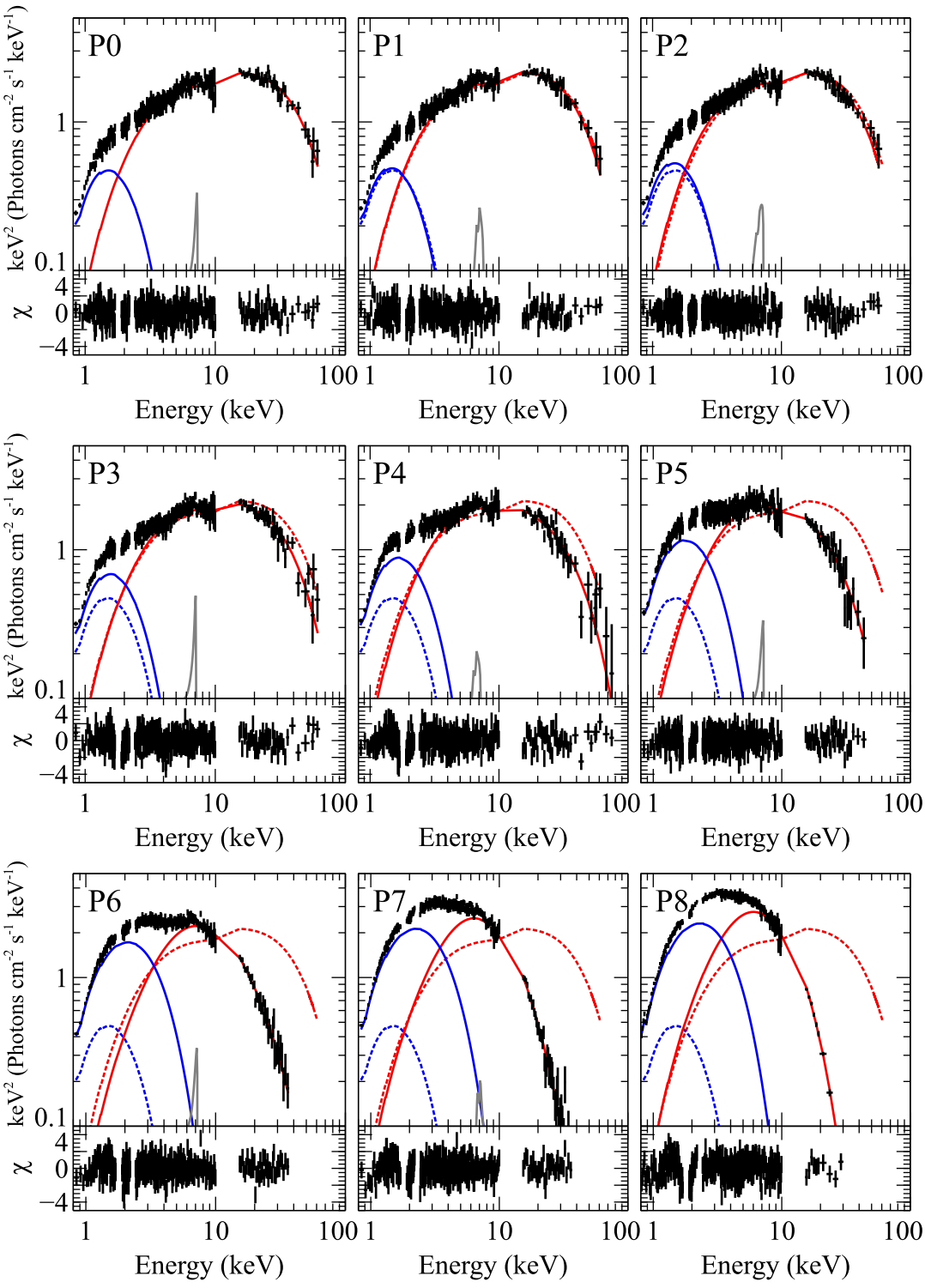

Figure 5.3: The same P0 to P8 spectra as in figure 5.1, presented in the $\nu F\nu$ form together with the best-fit model. Residuals are shown below each spectrum. In P1–P8, the best-fit P0 model is illustrated for reference in dotted lines.

Table 5.1: Parameters and 90% errors obtained from the fit of Aql X-1 spectra with the model `wabs*const*(diskbb+nthcomp+diskline)`.[e]

		`diskbb`		`nthcomp`				`diskline`					
#	L^{a}	$T_{\rm in}$ (keV)	$R_{\rm in}$ (km)[b,c]	$T_{\rm BB}$ (keV)	$R_{\rm BB}$ (km)[c,d]	$T_{\rm e}$ (keV)	τ	$E_{\rm c}$ (keV)	β	norm 10^{-3}	Q	y	$\chi^2_\nu(\nu)$
P0	3.5	$0.45^{+0.03}_{-0.03}$	$37.7^{+5.4}_{-4.3}$	$0.81^{+0.08}_{-0.08}$	$13.6^{+1.5}_{-0.7}$	$10.1^{+0.7}_{-0.6}$	5.3 ± 0.2	$6.6^{+0.4}_{-0.1}$	$-4.2^{+1.1}_{-}$	6 ± 2	$12.4^{+0.9}_{-0.8}$	$1.06^{+0.04}_{-0.05}$	1.09 (359)
P1	3.6	$0.44^{+0.02}_{-0.02}$	$41.8^{+4.7}_{-3.9}$	$0.82^{+0.06}_{-0.06}$	$13.8^{+1.5}_{-0.7}$	$9.6^{+0.7}_{-0.6}$	5.4 ± 0.2	$6.9^{+0.2}_{-0.3}$	$-2.5^{+0.6}_{-0.9}$	6 ± 2	$11.7^{+0.9}_{-0.8}$	1.04 ± 0.04	1.08 (357)
P2	3.7	$0.44^{+0.03}_{-0.03}$	$42.7^{+5.1}_{-4.5}$	$0.79^{+0.07}_{-0.07}$	$14.6^{+1.4}_{-0.7}$	$9.5^{+0.7}_{-0.6}$	5.4 ± 0.2	$6.6^{+0.1}_{-0.2}$	$-3.0^{+0.6}_{-1.3}$	7 ± 2	$12.0^{+0.9}_{-0.8}$	1.02 ± 0.04	0.98 (358)
P3	3.7	$0.49^{+0.02}_{-0.03}$	$38.2^{+4.1}_{-3.0}$	$0.89^{+0.07}_{-0.08}$	$12.1^{+1.2}_{-0.6}$	$9.0^{+0.9}_{-0.7}$	5.2 ± 0.3	$6.4^{+0.1}_{-0.1}$	$-5.0^{+1.6}_{-5.0}$	$8\pm^{3}_{2}$	$10.2^{+1.0}_{-0.8}$	0.91 ± 0.05	1.08 (359)
P4	3.7	$0.54^{+0.02}_{-0.02}$	$34.1^{+2.7}_{-2.3}$	$1.00^{+0.08}_{-0.08}$	$9.8^{+0.9}_{-0.6}$	$9.6^{+1.5}_{-1.1}$	$4.5^{+0.3}_{-0.4}$	$6.5^{+0.2}_{-0.2}$	$-2.6^{+0.8}_{-1.2}$	5 ± 2	$9.6^{+1.5}_{-1.1}$	0.76 ± 0.06	1.21 (361)
P5	3.8	$0.60^{+0.03}_{-0.03}$	$30.9^{+2.9}_{-2.3}$	$1.04^{+0.11}_{-0.11}$	$9.3^{+1.1}_{-0.8}$	$7.0^{+1.1}_{-0.8}$	5.1 ± 0.4	$6.5^{+0.2}_{-0.1}$	$-3.7^{+1.0}_{-}$	$7\pm^{3}_{2}$	$6.7^{+1.0}_{-0.7}$	0.64 ± 0.08	1.06 (354)
P6	4.1	$0.76^{+0.02}_{-0.02}$	$22.3^{+1.2}_{-1.1}$	$1.35^{+0.11}_{-0.11}$	$6.1^{+0.4}_{-0.6}$	$6.4^{+2.4}_{-1.1}$	$4.0^{+0.4}_{-0.7}$	$6.5^{+0.2}_{-0.2}$	$-2.3^{+0.7}_{-1.2}$	$5\pm^{3}_{2}$	$4.8^{+1.8}_{-0.8}$	0.37 ± 0.09	1.21 (352)
P7	4.7	$0.83^{+0.02}_{-0.04}$	$20.4^{+1.6}_{-1.3}$	$1.30^{+0.15}_{-0.11}$	$6.9^{+0.9}_{-0.7}$	$4.4^{+2.3}_{-0.7}$	$4.5^{+0.5}_{-1.0}$	$6.9^{+0.2}_{-0.5}$	$-2.2^{+1.4}_{-}$	$4\pm^{3}_{2}$	$3.4^{+1.7}_{-0.5}$	0.27 ± 0.13	1.19 (352)
P8	5.0	$0.85^{+0.04}_{-0.06}$	$19.9^{+2.2}_{-1.3}$	$1.21^{+0.14}_{-0.17}$	$8.3^{+1.6}_{-1.0}$	$3.2^{+0.5}_{-0.3}$	$6.2^{+0.4}_{-0.5}$	-	-	-	$2.6^{+0.4}_{-0.2}$	$0.30^{+0.14}_{-0.13}$	1.29 (365)

[a] Unabsorbed luminosity at 0.1–100 keV ($\times10^{37}$erg s^{-1}).
[b] Calculated using eq. (2.19), taking into account the inclination angle of 45° multiplying $1/\cos 45°$.
[c] Distance of 5.2 kpc is assumed. The distance uncertainty is not included in the errors.
[d] Calculated from the photon flux of `nthcomp` conserved through Comptonization.
[e] Errors are not written when only the upper or lower limit is obtained.

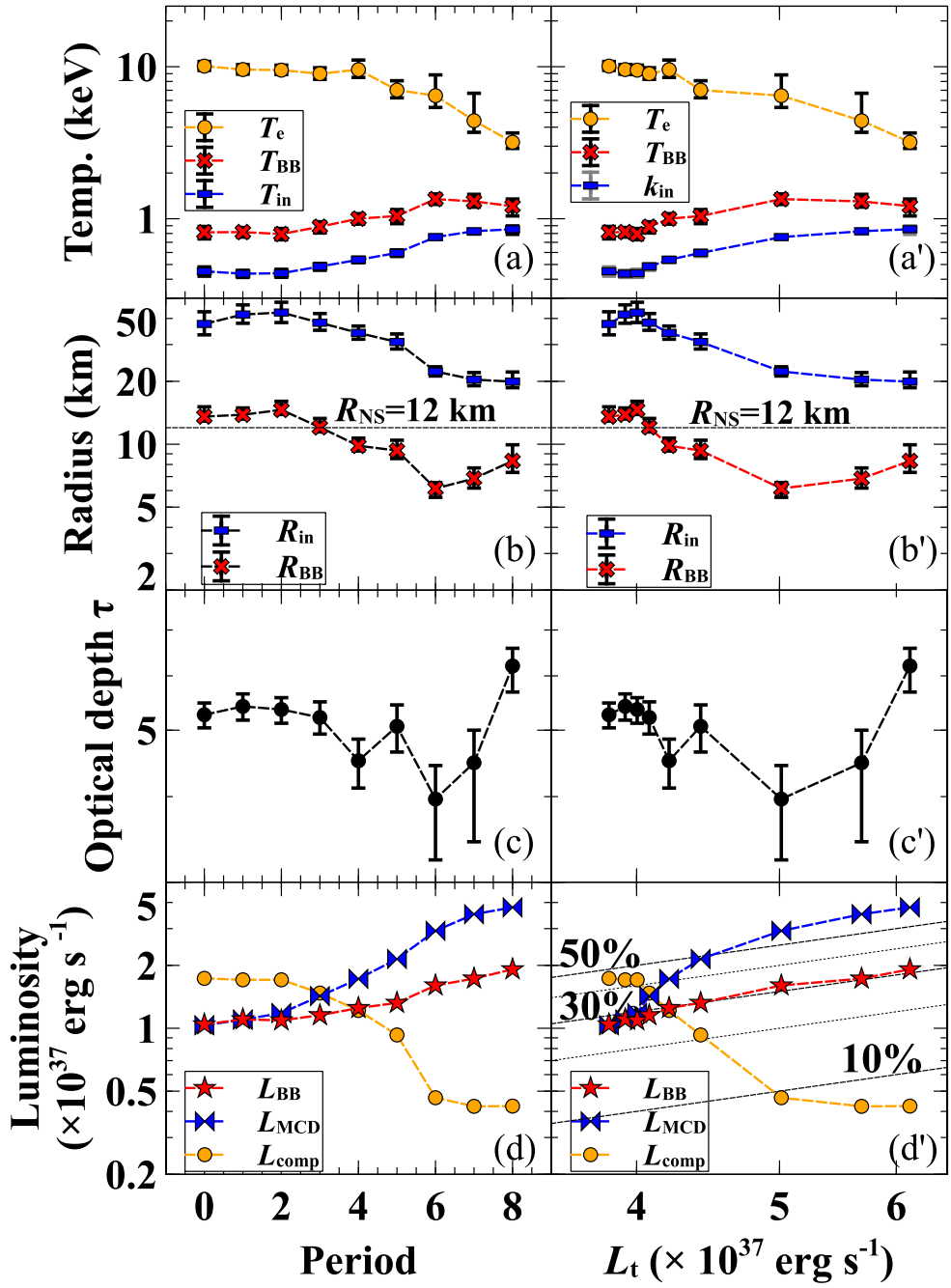

Figure 5.4: Evolutions of the spectral parameters in table 5.1, plotted against the period (panels a–d) and the 0.1–100 keV total luminosity (panels a'–d'). (a, a') The behavior of T_e, T_{BB}, and T_{in}. (b, b') R_{BB} and R_{in}. (c, c') Coronal optical depth. (d, d') The 0.1–100 keV luminosities of the Comptonization L_{comp} (see text for its definition), the blackbody (L_{BB}), and the disk (L_{MCD}). The total and disk luminosities are corrected for the assumed disk inclination of 45°.

creasing $T_{\rm in}$. The optical depth increased in the last three periods, making the Comptonized blackbody radiation similar to that of the blackbody with $T_{\rm BB} = 3$ keV.

The parameter changes revealed so far can be even better understood by calculating, as in figure 5.4 (d) and (d'), the behavior of three constituent luminosities. The disk luminosity $L_{\rm MCD}$ calculated with eq. (5.2) becomes dominant toward the Soft State. At the same time, the transition is characterized by a clear decrease of the Comptonization luminosity, which is defined as the pure Comptonization contribution as

$$L_{\rm comp} = L_{\texttt{nthcomp}} - L_{\rm BB}, \tag{5.4}$$

where $L_{\texttt{nthcomp}}$ refers to eq. (5.3), and

$$L_{\rm BB} = 4\pi R_{\rm BB}^2 T_{\rm BB}^4 \tag{5.5}$$

is the luminosity of the seed blackbody before it is Comptonized. As a result, the transition can be described successfully with the weakening Comptonization which accounts for the dramatic spectral softening, and with the increasing disk component which enhances the emission in < 10 keV. The decreasing $L_{\rm comp}$ causes an associated decrease in the y parameter, defined in eq. (2.22). Indeed, in figure 5.5 (a), y decreases toward the Soft State as the luminosity increases, as confirmed with 4U 1608-52 (Mitsuda et al. 1989).

Although $L_{\rm t}$ of eq. (5.1) can be obviously considered to be the dominant control parameter of the transition physics, its usage has two difficulties. One is that $L_{\rm t}$ is subject to distance uncertainties, which vary among the sample objects. The other is that the threshold $L_{\rm t}$ is usually higher in Hard-to-Soft transitions, than that in the Soft-to-Hard transitions; this is the hysteresis effects (§2.4.4). Therefore, we alternatively employ a new dimensionless quantity defined as

$$Q \equiv T_{\rm e}/T_{\rm BB}, \tag{5.6}$$

introduce by Makishima (2014), and used in Zhang et al. (2016). This Q expresses a balance between the heating of the corona by ions, represented by $T_{\rm e}$, and its cooling by the blackbody radiation, represented by $T_{\rm BB}$. Furthermore, Q is also a good indicator of the spectral shape, because $\log Q = \log T_{\rm e} - \log T_{\rm BB}$ is nearly equivalent to the logarithmic distance between the high energy end ($\sim 3T_{\rm e}$) and low energy end ($\sim 3T_{\rm BB}$) of the spectrum. As shown in figure 5.5 (c), Q decreased monotonically from $Q \sim 15$ to $Q \sim 2.5$, as $L_{\rm t}$ doubled. The Hard State (P0–P4) appears in $Q \gtrsim 6$, while the Soft State (P5–P8) in $Q \lesssim 6$, so that $Q \sim 6$ can be considered as the threshold. Similarly, as in figure 5.5 (b), y depends reasonably well on Q. Therefore, instead of $L_{\rm t}$, we may regard Q as the fundamental parameter mentioned in the question (A-ii) (§4.1.1).

To further characterize the role of Q, figure 5.6 plots plot the constituent luminosities divided by $L_{\rm t}$ against Q. The Hard-to-Soft transition is thus successfully explained, as a function of Q, as a dramatic decrease in $L_{\rm comp}/L_{\rm t}$, and a milder increase of $L_{\rm MCD}/L_{\rm t}$. As a result, one of the prospects in Chapter 5 has become to examine whether the other sources behave on figure 5.6 in the same way as Aql X-1, and whether the hysteresis effects can be successfully removed.

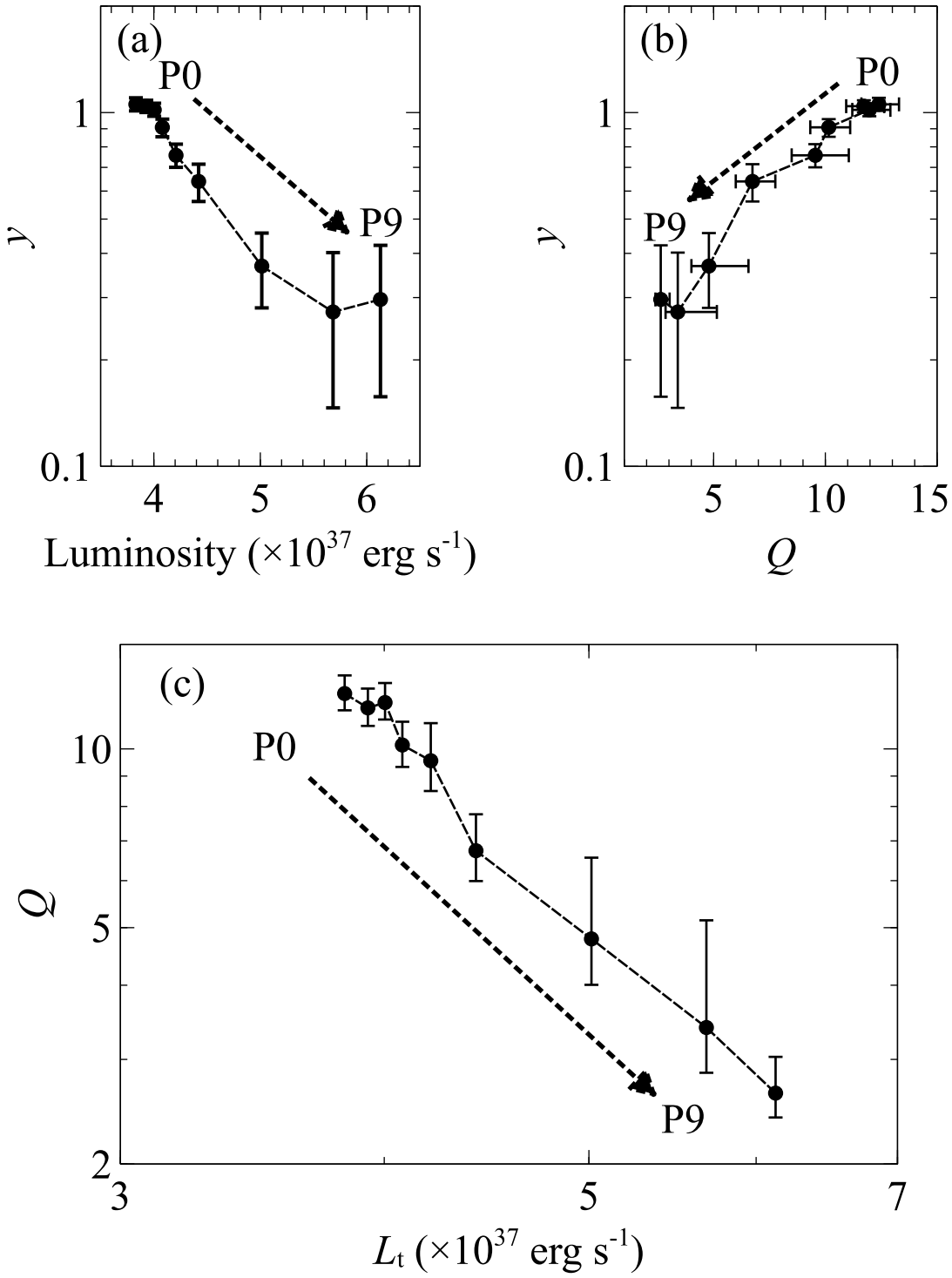

Figure 5.5: (a) Behavior of the y parameter of Aql X-1, defined by eq. (2.22), plotted against $L_{\rm t}$. (b) The y parameter as a function of Q of eq. (5.6). (c) The relation of Q vs $L_{\rm t}$ through the transition of Aql X-1. The numerical values are given in table 5.1.

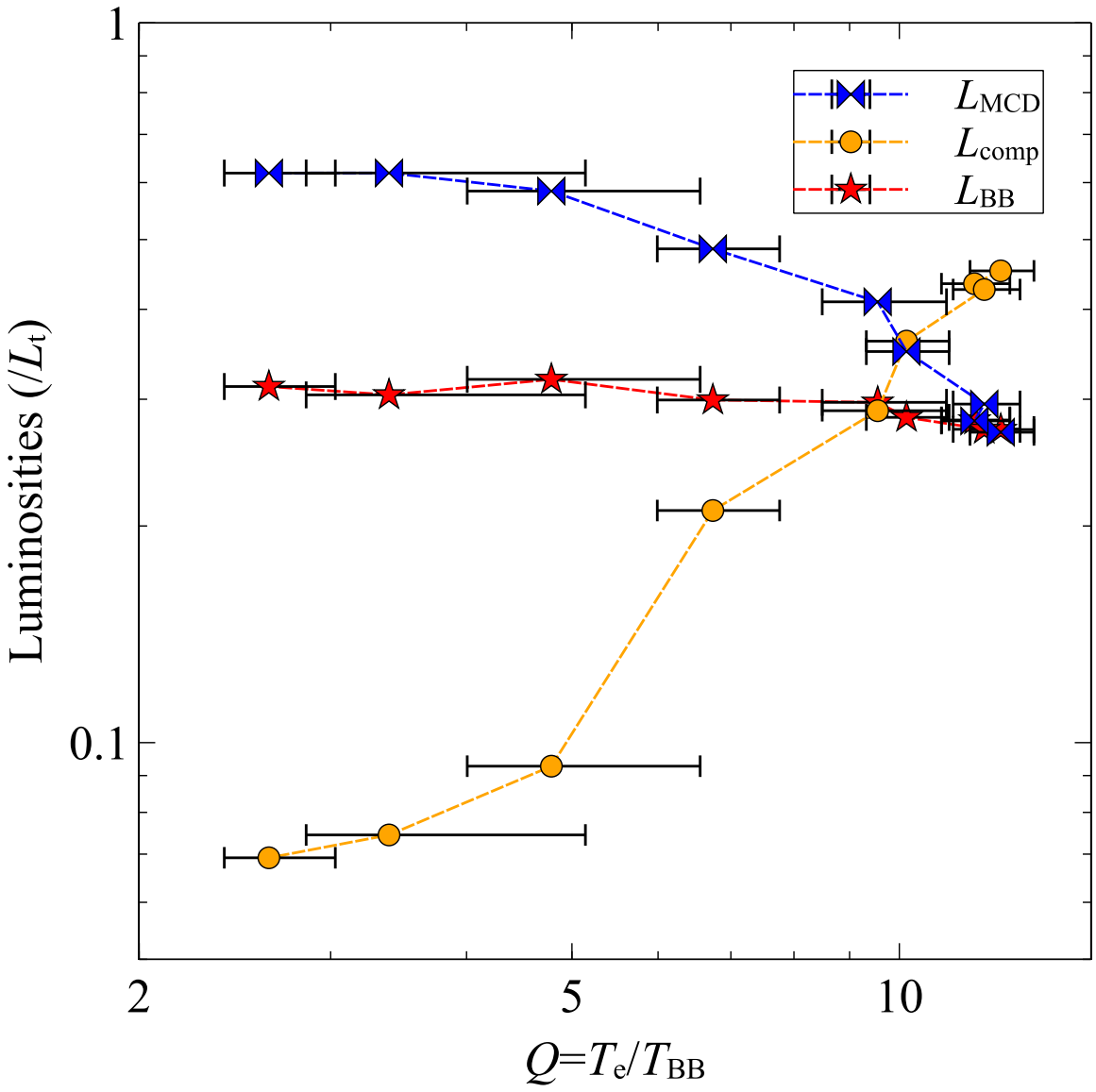

Figure 5.6: The behavior of the three constituent luminosities, all normilized to L_t and presented as a function of Q of eq. (5.6). The transition proceeded from right to left.

5.1.2 4U 1636-536

As shown in §4.2.3, the source exhibited significant variations in the hardness ratio, which negatively correlated with the 5–10 keV intensity. This suggests that the spectrum varies in a similar way to that of Aql X-1, although the changes are much smaller than in Aql X-1. Therefore, we divided the data into 5 sequential periods, P0 to P4, so that they contain the same number of 0.5–10 keV photons. In figure 5.7, the five spectra are presented. The variation is most prominent in $\gtrsim$ 10 keV, in such a way that the spectrum steepens as the intensity in $<$ 10 keV increases by a slight amount. The spectral shape is nearly the same as that of Aql X-1 in P6, which was regarded as in the Soft State in §5.1.1. This casts a doubt on our assignment of the 4U 1636-536 #2 data to the Hard State: it could be better regarded as the faintest end of the Soft State.

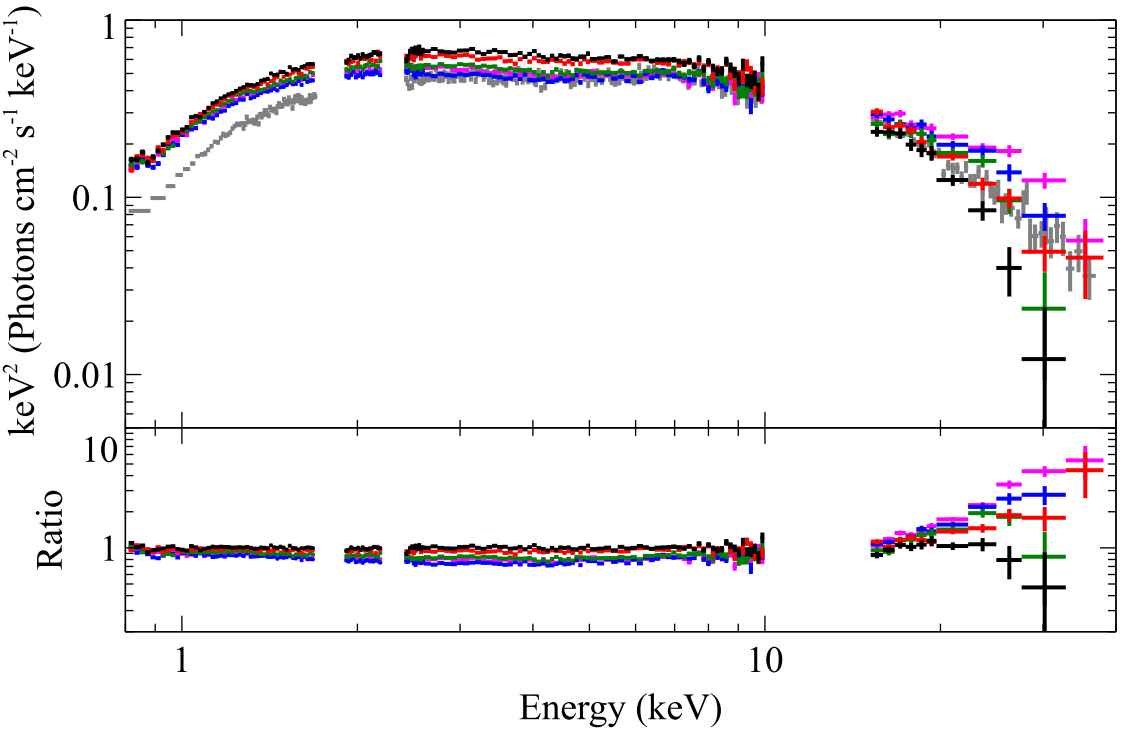

Figure 5.7: Background subtracted $\nu F\nu$ spectra of 4U1636-536 #2 in the 5 time periods, and ratios to the best fit model of the brightest data (black). The spectrum of Aql X-1 in P6 is plotted with gray for comparison, after decreasing its intensity by a factor of 5.

Since the spectra of 4U 1636-536 #2 are similar to that of Aql X-1 in P6, we fitted them with the same model as that for Aql X-1, namely `tbabs*const*(diskbb+nthcomp)`, but replacing `wabs` with a new absorption model `tbabs` which employs updated interstellar medium abundances (Wilms et al. 2000). As shown in figure 5.8, the spectra have been

Table 5.2: Parameters and 90% errors obtained by fitting 4U1636-536 #2 spectra with `diskbb+nthcomp`.[e]

		`tbabs`	`diskbb`		`nthcomp`						
#	$L^{a,c}$	$N_{\rm H}$	$T_{\rm in}$ (keV)	$R_{\rm in}$ (km)^{b,c}	$T_{\rm BB}$ (keV)	$R_{\rm BB}{}^{c,d}$ (km)	$T_{\rm e}$ (keV)	τ	Q	y	$\chi^2_\nu(\nu)$
P0	1.43	0.29 ± 0.01	$0.71\pm^{0.03}_{0.04}$	$15.7\pm^{1.4}_{1.3}$	$1.24\pm^{0.17}_{0.19}$	$4.1\pm^{0.7}_{0.4}$	$4.0\pm^{4.1}_{0.8}$	$5.8\pm^{0.8}_{2.1}$	$3.2\pm^{3.3}_{0.6}$	$0.37\pm^{0.27}_{0.24}$	1.15 (177)
P1	1.40	0.29 ± 0.01	$0.70\pm^{0.02}_{0.03}$	$15.9\pm^{1.1}_{0.9}$	$1.31\pm^{0.09}_{0.11}$	$3.6\pm^{0.3}_{0.2}$	$5.9\pm^{4.0}_{1.4}$	$4.0\pm^{0.7}_{1.1}$	$4.5\pm^{3.0}_{1.1}$	$0.34\pm^{0.13}_{0.11}$	1.12 (187)
P2	1.29	0.28 ± 0.01	$0.66\pm^{0.03}_{0.04}$	$16.8\pm^{1.8}_{1.4}$	$1.16\pm^{0.17}_{0.08}$	4.3 ± 0.6	$9.6\pm^{*}_{5.0}$	$3.1\pm^{1.8}_{*}$	$8.3\pm^{*}_{4.3}$	$0.41\pm^{0.14}_{0.15}$	1.07 (174)
P3	1.24	0.28 ± 0.01	0.64 ± 0.02	$17.3\pm^{1.1}_{1.0}$	$1.24\pm^{0.10}_{0.09}$	$3.7\pm^{0.3}_{0.7}$	$8.3\pm^{27.2}_{2.5}$	$3.5\pm^{0.9}_{2.3}$	$6.7\pm^{22.0}_{2.0}$	$0.43\pm^{0.11}_{0.13}$	1.22 (185)
P4	1.28	0.28 ± 0.01	$0.65\pm^{0.02}_{0.02}$	$16.9\pm^{1.2}_{1.1}$	1.18 ± 0.08	$4.1\pm^{0.4}_{0.2}$	$9.4\pm^{7.7}_{2.3}$	$3.4\pm^{0.7}_{1.1}$	$8.0\pm^{6.5}_{2.0}$	$0.46\pm^{0}.08$	1.08 (180)

[a] Unabsorbed luminosity at 0.1–100 keV ($\times10^{37}$erg s^{-1}).
[b] Calculated using eq. (2.19), taking into account the inclination angle of 45° multiplying $1/\cos 45°$.
[c] Distance of 5.9 kpc is assumed. The distance uncertainty is not included in the errors.
[d] Calculated from the photon flux of `nthcomp` conserved through Comptonization.
[e] Errors are not written when only the upper or lower limit is obtained.

reproduced successfully with the fit goodness of $\chi_\nu \lesssim 1.2$ for ~ 180 degree of freedom. The obtained parameters are listed on table 5.2. As expected from the spectral similarity to Aql X-1 in P6, the obtained parameters, such as $T_{\rm in} \sim 0.7$ keV, $T_{\rm BB} \sim 1.2$ keV, and $T_{\rm e} \sim 8$ keV, are very close to those of Aql X-1 in P5–P6, rather than those of the Hard State in P0–P4 with $Q \gtrsim 7$. As expected from the spectral shape change in figure 5.7, $T_{\rm e}$ increased with time (from P0 to P4) from ~ 4 keV to ~ 9 keV, as $L_{\rm t}$ decreased by $\sim 20\%$.

Figure 5.9 shows $L_{\rm MCD}/L_{\rm t}$, $L_{\rm BB}/L_{\rm t}$, and $L_{\rm comp}/L_{\rm t}$ as a function of $L_{\rm t}$ (panel a), and of Q (panel b). This makes our doubt raised above more conclusive; against our previous assumption (§5.1.2) that the source was in the Hard State, the source, with low $L_{\rm comp}$, clearly corresponds to the Soft State of Aql X-1. Thus, we conclude that the source was in the faintest end of the Soft State over the whole observation of #2, and varied toward the Hard State, but did not actually cross the threshold. In figure 5.9 (a), their behavior is similar to those of Aql X-1 (figure 5.4 d' and figure 5.5), but we find a systematic difference between the two objects. This is due to difference in their threshold luminosity, possibly depending on the direction of $L_{\rm t}$ change. In panel (b), this discrepancy is resolved, and the two objects behave in very similar ways. We hence confirm that Q is more appropriate than $L_{\rm t}$ as the state-specifying variable.

5.1.3 4U 1728-34

Quite similar to 4U 1636-536 #2, the source exhibited significant intensity and hardness variations in §4.2.3. In the same manner as in 4U 1636-536 #2, we divided the data into

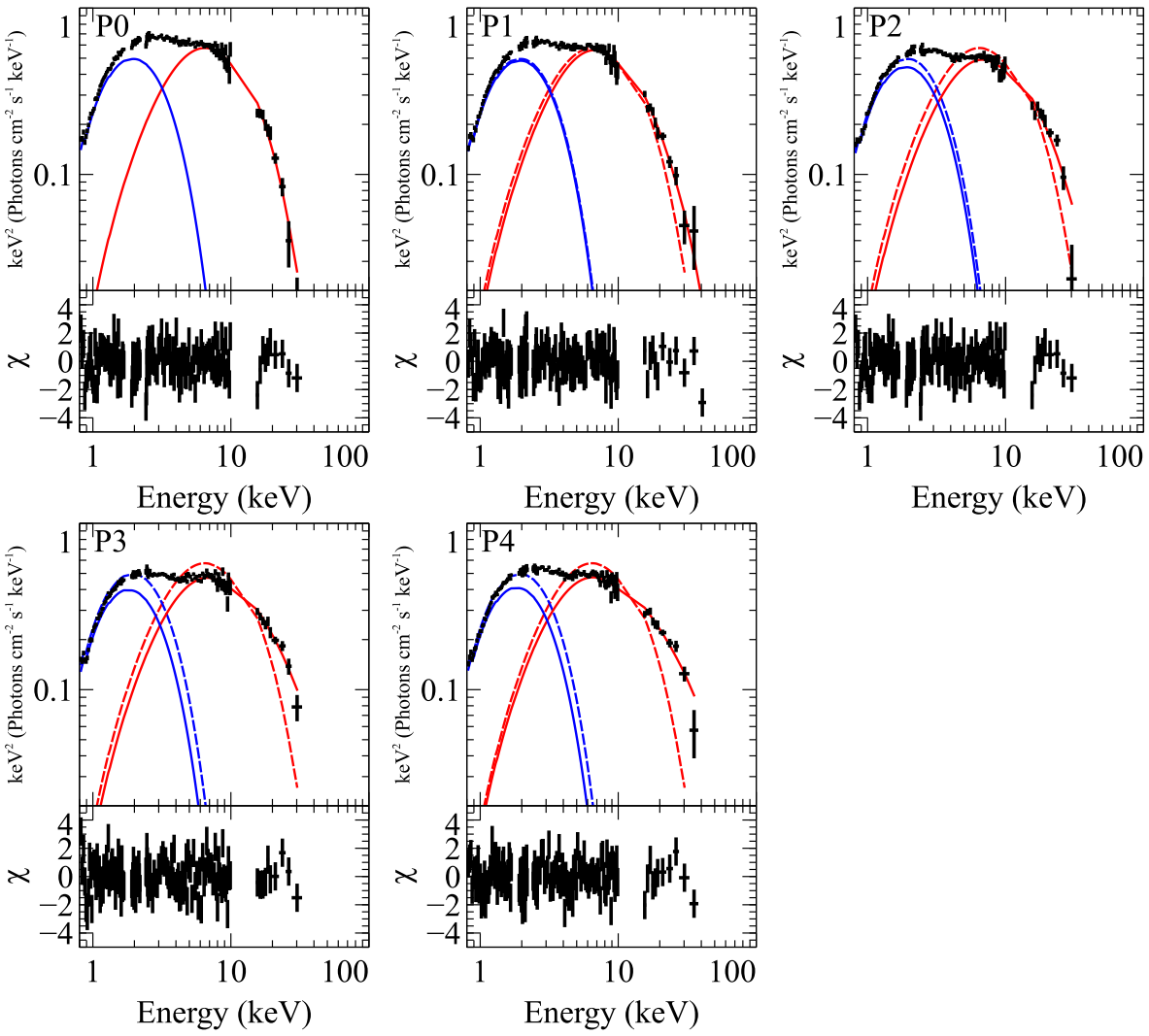

Figure 5.8: Model fits to the 5 spectra of 4U1636-536 #2 and the residuals. The `diskbb` (blue) and the `nthcomp` (red) components of the best-fit model are also shown. The best-fit model for P0 is overlaid with a dashed line on the other spectra.

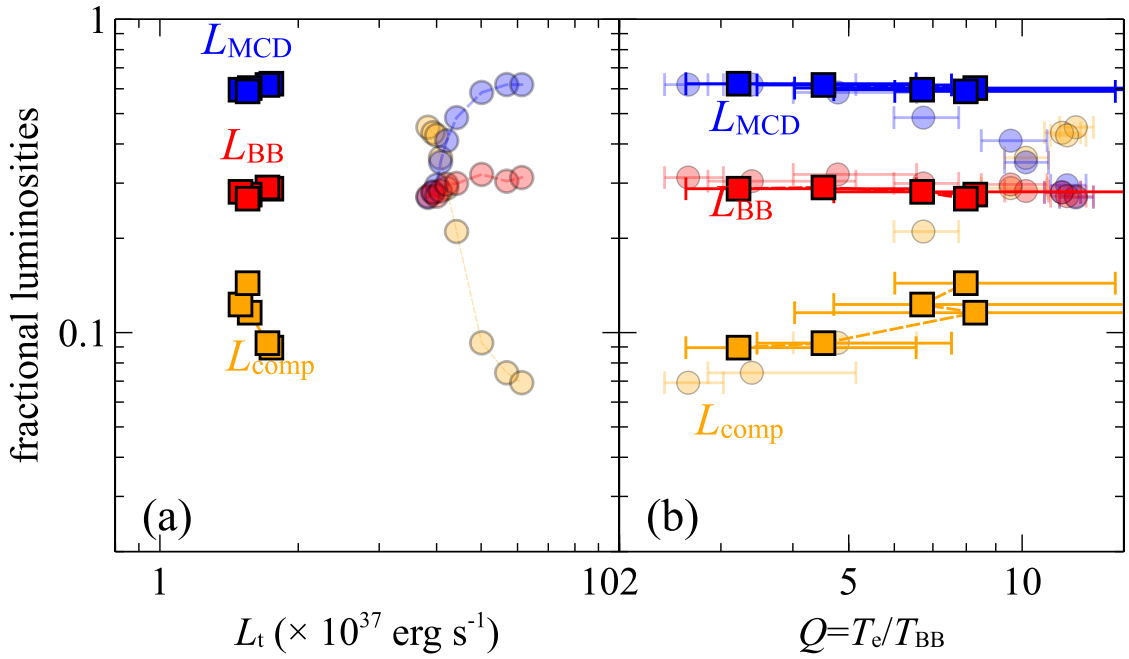

Figure 5.9: The same as figure 5.6 but for 4U 1636-536 #2, plotted against $L_{\rm t}$ (panel a), and Q (panel b). The results of Aql X-1 are overlaid with thin filled circles.

5 sequential periods, P0 to P4. Then, as presented in figure 5.10, 5 spectra were made. The intensity above $\sim$ 20 keV changed clearly, indicating a variation of $T_{\rm e}$. The spectral shape above $\sim$ 5 keV is nearly the same as that of Aql X-1 in P5. This again suggests that the source was actually in the Soft State, rather than the Hard State which we assumed in §4.1.2. The marked difference of the spectral shape at $\lesssim$ 5 keV is simply because 4U1728-34 suffers much stronger absorption (§4.2.3).

From the analogy to Aql X-1 and 4U 1636-536 #2, we again employed the same model `tbabs*const*(diskbb+nthcomp)`. Figure 5.11 shows residuals after fitting the spectra with the above model. Like in Aql X-1, positive residuals are slightly left at 6.6 keV, especially in P0. Again, this can be interpreted as Fe emission line. Since the residuals are rather weak, we incorporated a `gaussian`, rather than the complex `diskline` model, with three additional parameters; the energy centroid $E_{\rm c}$, the width σ and the normalization. To avoid a coupling of `gaussian` with `diskbb`, we fixed $E_{\rm c}$, σ and $N_{\rm H}$ in P1–P4 to the values obtained with the P0 spectrum which clearly showed the line structure.

By including the `gaussian`, the 5 spectra have all been reproduced successfully with the fit goodness of $\chi_\nu \lesssim 1.2$ for 365 degree of freedom. The fit results are shown in figure 5.12, and the obtained parameters are listed in table 5.3. Except the radius parameters which are subject to the distance uncertainty, all the parameters are similar to those of Aql X-1 around P5. As the luminosity decreased by $\lesssim$ 10%, all the parameters including Q and y changed by $\sim$ 15 to $\sim$ 50%, in the same manner as those of Aql X-1 and 4U 1636-536 #2. This means that the spectral shape, together with the physics behine, depend very sensitively on $L_{\rm t}$ (or $\dot{M}$), as a defining characteristic of the state transition phenomenon.

In figure 5.13, we show the behavior of the three luminosity components, in comparison with the preceding two sources. Thus, panel (a) reveals an even larger (factor $\sim$ 5) difference in $L_{\rm t}$ among the three data sets. In panel (b), the systematic difference is solved, and 4U 1728-34 is unified to the other two sources. We consider that 4U 1636-536 #2 and 4U 1728-34 are in the Soft State, with essentially the same behavior as Aql X-1 bellow $Q \sim 8$, but evolving in the opposite direction as a function of time.

Since all the data with the criterion (1) have now been analyzed, let us examine spectral parameters other than the three luminosity components. As shown in figure 5.14, we selected the three temperatures and the coronal optical depth, which are unaffected by the distance uncertainty. In panel (a), both 4U 1636-536 #2 and 4U 1728-536 cluster in $Q \lesssim 8$, and their three temperatures evolved in the same manner as Aql X-1, with $T_{\rm e}$ increasing and $T_{\rm BB}$ and $T_{\rm in}$ decreasing toward the Hard State ($Q \gtrsim 8$). In panel (b), the behavior of τ has become clearer, that it decreases toward the Hard State.

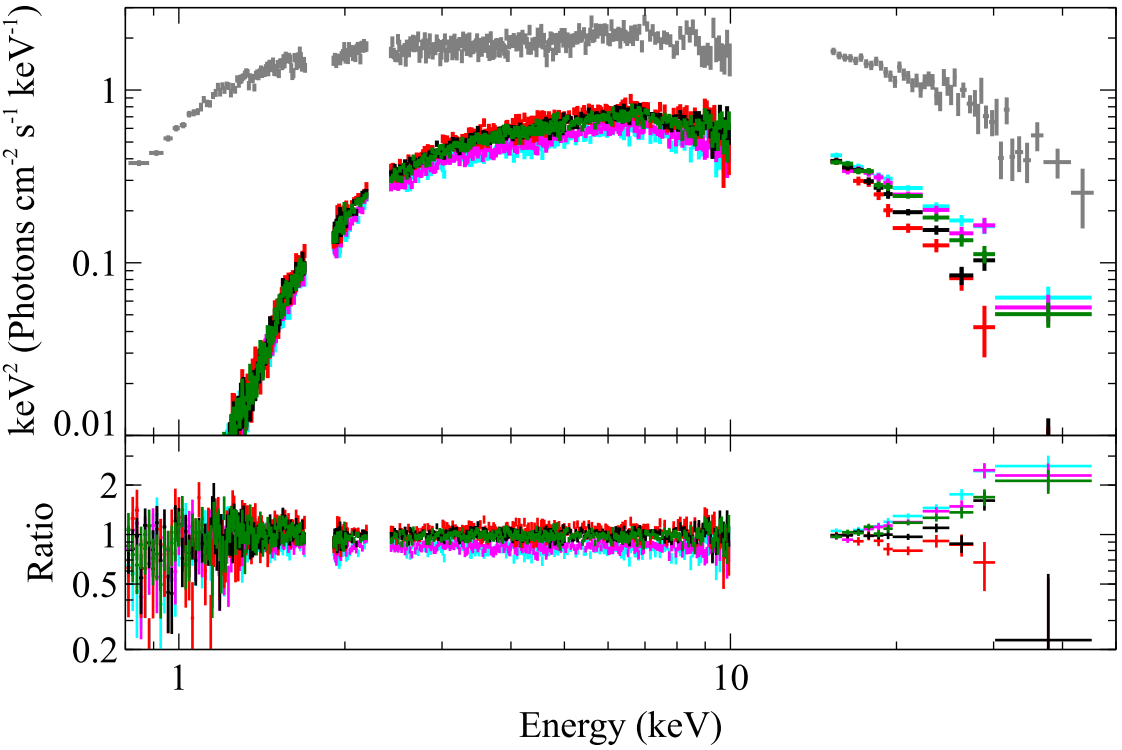

Figure 5.10: Background subtracted $\nu F\nu$ spectra of 4U1728-34 with the data divided into 5 segments, from P0 to P4, shown in black, red, green, cyan, and magenta, respectively. The ratios of the data to the best fit model of P0 are shown in the bottom panel. The spectrum of Aql X-1 in P5 is plotted for comparison (gray).

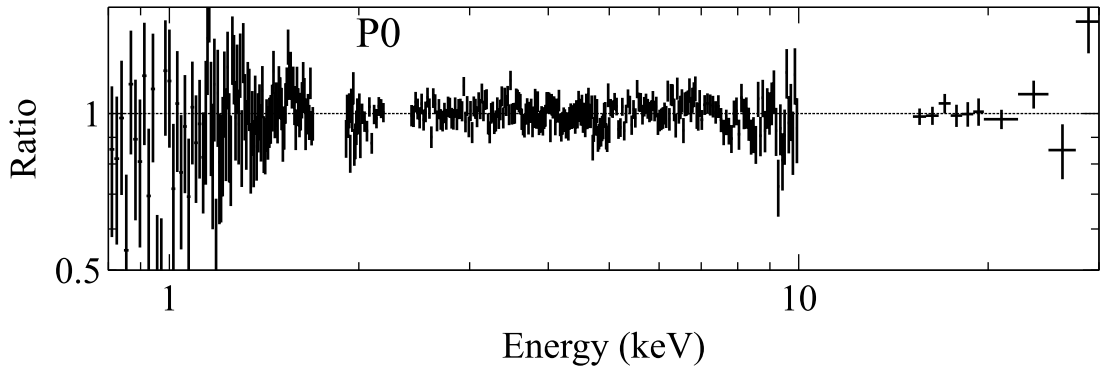

Figure 5.11: The spectrum of 4U 1728-34 for P0, presented as a ratio to the best-fit model consisting of `tbabs*const*(diskbb+nthcomp)`.

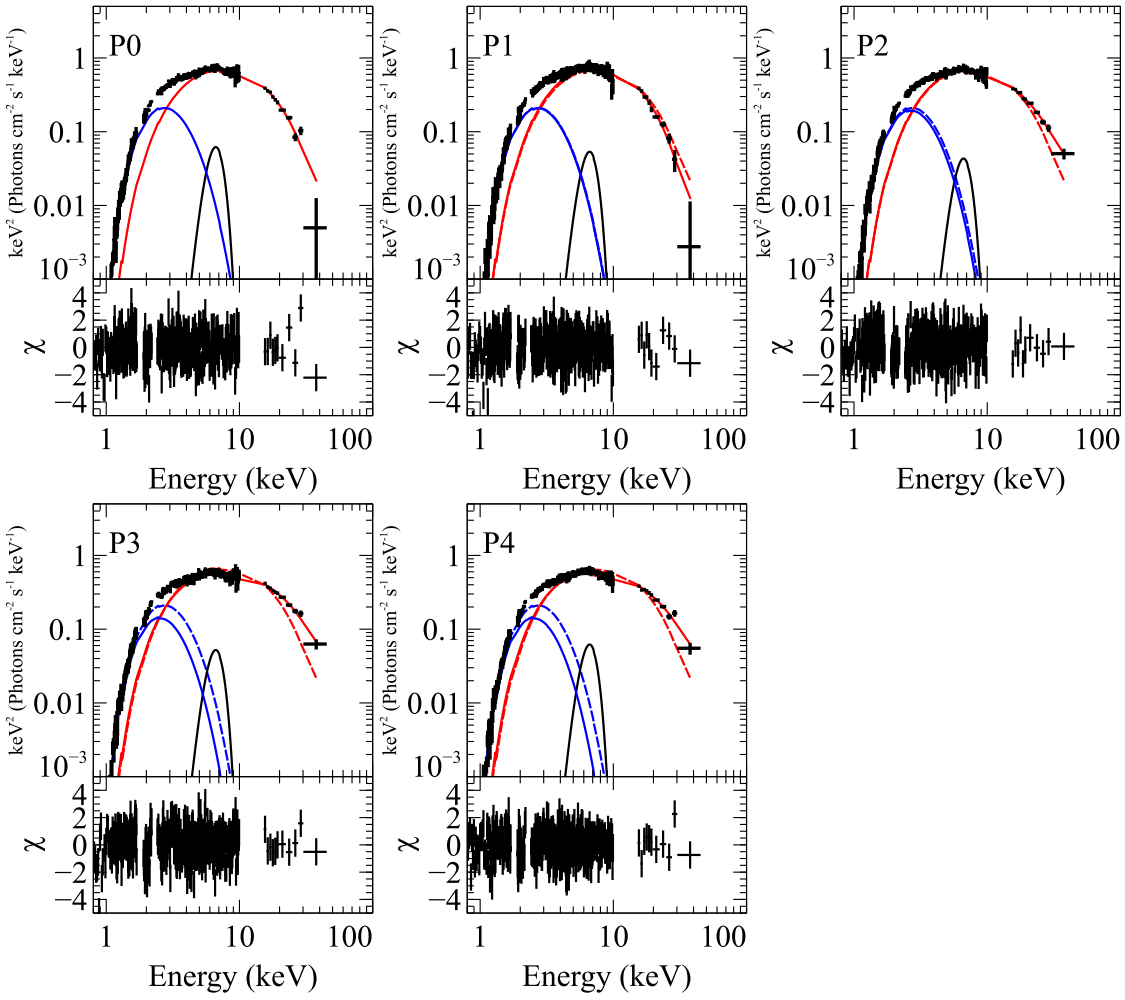

Figure 5.12: Model fits to the spectrum of 4U1728-34 from P0 to P4, shown in the same way as figure 5.3. The best-fit models in P0 are overlaid with dotted line.

Table 5.3: The parameters and 90% errors of the 4U1728-34 spectra in P0–P4 obtained with the model consisting of `tbabs*const*(diskbb+nthcomp+gaussian)`.

		`diskbb`		`nthcomp`				`gauss`[e]			
#	L[a]	$T_{\rm in}$ (keV)	$R_{\rm in}$ (km)[b,c]	$T_{\rm BB}$ (keV)	$R_{\rm BB}$ (km)[c,d]	$T_{\rm e}$ (keV)	τ	norm $\times 10^{-2}$	Q	y	$\chi^2_\nu(\nu)$
P0	1.26	$0.64^{+0.03}_{-0.05}$	$16.5^{+2.4}_{-0.7}$	$1.14^{+0.13}_{-0.11}$	$4.65^{+0.86}_{-0.46}$	$3.9^{+0.6}_{-0.4}$	$6.9^{+0.5}_{-0.6}$	$4^{+1.7}_{-0.7}$	$3.4^{+0.5}_{-0.4}$	$0.50^{+0.21}_{-0.15}$	1.12 (365)
P1	1.28	$0.64^{+0.04}_{-0.07}$	$16.7^{+3.7}_{-2.1}$	$1.13^{+0.30}_{-0.19}$	$4.75^{+1.51}_{-0.51}$	$3.4^{+0.7}_{-0.4}$	$7.8^{+0.6}_{-0.7}$	$4.3^{+2.9}_{-1.0}$	$3.0^{+0.6}_{-0.4}$	$0.51^{+0.32}_{-0.22}$	1.17 (365)
P2	1.26	$0.62^{+0.03}_{-0.03}$	$17.7^{+1.8}_{-1.5}$	$1.16^{+0.10}_{-0.09}$	$4.59^{+0.44}_{-0.31}$	$5.7^{+1.6}_{-0.8}$	$4.7^{+0.5}_{-0.8}$	$4.2^{+0.8}_{-0.6}$	$4.9^{+1.3}_{-0.7}$	$0.43^{+0.10}_{-0.09}$	1.25 (365)
P3	1.16	$0.55^{+0.04}_{-0.06}$	$21.3^{+4.7}_{-2.5}$	$0.96^{+0.17}_{-0.12}$	$5.94^{+1.27}_{-0.60}$	$5.6^{+1.0}_{-0.7}$	$5.7^{+0.5}_{-0.5}$	$4.9^{+2.2}_{-1.0}$	$5.9^{+1.0}_{-0.7}$	$0.60^{+0.11}_{-0.09}$	1.44 (365)
P4	1.17	$0.55^{+0.03}_{-0.04}$	$21.4^{+3.4}_{-2.3}$	$0.98^{+0.13}_{-0.10}$	$5.83^{+0.85}_{-0.53}$	$5.8^{+1.2}_{-0.8}$	$5.3^{+0.5}_{-0.6}$	$5.0^{+1.5}_{-0.9}$	$5.9^{+1.3}_{-0.8}$	$0.55^{+0.10}_{-0.09}$	0.96 (365)

[a] Unabsorbed luminosity at 0.1–100 keV ($\times 10^{37}$erg s^{-1}).

[b] Calculated using eq. (2.19), taking into account the inclination angle of 45° multiplying $1/\cos 45°$.

[c] Distance of 5.2 kpc is assumed. The distance uncertainty is not included in the errors.

[d] Calculated from the photon flux of `nthcomp` assuming that it is conserved through Comptonization.

[e] $E_{\rm c}$ and σ are fixed at 6.4 keV and 0.8 keV, respectively.

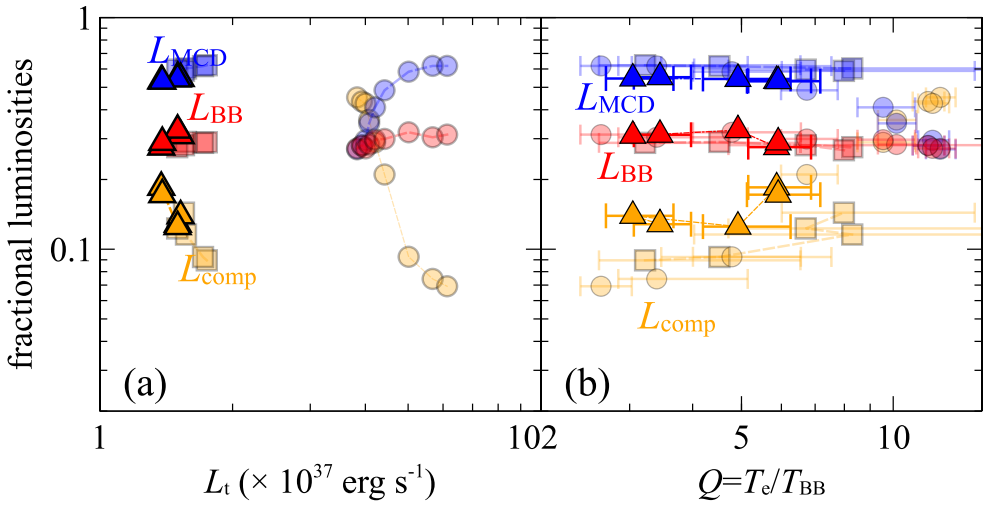

Figure 5.13: The same as figure 5.9, but for 4U 1728-34. Data points of Aql X-1 and 4U 1636-536 are plotted with transparent filled circle and square.

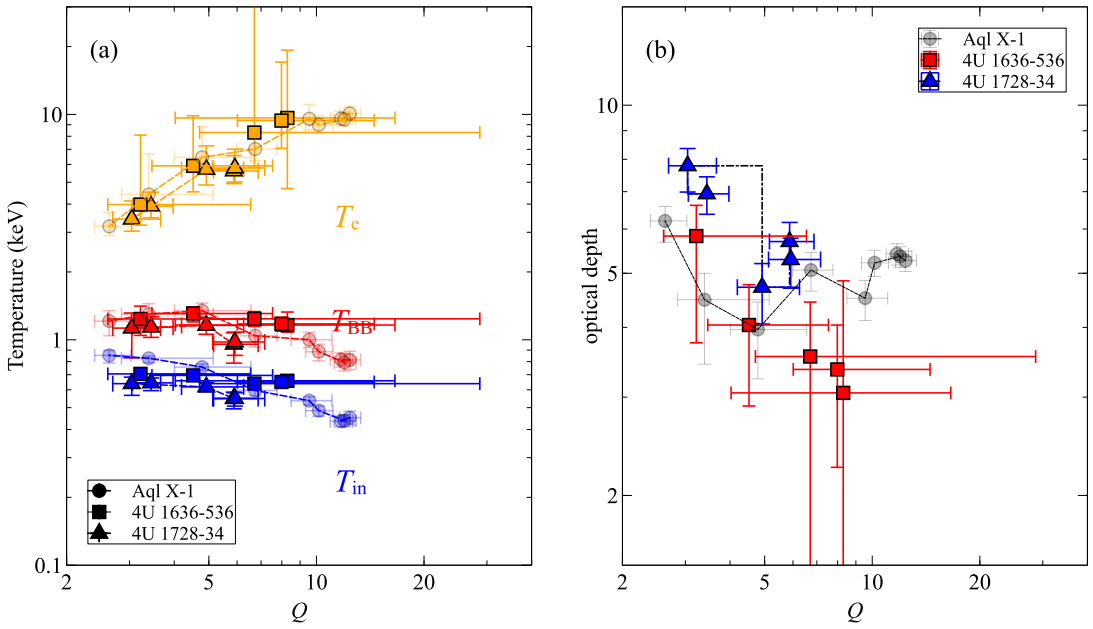

Figure 5.14: The behaviors of the temperatures (panel a) and the coronal optical depth (panel b), observed from Aql X-1, 4U 1636-536, and 4U 1728-34, shown against Q. In panel (a), $T_{\rm e}$, $T_{\rm BB}$, and $T_{\rm in}$ are plotted with orange, red, and blue, respectively. The data points of Aql X-1 are indicated with thin filled circles.

5.2 Data with the Criterion (2)

5.2.1 4U 1636-536

Four data sets of 4U 1636-536, #1, #3, #4, and #5, have been selected with the criterion (2), in addition to #2. During the first three observations, the source was in the Soft State, as indicated by the small hardness ratios of $H \lesssim 0.01$ (figure 4.1), while it was in the Hard State in #5 with $H \sim 0.1$. Unlike 4U 1636-536 #2, the source did not vary very much in the 4 observations (§4.2.2). Thus, to study the behavior of 4U 1636-536 in the deep Soft and Hard States, we made an average spectrum of each data set.

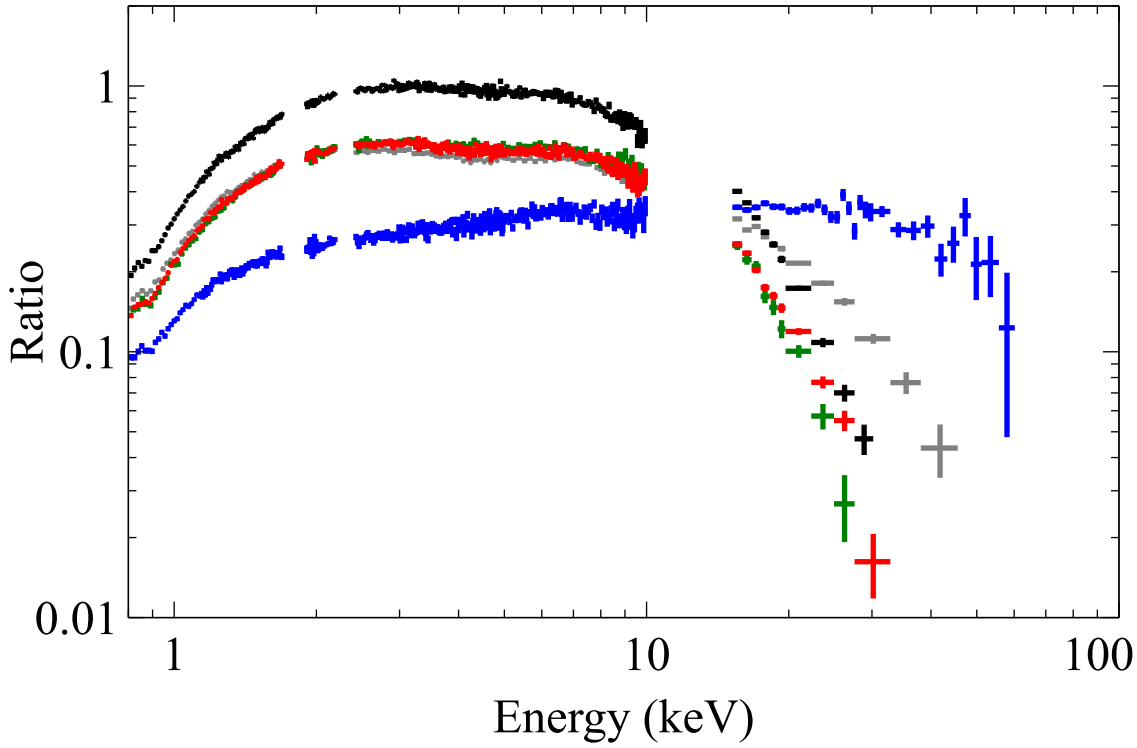

Figure 5.15: Background subtracted spectra of 4U 1636-536 taken with XIS0 plus XIS3 in 0.8–10 keV, and HXD-PIN in 15–60 keV, normalized with a $\Gamma = 2.0$ power-law, in the same way as in figure 5.1. The observation #1, #3, #4, and #5 are plotted with black, red, green, and blue, respectively. The average spectrum for of #2 is overlaid with gray for comparison.

Figure 5.15 shows the four average spectra derived in this way, where the bimodality is evident. As expected, the spectra of #1, #3, and #4 all show nearly the same convex thermal shape typical of the Soft State. The spectrum of #1 is brighter than those of #3 and #4 by a factor of $\sim$ 2. The spectrum of #5, on the other hand, shows a

typical Hard State shape with a power-low slope of $\Gamma \sim 2$ (eq. 2.24), and cutoff at ~ 50 keV. For all the spectra, we employed the same unified model as used in §5.1, expressed as `tbabs*const*(diskbb+nthcomp)`. When the spectrum shows positive residuals at ~ 6.4 keV, we added either `gauss` or `diskline` to the model.

As presented in figure 5.16, the spectra have been fitted successfully regardless of the spectral state. The obtained parameters are listed in table 5.4. Like the previous results, the parameters are physically reasonable, with $R_{\rm BB} < R_{\rm NS} < R_{\rm in}$. The parameters from #1, #3, and #4, including $Q \sim 3$ and $y \sim 0.7$, are also close to to one another, and those obtained with 4U 1636-536 #2 at P4 (table 5.2). In #5, the source was in a full Hard State as evidenced by the large value of $Q \sim 25$, wherein $T_{\rm e} = 15$ keV and $y = 1.1$ successfully explain the cut-off spectral shape with strong Comptonization.

Figure 5.17 shows the constituent luminosities. In panel (a), the data again show inconsistency with Aql X-1, with systematically smaller $L_{\rm t}$. In figure 5.17 (b), in contrast, the data points in the Soft State with $Q < 3$ line up with those of Aql X-1 and 4U 1636-536 #2, and those in the Hard State with $Q = 25$ are smoothly connected to the hardest end of Aql X-1. Figure 5.17 (b) thus expands the validity range of the new parameter Q.

5.2.2 4U 1608-52

As described in §4.2.4, we obtained four data sets of this transient LMXB, when the source was decaying from an outburst (figure 4.15). Figure 5.18 presents the average spectra of each data sets. The source was in the Soft State in the first two observations, #1 and #2, with typical convex spectral shapes. In #3, the spectrum was already in the Hard State, with the luminosity several times lower than in #1. Finally, the source reached the end of the outburst, when the luminosity decreased by more than an order of magnitude from #1, showing a flat spectrum with a photon index of ~ 2. Thus, the data sets would provide another valuable example (in addition to Aql X-1) of spectral evolution over a broader luminosity range than were covered by the criterion-(1) data. As described in §4.2.4, none of the four data sets showed much variation in H, nor in the 5–10 keV count rate. Thus, we analyzed the four time-averaged spectra in figure 5.18.

Following the previous successful fit, we employed the same unified model, but for #4 replacing `nthcomp` with an XSPEC model `compPS` (Poutanen & Svensson 1996). The new model `compPS` can be used when $\tau \leq 3$, and is suited for high electron temperature with more accurate relativistic effects, such as the cross section of Compton scattering. The inclination angle was tentatively set to be 60° (Kajava et al. 2017) to guarantee $R_{\rm in} > 12$ km.

As shown in figure 5.19, all the spectra are successfully reproduced with $\chi^2_\nu(\nu) \lesssim 1.3$ for $\sim 360 - 380$ degree of freedom. Parameter values for #1 and #2 listed on table 5.5, are all similar to those of the Soft State of 4U 1636-536 (table 5.4), reinforcing the unified view in the Soft State. The best-fit parameters for #3 and #4 are listed on table 5.6. We obtained the highest temperature of $T_{\rm e} = 25 - 45$ keV among the data sets analyzed so far, and enlarged the validity a range of Q.

Figure 5.20 shows constituent luminosities. Although it tells us nearly the same stories

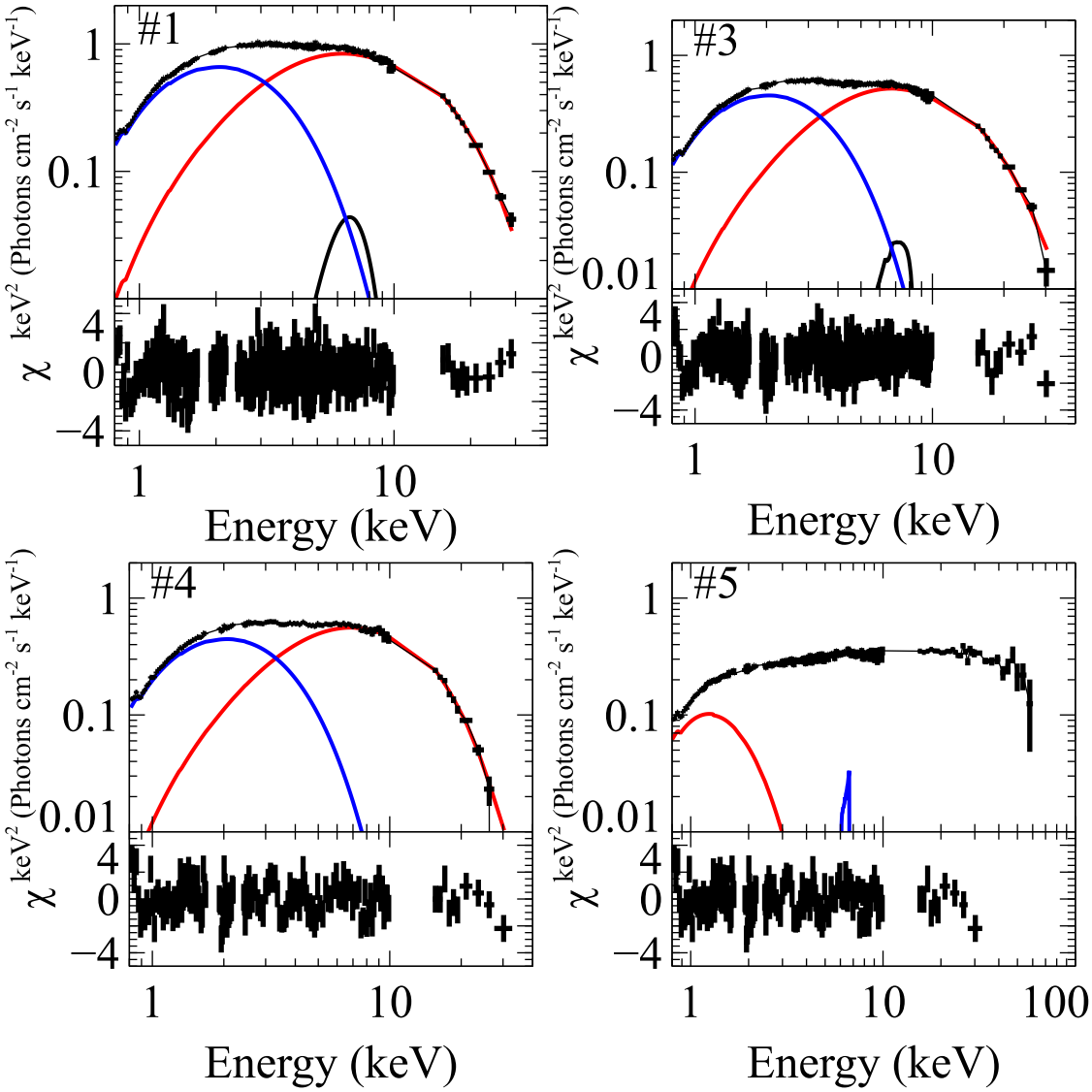

Figure 5.16: The best fit spectra of 4U1636-536 #1, #3, #4, and #5 and their residuals.

Table 5.4: Parameters and 90% errors obtained by fitting 4U1636-536 #3 and #4 spectra with `diskbb+nthcomp+gauss`.

Data		#1	#3	#4	#5
Luminosity	L ($\times 10^{37}$ erg s^{-1})[a,c]	2.00	1.28	1.28	0.89
`tbabs`	$n_{\rm H}$ ($\times 10^{22}$ cm^{-2})	0.292 ± 0.006	(0.28)	0.28 ± 0.01	0.23 ± 0.02
`diskbb`	$T_{\rm in}$ (keV)	$0.75\pm^{0.04}_{0.09}$	$0.74\pm^{0.01}_{0.02}$	$0.75\pm^{0.03}_{0.05}$	0.43 ± 0.04
	$R_{\rm in}$ (km)[b,c]	$15.9\pm^{3.7}_{1.2}$	$13.3\pm^{0.4}_{0.4}$	$12.9\pm^{1.5}_{0.9}$	$21.4\pm^{5.0}_{3.1}$
`nthcomp`	$T_{\rm BB}$ (keV)	$1.08\pm^{0.17}_{0.40}$	$1.29\pm^{0.10}_{0.12}$	$1.24\pm^{0.21}_{0.29}$	$0.61\pm^{0.07}_{0.08}$
	$R_{\rm BB}$ (km)[c,d]	$6.3\pm^{3.5}_{0.8}$	$3.6\pm^{0.3}_{0.2}$	$3.9\pm^{1.0}_{0.4}$	$11.1\pm^{1.7}_{0.8}$
	$T_{\rm e}$ (keV)	$3.2\pm^{0.3}_{0.2}$	$3.6\pm^{0.5}_{0.3}$	$2.8\pm^{0.5}_{0.2}$	$15.2\pm^{2.0}_{1.8}$
	τ	$8.4\pm^{0.3}_{0.4}$	$6.6\pm^{0.1}_{0.2}$	$9.6\pm^{0.5}_{0.8}$	$2.9\pm^{0.3}_{0.2}$
`gauss`	$E_{\rm c}$	$6.4^{0.3}_{0.4}$	-	–	–
	σ (keV)	$1.1\pm^{0.6}_{0.3}$	-	–	–
	norm ($\times 10^{-3}$)	$3\pm^{5}_{2}$	-	–	–
`diskline`	$E_{\rm c}$	-	$6.6\pm^{0.5}_{0.2}$	–	6.7 ± 0.02
	β	-	$-2.8\pm^{0.5}_{0.6}$	–	-3.0 ± 0.4
	norm ($\times 10^{-3}$)	-	$1\pm^{0.5}_{0.5}$	–	0.4 ± 0.1
	Q	$3.0\pm^{0.3}_{0.2}$	$3.0\pm^{0.3}_{0.2}$	$3.0\pm^{0.3}_{0.2}$	$24.9\pm^{3.3}_{3.0}$
	y	$0.52\pm^{0.16}_{0.18}$	$0.38\pm^{0.16}_{0.13}$	$0.48^{0.47}_{0.36}$	1.1 ± 0.03
Fit goodness	$\chi^2_\nu(\nu)$	1.28 (361)	1.10 (362)	1.32 (144)	1.14 (381)

[a] Unabsorbed luminosity at 0.1–100 keV ($\times 10^{37}$erg s^{-1}).

[b] Calculated using eq. (2.19), taking into account the inclination angle of 45° multiplying $1/\cos 45°$.

[c] Distance of 5.9 kpc is assumed. The distance uncertainty is not included in the errors.

[d] Calculated from the photon flux of `nthcomp` conserved through Comptonization.

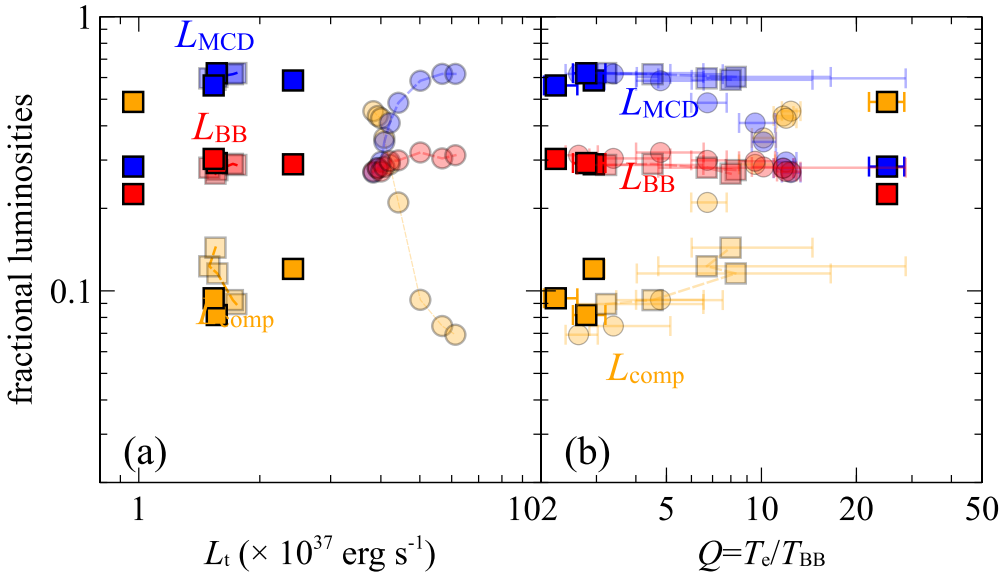

Figure 5.17: The same as figure 5.13, but for 4U 1636-536 #1, #3, #4, and #5. Data points of Aql X-1 and 4U 1636-536 #2 are overlaid with transparent filled circle and square.

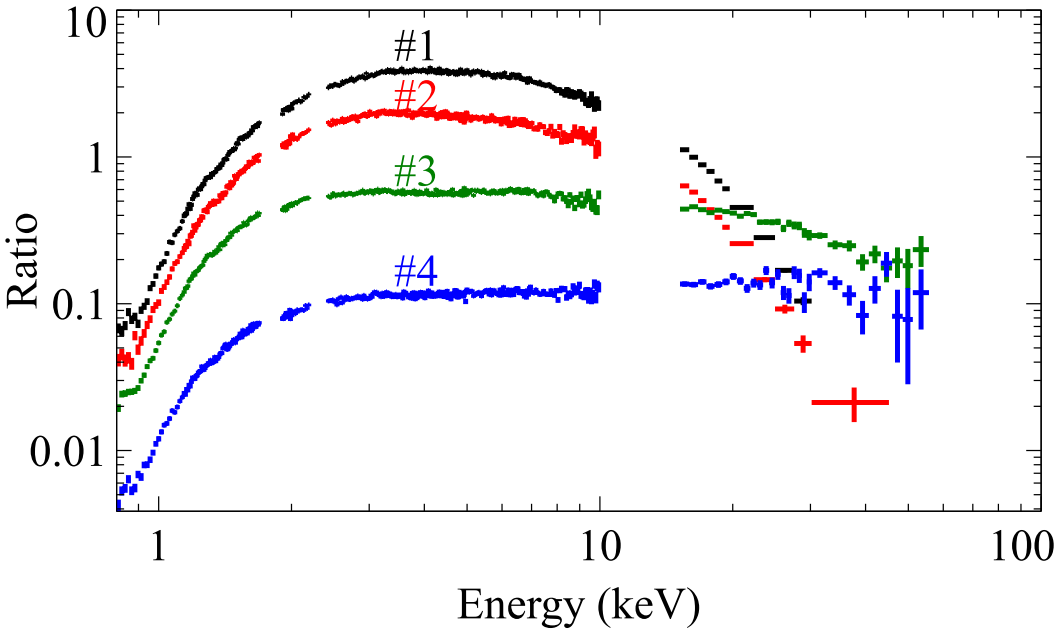

Figure 5.18: Background subtracted *Suzaku* spectra of 4U 1608-52 presented in the same way as figure 5.1. The observations #1, #2, #3, and #4 are shown in black, red, green, and blue, respectively.

as figure 5.13 and figure 5.17, one new observation is that some systematic differences still remain for 4U 1608-52 even when Q, instead of $L_{\rm t}$, is used as the control parameter. This could be a manifestation of the hysteresis (§2.4.4), because the four observations of 4U 1608-52 were performed in a series to cover a whole decaying phase of the outburst (figure 4.15), in which the luminosity changed by an order of magnitude encompassing $Q \lesssim 3$ to $Q = 94$. This makes a contrast to the case of 4U 1636-536 #2 and 4U 1728-34, of which $L_{\rm t}$ decreased only by $\sim 16\%$ or less, and the range of Q was limited to $\lesssim 8$. Using Q instead of $L_{\rm t}$, the hysteresis effects have largely been removed, but not completely.

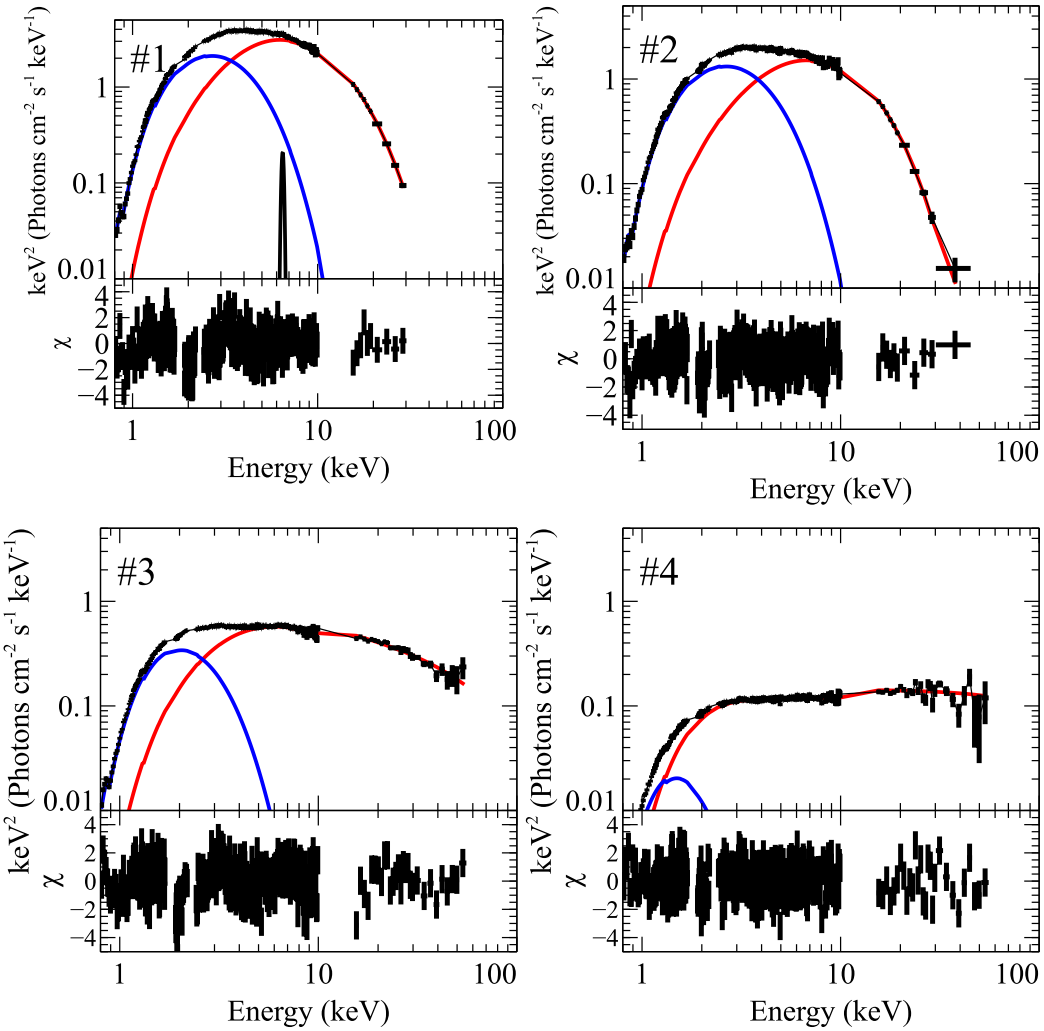

Figure 5.19: The best fit spectrum of 4U1608-52 #1, #2, #3, and #4, and their residuals.

Table 5.5: Parameters and 90% errors obtained by fitting the 4U1608-52 #1 and #2 spectra with `diskbb+nthcomp+gauss`[a].

Data		#1	#2
Luminosity	L ($\times 10^{37}$ erg s^{-1})	2.68	1.49
`tbabs`	$n_{\rm H}$ ($\times 10^{22}$ cm^{-2})	1.06 ± 0.01	1.05 ± 0.02
`diskbb`	$T_{\rm in}$ (keV)	$0.87\pm^{0.05}_{0.06}$	$0.86\pm^{0.04}_{0.06}$
	$R_{\rm in}$ (km)[b]	16.5 ± 1.5	$13.5\pm^{1.7}_{1.1}$
`nthcomp`	$T_{\rm BB}$ (keV)	$1.25\pm^{0.08}_{0.12}$	$1.33\pm^{0.18}_{0.23}$
	$R_{\rm BB}$ (km)	$5.7\pm^{0.8}_{0.3}$	$3.03.5\pm^{0.9}_{0.5}$
	$T_{\rm e}$ (keV)	$3.6\pm^{0.4}_{0.2}$	$3.2\pm^{0.6}_{0.3}$
	τ	$5.4\pm^{0.2}_{0.4}$	$6.6\pm^{0.4}_{0.7}$
`gauss`	$E_{\rm c}$	6.47 ± 0.08	–
	σ (keV)	$0.096\pm^{0.148}_{0.095}$	–
	norm ($\times 10^{-3}$)	$1\pm^{1}_{1}$	–
	Q	$2.9\pm^{0.4}_{0.2}$	$2.4\pm^{0.5}_{0.2}$
	y	$0.28\pm^{0.08}_{0.09}$	0.31 ± 0.2
Fit goodness	$\chi^2_\nu(\nu)$	1.15 (361)	1.12 (365)

[a] Details are the same as in table 5.1.
[b] Calculated using eq. (2.19), taking into account the inclination angle of 60° multiplying $1/\cos 60°$.

Table 5.6: Parameters obtained by fitting 4U1608-52 #3 spectrum with `diskbb+nthcomp+gauss`, and #4 spectrum with the same model but replacing `nthcomp` with `compPS`[a].

Data		#3	#4
Luminosity	L ($\times 10^{36}$ erg s^{-1})	7.01	1.98
`tbabs`	$n_{\rm H}$ ($\times 10^{22}$ cm^{-2})	1.04 ± 0.01	1.07 ± 0.06
`diskbb`	$T_{\rm in}$ (keV)	$0.54\pm^{0.01}_{0.02}$	0.28 ± 0.03
	$R_{\rm in}$ (km)	$20.8\pm^{1.3}_{1.1}$	$35.3\pm^{0.9}_{0.7}$
`nthcomp`/`compPS`	$T_{\rm BB}$ (keV)	0.91 ± 0.04	0.48 ± 0.03
	$R_{\rm BB}$ (km)	$4.6\pm^{0.3}_{0.1}$	$8.6\pm^{1.2}_{1.1}$
	$T_{\rm e}$ (keV)	$24.9\pm^{29.5}_{7.5}$	$44.9\pm^{5.9}_{6.7}$
	τ	$2.0\pm^{0.6}_{0.9}$	$2.2\pm^{0.4}_{0.3}$
	Q	$27\pm^{32}_{8}$	$94\pm^{12}_{14}$
	y	0.63 ± 0.03	$1.4\pm^{0.6}_{0.4}$
Fit goodness	$\chi^2_\nu(\nu)$	1.34 (383)	1.25 (383)

[a] Details are the same as table 5.5

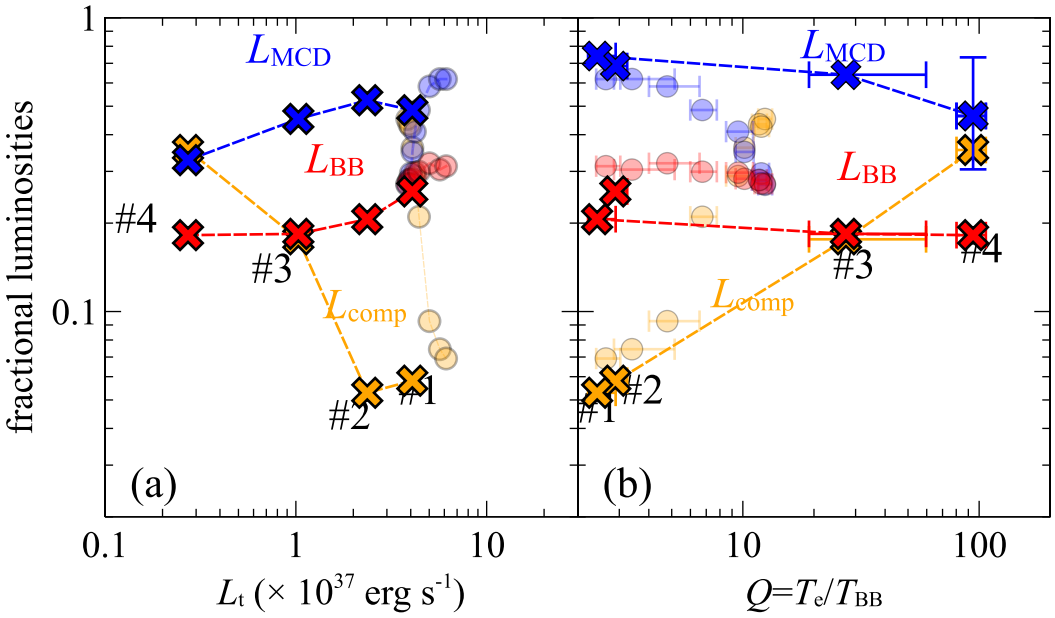

Figure 5.20: The same as figure 5.13, but for 4U 1608-52. The data points of Aql X-1 are plotted with thin colors.

5.2.3 4U 1705-44

As described in §4.2.5, the last source, 4U 1705-44, was selected by the criterion (2) with six data sets in the Soft State and additional two in the Hard State. Figure 5.21 shows spectra from all these 8 observations. Since a weak variation in H was seen in #8 (figure 4.23), the data were divided into two around 170 ks in the light curve.

As presented in figure 5.22, we again fitted all the 9 spectra with the same unified model. The fits are all successful with $\chi^2_\nu(\nu) \lesssim 1.3$ for ~ 380 degree of freedom, and the obtained parameters for #1 to #8 are summarized on table 5.7. The results reconfirmed our unified view constructed so far, but one problem is observed: in #3 and #6 when the source was very luminous at $\sim 10^{38}$ erg s^{-1}, we obtained $R_{\rm BB} = 15-22$ km which is clearly too large. In order to attribute the unphysical values the distance uncertainty, we would have to assume a $\sim 50\%$ smaller distance as $D \sim 1.9$ kpc, which would then provide too small $R_{\rm in} \sim 9$ km for an assumed inclination of $i = 45°$.

Figure 5.23 shows constituent luminosities. All the data points are consistent with those of Aql X-1 in panel (b) except for #3 and #6, with relatively good consistency also in panel (a). The ones in the Hard State with $Q \sim 30$ are smoothly connected with the Hard State of Aql X-1, extending our unified understanding.

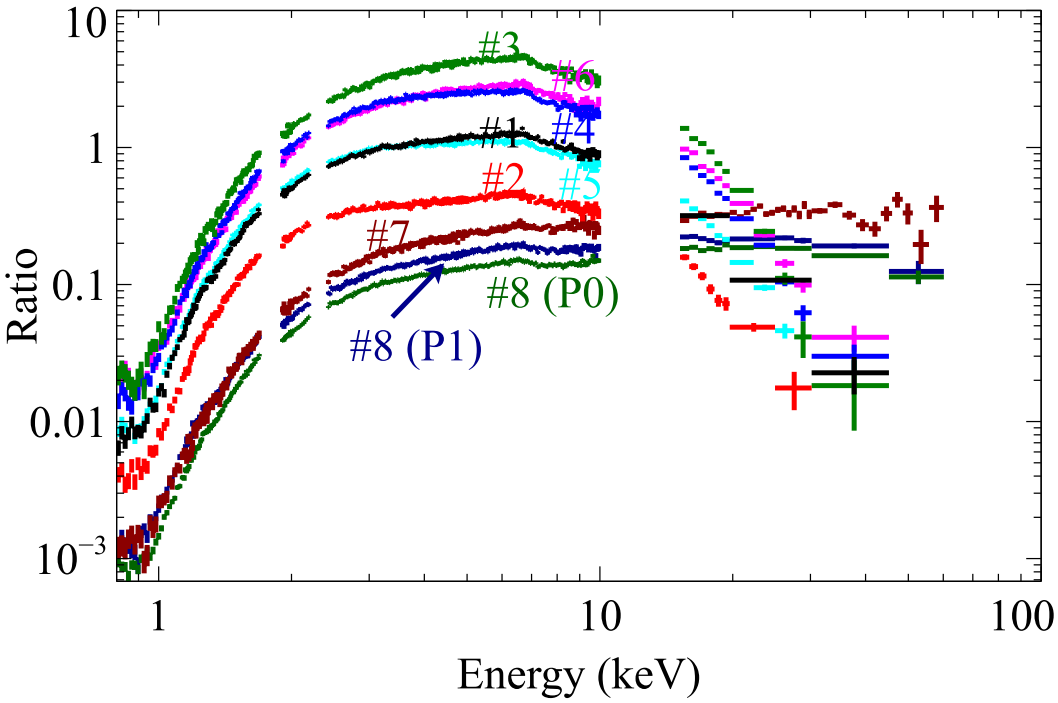

Figure 5.21: Background subtracted spectra of 4U 1705-52 from #1, #2, #3, #4, #5, #6, #7, #8 (P0), and #8 (P1), shown in black, red, green, blue, cyan, magenta, dark red, dark green, and dark blue, respectively. The style of presentation is the same as in figure 5.1.

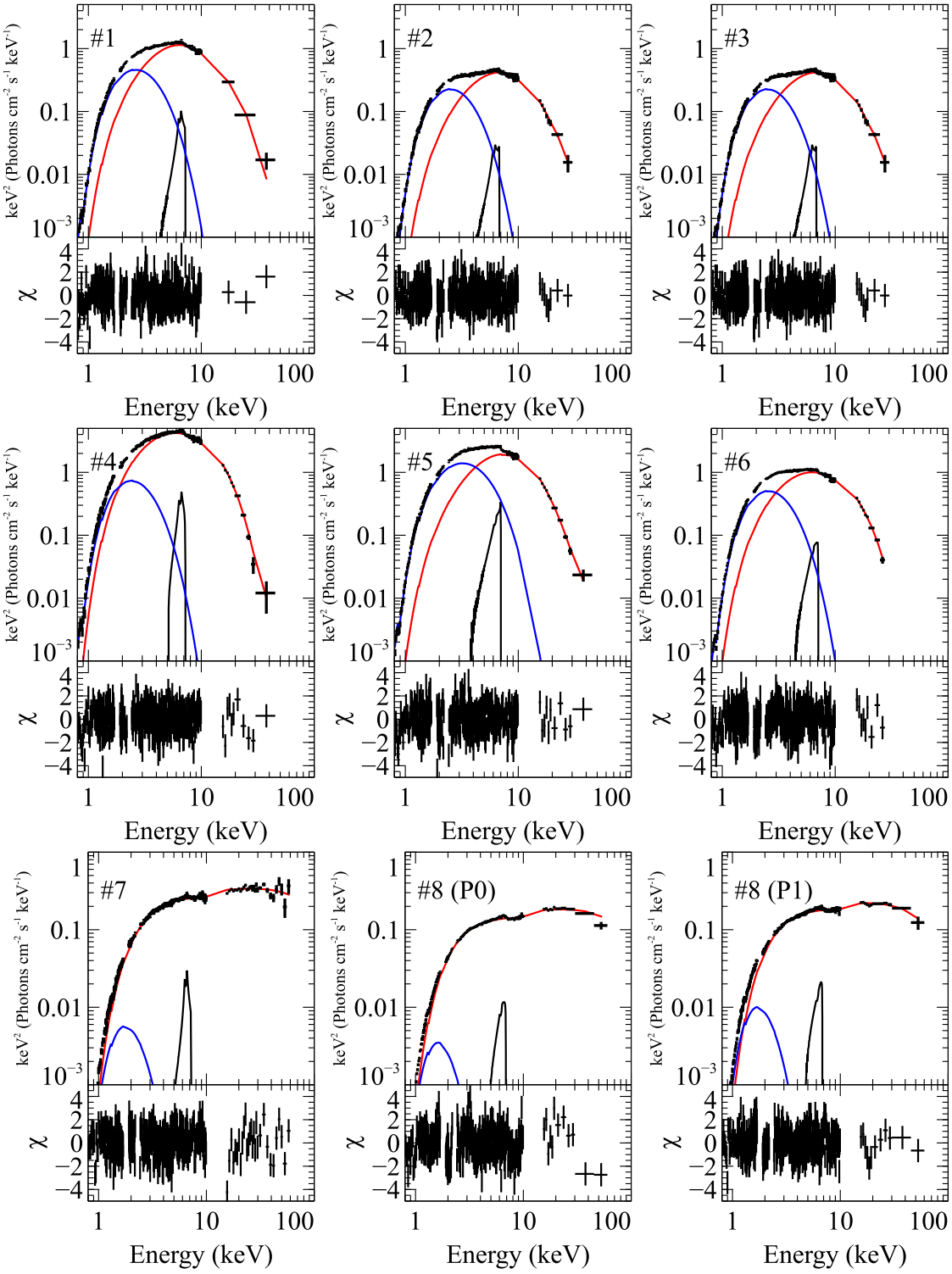

Figure 5.22: The same spectra as those in figure 5.21 from #1 to #6, with the best-fit model.

Table 5.7: Parameters and 90% errors obtained by fitting 4U1705-44 #1 through #7, #8 (P0), and #8 (P1) spectra with `diskbb+nthcomp+diskline`[a].

			`tbabs`	`diskbb`		`nthcomp`				`diskline`					
#		L^{a}	$n_{\rm H}$ ($\times10^{22}$ cm^{-2})	$T_{\rm in}$ (keV)	$R_{\rm in}$ (km)	$T_{\rm BB}$ (keV)	$R_{\rm BB}$ (km)	$T_{\rm e}$ (keV)	τ	$E_{\rm c}$ (keV)	β	norm 10^{-3}	Q	y	$\chi^2_\nu(\nu)$
1	-	3.6	1.64 ± 0.02	$0.75\,^{+0.03}_{-0.02}$	$20.0\,^{+1.3}_{-1.1}$	$1.31\,^{+0.09}_{-0.10}$	$6.6\,^{+0.5}_{-0.6}$	$3.6\,^{+1.2}_{-0.5}$	$5.1\,^{+0.5}_{-0.8}$	$6.5\,^{+0.1}_{-0.3}$	$-2.3\,^{+0.3}_{-1.0}$	2 ± 0.5	$2.8\,^{+0.9}_{-0.4}$	$0.25\,^{+0.11}_{-0.14}$	1.17 (354)
2	-	1.6	1.70 ± 0.03	$0.68\,^{+0.03}_{-0.01}$	$18.0\,^{+1.5}_{-1.3}$	$1.42\,^{+0.13}_{-0.22}$	$3.1\,^{+0.4}_{-0.2}$	$3.5\,^{*}_{-0.9}$	$5.1\,^{+1.5}_{-1.3}$	6.1 ± 0.1	-2.5 ± 0.4	1 ± 0.3	$2.4\,^{*}_{-0.6}$	$0.23\,^{+0.24}_{-0.50}$	1.09 (359)
3	-	11	$1.68\pm^{0.06}_{0.05}$	$0.63\,^{+0.10}_{-0.12}$	$38.9\,^{+13.2}_{-6.2}$	$0.97\,^{+0.14}_{-0.16}$	$21.9\,^{0}_{-0}$	2.6 ± 0.1	$9.6\,^{+0.2}_{-0.3}$	6.5 ± 0.1	2.4 ± 0.4	$10\,^{+2.5}_{-2.3}$	2.7 ± 0.1	$0.52\,^{+0.09}_{-0.15}$	1.22 (360)
4	-	1.6	1.63 ± 0.02	$1.05\,^{+0.05}_{-0.06}$	$15.6\,^{+1.4}_{-1.1}$	$1.65\,^{+0.12}_{-0.14}$	5.4 ± 0.5	5.4 ± 0.5	2.4 ± 0.5	6.3 ± 0.1	-2.8 ± 0.2	8 ± 1.2	$3.3\,^{+4.5}_{-1.2}$	$0.13\,^{+0.10}_{-0.18}$	1.29 (362)
5	-	3.7	$1.68\pm^{0.02}_{0.01}$	$0.72\,^{+0.04}_{-0.05}$	$23.5\,^{+2.8}_{-2.0}$	$1.10\,^{+0.12}_{-0.16}$	$8.5\,^{+1.5}_{-0.7}$	$8.5\,^{+1.5}_{-0.7}$	$8.3\,^{+0.3}_{-0.4}$	6.3 ± 0.1	-2.8 ± 0.3	2 ± 0.5	2.7 ± 0.2	$0.45\,^{+0.16}_{-0.17}$	1.07 (360)
6	-	7.4	(1.67)	0.67 ± 0.06	$30.3\,^{+4.9}_{-3.8}$	1.1 ± 0.1	$14.9\,^{+4.9}_{-3.8}$	$14.9\,^{+4.9}_{-3.8}$	$6.0\,^{+0.2}_{-0.3}$	7.2 ± 0.3	-2.6 ± 0.4	$7\,^{+1.5}_{-1.6}$	$2.9\,^{+0.3}_{-0.2}$	$0.40\,^{+0.10}_{-0.11}$	1.26 (363)
7	-	1.2	(1.67)	$0.31\,^{+0.07}_{-0.05}$	$28.9\,^{+11.9}_{-7.0}$	$0.61\,^{+0.04}_{-0.03}$	$13.1\,^{+0.2}_{-0.9}$	$25.6\,^{+21.8}_{-6.4}$	$2.0\,^{+0.5}_{-0.8}$	6.5 ± 0.1	-2.2 ± 0.4	1 ± 0.1	$42\,^{+36}_{-10}$	$1.15\,^{+0.03}_{-0.02}$	1.21 (382)
8	P0	0.70	(1.67)	0.27 ± 0.02	$35.9\,^{+4.6}_{-3.7}$	$0.52\,^{+0.01}_{-0.01}$	13.7 ± 0.1	$21.5\,^{+8.4}_{-3.9}$	$2.3\,^{+0.3}_{-0.5}$	6.2 ± 0.1	-2.8 ± 0.3	0.35 ± 0.04	$41\,^{+16}_{-7}$	1.13 ± 0.01	1.08 (363)
8	P1	0.86	(1.67)	0.31 ± 0.02	$45.7\,^{+4.3}_{-3.4}$	0.59 ± 0.02	$12.1\,^{+0.7}_{-0.04}$	$15.6\,^{+4.0}_{-2.3}$	$2.8\,^{+0.3}_{-0.4}$	6.2 ± 0.1	$-3.0\,^{+0.3}_{-0.4}$	0.6 ± 0.08	$27\,^{+7}_{-4}$	1.08 ± 0.02	1.03 (364)

[a] Details are the same as in table 5.1.

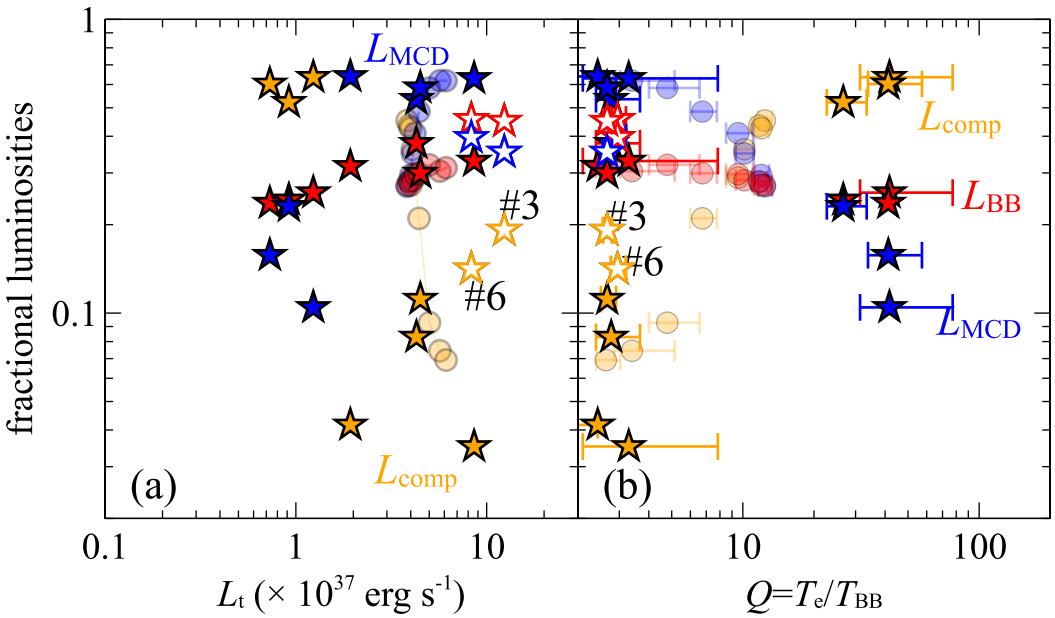

Figure 5.23: The same as figure 5.13, but for 4U 1705-44. The data for #3 and #6 are indicated with open stars. The data points of Aql X-1 are overlaid with filled thin circles.

5.3 Summary of the Data Analysis

Figure 5.24 shows a behavior of the three temperatures, τ, $R_{\rm in}$, and $R_{\rm BB}$, as a function of Q. As confirmed in §5.1.3, all the sources line up approximately on the same lines in panel (a), over even a wider range of $Q = 3 - 100$ (Of course, this result on $T_{\rm e}$ is partly trivial, because $Q = T_{\rm e}/T_{\rm BB}$ is by definition not independent of $T_{\rm e}$, and $T_{\rm BB}$ varies over a much narrower range than $T_{\rm e}$.). Thanks to the Hard-State spectra of 4U 1636-536, 4U 1608-52, and 4U 1705-44, the behavior of τ has become clearer than in §5.1.3, that τ monotonically decreases down to $\lesssim 1$, by an order of magnitude, as Q increases from ~ 3 to ~ 100. The luminosity between $Q \sim 3$ and $Q \sim 100$ are different by typically $\lesssim 2$ orders of magnitude, implying that the decrease of τ is caused partly by decreasing accretion rate, but also by other factors, such as the coronal geometry, or its dynamics (Sakurai et al. 2012; 2014). We duscuss this issue in §6.5.

In contrast to panel (a) and (b), the radii in panel (c) and (d) are not expressed as a single-valued function of Q. At a given value of Q, the two radii both scatter by up to a factor of 4, which is significant even considering the distance uncertainty. This difference is most prominent between the locus formed by Aql X-1 and that by 4U 1608-52. As already noticed in §5.2.2, this is thought to be a manifestation of residual hysteresis: as shown in

"arrow 2" in panels (c) and (d). Aql X-1 brightened from the Hard to Soft States, whereas 4U 1608-52 evolved in the opposite direction. The behavior of 4U 1636-53 and 4U 1728-34 may be similar to that of 4U 1608-52, if considering $\sim 30\%$ uncertainty of radii due to a combination of the distance and the inclination. To further confirm the suggested hysteresis effect, the data points of Aql X-1 in a decaying phase taken from Sakurai (2015) are shown. As expected, the evolution is quite similar to other data in a decaying phase, moving along the arrow 2. The sources are expected to evolve along the arrow 3 from the end of the decaying phase to the beginning of the rising phase.

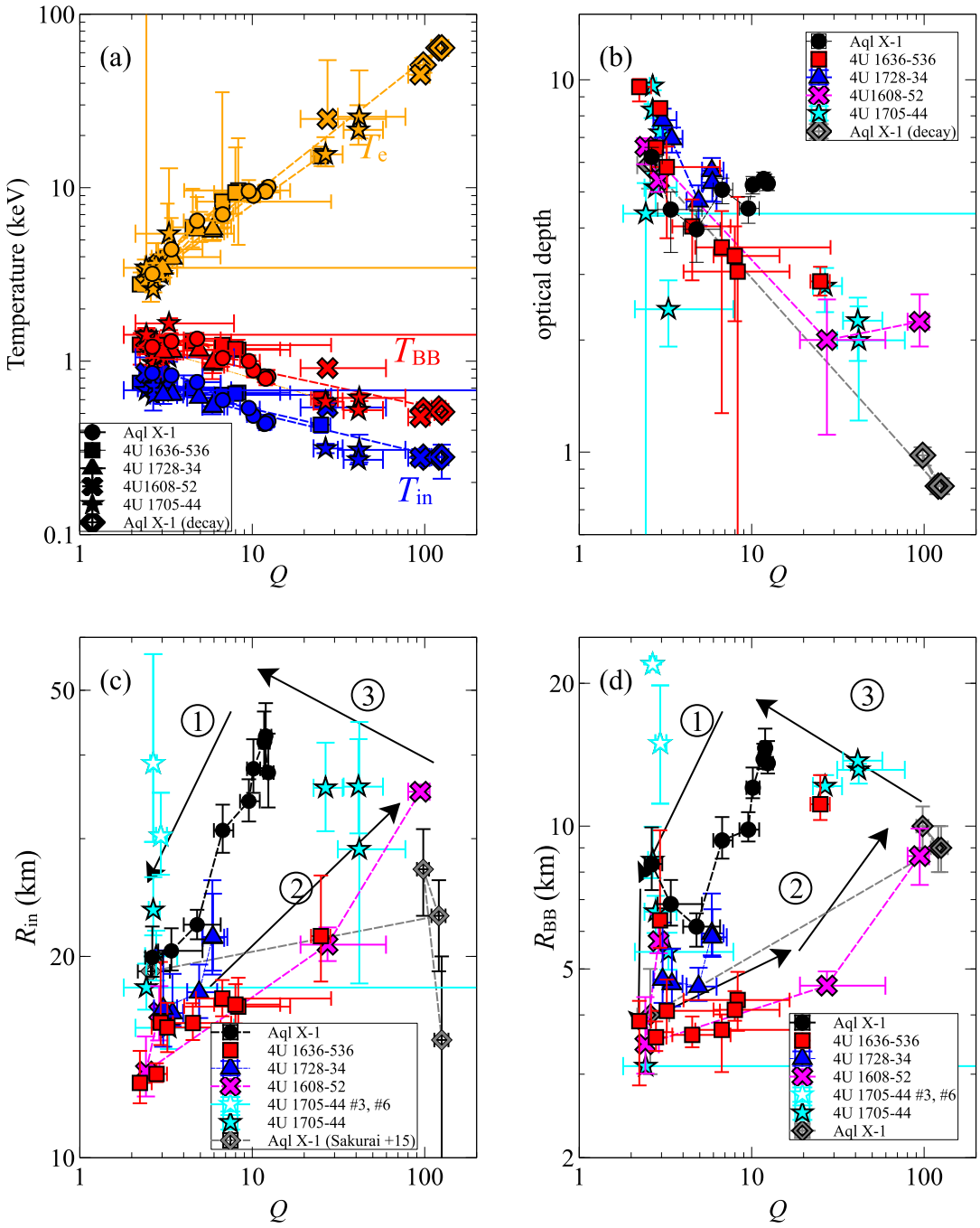

Figure 5.24: The temperatures (panel a), τ (panel b), $R_{\rm in}$ (panel c), and $R_{\rm BB}$ (panel d) of all data sets analyzed here, all presented as a function of Q. *Suzaku* results obtained from Aql X-1 in decaying phase of an outburst (Sakurai et al. 2014) are also added. In panel (a), $T_{\rm e}$, $T_{\rm BB}$, and $T_{\rm in}$ are shown with orange, red, and blue, respectively. The arrows 1 through 3 indicate the loci of LMXBs along their luminosity change.

Chapter 6

Discussion

6.1 Summary

In Chapter 5, we have analyzed 19 data sets of 5 LMXBs, using the unified spectral model proposed by Sakurai et al. (2012; 2014) which incorporates the MCD and Comptonized blackbody components. Compared with another canonical model comprising blackbody plus Comptonized MCD (White et al. 1988) which often gives inappropriate parameter values as $R_{\rm in} \ll R_{\rm NS}$ (Sakurai 2015) or unacceptable fit (Sakurai et al. 2012), our unified model with 19 data sets gave successful fit with physically reasonable values. In addition to Aql X-1 which showed the clear transition from the Hard State to the Soft State, the data sets of 4U 1636-536 #2 and 4U 1728-34 showed, in terms of Q, similar variations that are seen near the transition threshold, although they did not actually go through transitions. Out of the remaining 16 observations, 11 were in the typical Soft State, and 5 in the typical Hard State. We have thus confirmed that the spectral bimodality (§2.3.1) is a basic property that is common to LMXBs, including both persistent and transient ones. Furthermore, regardless of the spectral state, all spectra of all the sources have successfully been reproduced with the unified model. This answers affirmatively to the question (A-i) raised in §4.1.1.

Figure 6.1 (a) shows behavior of the three constituent luminosities calculated from eq. (5.2), (5.5), and (5.4) using the obtained model flux, all normalized by $L_{\rm t}$, as a function of $L_{\rm t}$. There, Aql X-1, 4U 1636-536 #2, and 4U 1728-34, selected by the criterion (1), change sensitively, and yet continuously, over a respective narrow range of total luminosity $L_{\rm t}$. This is best exemplified by Aql X-1, of which $L_{\rm comp}/L_{\rm t}$ varies by a factor of ~ 4 for only $\sim 5\%$ change of $L_{\rm t}$. Such strong dependence on $L_{\rm t}$ is also suggested by the data with the criterion (2), as large differences between the data points in the Hard State which are seen below $L_{\rm t} \sim 1.3 \times 10^{37}$ erg s^{-1}, and those in the Soft State above it. On the other hand, when an object is either in the Hard State or the Soft state, its luminosity allotment into the three components is rather stable without strong dependence on $L_{\rm t}$. This behavior provides the best evidence for the bimodal nature of the accretion flow (§2.3.1), that it tends to stay either in the optically thick thermal state represented by dominant $L_{\rm MCD}$, or optically thin and hot state represented by dominant $L_{\rm comp}$. However, as pointed out repeatedly in Chapter 5,

the threshold value in $L_{\rm t}$ between the two States differ by more than a factor of ~ 5 among the sources: this is due to distance and inclination uncertainties, as well as the hysteresis effects (§2.4.4) which generally make the Hard-to-Soft threshold higher than that for the Soft-to-Hard threshold.

As explained in §5.1.1, we introduced the new parameter $Q \equiv T_{\rm e}/T_{\rm BB}$ (eq. 5.6). Although Q itself of course depends on $L_{\rm t}$ as shown in figure 6.2, the large source-to-source threshold difference seen there (due to hysteresis, as well as distance and inclination uncertainties) is removed by using Q, instead of $L_{\rm t}$, as the control parameter. To see this, in figure 6.1 (b, c) we present the same data of $L_{\rm MCD}$ and $L_{\rm comp}$ as in panel (a), but as a function of Q. As already described in Chapter 5 when we analyze the data, different sources (except several data sets) now line up much better on the same loci. Therefore, Q can be regarded as a convenient variable characterizing the state transition phenomena. Specifically, we can regard the Soft State as $1 < Q \lesssim 6$, and the Hard State as $Q \gtrsim 8$. The former may be considered as "optically thick and cool" Comptonization, and the latter as "optically thin and hot" Comptonization. Incidentally, to calculate Q we need high sensitivity both in the hard X-ray range (to determine $T_{\rm e}$) and the soft energy band (to estimate $T_{\rm BB}$); this broad-band capability has been achieved for the first time with *Suzaku* (§3.3, §3.4).

In figure 6.1 (b) and (c), $L_{\rm comp}$ and $L_{\rm MCD}$ on a closer look still show two different loci as already touched on in §5.2.2. The most outstanding outlier is 4U 1608-52 (observed in an outburst decay), of which the data points are systematically offset toward larger values of Q. This large offset cannot be attributed to distance or inclination uncertainties. A hint of such an offset is found with 4U 1636-536 #2 as well, an observation which was conducted when the luminosity was decreasing. Furthermore, the difference is also found with Aql X-1 itself, between the data we analyzed (in the rising phase of an outburst), and another set of *Suzaku* data, acquired during a decay phase of another outburst and already analyzed extensively by Sakurai et al. (2014) and Sakurai (2015). As shown in figure 6.1 (b) and (c) with cyan-outlined symbols, this offset toward higher Q is seen predominantly among those data sets which were obtained in a luminosity-decreasing phase. Therefore, we infer that the transition hysteresis still remains, even using Q instead of $L_{\rm t}$. This systematic difference between rising and declining phases is discussed in §6.5 in terms of coronal accretion flow. Finally, again in figure 6.1 (a), $L_{\rm BB}/L_{\rm t}$ shows a unique behavior that it varies by only $\sim 20\%$. These issues are further discussed in §6.3. In the following section, let us examine the behavior of individual model components.

6.2 Disk Component

Over a wide range of luminosity from $\sim 10^{36}$ erg s^{-1} to $\sim 10^{38}$ erg s^{-1} covered by the 19 data sets, the softer end of the spectrum at $\lesssim 3$ keV have successfully been reproduced with the `diskbb` model, which represents an MCD emission. The inner disk temperature, typically $T_{\rm in} \lesssim 1$ keV, is comfortably lower than the Eddington temperature (~ 2.3 keV) for an NS of 1.4 $M_\odot$. The inner disk radius satisfies $R_{\rm in} > 12$ km, typically around $R_{\rm in} \lesssim 20$ km in the

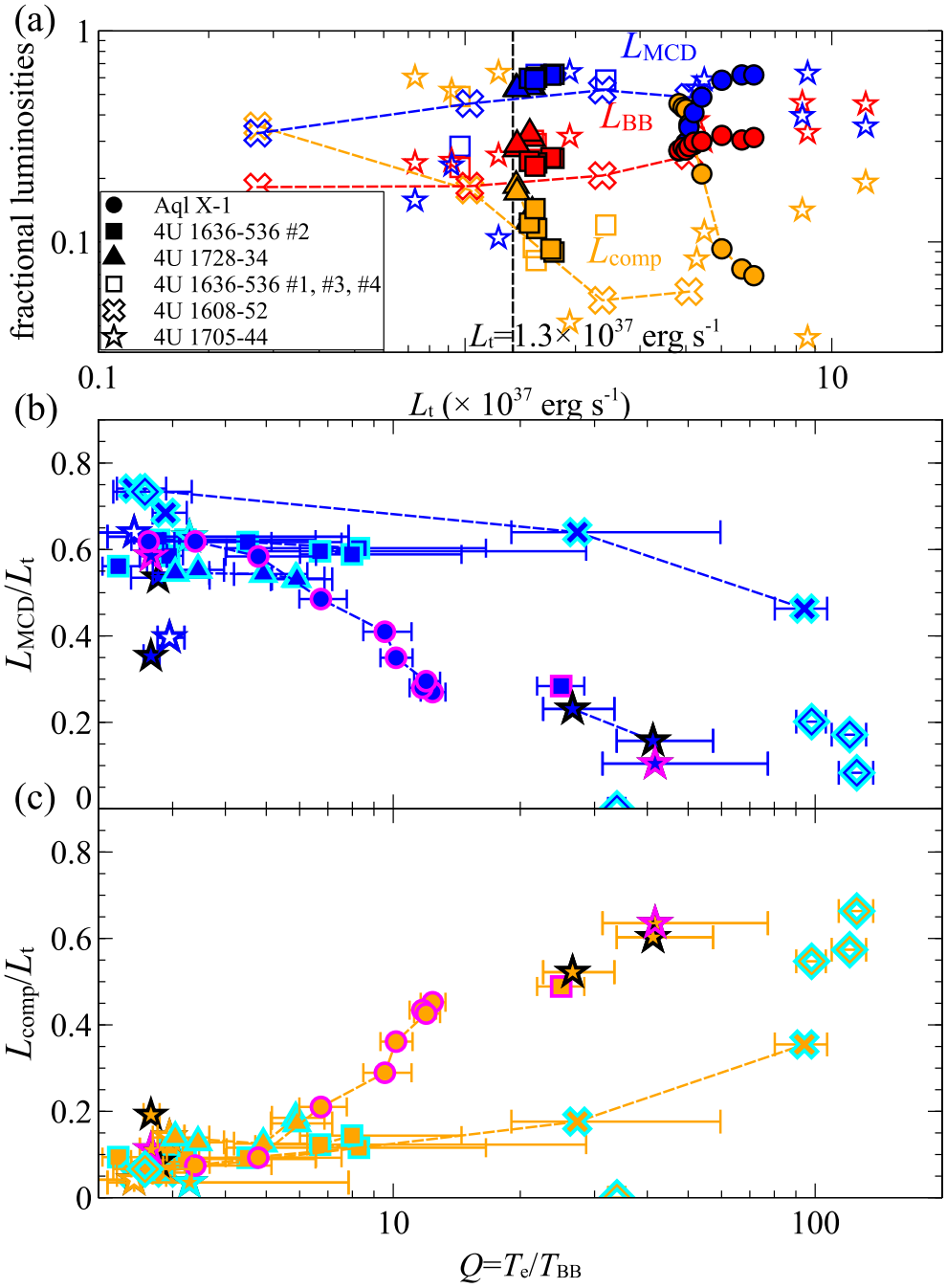

Figure 6.1: The three fractional luminosities of all the spectra, shown as a function of (a) L_t and (b) Q. In panel (a), data points from the criterion (2) are plotted with open symbols. In panel (b) and (c), data during luminosity decrease and rising are outlined in cyan, and magenta, respectively.

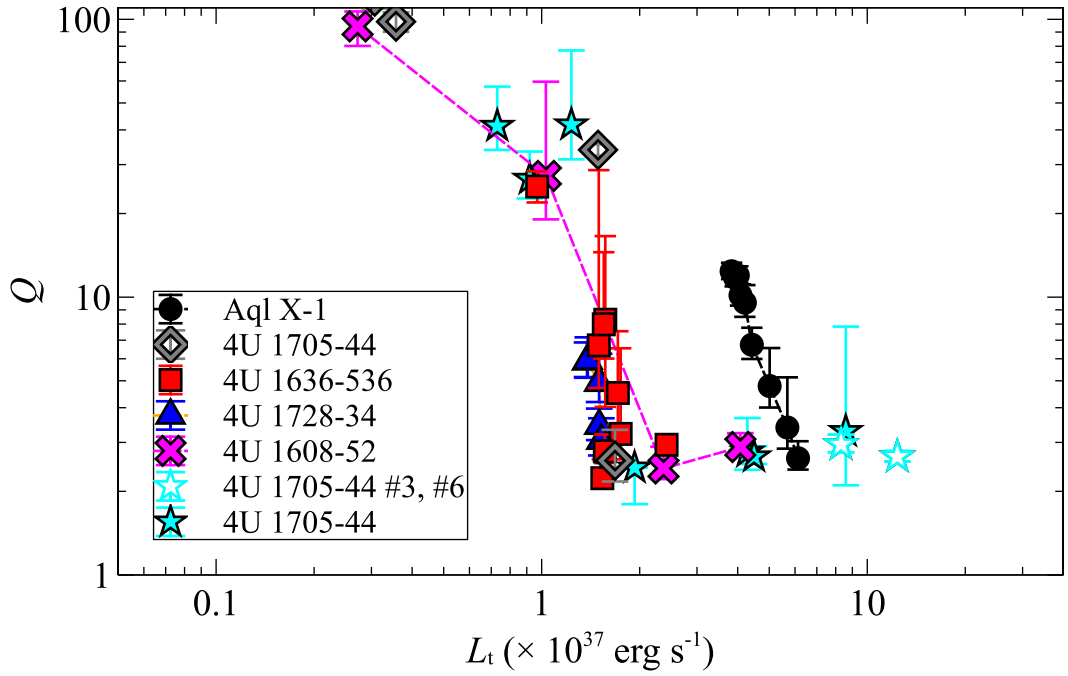

Figure 6.2: The behavior of Q of the sample LMXBs, shown as a function of L_t.

Soft State, when the inclination is tentatively assumed as $i = 45°$.

Before further discussing the behavior of the obtained `diskbb` parameters, let us examine if they satisfy the condition of a standard accretion disk (under the MCD approximation: §2.3.2, §2.3.3). From eq. (2.15), the disk luminosity L_{MCD} can be expressed with R_{in} and T_{in}. Since a standard disk should satisfy Virial theorem, it should also be expressed with R_{in} and L_t as in eq. (2.18). Equating these two equations, we obtain

$$L_t = \frac{8\pi\sigma_{SB}}{R_{NS}} \times R_{in}^3 T_{in}^4 \tag{6.1}$$

where $R_{in}^3 T_{in}^4$ represents the mass accretion rate through the disk. To examine this important property, figure 6.3 compiles the `diskbb` parameters obtained from all the spectra, on the plane of R_{in} vs $T_{in} L_t^{-1/4}$. The data points indeed line up with the prediction of eq. (6.1). On a closer look, we find that Aql X-1 and 4U 1705-44 show some systematic difference from eq. (6.1). This can arise from an overestimation of R_{in} by 10%, or an underestimation of L_t due to distance uncertainties, or energy escape into some channels other than radiation (e.g., outflows). A combination of the first two would provide the most likely explanation to the subtle difference. Thus, we have successfully confirmed that the accretion disks in the present objects can be regarded as in the standard-disk condition, not only in the Soft State, but also in the Hard State when the disk must be under strong irradiation by the Comptonized hard X-rays.

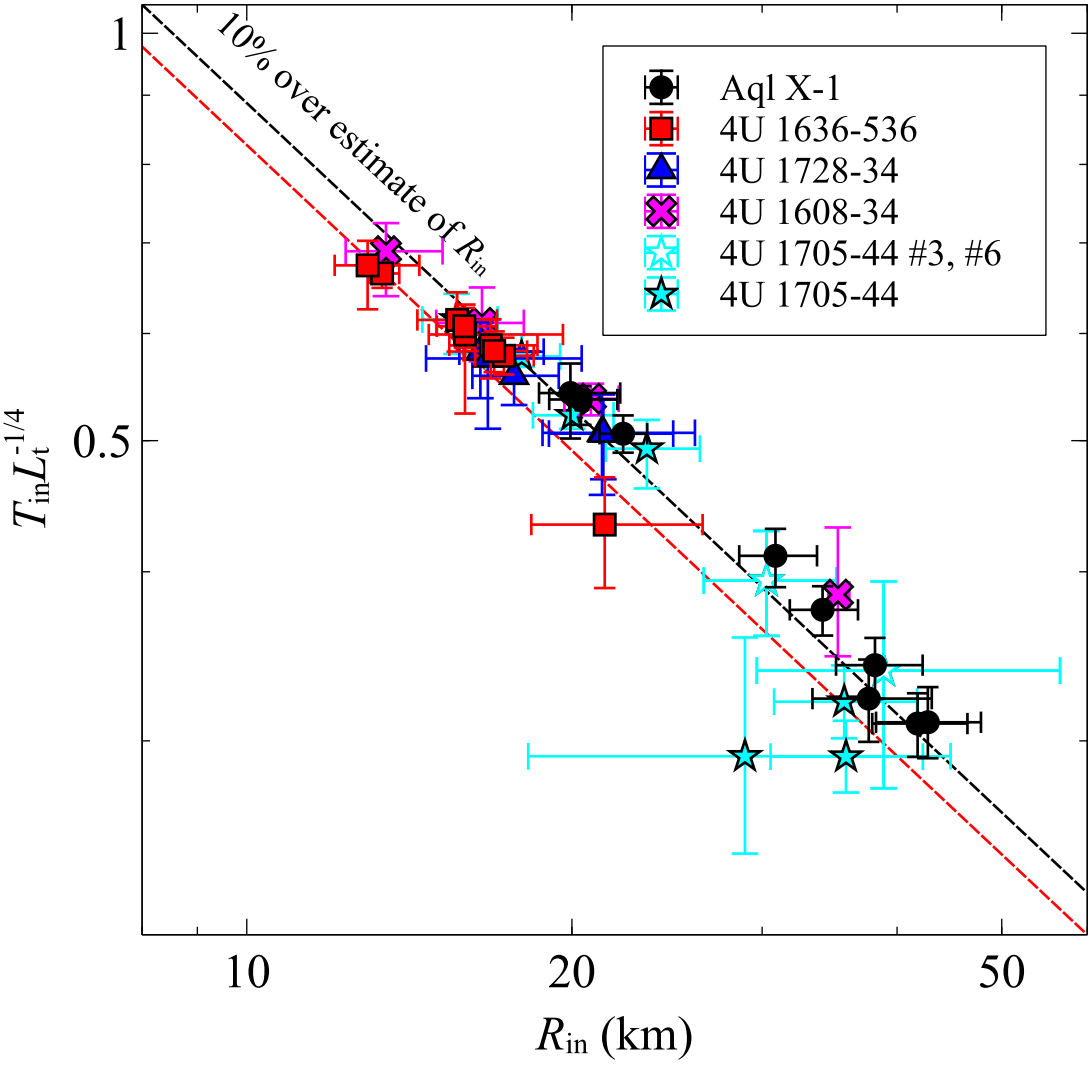

Figure 6.3: A scatterplot between $T_{\rm in}L_t^{-1/4}$ and $R_{\rm in}$. Red dashed line is a theoretical line representing eq. (6.1). The black dashed line is the same, but when $R_{\rm in}$ is over estimated by 10%, or when the radiation efficiency is reduced to 68% instead of 100%.

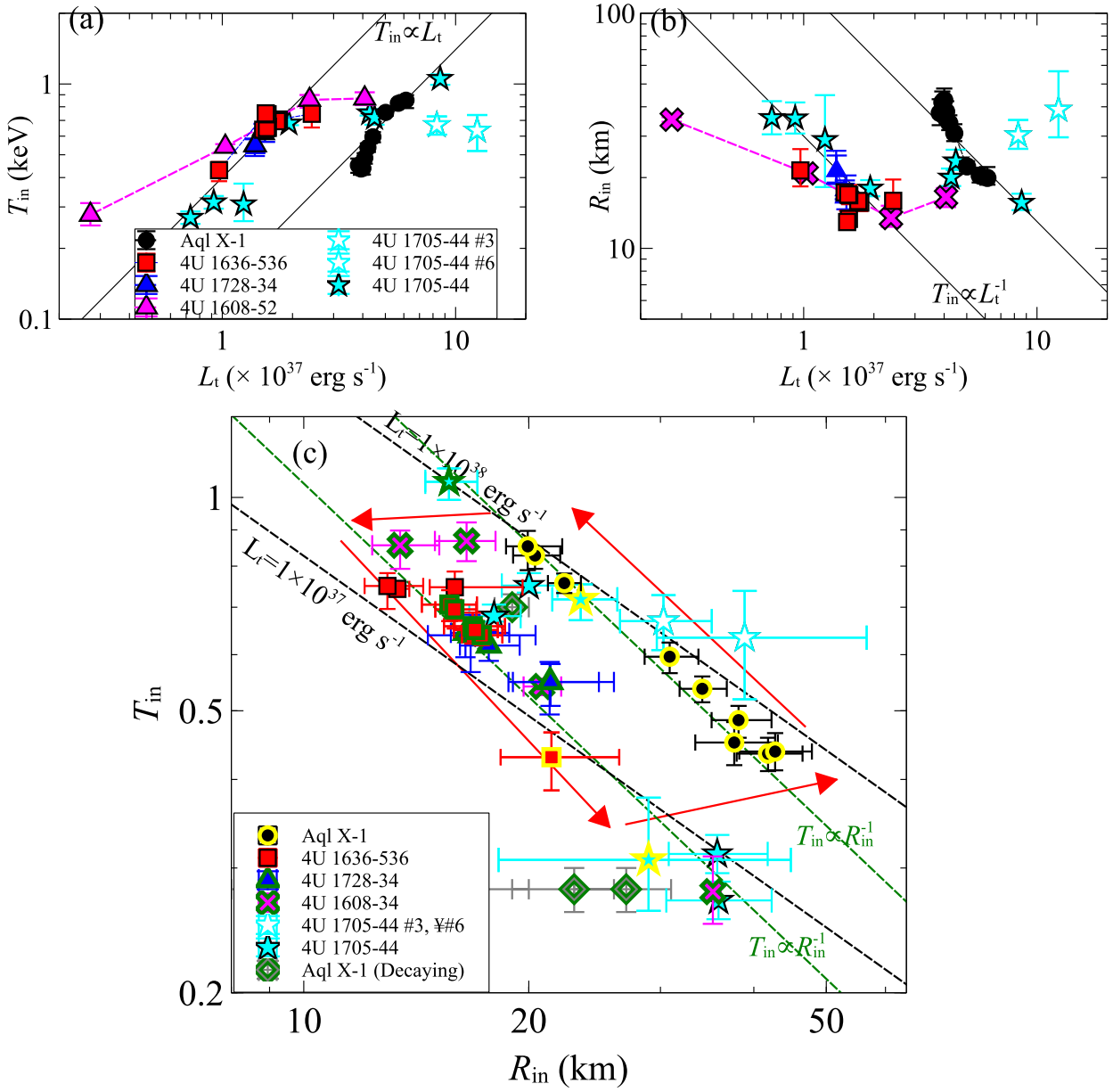

Figure 6.4: A scatter plot of $T_{\rm BB}$ against (a) $T_{\rm in}$, and (b) $R_{\rm in}$. Results from all the spectra are compiled. (c) The relation between $T_{\rm in}$ and $R_{\rm in}$, obtained by combining panel (a) and (b). The data acquired during a luminosity decreasing are outlined in green, and those during a luminosity increasing in yellow.

Figure 6.4 (a) and (b) respectively show $T_{\rm in}$ and $R_{\rm in}$, obtained from all the data, both as a function of $L_{\rm t}$. As $L_{\rm t}$ and hence the accretion rate increases, $T_{\rm in}$ increases as easily expected from eq. (6.1). In addition, figure 6.4 (a) and (b) both reveal data splitting into two subgroups, one encompassing 4U 1636-52 and 4U 1728-34, and the other the rising phase of Aql X-1. This is again likely to results from the hysteresis, because the former showed decreasing $L_{\rm t}$ during the *Suzaku* observations, while Aql X-1 was in the rising phase.

Putting aside the systematic differences between the two data groups, and focusing on individual sources, we find an approximate scaling as $L_{\rm t} \propto T_{\rm in}$. Since we expect from eq. (6.1) a relatin $L_{\rm t} \propto R_{\rm in}^3 T_{\rm in}^4$, the obesrved scaling suggests that $R_{\rm in}$ depends negatively on $L_{\rm t}$. Indeed, in figure 6.4 (b), $R_{\rm in}$ of each source decreases approximately as $R_{\rm in} \propto L_{\rm t}^{-1}$ when $L_{\rm t}$ increases. This agrees qualitatively with the previous results obtained in Sakurai et al. (2012; 2014), Zhang et al. (2016), and Ono et al. (2016), that the disk approaches the NS surface toward the Soft State.

Combining figure 6.4 (a) and (b), a scatter plot between $T_{\rm in}$ and $R_{\rm in}$ has been produced in panel (c). Interestingly, the data that were split into two subgroups in panel (a) and (b) now form a common elongated loop, evolving counter-clockwise as indicated by red arrows. The long sides of the loop are defined by the data during or near the transition, and have a slope of $T_{\rm in} \propto R_{\rm in}^{-1}$ which results from the scaling in panel (a), $T_{\rm in} \propto L_{\rm t}$, and that in (b), $R_{\rm in} \propto L_{\rm t}^{-1}$.

6.3 Blackbody Component

6.3.1 Hysteresis loop

The counter-clockwise hysteresis loop, suggested by figure 6.4 (c), has bcome much clearer in figure 6.5, where all the data are summarized on a $R_{\rm BB}$ vs. $T_{\rm BB}$ plane. In this figure, an LMXB is considered to move along the following sequence.

- The source starts from a dim Hard State "H1", where $R_{\rm BB}$ is somewhat smaller than $R_{\rm NS}$ ($\simeq 12$ km).
- As $\dot{M}$ increases, the source moves to "H3", a luminous Hard State, through "H2"; $T_{\rm in}$ increase from eq. (6.1), and $R_{\rm BB}$ saturates at $R_{\rm NS}$ because the accretion flow is more inflated due to increased thermal pressure, and accretes onto nearly whole the NS surface.
- Then, the source quickly goes through transition "T", and reaches the brightest Soft State "S1". Meantime, $L_{\rm comp}/L_{\rm t}$ decreases rapidly to $\ll 0.1$. At "S1", the matter accretes mainly onto equatorial zones of the NS making $R_{\rm BB}$ even smaller.
- When $\dot{M}$ starts to decline past the outburst peak, both $R_{\rm in}$ and $R_{\rm BB}$ further shrink until "S2".

- As $\dot{M}$ continues to decrease, $T_{\rm in}$ starts to get smaller while $R_{\rm in}$ increases, till the source reaches the dimmest Soft State "S3".
- Finally, the source makes a Soft to Hard transition to return to "H1", even though this transition episodes were not found among our present sample.

As demonstrated in figure 6.5 (a) and (b), the relation between $R_{\rm in}$ and $R_{\rm BB}$ is approximately single-valued; so is the $T_{\rm in}$ vs. $T_{\rm BB}$ correspondence. These imply that the loop in figure 6.5 is roughly synchronized with the loop on the $T_{\rm in}$ vs $R_{\rm in}$ plane in figure 6.4 (c). Thus, the question (C) has been answered in figure 6.5.

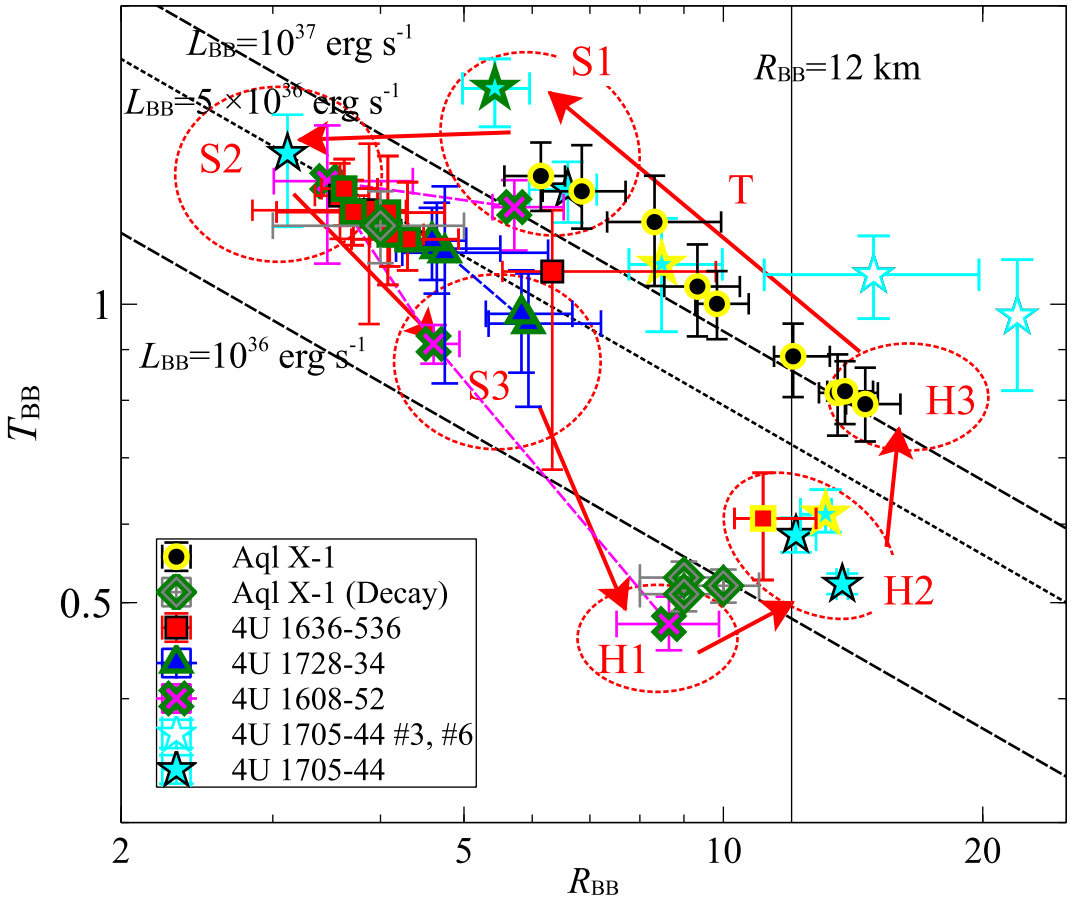

Figure 6.5: A unified hysteresis loop on the $R_{\rm BB}$ vs. $T_{\rm BB}$ plane, drawn by all the data analyzed in the present thesis. The Aql X-1 results in the declining phase (Sakurai et al. 2014) are also included. The constant $L_{\rm MCD}$ loci, defined by eq. (2.15), are indicated by three dashed lines. See text for the meanings of H1, H2, H3, T, S1, S2, and S3, as well as those of the arrows.

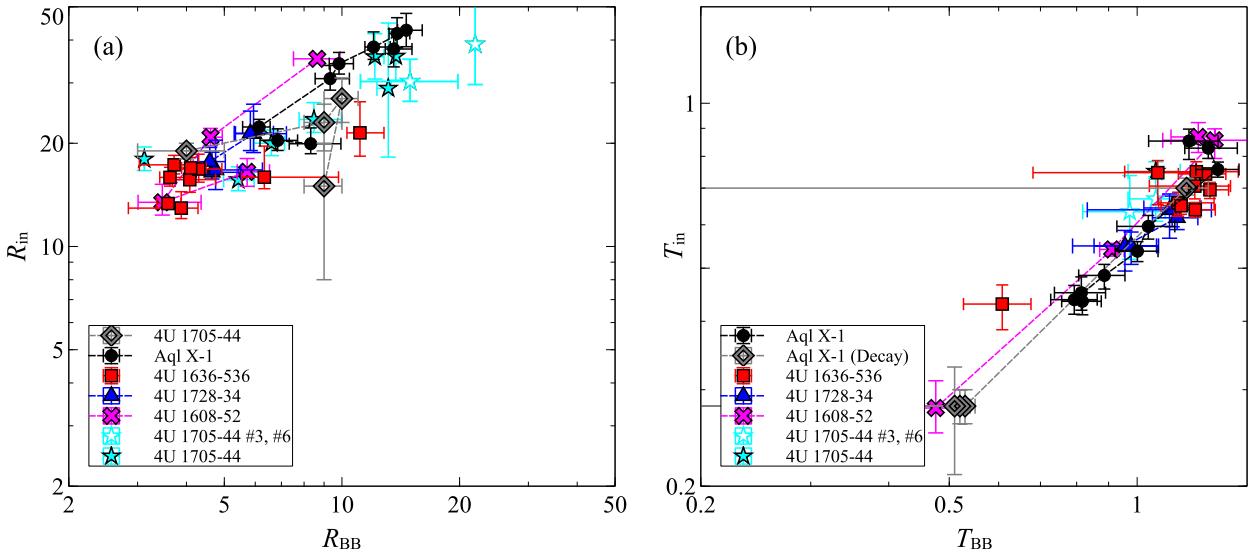

Figure 6.6: (a) The correlation between $R_{\rm in}$ and $R_{\rm BB}$. (b) That between $T_{\rm in}$ and $T_{\rm BB}$.

6.3.2 Interpretation of the blackbody luminosity $L_{\rm BB}$

In this section, let us examine the behavior of $L_{\rm BB}$ and its absolute values. As already explained and confirmed in §6.2, the accreting gas releases half the gravitational energy through the MCD emission by the time it reaches $R_{\rm in}$. Thus, the remaining energy available for the blackbody and the Comptonization process is expressed as

$$\frac{L_{\rm BB}+L_{\rm comp}}{L_{\rm t}} = 1-\frac{R_{\rm NS}}{2R_{\rm in}}. \tag{6.2}$$

Assuming that a fraction α $(0<\alpha<1)$ of this remainder goes to the Comptonization, $L_{\rm BB}$ and $L_{\rm comp}$ can be expressed as

$$\frac{L_{\rm BB}}{L_{\rm t}} = (1-\alpha)\times\left(1-\frac{R_{\rm NS}}{2R_{\rm in}}\right), \tag{6.3}$$

$$\frac{L_{\rm comp}}{L_{\rm t}} = \alpha\times\left(1-\frac{R_{\rm NS}}{2R_{\rm in}}\right). \tag{6.4}$$

In figure 6.7, the observed values of $L_{\rm BB}/L_{\rm t}$ are plotted as a function of $R_{\rm in}$ where a weak dependence of $L_{\rm BB}$ on $R_{\rm in}$ is observed towards smaller $R_{\rm in}$. Less and less energy is allotted to the Comptonization, from $\alpha\sim0.7$ to $\alpha\lesssim0.5$. This agrees qualitatively with the behavior seen in figure 6.1 (b), that $L_{\rm comp}/L_{\rm t}$ decreases significantly while $L_{\rm BB}/L_{\rm t}$ slightly increases towards the Soft State (with decreasing $R_{\rm in}$).

In addition to the relative changes of $L_{\rm BB}/L_{\rm t}$, we may further examine its absolute values. If $\alpha=0$ and $R_{\rm in}=R_{\rm NS}$ in the Soft State, eq. (6.3) demands $L_{\rm BB}/L_{\rm t}=0.5$. In

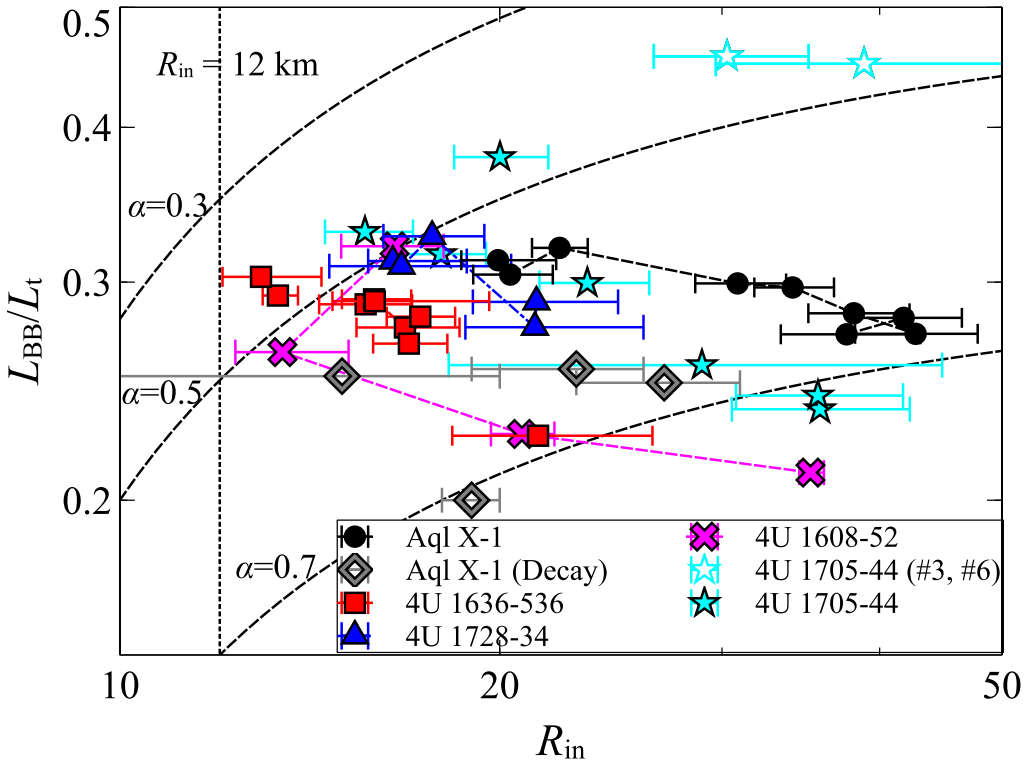

Figure 6.7: The behavior of the fraction L_{BB}/L_t as a function of R_{in}. The three curves represent the predicted energy share by L_{BB}, as calculated by eq. (6.3).

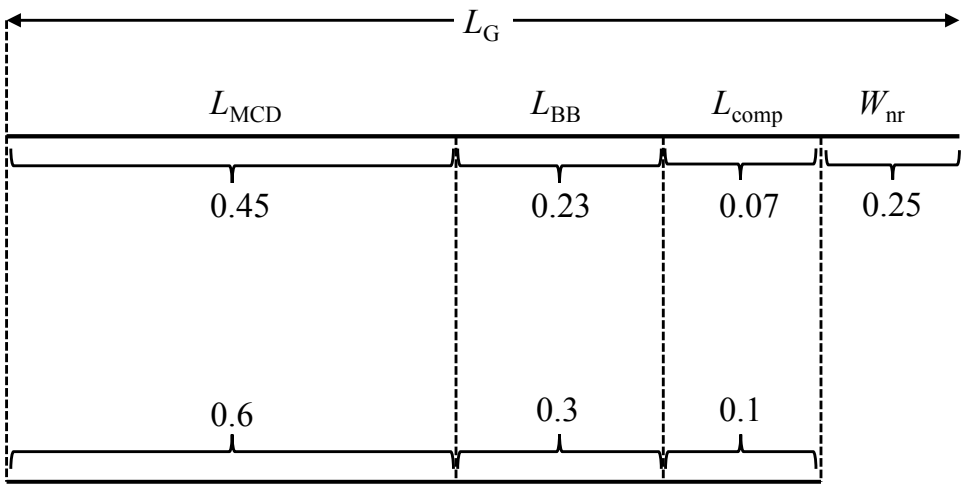

Figure 6.8: Relations of the actual luminosities and the observed ones.

addition, taking into account the effects of general relativity on the gravitational potential, $L_{\rm BB}/L_{\rm t} \sim 0.7$ is predicted (Syunyaev & Shakura 1986). In reality, we further need to consider effects of the NS spin, since the spin in LMXBs is fast in many cases, as exemplified by $f = 550.27$ Hz of Aql X-1 (Casella et al. 2008), $f = 581$ Hz of 4U 1636-536 (Zhang et al. 1997; Strohmayer & Markwardt 2002), and $f = 363$ Hz of 4U 1728-34. Such a fast spin requires two corrections on $L_{\rm BB}/L_{\rm t}$. One is a Newtonian decrease of $L_{\rm BB}$, because the accreted gas still rotates moderately fast together with the spinning NS, and hence some portion of the rotational energy is retained rather than radiated. The other is a general relativistic correction on the gravitational potential due to space-time dragging. Incorporating such effects of the NS spin, $L_{\rm BB}/L_{\rm t} \sim 0.5$ is finally predicted for an assumed spin of $f = 500$ Hz (Gilfanov & Sunyaev 2014).

Compared with this prediction of $L_{\rm BB}/L_{\rm t} \sim 0.5$, $L_{\rm BB}/L_{\rm t}$ has been observed to be rather small as $\lesssim 0.5$ (figure 6.7). This could be most easily attributed to the inclination uncertainty of the disk. However, this is not realistic for the following three reasons. First, the correction factor for $L_{\rm MCD}$ is in fact only $1/\cos 45^\circ \sim 1.4$; therefore, even assumig a face on geometry as $i = 0$ for 4U 1636-536 for example, $L_{\rm BB}/L_{\rm t}$ would not exceed even 0.4. Second, the systematically small $L_{\rm BB}/L_{\rm t}$ is observed from all the sources; inclination errors would average out. Third, if assuming $i = 0$, $R_{\rm in}$ of 4U 1636-536 and 4U 1608-536 would become too small compared with $R_{\rm NS}$.

An alternative explanation to the above problem is that still some energy (e.g., $\alpha \sim 0.3$ in figure 6.7) is released into Comptonization even at the full Soft State. This may be partly true, because most data points in the Soft State in figure 6.1 show $L_{\rm comp}/(L_{\rm BB}+L_{\rm comp}) \sim 0.15$ rather than ~ 0. In other words, $L_{\rm BB}$ calculated via eq. (5.5) is slightly lower than $L_{\texttt{nthcomp}}$ derived from the fitted `nthcomp` model, because the effective temperature $T_{\rm BB}$ is somewhat lower than the color temperature of the Comptonized blackbody.

Yet another interesting possibility is that the missing $\sim 20\%$ of $L_{\rm t}$, typically $\lesssim 10^{36}$ erg s^{-1} in the Soft State, goes to non-radiative forms, such as work to spin up the NS. Such possibility was in fact considered by Sakurai (2015), who concluded that an initially slow-rotating NS can be spun up to ~ 700 Hz in about 1/10 of the Hubble time, if $\sim 10^{36}$ erg s^{-1} out of the accretion energy is spent in this mechanical work. This scenario is consistent with the ubiquity of fast-spinning LMXBs. In summary, we conclude that the small deficit of $L_{\rm BB}/L_{\rm t}$ is real, and can be explained by the remaining low-level Comptonization and the work to accelerate the NS rotation.

The discussion so far made in this subsection can be clearer by introducing the work $W_{\rm su}$ to spin up the NS, and the total gravitational energy release as

$$L_{\rm G} = L_{\rm t} + W_{\rm su} = L_{\rm MCD} + [L_{\rm BB} + L_{\rm comp} + W_{\rm su}] \,. \tag{6.5}$$

Here, $L_{\rm MCD}$ and the term in square brackets are expected, from Virial theorem, to be approximately equal, both carrying $\sim 50\%$ of $L_{\rm G}$ (not $L_{\rm t}$). Then, the various luminosities are related to one anther as illustrated in figure 6.8. If, for example, $W_{\rm su}$ is about 17% of $L_{\rm G}$, the fractional luminosities are calculated as $L_{\rm MCD}/L_{\rm t} \sim 0.60$, $L_{\rm BB}/L_{\rm t} \sim 0.30$, and $L_{\rm comp}/L_{\rm t} \sim 0.10$, which agree very well with the observations in figure 6.1(b) at $Q \to 0$. Fur-

thermore, the intrinsic value of α which incorporates $W_{\rm su}$ becomes ~ 0.5, and is consistent with figure 6.7.

6.4 Comptonized Component

Finally, let us examine the Comptonized component, which plays an important role in the spectral state evolution. The Comptonization is one of the most complex and difficult phenomena to understand in LMXBs, because it involves three different temperatures; the ion temperature $T_{\rm i}$ of the Comptonizing corona, the electron temperature $T_{\rm e}$ of the corona, and the seed-photon temperature which we identify with $T_{\rm BB}$. As explained in §5.1.1, $T_{\rm e}$ is thought to be determined through a balance between the Coulomb heating by the ions and Compton cooling by the seed photons, both working on the coronal electrons. Furthermore, $T_{\rm i}$, which is realized by viscous heating and also possibly by a shock, cannot be measured with X-ray spectroscopy, so that important information of the Comptonizing process, including in particular the geometry, dynamics, and density of the corona, can be obtained only through $T_{\rm e}$, τ, and the blackbody parameters. In this subsection, let us grasp the nature of the corona through examinations of the `nthcomp` or `compPS` parameters in rather phenomenological ways.

Figure 6.9 (a) reproduces (originally in figure 5.24) the temperatures relevant to the Comptonization, as a function of Q which has been introduced in eq. (5.6) as a quantity to express the balance between the heating and cooling of the coronal electrons. In panel (a), $T_{\rm e}$ and $T_{\rm BB}$ both form a single locus as a function of Q, although these results are partially trivial because neither $T_{\rm e}$ nor $T_{\rm BB}$ is independent of Q. In panel (b), τ is plotted as a function of Q, where all the data points are approximately aligned on a single locus, with Aql X-1 possibly showing somewhat different evolution. Thus, Q is considered to be an appropriate quantity to describe the physical state of the corona, including its heating and cooling processes.

In figure 6.10, the y parameter in eq. (2.22) is shown as a function of Q. As explained in §2.3.4, y is a good indicator of the Comptonization strength, and is obtained combining $T_{\rm e}$ in figure 6.9 (a) and τ in (b). The figure reveals several interesting properties. First, at $Q \gtrsim 8$ (i.e., the Hard State), the values of y are distributed over a narrow range of $y = 0.4-1.3$, even though $T_{\rm e}$ and τ both scatter by more than an order of magnitude (figure 6.10). Therefore, the corona is inferred to adjust by itself, so that $T_{\rm e}$ and τ are negatively correlated to realize $y \sim 1$. Secondly, at $Q \lesssim 6$ (i.e., the Soft State), the y-parameter systematically decreases toward $y \sim 0$. This is however rather trivial, because $Q \to 1$ means $T_{\rm e} \to T_{\rm BB}$ and hence $y \to 0$ via (2.22). Finally, all data points rather well line up on a single locus on the (Q, y) plane, including the rise and decline phases of Aql X-1. In other words, the hysteresis effects appears to vanish. According to Makishima (2014), even accreting black hole objects also fall on the same locus.

We may point out another interesting behavior of the corona. As already stated in §5.3, and reported previously by Sakurai et al. (2014), τ decreased only by an order of

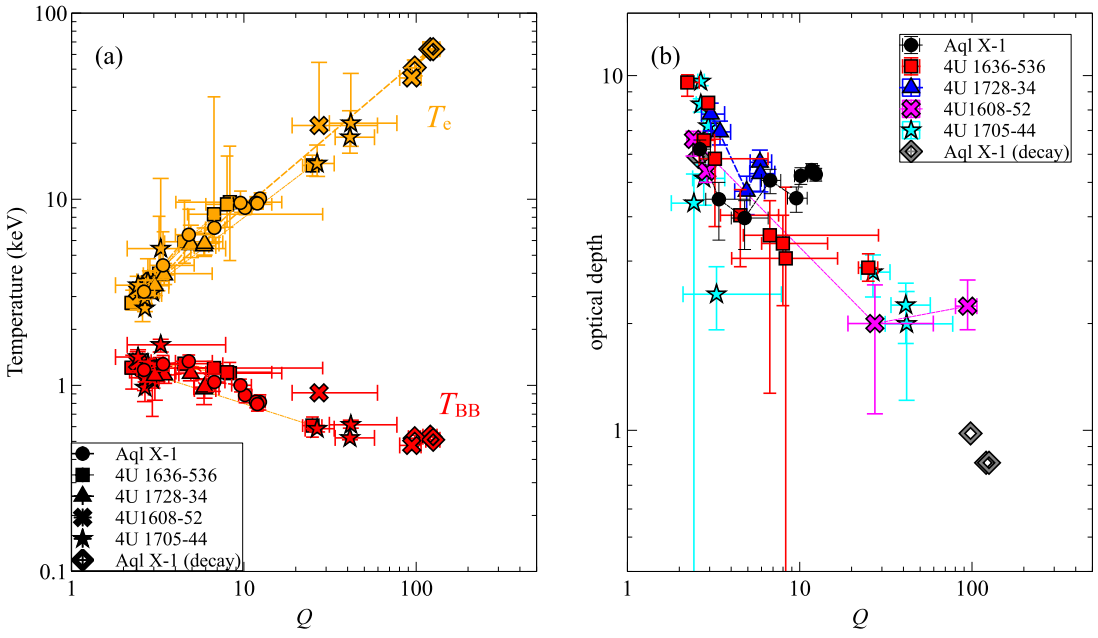

Figure 6.9: The same as figure 5.24 (a) and (b), but excluding $T_{\rm in}$.

magnitude when $L_{\rm t}$ changed by two orders of magnitude between $Q \sim 3$ and ~ 100. Since τ is proportional to the mass accretion rate, and hence to $L_{\rm t}$, the much smaller swing of τ, than that of $L_{\rm t}$, inevitably requires some $L_{\rm t}$-dependent changes of the condition of the Comptonizing corona, such as its geometry or velocity field. This is discussed in detail in §6.5.

6.5 Coronal Accretion

6.5.1 Coronal geometry and dynamics (I)

To understand the physical conditions and dynamics of the Comptonizing corona, we consider its three important physical quantities; the electron density $n_{\rm e}(R)$, the radial in-fall velocity $v_{\rm r}(R)$, and the scale height, with R meaning the radius coordinate. To quantify the scale height, let us assume the corona to have an axis-symmetric shape extending radially as shown in figure 6.11, with an angular aperture $\pm\theta$ above and below the accretion plane. Then, we can construct two independent constraints from the observations.

The first constraint utilizes $L_{\rm t}$, or the accretion rate $\dot{M}$, which is directly related to the above three quantities through the equation of the coronal continuity as

$$\dot{M} = S(R) v_{\rm r}(R) \mu m_{\rm p} n_{\rm e}(R). \tag{6.6}$$

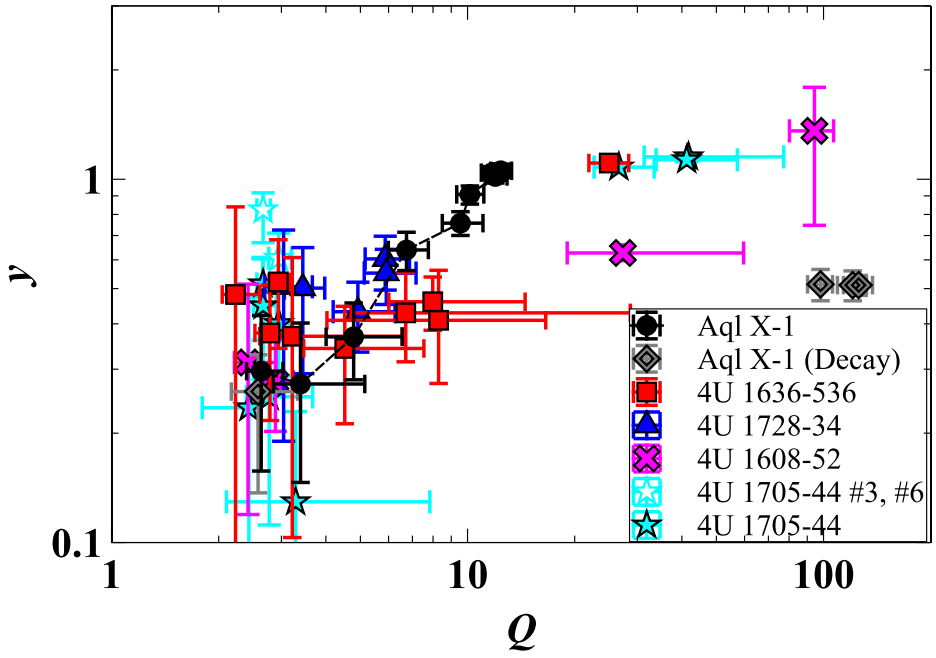

Figure 6.10: The relation between Q and the y parameter, when all the data analyzed are compiled. The data points for Aql X-1, obtained during a declining phase (Sakurai et al. 2014), are also shown.

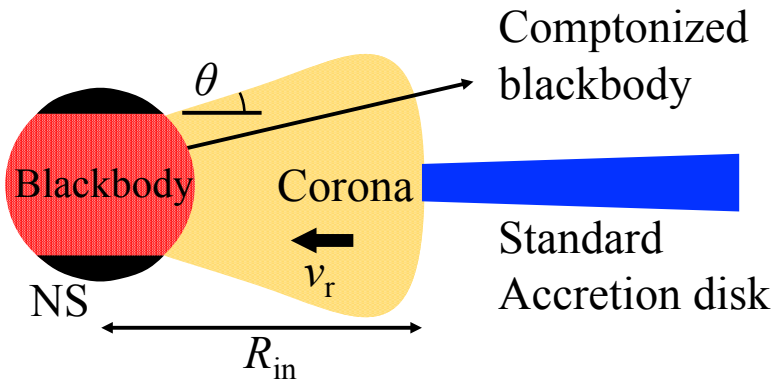

Figure 6.11: A schematic view of the coronal accretion flow we assume.

Here, $\mu = 1.2$ is the nucleon-to-electron number ratio in the accreting gas, and $S(R)$ is the cross section (as seen from $R = 0$) of the corona defined as

$$S(R) = 4\pi R^2 \times \sin\theta = 4\pi R^2 \zeta, \tag{6.7}$$

where $\zeta \equiv \sin\theta$ is assumed to be constant. Similarly, $v_{\rm r}(R)$ may be scaled by the free-fall velocity $v_{\rm ff}$ as

$$v_{\rm r}\,(R) = g \times v_{\rm ff}\,(R) = g \times \sqrt{\frac{2GM_{\rm NS}}{R}}, \tag{6.8}$$

where the normalized dimension-less radial velocity g $(0 < g < 1)$ is assumed to be constant for simplicity. Substituting eq. (6.7) and eq. (6.8), and using eq. (2.1) to convert $\dot{M}$ to $L_{\rm t}$, eq. (6.6), can be written as

$$\zeta g n_{\rm e}(R) = \frac{1}{4\pi\sqrt{2}} \frac{L_{\rm t}}{\mu m_{\rm p}} \frac{R_{\rm NS}}{(GMR)^{3/2}} \tag{6.9}$$

As the other constraint, $n_{\rm e}$ is independently related to τ of the corona as

$$\tau = \int_{R_{\rm NS}}^{R_{\rm in}} n_{\rm e}\,(R)\,\sigma_{\rm T} dR, \tag{6.10}$$

where $R_{\rm in}$ is the same inner-disk radius as so far employed. This is based on assumptions in figure 6.11, that the standard accretion disk terminates at $R = R_{\rm in}$ and inflates at that radius into the corona, and that we are observing the NS through the corona from a direction between $-\theta$ to $+\theta$ from the accretion plane, and $n_{\rm e}(R)$ is approximately constant from $-\theta$ to θ. Combining the two constraints obtained above, namely eq. (6.9) and eq. (6.10), we can eliminate $n_{\rm e}(R)$ to obtain

$$g\zeta = \frac{0.16}{\tau} \left(\frac{1.2}{\mu}\right) \left(1 - \sqrt{\frac{R_{\rm NS}}{R_{\rm in}}}\right) \left(\frac{L_{\rm t}({\rm erg\,s^{-1}})}{10^{37}}\right). \tag{6.11}$$

Thus, the knowledge of $L_{\rm t}$, τ, and $R_{\rm in}$ from observations can constrain the product $g\zeta$, although g and ζ cannot yet be estimated independently. The meaning of eq. (6.11) is that, for a given luminosity and $R_{\rm in}$, a larger τ requires a slowly falling ($v_{\rm r} \ll v_{\rm ff}$) and/or geometrically thinner (smaller θ) corona to realize a larger density. Since the observed τ is relatively large as $\tau \gtrsim 1$ in general (figure 5.24 b), $g\zeta$ should be much smaller than unity as already pointed out by Sakurai et al. (2014).

Because Q parameter was successful in §6.4 to express the Comptonization (though possibly suffering the hysteresis effect weakly in figure 6.10), the values of $g\zeta$calculated via eq. (6.11) are shown against Q in figure 6.12. The calculation of $g\zeta$ assumed $\mu = 1.2$ and $R_{\rm NS} = 12$ km. There, the data points are clustered along two loci of $g\zeta \sim 0.02 - 0.04$ and $g\zeta \sim 0.003 - 0.02$, which are connected at $Q \sim 3$ in the Soft State. The systematic differences primarily arise in the systematic difference of $L_{\rm t}$, and partly in $R_{\rm in}$ which is shown in figure

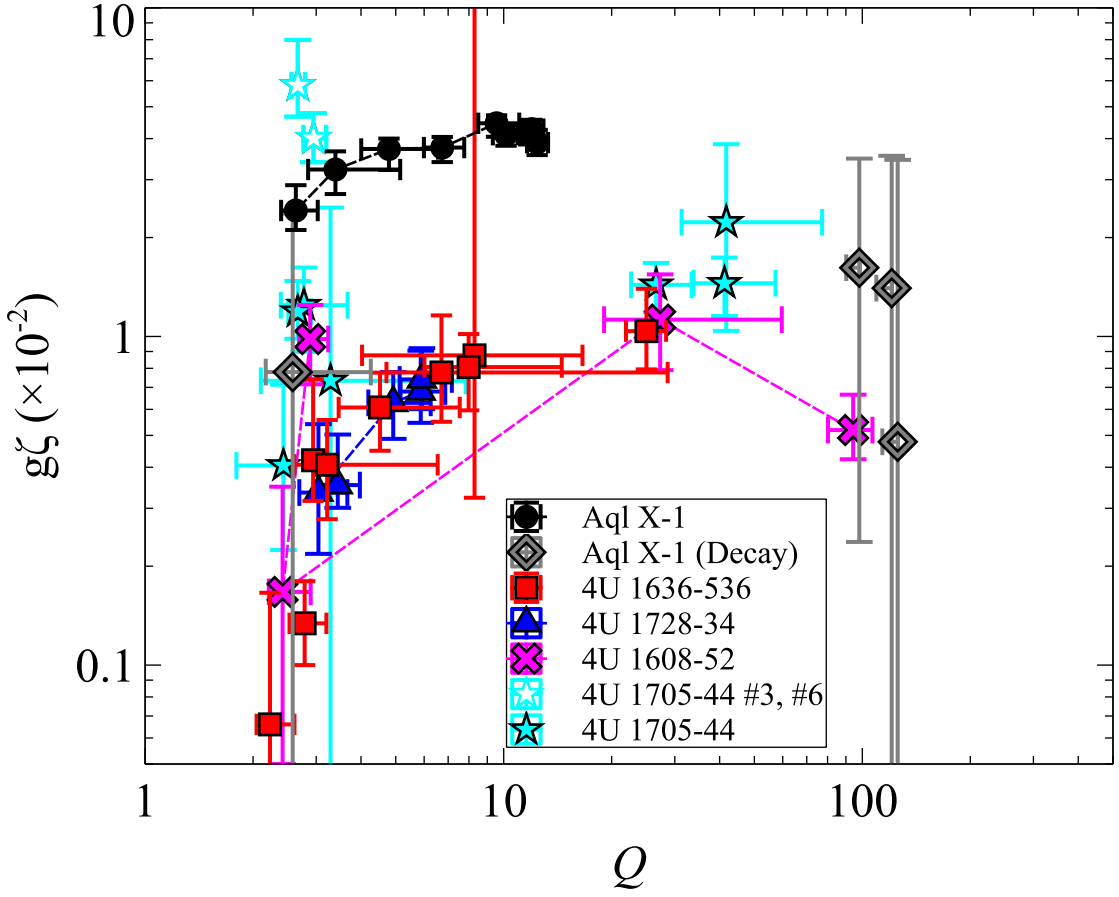

Figure 6.12: The product $g\zeta$, calculated from the spectral parameters using eq. (6.11), shown as a function of Q.

5.24 (c). This is evidently due to the hysteresis between the rising and falling evolutions. Apart from this split, the indicated values of $g\zeta < 0.04$ over the whole data sets are indeed rather small, and require the corona to be rather slowly falling ($g \ll 1$), or flattened ($\zeta \ll 1$), or both.

By substituting $g\zeta$ back to eq. (6.9), we can estimate $n_{\rm e}$ as

$$n_{\rm e}(R) = 1.02 \times 10^{18} \times \left(\frac{\mu}{1.2}\right) \cdot \left(\frac{L_{\rm t}}{10^{37}}\right) \cdot \left(\frac{R}{R_{\rm NS}}\right)^{-1.5} \cdot \left(\frac{g\zeta}{0.1}\right)^{-1} \ {\rm cm}^{-3} \tag{6.12}$$

where $M = 1.4 M_\odot$ and $R_{\rm NS} = 12$ km are assumed. As an interesting consequence, this equation can give an estimate of the bremsstrahlung luminosity of the corona which we have assumed to be negligible. Indeed, calculating a bremsstrahlung emission measure of $\int n_{\rm e}^2 dV$, the Comptonization process is found to dominate over the bremsstrahlung emission in the corona, as shown in figure A.7. Therefore, as long as $g\zeta$ is low, the corona is not self-emitting, and hence it could not collapse into the optically-thick/geometrically thin state. In short, our scenario is self-consistent.

6.5.2 Coronal geometry and dynamics (II)

As discussed in §6.3.1, $R_{\rm BB}$ behavior should reflect the evolution of the coronal scale height. Thus, the area of the corona covering the NS surface, $4\pi R_{\rm NS}^2 \zeta$ from eq. (6.7), should be equal to the blackbody surface area of $4\pi R_{\rm BB}^2$. Combining this relation as $\sqrt{\zeta} R_{\rm NS} = R_{\rm BB}$ and figure 6.12, g and ζ can be obtained as shown in figure 6.13. For all the data sets, the radial velocity has been shown to be rather low, typically a few percent of the free fall velocity. This makes a clear difference from a classical understanding that the corona is plunging onto the NS surface with free fall velocity.

To further comprehend the behavior in figure 6.13, let us consider additional observational information. On the NS surface, the energy released by the corona should be equal to a sum of their internal energy, radial kinetic energy, $\frac{1}{2} m_{\rm p} g^2 v_{\rm ff}^2$ per proton, and the azimuthal kinetic energy relative to the NS's spin, namely $\frac{1}{2} m_{\rm p} (v_\theta^2 - v_{\rm spin}^2)$ per proton, when v_θ is the azimuthal velocity of ions and $v_{\rm spin}$ is the NS's rotational speed at the surface. Representing those quantities with the average values, the relation is expressed as

$$\frac{L_{\rm BB}}{L_{\rm t}} = \frac{\dot{N}}{L_{\rm t}} \times \left[kT_{\rm i} + \frac{1}{2} m_{\rm p} g^2 v_{\rm ff}^2 + \frac{1}{2} m_{\rm p} (v_\theta^2 - v_{\rm spin}^2) \right]. \tag{6.13}$$

where $\dot{N}$ (s^{-1}) is the accretion rate in ion number, and $T_{\rm i}$ is a sum of thermal energy of ions and their turbulence energy. This $T_{\rm i}$ is related with the coronal scale height as

$$\sqrt{\frac{2T_{\rm i}}{T_{\rm ff}}} \sim \frac{H(R)}{R} = \tan\theta = \frac{\zeta}{\sqrt{1-\zeta^2}} \tag{6.14}$$

where $T_{\rm ff} = m_{\rm p} v_{\rm ff}^2 / 2$ is the virial temperature. We hence obtain

$$T_{\rm i} = T_{\rm ff} \times \frac{\zeta^2}{1-\zeta^2}. \tag{6.15}$$

Combining eq. (6.13) and eq. (6.15), $L_{\rm BB}/L_{\rm t}$ can be expressed as

$$\frac{L_{\rm BB}}{L_{\rm t}} = \left[\frac{\zeta^2}{2(1-\zeta^2)} + g^2 + \left\{\left(\frac{v_\theta}{v_{\rm ff}(R_{\rm NS})}\right)^2 - \left(\frac{v_{\rm spin}}{v_{\rm ff}(R_{\rm NS})}\right)^2\right\}\right] \equiv \left(\frac{\zeta^2}{2(1-\zeta^2)} + g^2 + \Delta\epsilon_\theta\right), \quad (6.16)$$

where $\Delta\epsilon_\theta \equiv (v_\theta^2 - v_{\rm spin}^2)/v_{\rm ff}^2$.

In figure 6.13, eq. (6.16) is shown assuming a typical value of $L_{\rm BB}/L_{\rm t} = 0.30$. These curves consist of horizontal sections where $\frac{1}{2}m_{\rm p}v_{\rm r}^2$ dominates over $kT_{\rm i}$, and vertical sections which are characterized by $\frac{1}{2}m_{\rm p}v_{\rm r}^2 \ll kT_{\rm i}$. Thus, in figure 6.13, the ion thermal energy dominates the coronal energy over infall kinetic energy, as discussed above. The approximate relation in eq. (6.16) indicate that in the Hard State denoted as H3 and H1, $\Delta\epsilon_\theta$ should be negligible. In other words, most of the coronal energy in the Hard State is carried by thermal energy, and hence the corona is inflated. On the other hand, in the Soft State as S1 and S2, $\Delta\epsilon_\theta \sim L_{\rm BB}/L_{\rm t} = 0.30$. This represents that the coronal energy is dominated by the rotational energy, and consequently the corona is rather flat with $\zeta \sim 0.1$. As a result, the corona in the Soft State is considered to look like the schematic view in figure 6.14. Since $R_{\rm in} \lesssim 15$ km in the Soft State, the corona is considered to be flat also radially.

To summarize, from the Hard State to the Soft State in $L_{\rm t}$ increasing phase, the corona shrinks both radially and vertically, with decreasing ζ. When the sources change to $L_{\rm t}$ decreasing phase, the corona further shrinks, and covers a narrow equatorial zone of the NS surface. In $L_{\rm t}$ decreasing phase, the coronal inflow velocity is systematically slower, and is more flat. Toward the Hard State, the corona expands both in radial and vertical direction, returning to the initial Hard State. There, the corona has a relatively large scale height, e.g., $\theta \gtrsim 40^\circ$ calculated from ζ in the Hard State, so that it has a high $T_{\rm i}$ via eq. (6.14), and relatively low density via eq. (6.12). These agree with the basic concept of "geometrically thick and optically thin" accretion flow (§2.3.1). Presumably, some standing shocks are converting radial and azimuthal energy into $T_{\rm i} \sim 0.6T_{\rm ff}$ from eq. (6.15), although we cannot at present identify the shock location.

6.5.3 Magnetic field pressure in the corona

Using the coronal density and the ion temperature, we can examine if the coronal accretion should be affected by a magnetic field or not. From eq. (6.12), the typical density of the corona is obtained as $n_{\rm e} \sim 10^{18}$ cm^{-3}. Since $\zeta \gtrsim 0.1$ in figure 6.13, the ion temperature is $\gtrsim 2$ MeV from eq. (6.15). As a result, the gas pressure in the corona is expressed as

$$P_{\rm g} \sim n_{\rm e}kT = 3.2 \times \left(\frac{n}{10^{18}\ {\rm cm}^{-3}}\right)\left(\frac{T}{2\ {\rm MeV}}\right) \times 10^{11}\ {\rm Pa} \quad (6.17)$$

where k is the Boltzmann constant. More precisely, in the Soft State, the coronal energy is dominated by the rotational energy rather than by the thermal one. Thus, the effective

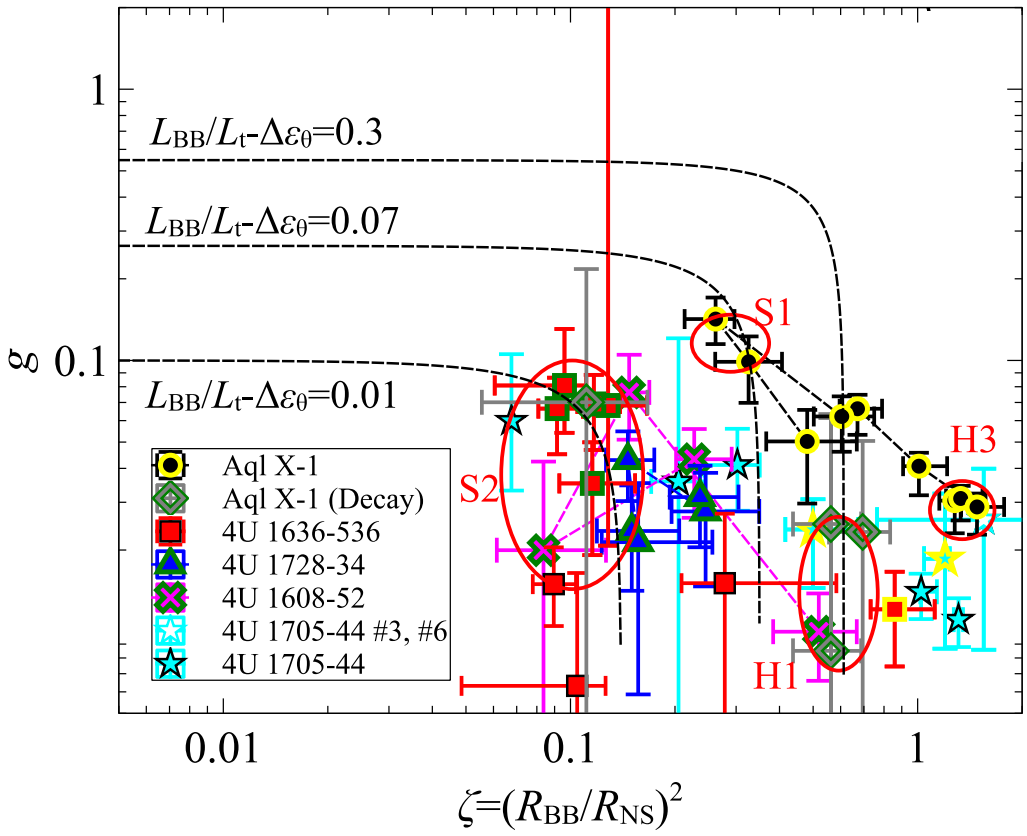

Figure 6.13: Estimated radial velocity g and scale height $\zeta \equiv \sin\theta$ of the corona. Relation of g and ζ from eq. (6.16) are shown with black curves. The data points with decreasing L_t and those with increasing L_t are outlined in green and yellow, respectively. The labels H3, S1, S2, and H1 are the same as in figure 6.5.

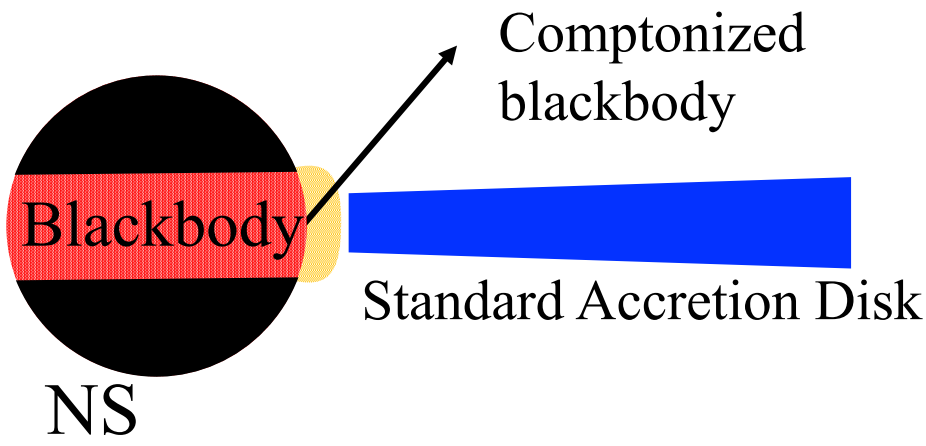

Figure 6.14: The coronal geometry in the Soft State (S2 to S3 in figure 6.5) indicated from the results in §6.5.3.

gas pressure $P_{\rm g}^{\rm eff}$ including the bulk energy, is larger than $P_{\rm g}$ by a factor of ~ 5. Assuming $B = 10^3$ T which is suggested in Sakurai (2015) from the Alfven radius argument, the magnetic field pressure is expressed as

$$P_{\rm m} = \frac{B^2}{2\mu_0} = 4.0 \times \left(\frac{B}{10^3 \text{ T}} \right)^2 \times 10^{11} \text{ Pa} \tag{6.18}$$

where $\mu_0 = 4\pi \times 10^{-7}$ is the permeability constant. As a result, $P_{\rm g}^{\rm eff} > P_{\rm g} \gtrsim P_{\rm m}$, and the corona can accrete onto the NS equator, rather than onto the magnetic pole. On the other hand, the magnetic field starts to appear in the corona when $L_{\rm t} \lesssim 10^{36}$ erg s^{-1}, and becomes even clear when $L_{\rm t} \sim 10^{34}$ erg s^{-1} and the corona is radially expanded, with $n_{\rm e} \lesssim 10^{15}$ cm^{-3}. In such a case, substituting $T = T_{\rm ff} \sim 200$ MeV, still $P_{\rm g} \sim 0.1 \times P_{\rm m}$. Thus, the coronal accretion should be strongly confined to the magnetic pole, as observed in Sakurai (2015). As a result, the geometry of the coronal accretion flow is self-consistent considering the coronal gas pressure and the magnetic field pressure with $B = 10^3$ T, including the range of $L_{\rm t} < 10^{36}$ which is examined in Sakurai (2015).

Chapter 7

Conclusion

In the present thesis, 19 data sets of 5 LMXBs taken with *Suzaku* were analyzed. The objects were found over a luminosity range of $L_{\rm t} \sim 10^{36-38}$ erg s^{-1}. The following results have been obtained.

1. Out of the 19 observations, 5 were in the Hard State, 13 in the Soft State, and the remaining one successfully caught a Hard-to-Soft transition. Thus, the bimodal behavior of accretion flows has been confirmed to be a general phenomenon.

2. Regardless of the spectral state, the broadband spectra of essentially all the 19 data sets have been reproduced successfully with a unified model, consisting of a multi-color disk emission plus a Comptonized blackbody emission.

3. The transition between the Hard State ($L_{\rm t} \lesssim 5 \times 10^{37}$ erg s^{-1}) and the Soft State ($L_{\rm t} \gtrsim 3 \times 10^{37}$ erg s^{-1}) appear as very quick changes in $L_{\rm comp}/L_{\rm t}$ and $L_{\rm MCD}/L_{\rm t}$, in response to small changes in $L_{\rm t}$. This behavior is described in a unified way by introducing a quantity $Q \equiv T_{\rm e}/T_{\rm BB}$ as a new variable.

4. We confirmed clear hysteresis effects between the brightening and dimming phases. It appears as a factor ~ 5 difference in the threshold luminosity, and a much smaller difference in the Q values. These effects have been successfully understood as a unified loop on the $R_{\rm BB}$ vs $T_{\rm BB}$ plane, along which essentially all LMXBs evolve.

5. The Comptonizing corona was found to have relatively small radial infall velocities, typically $\sim 10\%$ of the free fall velocity. In the brightening phase from the Hard State to the Soft State, the radial velocity and the scale height of the corona both decrease. When a source becomes dimmer from the Soft State to the Hard State, the opposite changes take place, but the scale height and/or the infall velocity are systematically lower, corresponding to the hysteresis.

6. Some fraction ($\lesssim 20\%$) of the accretion energy is suggested to spin up the neutron star.

7. The obtained results provide universal understandings of LMXBs, as they evolve over a large luminosity range from $\sim 10^{36}$ erg s^{-1} to $\lesssim 10^{38}$ erg s^{-1} involving hysteresis effects. In particular, the behavior of the corona through the hysteresis loop has been clarified for the first time.

Acknowkedgement

I would like to express my gratitude to Prof. Kazuo Makishima for helping me write thesis. It would be impossible to complete the thesis without his help. I appreciate his patience for helping me construct thesis and correcting texts. It is like a miracle for me that I got a chance to spend five years with him, and could learn the true beauty of the physic, how to write papers, applications, how to make presentation materials, how to talk... He has also been the best teacher of life in general, and I could learn many things from him such as strong responsibility as a leader and as a supervisor, how the professional work is, and his dedication to every single person.

I would also like to thank Ass. Prof. Kazuhiro Nakazawa for helping me write thesis, prepare for defense, and supporting my experiments, as well as being consulted about various issues. I thank Ass. Prof. Aya Bamba for helping me write thesis and prepare for the defense. I could spend a comfortable research life during the last one year thanks to her.

I am grateful to Dr. Soki Sakurai who had helped my research of LMXBs through discussion. The present thesis is based on his important works on LMXBs. I also thank Dr. Kazutaka Yamaoka for helping me write a paper which is included in the present thesis.

I thank Katsuma Miyake and Yuichi Kato. I could spend invaluable time for five years in Makishima, Nakazawa, and Bamba laboratories. I thank senior colleagues Daigo Umemoto, Hiroaki Murakami, and Shogo Kobayashi for taking care of me and discussing research with me. I thank all my colleagues, Yoshihiro Furuta, Yuki Murota, Kazuhumi Okuda, Yuuki Wada, Hiromasa Suzuki, Manami Seino, Tomoaki Kasuga, and Takahiro Matsumoto, for providing great environment and experience in the office.

At the end, I would like to express my appreciation and dedicate thesis to my family and my wife for patience, support, and understanding.

References

Abramowicz, M. A., Chen, X., Kato, S., Lasota, J.-P., & Regev, O. 1995, ApJL, 438, L37

Asai, K., Matsuoka, M., Mihara, T., et al. 2012, PASJ, 64, 128

Barret, D., & Olive, J.-F. 2002, ApJ, 576, 391

Barret, D., Olive, J. F., Boirin, L., et al. 2000, ApJ, 533, 329

Barret, D., Mereghetti, S., Roques, J. P., et al. 1991, ApJL, 379, L21

Barret, D., Grindlay, J. E., Bloser, P. F., et al. 1996, A&AS, 120, 121

Basinska, E. M., Lewin, W. H. G., Sztajno, M., Cominsky, L. R., & Marshall, F. J. 1984, ApJ, 281, 337

Bloser, P. F., Grindlay, J. E., Barret, D., & Boirin, L. 2000a, ApJ, 542, 989

Bloser, P. F., Grindlay, J. E., Kaaret, P., et al. 2000b, ApJ, 542, 1000

Boella, G., Butler, R. C., Perola, G. C., et al. 1997, A&AS, 122, 299

Boroson, B., Kim, D.-W., & Fabbiano, G. 2011, ApJ, 729, 12

Bradt, H. V., Rothschild, R. E., & Swank, J. H. 1993, A&AS, 97, 355

Camenzind, M. 2006, Sterne und Weltraum, 45, 89

Casella, P., Altamirano, D., Patruno, A., Wijnands, R., & van der Klis, M. 2008, ApJL, 674, L41

Chen, Y.-P., Zhang, S., Torres, D. F., Wang, J.-M., & Li, T.-P. 2010, A&A, 510, A81

Chevalier, C., Ilovaisky, S. A., Leisy, P., & Patat, F. 1999, A&A, 347, L51

Di Salvo, T., Iaria, R., Burderi, L., & Robba, N. R. 2000, ApJ, 542, 1034

Fabian, A. C., Rees, M. J., Stella, L., & White, N. E. 1989, MNRAS, 238, 729

Fujimoto, M. Y., & Taam, R. E. 1986, ApJ, 305, 246

Fukazawa, Y., Mizuno, T., Watanabe, S., et al. 2009, PASJ, 61, S17

Galloway, D. K., Chakrabarty, D., Muno, M. P., Psaltis, D., & Cumming, A. 2003, in Bulletin of the American Astronomical Society, Vol. 35, American Astronomical Society Meeting Abstracts, 1320

Galloway, D. K., Muno, M. P., Hartman, J. M., Psaltis, D., & Chakrabarty, D. 2008, ApJS, 179, 360

Giacconi, R., Gursky, H., Paolini, F. R., & Rossi, B. B. 1962, Physical Review Letters, 9, 439

Gierliński, M., & Done, C. 2002, MNRAS, 337, 1373

Gilfanov, M. R., & Sunyaev, R. A. 2014, Physics-Uspekhi, 57, 377

Grimm, H.-J., Gilfanov, M., & Sunyaev, R. 2002, A&A, 391, 923

Guainazzi, M., Parmar, A. N., Segreto, A., et al. 1998, A&A, 339, 802

Haberl, F., & Titarchuk, L. 1995, A&A, 299, 414

Hoffman, J. A., Lewin, W. H. G., Doty, J., et al. 1976, ApJL, 210, L13

Ichimaru, S. 1976, ApJ, 208, 701

Jonker, P. G., & Nelemans, G. 2004, MNRAS, 354, 355

Kajava, J. J. E., Koljonen, K. I. I., Nättilä, J., Suleimanov, V., & Poutanen, J. 2017, MNRAS, 472, 78

Kitamoto, S., Tsunemi, H., Miyamoto, S., & Roussel-Dupre, D. 1993, ApJ, 403, 315

Kokubun, M., Makishima, K., Takahashi, T., et al. 2007, PASJ, 59, 53

Kondo, I., Inoue, H., Koyama, K., et al. 1981, Space Science Instrumentation, 5, 211

Kong, A. K. H., Homer, L., Kuulkers, E., Charles, P. A., & Smale, A. P. 2000, MNRAS, 311, 405

Koyama, K., Tsunemi, H., Dotani, T., et al. 2007, PASJ, 59, 23

Kubota, A., Tanaka, Y., Makishima, K., et al. 1998, PASJ, 50, 667

Kuulkers, E., den Hartog, P. R., in't Zand, J. J. M., et al. 2003, A&A, 399, 663

Lasota, J.-P. 2001, New Astronomy Review, 45, 449

Lewin, W. H. G., Hoffman, J., & Doty, J. 1976, in BAAS, Vol. 8, Bulletin of the American Astronomical Society, 442

Lightman, A. P., & Eardley, D. M. 1974, ApJL, 187, L1

Lightman, A. P., & Zdziarski, A. A. 1987, ApJ, 319, 643

Lin, D., Remillard, R. A., & Homan, J. 2010, ApJ, 719, 1350

Liu, Q. Z., van Paradijs, J., & van den Heuvel, E. P. J. 2007, A&A, 469, 807

Lochner, J. C., & Roussel-Dupre, D. 1994, ApJ, 435, 840

Maejima, Y., Makishima, K., Matsuoka, M., et al. 1984, ApJ, 285, 712

Makino, F. 1987, Astrophys. Lett., 25, 223

Makishima, K. 2014, in Expanding the Frontiers of the X-ray Universe, Suzaku Maxi conference

Makishima, K. 2016, Proceeding of the Japan Academy, Series B, 92, 135

Makishima, K., Maejima, Y., Mitsuda, K., et al. 1986, ApJ, 308, 635

Makishima, K., Ishida, M., Ohashi, T., et al. 1989, PASJ, 41, 531

Makishima, K., Takahashi, H., Yamada, S., et al. 2008, PASJ, 60, 585

Matsuoka, M., Kawasaki, K., Ueno, S., et al. 2009, PASJ, 61, 999

Meyer, F., & Meyer-Hofmeister, E. 1981, A&A, 104, L10

Mitsuda, K., Inoue, H., Nakamura, N., & Tanaka, Y. 1989, PASJ, 41, 97

Mitsuda, K., Inoue, H., Koyama, K., et al. 1984, PASJ, 36, 741

Mitsuda, K., Bautz, M., Inoue, H., et al. 2007, PASJ, 59, S1

Nakamura, N., Dotani, T., Inoue, H., et al. 1989, PASJ, 41, 617

Narayan, R., Mahadevan, R., & Quataert, E. 1998, in Theory of Black Hole Accretion Disks, ed. M. A. Abramowicz, G. Björnsson, & J. E. Pringle, 148

Narayan, R., & Yi, I. 1994, ApJL, 428, L13

Ono, K., Makishima, K., Sakurai, S., et al. 2017, PASJ, 69, 23

Ono, K., Sakurai, S., Zhang, Z., Nakazawa, K., & Makishima, K. 2016, PASJ, 68, S14

Osaki, Y. 1974, PASJ, 26, 429

Papitto, A., Ferrigno, C., Bozzo, E., et al. 2013, Nature, 501, 517

Parsignault, D. R., & Grindlay, J. E. 1978, ApJ, 225, 970

Patruno, A., Archibald, A. M., Hessels, J. W. T., et al. 2014, ApJL, 781, L3

Poutanen, J., & Svensson, R. 1996, ApJ, 470, 249

Priedhorsky, W. C., & Terrell, J. 1984, ApJ, 280, 661

Sakurai, S. 2015, PhD thesis, The University of Tokyo

Sakurai, S., Yamada, S., Torii, S., et al. 2012, PASJ, 64, 72

Sakurai, S., Torii, S., Noda, H., et al. 2014, PASJ, 66, 10

Sandage, A., Osmer, P., Giacconi, R., et al. 1966, ApJ, 146, 316

Seifina, E., & Titarchuk, L. 2012, ApJ, 747, 99

Serlemitsos, P. J., Soong, Y., Chan, K.-W., et al. 2007, PASJ, 59, S9

Shakura, N. I., & Sunyaev, R. A. 1973, A&A, 24, 337

Shibazaki, N., & Hōshi, R. 1975, Progress of Theoretical Physics, 54, 706

Shih, I. C., Bird, A. J., Charles, P. A., Cornelisse, R., & Tiramani, D. 2005, MNRAS, 361, 602

Shimura, T., & Takahara, F. 1995, ApJ, 445, 780

Stappers, B. W., Archibald, A. M., Hessels, J. W. T., et al. 2014, ApJ, 790, 39

Strohmayer, T. E., & Markwardt, C. B. 2002, ApJ, 577, 337

Strohmayer, T. E., Zhang, W., Swank, J. H., et al. 1996, ApJL, 469, L9

Swank, J. H., Becker, R. H., Pravdo, S. H., Saba, J. R., & Serlemitsos, P. J. 1976, IAU Circ., 3000

Syunyaev, R. A., & Shakura, N. I. 1986, Pisma v Astronomicheskii Zhurnal, 12, 286

Takahashi, H., Sakurai, S., & Makishima, K. 2011, ApJ, 738, 62

Takahashi, T., Abe, K., Endo, M., et al. 2007, PASJ, 59, 35

Takata, J., Li, K. L., Leung, G. C. K., et al. 2014, ApJ, 785, 131

Tanaka, Y., Inoue, H., & Holt, S. S. 1994, PASJ, 46, L37

Tanaka, Y., Fujii, M., Inoue, H., et al. 1984, PASJ, 36, 641

Tarana, A., Bazzano, A., & Ubertini, P. 2008, ApJ, 688, 1295

van Paradijs, J. 1978, Nature, 274, 650

van Paradijs, J., van der Klis, M., van Amerongen, S., et al. 1990, A&A, 234, 181

Welsh, W. F., Robinson, E. L., & Young, P. 2000, AJ, 120, 943

White, N. E., & Mason, K. O. 1985, Space Sci. Rev., 40, 167

White, N. E., Stella, L., & Parmar, A. N. 1988, ApJ, 324, 363

Wilms, J., Allen, A., & McCray, R. 2000, ApJ, 542, 914

Winkler, C., Courvoisier, T. J.-L., Di Cocco, G., et al. 2003, A&A, 411, L1

Yamada, S., Uchiyama, H., Dotani, T., et al. 2012, PASJ, 64, 53

Yu, W., & Yan, Z. 2009, ApJ, 701, 1940

Zdziarski, A. A., Johnson, W. N., & Magdziarz, P. 1996, MNRAS, 283, 193

Zhang, W., Jahoda, K., Kelley, R. L., et al. 1998, ApJL, 495, L9

Zhang, W., Lapidus, I., Swank, J. H., White, N. E., & Titarchuk, L. 1997, IAU Circ., 6541

Zhang, Z., Gilfanov, M., & Bogdán, Á. 2012, A&A, 546, A36

Zhang, Z., Makishima, K., Sakurai, S., Sasano, M., & Ono, K. 2014, PASJ, 66, 120

Zhang, Z., Sakurai, S., Makishima, K., et al. 2016, ApJ, 823, 131

Życki, P. T., Done, C., & Smith, D. A. 1999, MNRAS, 309, 561

Appendix A

Appendix

A.1 Suzaku Arcival data

Table A.1: The *Suzaku* archival data of LMXBs taken from Sakurai (2015).

Name	Obs. ID	Date	E^{a}	$L_{abs}{}^{b}$(erg s^{-1})	H ($\times 10^{-3}$)	D (kpc)
4U1608-52	404044010	10/03/11	28.0	1.4×10^{37}	4.65 ± 0.04	3.6
	404044020	10/03/15	25.2	7.7×10^{36}	5.38 ± 0.07	
	404044030	10/03/18	14.2	3.3×10^{36}	39.7 ± 0.4	
	404044040	10/03/22	14.5	1.0×10^{36}	51.9 ± 0.9	
4U1636-536	401050010	07/02/09	20.3	6.5×10^{36}	51.8 ± 0.5	5.9
	401050020	07/02/22	33.2	1.1×10^{37}	5.85 ± 0.07	
	401050030	07/03/01	45.2	8.7×10^{36}	16.4 ± 0.1	
	401050040	07/03/27	26.1	8.5×10^{36}	6.6 ± 0.1	
	401050050	07/03/29	11.0	8.6×10^{36}	5.0 ± 0.1	
4U1705-44	401046010	06/08/29	14.4	8.1×10^{36}	45.9 ± 0.5	$7.4^{+0.8}_{-1.1}$
	401046020	06/09/18	14.7	1.7×10^{37}	2.46 ± 0.06	
	401046030	06/10/06	16.7	6.7×10^{36}	2.14 ± 0.08	
	402051010	07/09/05	8.8	5.7×10^{37}	3.48 ± 0.06	
	402051020	07/10/08	14.8	3.7×10^{37}	3.44 ± 0.06	
	402051030	08/02/20	19.5	1.5×10^{37}	4.16 ± 0.09	
	402051040	08/03/18	12.4	4.0×10^{37}	3.60 ± 0.06	
	406076010	12/03/27	84.5	4.6×10^{36}	61.0 ± 0.4	
4U 1728-34	405048010	10/10/04	88.3	5.9×10^{36}	17.7 ± 0.1	5.2 ± 0.7
4U1812-12	406008010	11/10/04	49.9	1.4×10^{36}	120.8 ± 0.9	4

[a] Net exposure per XIS (ks).
[b] Absorbed 0.8–60 keV luminosity (erg s^{-1}).

Table A.2: The *Suzaku* archival data of LMXBs taken from Sakurai (2015).[a]

Name	Obs. ID	Date	E	$L_{\rm abs}$[b](erg s^{-1})	H ($\times 10^{-3}$)	D (kpc)
Aquila X-1	402053010	07/09/28	12.5	9.6×10^{36}	2.06 ± 0.08	5.2 ± 0.7
	402053020	07/10/03	11.2	1.9×10^{36}	72 ± 1	
	402053030	07/10/09	16.1	2.3×10^{36}	66 ± 1	
	402053040	07/10/15	16.3	1.8×10^{36}	71 ± 1	
	402053050	07/10/19	15.9	35×10^{35}	71 ± 3	
	402053060	07/10/24	19.8	9.1×10^{33}	60 ± 20	
	402053070	07/10/30	13.4	1.1×10^{34}	120 ± 30	
	406010010	11/10/18	32.8	1.0×10^{37}	68.9 ± 0.3	
	406010020	11/10/21	35.2	$(2.7 - 3.7) \times 10^{37}$	$120 - 8$	
	406010030	11/10/24	34.0	4.7×10^{3}	3.08 ± 0.02	
4U1636-536	401050010	07/02/09	20.3	6.5×10^{36}	51.8 ± 0.5	5.9
	401050020	07/02/22	33.2	1.1×10^{37}	5.85 ± 0.07	
	401050030	07/03/01	45.2	8.7×10^{36}	16.4 ± 0.1	
	401050040	07/03/27	26.1	8.5×10^{36}	6.6 ± 0.1	
	401050050	07/03/29	11.0	8.6×10^{36}	5.0 ± 0.1	
Cen X-4	403057010	09/01/16	124.0	5.1×10^{31}	90 ± 30	1.2 ± 0.3
Cyg X-2	401049010	06/05/16	34.5	5.7×10^{37}	2.15 ± 0.02	7.2
	403063010	08/07/01	81.9	5.9×10^{37}	6.50 ± 0.04	
GS 1826-238	404007010	09/10/21	82.0	1.1×10^{37}	103.8 ± 0.4	$7 \pm ^{1}_{3}$
GX17+2	402050010	07/09/19	15.0	1.5×10^{38}	6.23 ± 0.05	9.8
	402050020	07/09/27	17.7	7.2×10^{37}	19.2 ± 0.1	
	402050030	11/10/19	81.1	1.8×10^{38}	6.28 ± 0.02	
GX340+0	403060010	09/03/02	80.3	8.5×10^{37}	9.05 ± 0.04	11 ± 3
GX349+2	400003010	06/03/14	18.7	4.5×10^{37}	3.82 ± 0.03	5
	400003020	06/03/19	23.9	1.9×10^{37}	4.57 ± 0.04	
GX9+9	404071010	10/03/16	57.6	7.6×10^{37}	4.57 ± 0.04	10
LMC X-2	401012010	06/04/24	69.0	1.5×10^{38}	1.01 ± 0.05	50
Ser X-1	401048010	09/03/11	15.3	4.8×10^{37}	2.82 ± 0.03	8.4
SLX 1737-282	503103010	06/10/24	29.0	3.5×10^{35}	82 ± 4	$5 - 8$

[a] Details are the same as A.1.

A.2 Light Curves

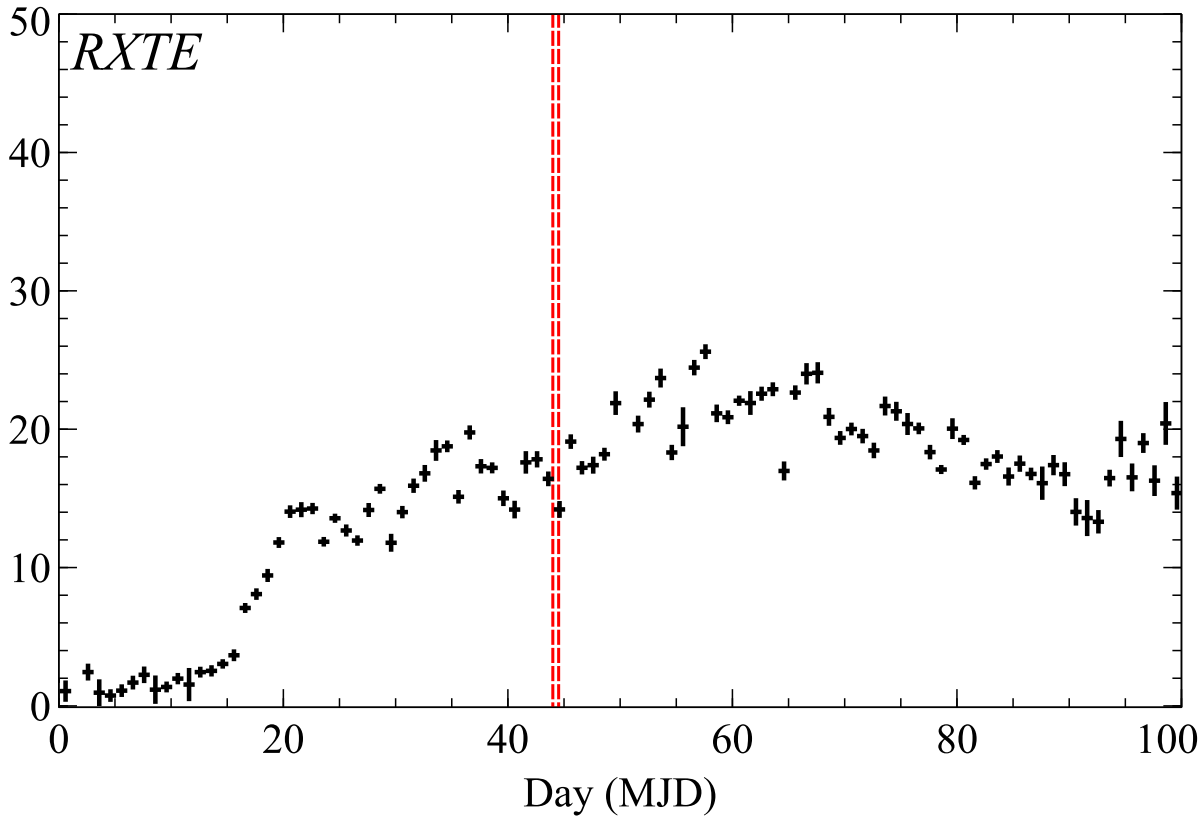

Figure A.1: The same long-term *RXTE* light curve as figure 4.5, but for 4U1705-44. The observation 4U 1705-44 #8 is shown in red dashed line.

A.3 Coronal Emissivity by Bremsstrahlung

Using eq. (6.9) and eq. (6.11), the luminosity of the corona by the bremsstrahlung can be estimated from an emission measure $\int n_{\rm e}^2(R)dV$, integrating whole the coronal volume. For simplicity, we assumed $T_{\rm e} = 5$ keV, and multiplied the maximum volume of $(4/3\pi)R_{\rm in}^3$ and $n_{\rm e}(R_{\rm in})$.

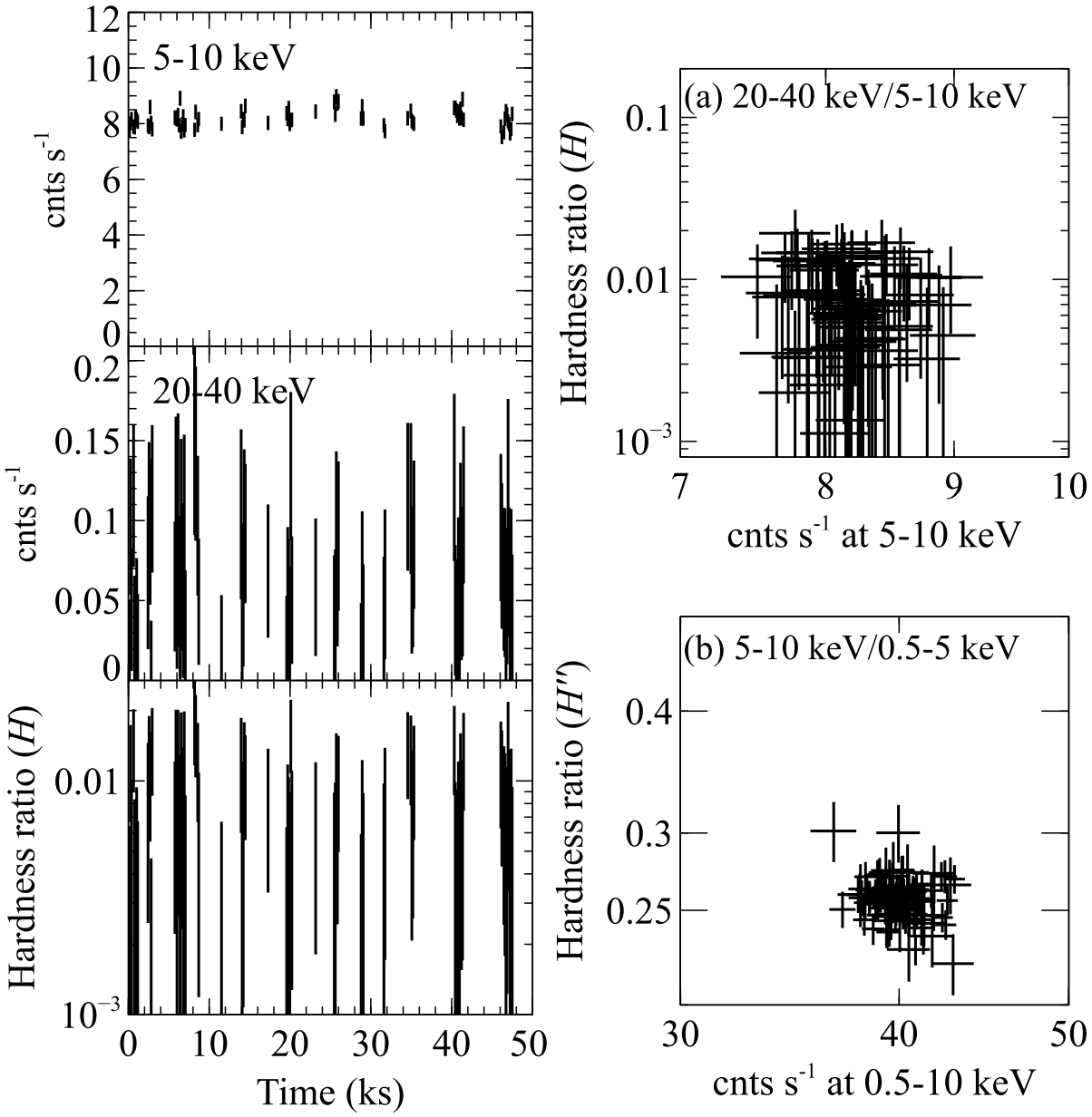

Figure A.2: The same *Suzaku* data as figure 4.9, but for 4U1705-44 #2.

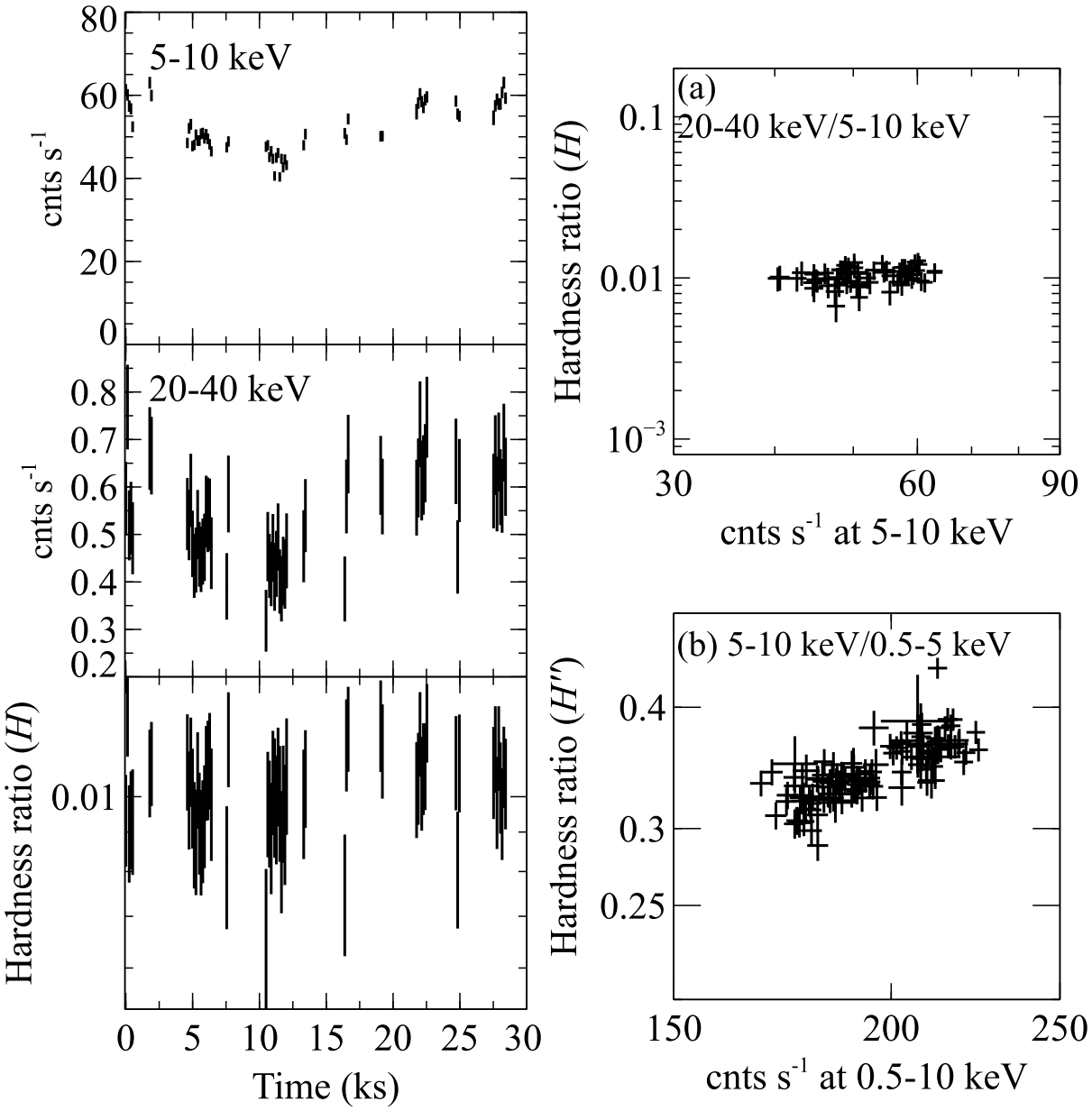

Figure A.3: The same *Suzaku* data as figure 4.9, but for 4U1705-44 #3.

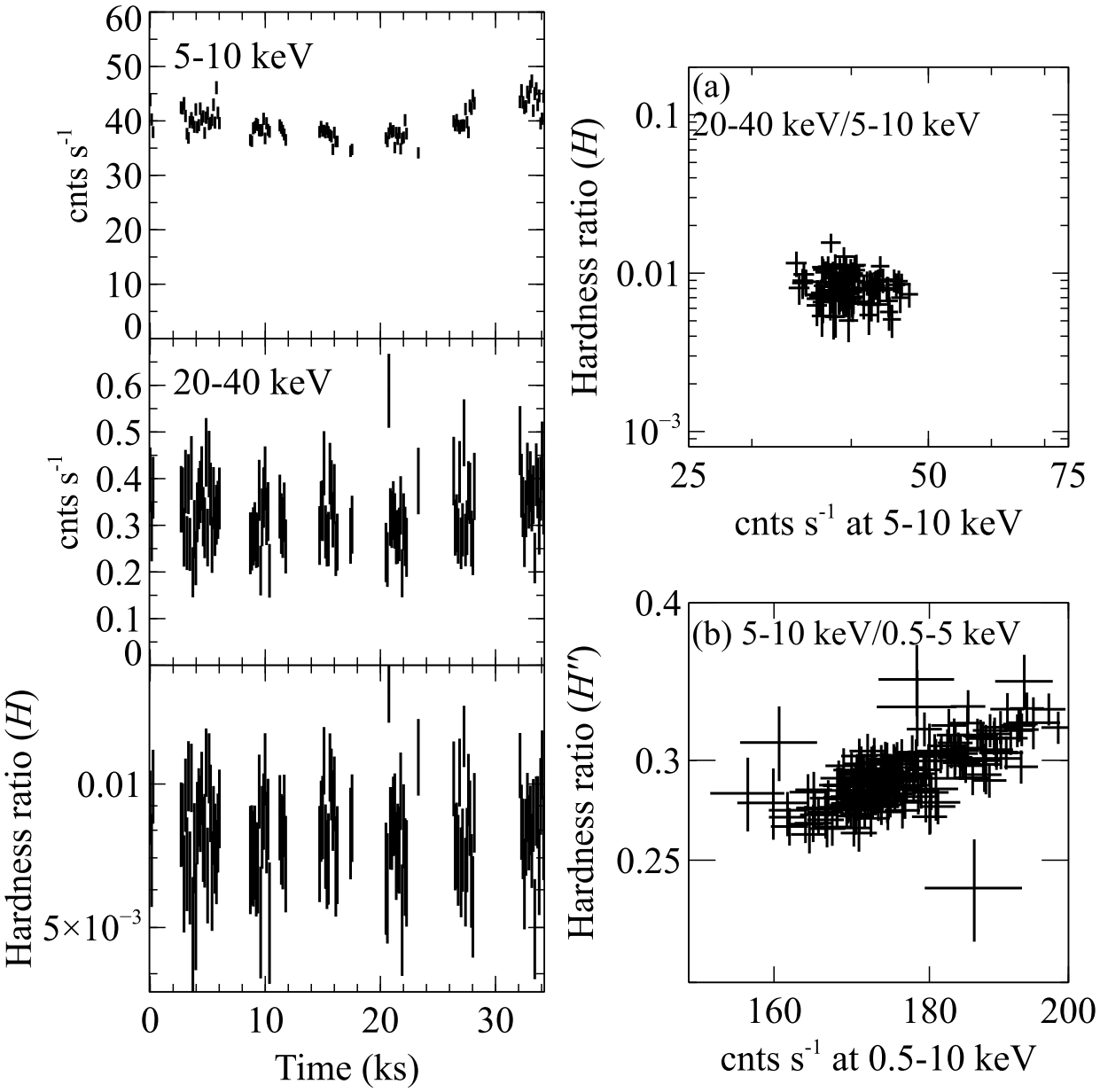

Figure A.4: The same *Suzaku* data as figure 4.9, but for 4U1705-44 #4.

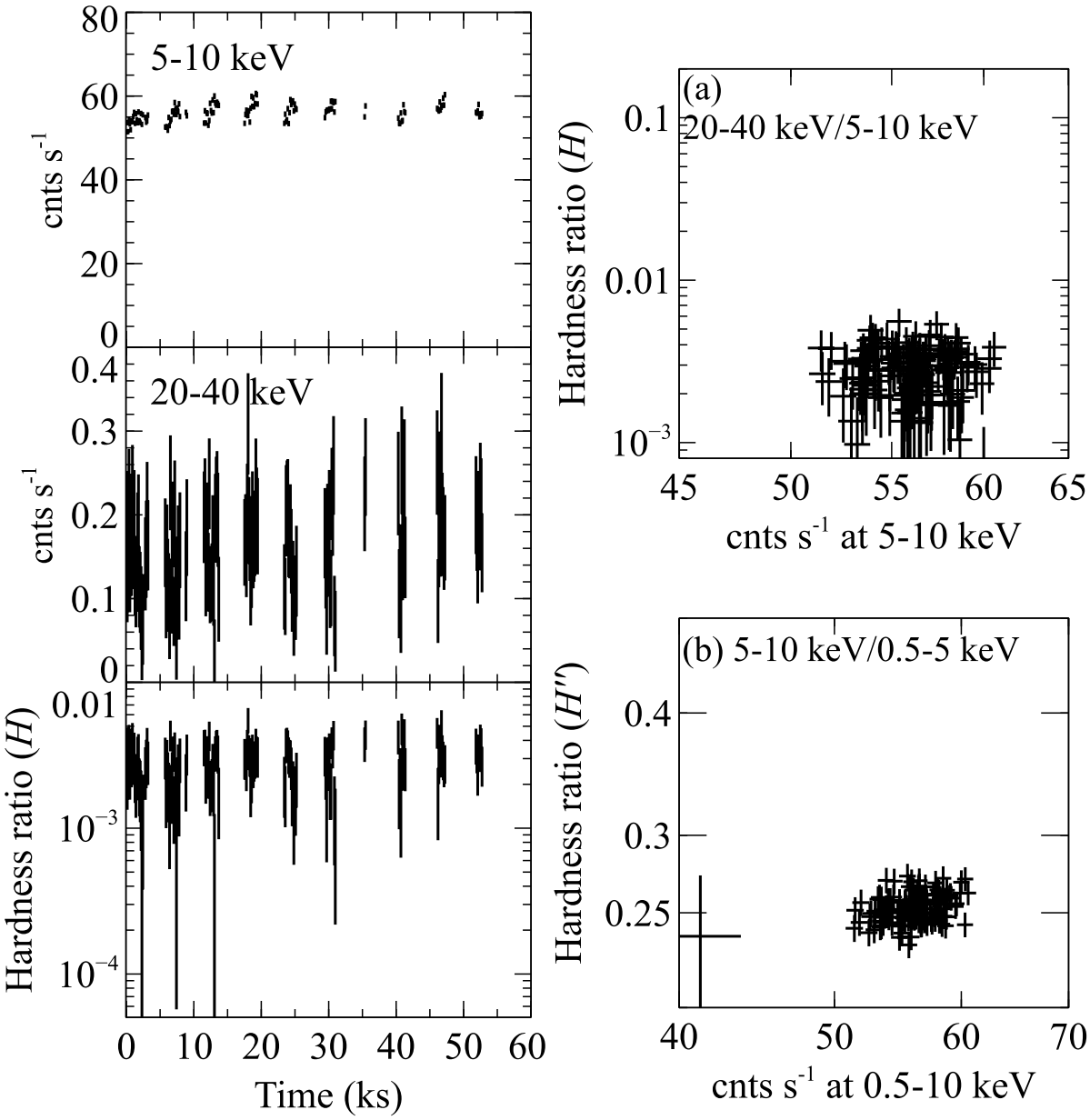

Figure A.5: The same *Suzaku* data as figure 4.9, but for 4U1705-44 #5.

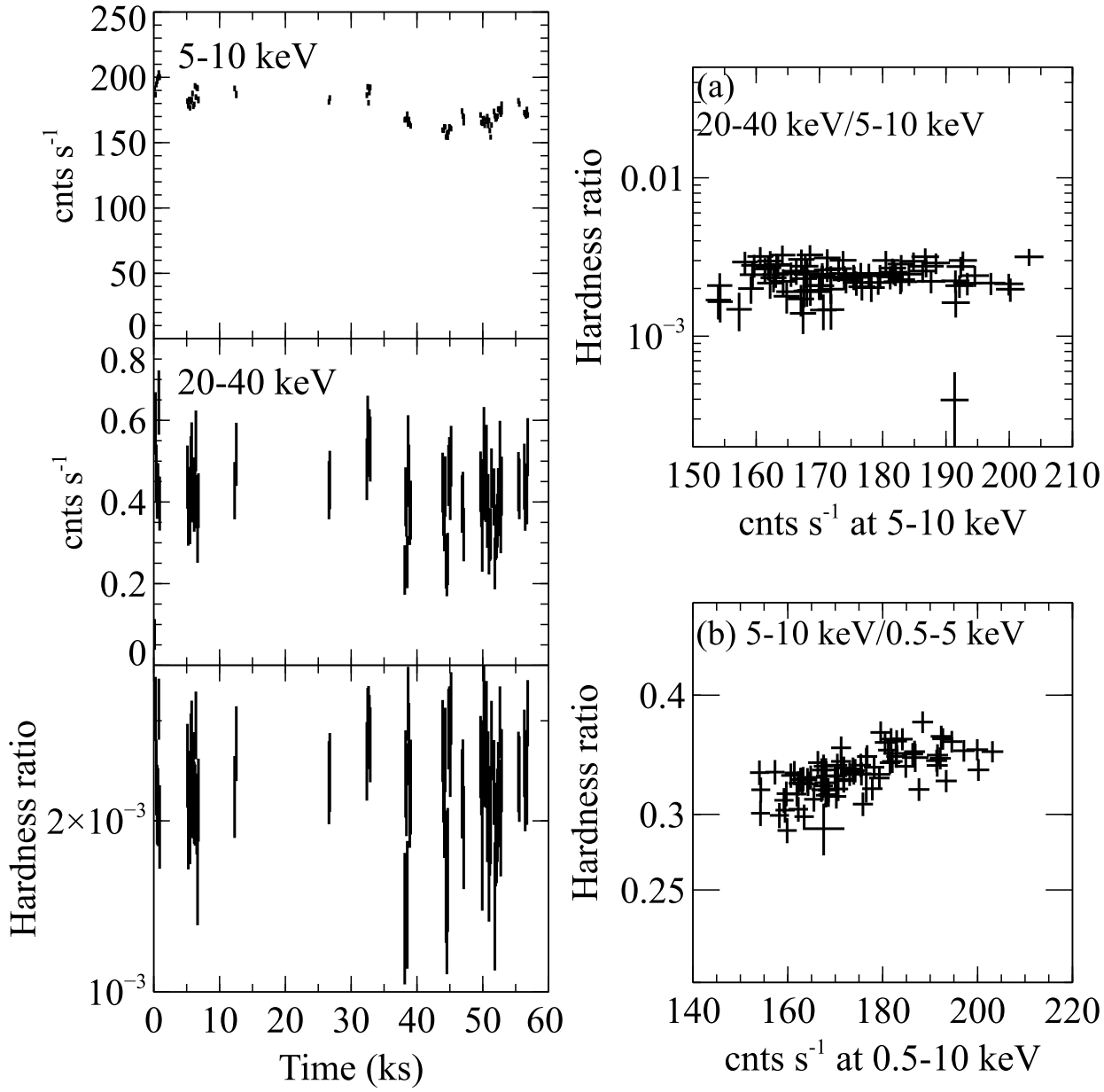

Figure A.6: The same *Suzaku* data as figure 4.9, but for 4U1705-44 #6.

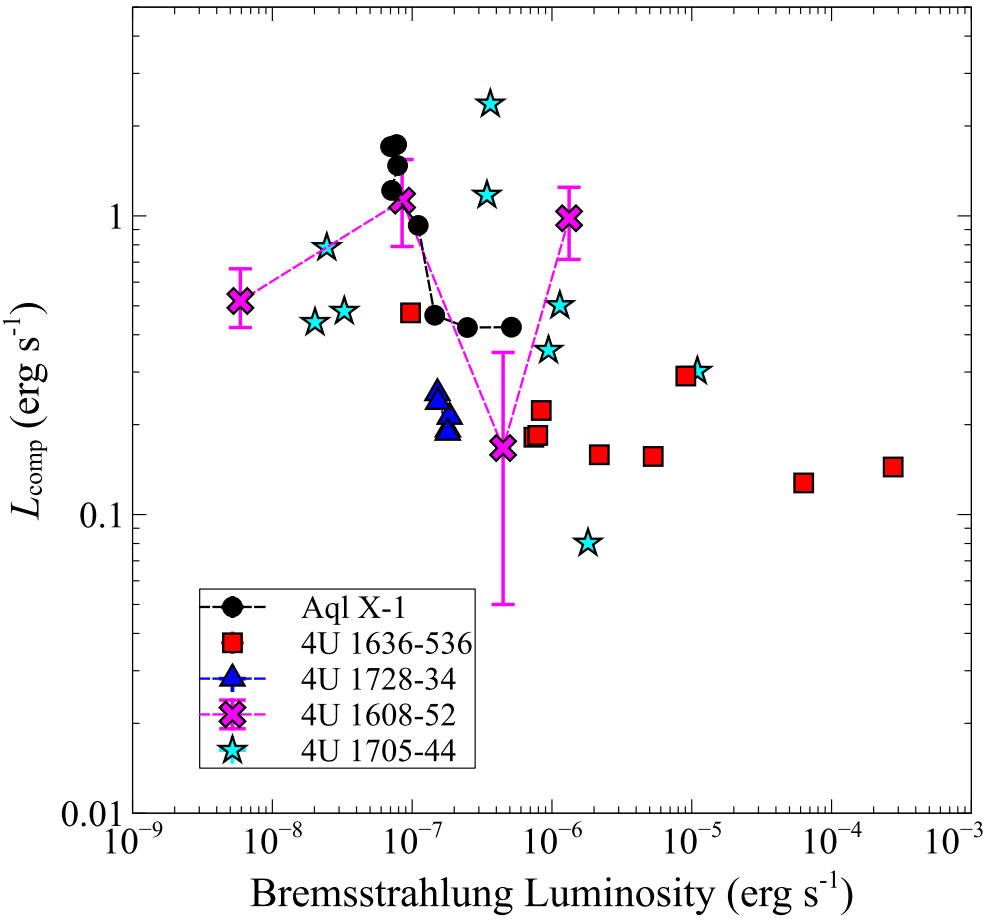

Figure A.7: Comparison of $L_{\rm comp}$ and an estimated coronal luminosity by the bremsstrahlung, using $n_{\rm e}$ in eq. (6.9) and eq. (6.11).